Seismic liquefaction analysis of a critical facility with PM4Sand in Plaxis

by

Victor Hugo Portugal Quevedo

to obtain the degree of Master of Science
at the Delft University of Technology,
to be defended publicly on Friday December 20, 2019 at 13:00.

Committee members
Prof. dr. Michael A. Hicks (TU Delft)
Dr. ir. Ronald B. J. Brinkgreve (TU Delft)
Assistant Prof. dr. Federico Pisanò (TU Delft)
Dr. ir. Carolina Sigaran-Loria (Royal HaskoningDHV)
M.Sc. ir. Jan Doeksen (Royal HaskoningDHV)

Civil Engineering and Geosciences
Delft University of Technology
Netherlands
December, 2019

Royal HaskoningDHV
Enhancing Society Together

TU Delft Delft University of Technology

Abstract

In seismically active areas, liquefaction hazards have always been a complicated aspect to evaluate as part of the seismic design of a project. In the case of the design of critical facilities, this becomes crucial, as beyond design basis conditions may elevate the seismic loads significantly and create a considerable liquefaction risk in areas of deep alluvial deposits. Furthermore, traditional semi-empirical methods lose their applicability at depths larger than 15 m, which becomes problematic if one wishes to analyse the liquefaction hazard of deep Holocene deposits. Given this shortcoming and the rapid growth of numerical tools available for geotechnical earthquake engineering, the use of liquefaction-predicting constitutive models, like PM4Sand, provides the opportunity to obtain more accurate and physically-consistent results. For this purpose, this research is divided in three main parts. The first part covers the study of the onset of liquefaction with the use of two cyclic undrained direct simple shear test databases and the identification of liquefaction-triggering criteria, in terms of pore pressures and shear strains which can consistently define a liquefied state in sands. The second part includes the thorough analysis of the capabilities of the PM4Sand model, in Plaxis, through a benchmark calibration study using one of the previously mentioned laboratory test databases, concluding in the proposal of a modified calibration methodology based on r_u and γ liquefaction-triggering criteria. The third and last part covered a practical case study oriented towards the design of a critical facility, where a beyond design liquefaction hazard analysis of a hypothetical site was evaluated incorporating the findings from the previous parts. A one-dimensional liquefaction hazard analysis was performed using a single earthquake signal and soil profile, where the consistency of the PM4Sand model in terms of liquefaction-triggering was evaluated and the numerically-obtained results were compared to those calculated through one semi-empirical method. Additionally, the one-dimensional model was extended and a two-dimensional liquefaction hazard analysis, including the presence of a simplified structure, was performed with the aim of evaluating the effects of soil-structure interaction and structural load variation on the liquefaction hazard of the soil profile over distance.

Executive summary

The main goal of this research was to find a way to adequately implement theoretical and experimental knowledge regarding liquefaction behaviour into methods used for the practical evaluation of liquefaction hazard. Given that semi-empirical methods lose their applicability at very shallow depths, it was deemed advantageous to thoroughly study liquefaction through the use of cyclic undrained direct simple shear databases and implement the findings through the calibration and implementation of the PM4Sand in a practical case. For this purpose the dissertation was structured as shown below, where the main objects and findings are described.

1. The first part of the dissertation involved the thorough study of cyclic undrained behaviour using as reference 2 cyclic undrained direct simple shear test databases. The available tests were analysed and relevant liquefaction-triggering criteria were evaluated in terms of moment of occurrence, relationship to each other and variations between different types of shearing and initial state conditions in sands. The main findings were that liquefaction can be quantitatively characterised for sands in general using two parameters and corresponding values: $r_u = 0.95$ and $\gamma = 3\%$. These criteria were used to calibrate the PM4Sand layers in both the second and third parts of this dissertation.

2. The second part involved the creation of a benchmark calibration study, where the previously found liquefaction triggers were used to try and simulate dense and loose sand behaviour shared at different conditions. The main findings were that the PM4Sand model was able to capture net contractive behaviour reasonably well, whereas it had great difficulty modelling net dilative behaviour, which is typical of dense sands. This was the reason why a second calibration methodology was proposed, where both previously mentioned liquefaction triggers were used to calibrate the model and the h_{p0}-parameter was adjusted to try and reach both markers while allowing D_{R0} to reduce. The implementation of this calibration methodology allowed for the consistent triggering of liquefaction both in terms of pore pressures and shear strains. This was especially true for sands with net dilative behaviour.

3. The third part presented a two-part case study involving a 1D liquefaction hazard analysis, where the effectiveness of the PM4Sand model with two calibration methodologies was evaluated, and a 2D liquefaction hazard analysis including the presence of a simplified structure, where the main objective was to determine if the presence of soil-structure interactions were detrimental to the soil profile's liquefaction resistance. Additionally, 1-dimensional results were compared to semi-empirically obtained ones to demonstrate the advantage of the use of properly-calibrated numerical tools. The research concluded that the proposed calibration methodology properly identified the triggering of liquefaction in a physically-consistent manner in the one-dimensional model, complying with experimental behaviour of liquefaction in terms of pore pressure and shear strain evolution. Also, the numerically-obtained results showed a significant reduction in liquefaction risk compared to results calculated with the semi-empirical method, which may lead to improvements in the liquefaction hazard assessment of foundations in general. The study also concluded that soil-structure interactions do have a detrimental effect on the liquefaction hazard of

the soil profile, increasing the presence of liquefied regions approximately within a 10 m thick annulus around the structure. Lastly, structural load variations do not seem to have a significant effect on liquefaction hazard if the dimensions of the structure are maintained.

Acknowledgements

Research in engineering is always a collective effort, which is why I would like to express my gratitude to all the professors, professionals and colleagues who helped me achieve my goal of doing interesting and useful research in geotechnical earthquake engineering. First, I would like to give a very special thanks to my company and university supervisors, Carolina Sigaran-Loria and Jan Doeksen, from Royal HaskoningDHV, and Ronald Brinkgreve, Federico Pisanò and Michael Hicks, from the faculty of Civil Engineering and Geosciences at Delft University of Technology. Their expertise in geotechnical and earthquake engineering, both practical and in numerical modelling, helped me immensely in adequately interpreting my results and in brainstorming all aspects of my research during long hours of discussion. Second, I would like to thank Royal HaskoningDHV for sponsoring my research, as well as all of my Royal HaskoningDHV colleagues. Especially, I would like to extend my gratitude to Ravikanth Chinthapandu, Tina Marinatou, Antonios Mavritsakis, Shuhong Tan and Raluca Toma who helped me with my simulations, with whom I bounced off ideas during my research and who provided me with valuable opinions when analysing my results. Lastly, I would like to thank all my MSc colleagues and friends with whom I shared countless hours of work and fun throughout the master's programme. Their moral support and personalities fuelled and inspired me every step along the way.

Dedication

I dedicate this to my family. Their unending support, encouragement and guidance allowed me to fulfil my dream of studying abroad and to overcome all the obstacles that reaching this goal involved. And to my new family here in the Netherlands and spread around the world, for sharing a little bit of themselves with me and for making me feel at home half a world away from my own. To all, thank you for all the love and joy you bring to my life.

Nomenclature

Technical terms

ALS Accidental limit state

ANVS Authority for Nuclear Safety and Radiation Protection

ATH Acceleration time history

BDBE Beyond design basis earthquake

CM Calibration methodology

CPT Cone penetration test or testing (continuous)

CRR [-] Cyclic resistance ratio

CS Critical state

CSR [-] Cyclic stress ratio

CUDSS Cyclic undrained direct simple shear

DA Double amplitude (used in terms of cyclic shear strain)

DSS Direct simple shear

EG2018 *CUDSS* test database from El Ghoraiby and Manzari (2018)

FE Finite element

FD Finite difference

FLAC Fast Lagrangian Analysis of Continua

GP USCS classification acronym for poorly graded gravels

GW USCS classification acronym for well graded gravels

GWT Ground water table

HSsmall Hardening Soil model compatible with small-strain behaviour

IAEA International Atomic Energy Agency

JSSMFE Japanese Society of Soil Mechanics and Foundation Engineering

LPA Liquefaction potential analysis

MUDSS Monotonic undrained direct simple shear

NIST National Institute of Standard and Technology

PB2016 *CUDSS* test database from Parra, 2016

PEER Pacific Earthquake Engineering Research Center

PGA Peak ground acceleration

PGD Peak ground displacement

PGV Peak ground velocity

PM4Sand Sand plasticity model for geotechnical earthquake engineering applications created by (Boulanger and Ziotopoulou, 2017)

SA Single amplitude (used in terms of cyclic shear strain)

SAR Strain accumulation rate

SBL Seismic base layer

SLS Serviceability limit state

SP USCS classification acronym for poorly graded sands

SPT Standard penetration test or testing

SRA Site response analysis

SS Steady state

SSI Soil-structure interaction

SW USCS classification acronym for well graded sands

TXC Triaxial compression test

TXE Triaxial extension test

UCB University of California at Berkeley

UCD University of California at Davis

ULS Ultimate limit state

USCS Unified soil classification system

USNRC United States Nuclear Regulatory Commission

UW Unit weight abbreviation

Variables

α **[-]** Static shear stress ratio, defined by $\frac{\tau_{static}}{\sigma'_{v0}}$

$\alpha_{\mathbf{R}}$ **[-]** Rayleigh damping coefficient modifies the mass matrix in the equation of motion

$\mathbf{a_{max}}$ **[L/T²]** Maximum horizontal ground surface acceleration

$\beta_{\mathbf{R}}$ **[-]** Rayleigh damping coefficient modifies the stiffness matrix in the equation of motion

$\mathbf{C_c}$ **[-]** Curvature index of particle size distribution

$\mathbf{C_u}$ **[-]** Uniformity index of particle size distribution

$\mathbf{C_V}$ **[-]** Shear wave overburden correction factor according to Andrus and Stokoe (2000)

$\mathbf{D_{10}}$ **[%]** Sieve opening size that allows 10% of the total soil mass to pass

$\mathbf{D_{30}}$ **[%]** Sieve opening size that allows 30% of the total soil mass to pass

$\mathbf{D_{50}}$ **[%]** Sieve opening size that allows 50% of the total soil mass to pass

$\mathbf{D_{60}}$ **[%]** Sieve opening size that allows 60% of the total soil mass to pass

$\mathbf{D_{R0}}$ **[- or %]** In-situ relative density of soil deposit, primary soil parameter used in the PM4Sand model

η **[-]** Soil porosity

$\mathbf{E_{50}^{ref}}$ **[F/L²]** Reference secant elastic modulus of soil (taken at 50% of the ultimate stress)

$\mathbf{E_{oed}^{ref}}$ **[F/L²]** Reference oedometric elastic modulus of soil, used in the HSsmall model

$\mathbf{E_{ur}^{ref}}$ **[F/L²]** Reference unload/reload elastic modulus of soil, used in the HSsmall model

$\mathbf{e_0}$ **[-]** Initial void ratio

$\mathbf{e_{max}}$ **[-]** Maximum void ratio

$\mathbf{e_{min}}$ **[-]** Minimum void ratio

FC [- or %] Fines content

$\mathbf{f_{ck}}$ **[F/L²]** Characteristic compressive strength of concrete

γ **[- or %]** Shear strain

$\gamma_{0.7}$ **[- or %]** Reference shear strain for the small-strain shear modulus degradation curve, used in the HSsmall model

γ_{sat} **[F/L³]** Saturated unit weight of soil

γ_{dry} **[F/L³]** Dry unit weight of soil

g [L/T²] Gravitational acceleration experienced at ground level (assumed as 9.81 m/s^2)

$\mathbf{G_0}$ **[-]** Normalised initial, or maximum, small-strain shear modulus or modulus coefficient, primary model parameter used in the PM4Sand model

$\mathbf{G_0^{ref}}$ **[F/L²]** Reference small-strain shear modulus used in the HSsmall model

$\mathbf{G_{max}}$ **[F/L²]** Initial, or maximum, small-strain shear modulus

$\mathbf{G_s}$ **[-]** Specific gravity

$\mathbf{h_{p0}}$ **[-]** Primary model parameter of the PM4Sand model describing the cyclic resistance of the sample

$\mathbf{I_c}$ **[-]** Soil behaviour type index specified in Robertson (2010)

k [L/T] Hydraulic conductivity (permeability) of soil

$\mathbf{K_0}$ **[-]** In-situ lateral earth pressure coefficient (includes OCR effect)

$\mathbf{K_0^{nc}}$ **[-]** Normally consolidated in-situ lateral earth pressure coefficient

$\mathbf{K_\sigma}$ **[-]** Overburden stress correction factor for cyclic resistance ratio

MSF [-] Magnitude scaling factor for cyclic resistance ratio

$\mathbf{M_w}$ **[-]** Moment magnitude of earthquake motion

N [-] Blow count for *SPT*

$(\mathbf{N_1})_{60}$ **[-]** Normalised blow count for *SPT*

OCR [-] Overconsolidation ratio

p [F/L²] Mean total stress

$\mathbf{p_a}$ **[F/L²]** Atmospheric pressure at sea level (= 101.3 kPa)

$\mathbf{p'}$ **[F/L²]** Mean effective stress

$\mathbf{p'_c}$ **[F/L²]** Mean effective confinement stress

$\phi'_\mathbf{p}$ **[°]** Peak effective friction angle

$\phi'_\mathbf{cv}$ **[°]** Steady-state or constant volume friction angle, secondary model parameter used in the PM4Sand model

PGA [L/T²] Peak ground acceleration

PGV [L/T] Peak ground velocity

PGD [L] Peak ground displacement

q [F/L²] Deviatoric stress

$\mathbf{Q}$ **[-]**	Bolton's parameter, assumed equal to 10 for quartzitic sands, secondary parameter used in the PM4Sand model
$\mathbf{q_c}$ **[F/L^2]**	Cone penetration resistance for *CPT*
$\mathbf{q_{c1N}}$ **[-]**	Normalised cone penetration resistance for *CPT*
$\mathbf{q_{c1N,cs}}$ **[-]**	Normalised cone penetration resistance, fines-corrected, for *CPT*
$\mathbf{R}$ **[-]**	Bolton's parameter, secondary parameter used in the PM4Sand model
$\rho_\mathbf{w}$ **[M/L^3]**	Density of water
$\mathbf{r_u}$ **[-]**	Pore water pressure ratio, defined as u/σ'_{v0}
$\sigma_\mathbf{v}$ **[F/L^2]**	Total vertical stress
$\sigma'_\mathbf{v}$ **[F/L^2]**	Effective vertical stress
$\sigma'_\mathbf{v0}$ **[F/L^2]**	Initial vertical effective stress
$\sigma'_\mathbf{v}/\sigma'_\mathbf{v0}$ **[-]**	Normalised vertical effective stress
τ **[F/L^2]**	Shear stress
$(\tau_\mathbf{max})_\mathbf{r}$ **[F/L^2]**	Maximum horizontal earthquake-induced shear stress applied at the base of the soil column using Seed and Idriss's simplified method
$\tau/\sigma'_\mathbf{v0}$ **[-]**	Normalised shear stress
$\mathbf{u}$ **[F/L^2]**	Pore water pressure
$\mathbf{V_s}$ **[L/T]**	Shear wave velocity
$\mathbf{V_{s1}}$ **[L/T]**	Normalised shear wave velocity
$\xi_\mathbf{R}$ **[-]**	relative state parameter index
$\mathbf{z}$ **[L]**	Depth

Contents

Abstract i

Executive summary iii

Acknowledgements iv

Dedication v

Nomenclature vii

Introduction 1

I Theoretical background and literature review 2

---

1 What is liquefaction? 3

2 Reference soil for benchmark calibration study: Ottawa F-65 sand 5
2.1 Characterisation of Ottawa F-65 sand . . . 5
2.1.1 Grain size distribution . . . 6
2.1.2 Specific gravity . . . 7
2.1.3 Maximum and minimum void ratios . . . 7
2.1.4 Hydraulic conductivity . . . 8
2.1.5 Shear wave velocity, small-strain shear modulus and modulus coefficient . 10
2.2 Direct simple shear testing . . . 14
2.3 Undrained monotonic behaviour . . . 15
2.3.1 The steady-state line . . . 15
2.3.2 The steady-state friction angle . . . 17
2.4 Undrained cyclic behaviour . . . 17
2.4.1 Effect of initial relative density . . . 18
2.4.2 Effect of effective vertical confinement pressure . . . 19
2.4.3 Effect of cyclic stress ratio . . . 19
2.4.4 Effect of duration of cyclic loading . . . 20
2.4.5 Effect of sample disturbances or accidental biases . . . 20
2.5 Preliminary conclusions regarding the cyclic undrained behaviour of Ottawa F-65 sand . . . 21

3 Evaluation of liquefaction-triggering criteria 28
3.1 Liquefaction-triggering analysis in loose and dense sands using *CUDSS* tests on Ottawa F-65 sand . . . 29
3.1.1 Preliminary remarks on *CUDSS* test groups . . . 34
3.1.2 Effect of *CSR* on the behaviour of liquefaction in loose and dense sands . 34

3.1.3 Effect of confinement pressure on liquefaction onset in loose and dense sands 40
3.2 Discussion and preliminary conclusions regarding liquefaction-onset in loose and dense Ottawa F-65 sand . . . 41

4 The PM4Sand model 52
4.1 Model input parameters . . . 54

II Benchmark calibration study using the PM4Sand model 57

5 A unified calibration methodology 58

6 Calibration of the PM4Sand model using *CUDSS* tests from PB2016 62
6.1 Discussion and preliminary conclusions regarding the benchmark calibration study 68
6.1.1 Parameter trends found . . . 68
6.1.2 Limitations of the PM4Sand model . . . 69
6.1.3 Remarks regarding the calibration process for PM4Sand . . . 70

III Practical case study 72

7 Introduction to the case study 73
7.1 Design philosophy of a critical facility and earthquake input motion . . . 73
7.2 Site characterisation . . . 75
7.2.1 Power of stress-level dependency **m** . . . 77
7.2.2 Fines content . . . 77
7.2.3 Estimation of e_{max}, e_{min} and D_{R0} . . . 79
7.2.4 Rayleigh damping ratios α and β . . . 79
7.2.5 Cyclic resistance ratios . . . 80
7.3 Calibration of liquefiable layers . . . 81

8 1D site response and liquefaction potential analysis 93
8.1 Site response analysis of the 1D soil column using only HSsmall . . . 94
8.1.1 Modelling conditions . . . 94
8.2 1D liquefaction hazard assessment with PM4Sand in Plaxis . . . 95
8.2.1 Liquefaction hazard in model when subjected to the Umbria Marche *BDBE* signal . . . 95
8.3 Comparison of numerical and semi-empirical liquefaction hazard assessment results 106
8.4 Discussion and preliminary conclusions regarding the liquefaction potential analysis in a 1D setting . . . 107

9 2D liquefaction hazard 110
9.1 Mesh- and domain-size sensitivity analyses . . . 111
9.1.1 Mesh size sensitivity . . . 111
9.1.2 Domain size sensitivity . . . 118
9.2 Soil-structure interaction effects on liquefaction hazard . . . 120
9.2.1 Comparison of 1D and 2D liquefaction hazard under supposed free-field conditions . . . 121
9.2.2 Evaluation of soil-structure interaction effects on liquefaction hazard over distance . . . 123

9.2.3 Evaluation of effects of structural load variation on liquefaction hazard over distance . . . 124
9.3 Discussion and preliminary conclusions regarding the soil-structure interaction effect on liquefaction hazard in 2D . . . 124

IV Conclusions and recommendations 126

10 Conclusions and recommendations 127
10.1 Conclusions . . . 127
10.1.1 Regarding the characterisation of Ottawa F-65 sand . . . 127
10.1.2 Regarding the identification of quantitative measurements to define liquefaction . . . 127
10.1.3 Regarding the modelling effectiveness of PM4Sand . . . 128
10.1.4 Regarding the proposed calibration methodology . . . 128
10.1.5 Regarding the 1D liquefaction hazard analysis . . . 128
10.1.6 Regarding soil-structure interaction effects on liquefaction hazard . . . 129
10.2 Recommendations . . . 129
10.2.1 Regarding future research . . . 129
10.2.2 Regarding engineering applications . . . 130

Bibliography 136

Appendix 136

List of Figures

1.1 Consequences of liquefaction after the Canterbury, New Zealand, 2011 earthquake 3

2.1 Gradation curve of Ottawa F-65 sand from Parra (2016) 7
2.2 Comparison of mean maximum and minimum void ratios from Cooper Lab (2013), Parra (2016), Ruffatto (2013) and Vasko et al. (2014). 8
2.3 Comparison of hydraulic conductivity trends from different sources 10
2.4 Shear wave velocity dependence on porosity (a) and confinement pressure (b) (Huang et al., 2017) 11
2.5 Comparison of several V_{s1}-correlations with measured values in EG2018 12
2.6 Comparison of estimated G_0-values for dense sands in EG2018 at 40 kPa and 100 kPa 13
2.7 Direct simple shear test and primary mode of deformation (Klar et al., 2019) . . 14
2.8 Comparison of steady-state lines, according to Boulanger (2003), fitted to *MUDSS* samples which have reached or were close to reaching the steady-state. 16
2.9 Determination of ϕ_{cv} 17
2.10 Effect of σ'_{vc} on cyclic resistance in terms of pore water pressure evolution in *CUDSS* test samples from Parra (2016) and El Ghoraiby and Manzari (2018) . . 22
2.11 Effect of σ'_{vc} on cyclic resistance in terms of stress-strain behaviour in *CUDSS* test samples from Parra (2016) and El Ghoraiby and Manzari (2018) 23
2.12 Effect of *CSR* on cyclic resistance in terms of pore water pressure evolution in *CUDSS* test samples from Parra (2016) (loose samples sheared at low to intermediate *CSRs* and dense samples sheared at high *CSRs*) 24
2.13 Effect of *CSR* on cyclic resistance in terms of stress-strain behaviour evolution in *CUDSS* test samples from Parra (2016) (loose samples sheared at low to intermediate *CSRs* and dense samples sheared at high *CSRs*) 25
2.14 Effect of *CSR* on cyclic resistance in terms of pore water pressure evolution in *CUDSS* test samples from Parra (2016) and El Ghoraiby and Manzari (2018) sheared within a low to intermediate range of *CSRs*. 26
2.15 Effect of apparent unintentionally-introduced bias in *CUDSS* test sample from El Ghoraiby and Manzari (2018) compared to a *CUDSS* test sample with no apparent bias from Parra (2016) 27

3.1 Illustration of identification of r_u and γ liquefaction-triggering markers in loose (a, c) and dense (b, d) Ottawa F-65 sand samples from Parra (2016) in terms of pore pressure accumulation and stress-strain behaviour 30
3.2 Comparison of triggering of γ-thresholds in loose and dense samples confined at 100 kPa and sheared at a comparable *CSR* 36
3.3 Outlying test results in dense Ottawa F-65 sand *CUDSS* tests confined at 50 kPa from PB2016 37

3.4 Abnormality of stress-strain behaviour in dense *CUDSS* tests from El Ghoraiby and Manzari (2018) compared to typically observed cyclic stress-strain behaviour in dense sands in Parra (2016), El Ghoraiby, Park, et al. (2017) and Sriskandakumar (2004) 39
3.5 Group 1: Analysis of liquefaction onset in dense Ottawa F-65 sand *CUDSS* tests from El Ghoraiby and Manzari (2018) confined at 40 kPa and with increasing *CSR* 43
3.6 Group 2: Analysis of liquefaction onset in dense Ottawa F-65 sand *CUDSS* tests from Parra (2016) confined at 50 kPa and with increasing *CSR* 44
3.7 Group 3a: Analysis of liquefaction onset in loose and dense Ottawa F-65 sand *CUDSS* tests from Parra (2016) confined at 100 kPa and with increasing *CSR* . . 45
3.8 Group 3b: Analysis of liquefaction onset in loose and dense Ottawa F-65 sand *CUDSS* tests from Parra (2016) and El Ghoraiby and Manzari (2018), respectively, confined at 100 kPa and with increasing *CSR* 46
3.9 Group 3c: Analysis of liquefaction onset in dense Ottawa F-65 sand *CUDSS* tests from El Ghoraiby and Manzari (2018) confined at 100 kPa and with increasing *CSR* 47
3.10 Group 4: Analysis of liquefaction onset in loose and dense Ottawa F-65 sand *CUDSS* tests from Parra (2016) confined at 400 kPa and with increasing *CSR* . . 48
3.11 Group 5a: Analysis of liquefaction onset in loose and dense Ottawa F-65 sand *CUDSS* tests from Parra (2016) at equivalent *CSRs* and increasing confinement pressure 49
3.12 Group 5b: Analysis of liquefaction onset in loose and dense Ottawa F-65 sand *CUDSS* tests from Parra (2016) at equivalent *CSRs* and increasing confinement pressure 50
3.13 Group 6: Analysis of liquefaction onset in dense Ottawa F-65 sand *CUDSS* tests from El Ghoraiby and Manzari (2018) at equivalent *CSRs* and increasing confinement pressure 51

6.1 $N - r_u$-evolution curves of selected loose and dense sands at 50, 100 and 400 kPa confinement pressures from PB2016, including liquefaction-triggering markers, to illustrate the calibration process 64
6.2 Comparison of $N - r_u$-curves of selected loose and dense sands at 50, 100 and 400 kPa confinement pressures from PB2016 and calibrated model with *CM1* and *CM2*. 65
6.3 γ-evolution curves of selected loose and dense sands at 50, 100 and 400 kPa confinement pressures from PB2016, including liquefaction-triggering markers, to illustrate the calibration process 66
6.4 Comparison of $N - \gamma$-curves of selected loose and dense sands at 50, 100 and 400 kPa confinement pressures from PB2016 and calibrated model with *CM1* and *CM2* 67
6.5 h_{p0}-trends of all calibrated *CUDSS* tests from PB2016 using calibration methodologies *CM1* and *CM2*. 69

7.1 Umbria Marche *BDBE* signal (scaled from original signal which occurred in September 1997) 75
7.2 Generalised soil profile for case study 76
7.3 G_0 degradation curves for all soil profile sub-layers 77
7.4 Transformation of q_c- to $q_{c1N,cs}$-magnitudes 78
7.5 $q_{c1N,cs}$- and calculated D_{R0}-profiles of the entire soil column domain 80
7.6 Calculated $q_{c1N,cs}$- and CRR-profiles of liquefiable layers 82
7.7 Zonification of PM4sand and HSsmall modelled regions and estimated CRR-magnitudes for calibration 84
7.8 Calibrated $N - r_u$ curves using calibration methodologies 1 and 2 of shallow and deep layers 1-3-NASC-MS and 7-1-EE-MS, respectively. 85

7.9 Calibrated $N-\gamma$ curves using calibration methodologies 1 and 2 of shallow and deep layers 1-3-NASC-MS and 7-1-EE-MS, respectively. 86
7.10 to obtain *CM2*-based calibrated parameters 86

8.1 Comparison of Umbria Marche *BDBE PGA*- and *PGD*-profiles in an *SRA* and *LPA* setting, using both *CM1* and *CM2* to calibrate the PM4Sand layers 97
8.2 r_u- and γ-time histories responses to the Umbria Marche *BDBE* signal at select points within layer 1-NASC-MS. 98
8.3 r_u- and γ-time histories responses to the Umbria Marche *BDBE* signal at select points within layer 3-BX-FS. 100
8.4 r_u- and γ-time histories responses to the Umbria Marche *BDBE* signal at select points within layer 3-BX-FS (continued). 101
8.5 r_u- and γ-time histories responses to the Umbria Marche *BDBE* signal at select points within layer 5-BX-MS. 102
8.6 r_u- and γ-time histories responses to the Umbria Marche *BDBE* signal at select points within layer 7-EE-MS. 103
8.7 Comparison of Umbria Marche *BDBE* $r_{u,max}$- and γ- profiles of *CM1* and *CM2* models 104
8.8 Comparison of Umbria Marche *BDBE SRA* and *LPA*-*CM2* acceleration time histories at select locations along depth 105
8.9 Comparison of semi-empirically-calculated and numerically-calculated safety factors against liquefaction using *CRR*-values calculated with method proposed by Idriss and Boulanger (2014). 107

9.1 Vertical distribution of $r_{u,max}$-magnitudes in models with specified mesh sizes of 0.25 m to 4.00 m. 113
9.2 Vertical distribution of $r_{u,max}$-magnitudes in models with specified mesh sizes of 0.25 m and 4.50 m to 15.00 m. 114
9.3 Percentage of frequency of occurrence within specific $r_{u,max}$-ranges. 115
9.4 Percentage of frequency of occurrence within specific $r_{u,max}$-ranges. 116
9.5 Horizontal distribution of $r_{u,max}$-magnitudes of models with specified mesh sizes of 0.25 m to 2.00 m. 117
9.6 Comparison of $r_{u,max}$-magnitude distributions between models using 15-node and 6-node elements. 117
9.7 Vertical distribution of $r_{u,max}$-magnitudes in models with domain sizes from 0.25 m to 4.50 m. 119
9.8 Percentage of frequency of occurrence within specific $r_{u,max}$-ranges in domain-size sensitivity analysis 120
9.9 Area of influence of static structural load before the start of the earthquake signal 121
9.10 Comparison of $r_{u,max}$-profiles at supposed free-field conditions in 1D and 2D settings 122

10.1 Comparison of calibrated *CM1* and *CM2* models in layer 1-3-NASC-MS 138
10.2 Comparison of calibrated *CM1* and *CM2* models in layer 1-4-NASC-MS 139
10.3 Comparison of calibrated *CM1* and *CM2* models in layer 1-5-NASC-MS 140
10.4 Comparison of calibrated *CM1* and *CM2* models in layer 3-1-BX-FS 141
10.5 Comparison of calibrated *CM1* and *CM2* models in layer 3-2-BX-FS 142
10.6 Comparison of calibrated *CM1* and *CM2* models in layer 3-3-BX-FS 143
10.7 Comparison of calibrated *CM1* and *CM2* models in layer 3-4-BX-FS 144
10.8 Comparison of calibrated *CM1* and *CM2* models in layer 5-BX-MS 145
10.9 Comparison of calibrated *CM1* and *CM2* models in layer 7-1-EE-MS 146
10.10Comparison of calibrated *CM1* and *CM2* models in layer 7-2-EE-MS 147
10.11Comparison of calibrated *CM1* and *CM2* models in layer 7-3-EE-MS 148

10.12Comparison of calibrated *CM1* and *CM2* models in layer 7-4-EE-MS 149
10.13Comparison of calibrated *CM1* and *CM2* models in layer 7-5-EE-MS 150
10.141D r_u-time history response of layer 1-NASC-MS at all and select locations to Umbria Marche *BDBE* signal 151
10.151D r_u-time history response of layer 3-BX-FS at all and select locations to Umbria Marche *BDBE* signal 152
10.161D r_u-time history response of layer 5-BX-MS at all and select locations to Umbria Marche *BDBE* signal 153
10.171D r_u-time history response of layer 7-EE-MS at all and select locations to Umbria Marche *BDBE* signal 154
10.181D γ-time history response of layer 1-NASC-MS at all and select locations to Umbria Marche *BDBE* signal 155
10.191D γ-time history response of layer 3-BX-FS at all and select locations to Umbria Marche *BDBE* signal 156
10.201D γ-time history response of layer 5-BX-MS at all and select locations to Umbria Marche *BDBE* signal 157
10.211D γ-time history response of layer 7-EE-MS at all and select locations to Umbria Marche *BDBE* signal 158
10.22Umbria Marche *BDBE* comparison of *SRA* and *LPA-CM1 ATHs* 159
10.23Umbria Marche *BDBE* comparison of *SRA* and *LPA-CM1 ATHs* (continued) . . 160
10.24Umbria Marche *BDBE* comparison of *SRA* and *LPA-CM1 ATHs* (continued) . . 161
10.25Umbria Marche *BDBE* comparison of *SRA* and *LPA-CM2 ATHs* 162
10.26Umbria Marche *BDBE* comparison of *SRA* and *LPA-CM2 ATHs* (continued) . . 163
10.27Umbria Marche *BDBE* comparison of *SRA* and *LPA-CM2 ATHs* (continued) . . 164
10.28$r_{u,max}$-contour map of the 2D model at the end of the Umbria Marche *BDBE* signal165
10.29Comparative overview of *PGA*-profiles at select distances from the centre of the structure for all three structural loads 166
10.30Comparative overview of *PGA*-profiles at select distances in the vicinity of the structure for all three structural loads 167
10.31Comparative overview of *PGD*-profiles at select distances from the centre of the structure for all three structural loads 168
10.32Comparative overview of *PGD*-profiles at select distances in the vicinity of the structure for all three structural loads 169
10.33Comparative overview of $r_{u,max}$-profiles at select distances from the centre of the structure for all three structural loads 170
10.34Comparative overview of $r_{u,max}$-profiles at select distances from the centre of the structure for all three structural loads (reduced r_u-scale) 171
10.35Comparative overview of $r_{u,max}$-profiles at select distances in the vicinity of the structure for all three structural loads 172
10.36Comparative overview of $r_{u,max}$-profiles at select distances in the vicinity of the structure for all three structural loads (reduced r_u-scale) 173
10.37Comparative analysis of effect of structural load on *PGA*-profiles at select distances from the centre of the structure (reduced *PGA*-scale) 174
10.38Comparative analysis of effect of structural load on *PGA*-profiles at select distances from the centre of the structure 175
10.39Comparative analysis of effect of structural load on *PGD*-profiles at select distances from the centre of the structure (reduced *PGD*-scale) 176
10.40Comparative analysis of effect of structural load on *PGD*-profiles at select distances from the centre of the structure 177
10.41Comparative analysis of effect of structural load on $r_{u,max}$-profiles at select distances from the centre of the structure (reduced *PGD*-scale) 178

10.42Comparative analysis of effect of structural load on $r_{u,max}$-profiles at select distances from the centre of the structure 179

List of Tables

2.1 Gradation characteristics of Ottawa F-65 sand used to characterise samples from Parra (2016) and El Ghoraiby and Manzari (2018) . . . 6
2.2 e_{max} and e_{min} from different researchers. . . . 8
2.3 k_{loose} and k_{dense} from different researchers. . . . 9
2.4 Sets of MUDSS samples which reached or were close to the steady state used for fitting the steady-state line defined by Boulanger (2003). . . . 16
2.5 Fitted values for R. . . . 16

3.1 Shear strain- and pore pressure-based liquefaction-triggering criteria found in literature . . . 29
3.2 *CUDSS* tests from El Ghoraiby and Manzari (2018) . . . 31
3.3 *CUDSS* tests from Parra (2016) . . . 32

5.1 Optimised secondary constitutive model parameters for the calibration of the PM4Sand model using Ottawa F-65 sand. . . . 60
5.2 Initial state and shearing conditions for *CUDSS* tests from Parra (2016) . . . 61

6.1 Calibrated constitutive model parameter sets for selected *CUDSS* tests from Parra (2016) . . . 63

7.1 Calibrated primary PM4Sand model parameters based on CRR calculated with $q_{c1N,cs}$-correlation from Idriss and Boulanger (2014) and using both calibration methodologies . . . 83
7.2 Soil layer descriptions at the hypothetical project site (*:Abbreviation; **: Relative to NAP) . . . 87
7.3 Soil layer descriptions at the hypothetical project site (continued; *:Abbreviation; **: Relative to NAP) . . . 88
7.4 Soil layer properties at the hypothetical project site . . . 89
7.5 Soil layer properties at the hypothetical project site (continued) . . . 90
7.6 Soil layer properties at the hypothetical project site (continued) . . . 91
7.7 Soil layer properties at the hypothetical project site (continued) . . . 92

8.1 Activation times of r_u- and γ-based liquefaction triggering criteria in layer 3-BX-FS in models *CM1* and *CM2* for Umbria Marche *BDBE* scenario (layers 3-2- and 3-4-BX-FS did not exhibit liquefaction) . . . 99

9.1 Average mesh size, element, node and stress-point numbers per specified referential mesh size. . . . 112
9.2 Average mesh size, element, node and stress-point numbers per specified domain width. . . . 118

Introduction

Liquefaction hazard is an intrinsic part of the seismic analysis and design of a structure when saturated alluvial deposits are present. Depending on the seismicity in the region, this hazard will fluctuate between minimal, or non-existent, and extremely likely. When considering the design of a critical facility, however, incorporating beyond design conditions for the seismic design significantly increases the likelihood of liquefaction occurring if the conditions are right. Furthermore, this increased hazard may extend downwards towards deep alluvial deposits of dense sands, depths at which semi-empirical correlations loose their validity. In view of this shortcoming, the use of numerical tools and liquefaction-triggering constitutive models become essential for such important projects. Therefore, this research aimed at understanding the process of liquefaction so that it could be adequately implemented in engineering design through the use of the PM4Sand model. For this purpose, the scope of this research included work related to two main research questions, containing 8 specific research sub-questions which were addressed throughout this document. Where relevant, each chapter addressed one or more sub-questions, which were evaluated and then referred to at the preliminary conclusions level at the end of each chapter.

1. How is the PM4Sand model calibrated?
    (a) How does sand behave under cyclic undrained loading conditions?
    (b) How can liquefaction-triggering criteria be quantitatively characterised?
    (c) Can the PM4Sand model adequately identify the triggering of liquefaction and simulate an adequate evolution of pore pressures and shear strains?
    (d) Can the PM4Sand model be calibrated in a way that is consistent with experimental findings?
    (e) Are there any trends in the PM4Sand model parameters given varying shearing conditions?
2. What is the added value of PM4Sand in practical applications?
    (a) What is the effect of the calibration methodology of PM4Sand on liquefaction hazard?
    (b) Does the implementation of the PM4Sand model provide better insight into liquefaction compared to semi-empirical methods?
    (c) What insight does the PM4Sand model provide in terms of soil-structure interaction effect on liquefaction hazard over distance? Do structural load variations affect the liquefaction hazard?

To tackle these research questions, this document was structured in three main parts. The first was oriented towards the study of the phenomenon of liquefaction, and how it can be quantitatively characterised within cyclic undrained behaviour in a laboratory setting. For this purpose, two cyclic undrained direct simple shear test database of Ottawa F-65 sand (Parra, 2016; El Ghoraiby and Manzari, 2018) were taken as a references for the analysis of monotonic and cyclic undrained behaviour of sands, as well as for the evaluation of the onset of liquefaction

and the identification of quantitative liquefaction-triggering criteria used as starting points for the calibration of liquefaction-simulating models like PM4sand. Additionally, an introductory chapter to the PM4Sand model was included. This leads to the second part of the dissertation, where these liquefaction-triggering criteria were used to try and replicate the cyclic undrained behaviour of one of the previous laboratory test databases. Based on the preliminary findings, part 2 concludes in the proposal of an optimised holistic calibration methodology for modelling liquefaction using PM4Sand which allows the user to identify liquefaction in a physically-consistent way. Next, part three presents the application of all previous findings into a two-part practical case study. First a 1D liquefaction hazard assessment of a soil profile is performed, where the effectiveness of the proposed calibration methodology was contrasted with the original one. Additionally, numerically-obtained results were compared to semi-empirically obtained ones, showing the advantage of the use of properly calibrated constitutive models in engineering design. Second, the 1D model was extended into a 2D model which evaluated liquefaction hazard with the presence of a simplified structure of a critical facility. Through this last exercise, the objective was to identify possible soil-structure interaction effects on the soil profile's initial liquefaction hazard, as well as determine if structural load variations had any additional effect on the latter.

In the interest of providing the reader with all the necessary information regarding elaboration of this dissertation, and given that this work had a limited time frame, the following limitations to the scope of the research apply and need to be taken into consideration.

- Out of the main sources for semi-empirical liquefaction potential correlations found in literature (Andrus, Hayati, et al., 2009; Idriss and Boulanger, 2010; Idriss and Boulanger, 2014; Robertson and Wride, 1998), only the ones proposed by Idriss and Boulanger; Robertson and Wride were included in the semi-empirical analysis. A third correlation, proposed by Andrus, Hayati, et al. (2009) was preliminarily evaluated, compared to the other correlations and deemed unreliable to be included in the final analysis.

- The scope of the benchmark study was limited to determining the optimised values for PM4Sand's primary model parameters. Most secondary model parameters were calibrated based on experimental data or left at their default values and were not optimised.

- The calibration methodology for the PM4Sand model in part III was limited intentionally in terms of secondary model parameters to try to account for most design situations, where very limited information is available. This meant that all secondary model parameters were left at default.

- For the soil-structure interaction analysis, an idealised block-structure was used. Simulating a detailed excavation, construction sequence or a piled foundation (which would be the go-to option in cases where liquefaction could be an issue) would have added much more computational cost to the already computationally-expensive 2D simulations. Therefore, given that the intention of this part of the research was to see the effect of soil-structure interaction on liquefaction hazard, the idealised block structure was assumed to have been installed via a Caisson-method.

- The evaluation of the beyond design basis seismic hazard in III focused only on the liquefaction hazard analysis and ignored potential structural damage that the simplified structure could have sustained. Including non-linear behaviour in the simplified structure would have expanded the scope of this dissertation, as well as exponentially increased the computational-cost of the 2D simulations.

Part I

Theoretical background and literature review

Chapter 1

What is liquefaction?

One of the causes of damage to structures during earthquakes is the occurrence of liquefaction in saturated, loose sand deposits which tend to contract under cyclic loading imposed by seismic shaking. When conditions are such that a cohesionless deposit's hydraulic conductivity is low enough to difficult drainage through the pore matrix, normal stress is transferred from the sand matrix to the pore water during shaking, which causes the reduction of the effective confining stress within the soil. Given that the effective stress within a soil medium is related to its strength and stiffness, its continuous reduction due to increases in pore pressure lead to reductions in both strength and stiffness, which may cause the soil deposit to reach a state where the soil behaves as a viscous fluid and essentially exhibits flow deformation. This phenomenon is known as liquefaction, where common physical manifestations include the formation of sand boils or mud spouts at the ground surface by seepage of water through ground cracks and formation of quicksand-like conditions over large areas (see Figure 1.1). Furthermore, possible consequences of liquefied soils in engineering may include lateral and vertical ground displacements, landslides, foundation bearing failure, buoyant uplift of buried structures (such as tunnels), increased lateral earth pressure on walls, among others (Idriss and Boulanger, 2008).

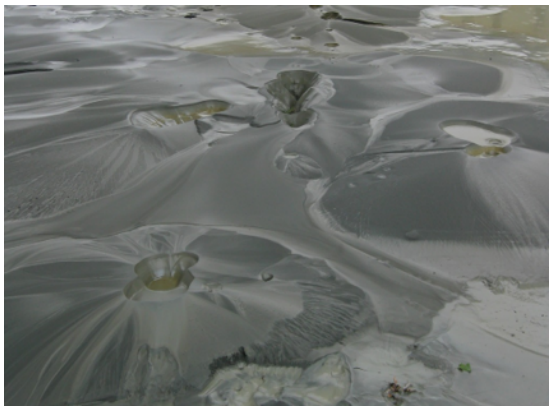

(a) Surface sand boils

(b) Differential settlements in pavement and embankment structure

Figure 1.1: Consequences of liquefaction after the Canterbury, New Zealand, 2011 earthquake

In theoretical terms, and with the use of the Terzaghi's theory of effective stresses, liquefaction can be defined as the complete loss of contact between grains caused by the continued increase in pore water pressure, reaching the magnitude of the total stress. This physical state is mathematically represented by a mean effective stress of $p' = 0$ or a pore pressure ratio of $r_u = 1.0$[1]. Furthermore, it was not until the second half of the 20^{th} century that some earthquakes, like

the 1964 Niigata, Japan, and 1964 Prince William Sound, Alaska, earthquakes helped to identify seismic liquefaction as a major problem in earthquake engineering. Since then, additional major earthquakes have provided similar and additional observations related to liquefaction. Among those were the

- 1964 Niigata, Japan,
- 1964 Prince William Sound, Alaska, USA,
- 1971 San Fernando, California, USA (helped make major changes in embankment dam engineering due to the near catastrophic event of the lower San Fernando dam),
- 1989 Loma Prieta, California, USA,
- 1995 Kobe, Japan (caused extensive damage to quay walls around the port facilities),
- 1999 Kocaeli, Turkey,
- 1999 Chi-Chi, Taiwan,
- and 2007 Pisco (added to cited list), Peru, earthquakes (Idriss and Boulanger, 2008).

In engineering design, the previously-mentioned site conditions may cause the need for the geotechnical and structural design of the project to consider, not only seismic loading (based on the seismicity of the region), but also liquefaction of vulnerable layers. Depending on the foundation type and depth of the super- or underground structure (for example), scenarios of potential liquefaction of layers above, or below the foundation layer become a critical part of the seismic design of the project. This type of seismic check, which may lead to a modified foundation type or mitigation actions, is called a liquefaction hazard assessment, where the main questions that usually need to be answered are the following (Idriss and Boulanger, 2008).

1. Will liquefaction be triggered given the selected design ground motions?
2. What would the consequences of liquefaction be for the structure?
3. What options are there for reducing said liquefaction risk?

For the solution of these questions through the development of engineering procedures, both theoretical and empirical knowledge is needed. For instance, one of the most important components for the assessment of liquefaction potential is the cyclic resistance of soils. Deriving said resistance can be performed either through extensive laboratory testing or through semi-empirical correlations, both of which have their specific limitations. For example, given the lack of cohesion in granular soils, normal sampling methods can only provide disturbed testing samples which will not be able to represent in-situ strength properties of the soil deposit, whereas advanced sampling techniques, such as soil freezing, are very expensive and cumbersome to obtain in cohesionless deposits. Therefore, the development of semi-empirical penetration- and shear wave velocity-based correlations, such as with the Standard Penetration test (SPT), the Cone Penetration test (CPT), and shear wave velocity (V_s), became necessary to use for the estimation of in-situ cyclic resistance properties of sands and other cohesionless soils (Idriss and Boulanger, 2008). As for cohesive soils, significant strains can develop during earthquake loading, leading to ground softening and large deformations, but liquefaction conditions arise. Therefore, it is best to refer to ***liquefaction*** when dealing with cohesionless soils and to ***cyclic softening*** when dealing with cohesive soils (Idriss and Boulanger, 2008).

[1] In practice, these theoretical stress-based definitions are not necessarily reached during liquefaction. This, as will be explained in part II, can be due to a number of reasons ranging from the initial relative state of the sand, the imposed boundary conditions, soil granulometry, among other things.

Chapter 2

Reference soil for benchmark calibration study: Ottawa F-65 sand

The interest behind using Ottawa F-65 sand as the basis for understanding undrained monotonic and cyclic and liquefaction behaviour, as well as how to appropriately calibrate the PM4Sand model was because it has become, since the LEAP projects started in 2015, the new standard sand used in liquefaction-triggering studies. Both the LEAP-2015-GWU and LEAP-2017-UCD used Ottawa F-65 sand in their centrifuge tests (Carey et al., 2018; Zhou et al., 2018; Kutter, Carey, Hashimoto, et al., 2015; Kutter, Carey, Zheng, et al., 2018; Tobita et al., 2018; Kokkali et al., 2018; Manzari et al., 2018) and the most recent laboratory test databases (Vasko et al., 2014; Parra, 2016; El Ghoraiby, Park, et al., 2017; Carey et al., 2018; El Ghoraiby and Manzari, 2018) used this specific sand to study, the pre- and post-liquefaction behaviour of sand under diverse initial state and shearing conditions. Therefore, the first part of this chapter presented the determination of the intrinsic physical and mechanical properties of Ottawa F-65 sand through the analysis of several laboratory test databases and researches. This characterisation would provide the basis for the adequate calibration of secondary model parameters used in the benchmark calibration study in part II. After the sand was characterised, the second part of this chapter described the undrained monotonic and cyclic behaviour of Ottawa F-65 sand when tested in direct simple shear conditions, tackling the first research sub-question proposed in the introduction of this dissertation. This section served as basis and reference for posterior parts of this dissertation, including chapter 3 and parts II and III. For this second part, the *CUDSS* test databases from Parra (2016) and El Ghoraiby and Manzari (2018), described hereon as *PB2016* and *EG2018*, were analysed in detail.

2.1 Characterisation of Ottawa F-65 sand

As mentioned earlier, the main purpose of the characterisation of the intrinsic properties of Ottawa F-65 sand was to describe the intrinsic physical properties of the sand which were later used in the PM4Sand model. For this purpose, the specific gravity (G_s), grain-size distribution (D_{10}, D_{30}, D_{50}, D_{60}, C_u), maximum and minimum void ratios (e_{max} and e_{min}), hydraulic conductivity (k), shear wave velocity (V_s) and the small-strain shear modulus and modulus coefficient (G_{max} and G_0) were analysed in diverse publications and best-estimate values for each property were determined. Parra (2016) conveniently summarised estimations for some of these properties from several sources in her doctoral thesis, which will also be mentioned in this work.

2.1.1 Grain size distribution

One of the most common laboratory tests performed in granular soils is the grain size distribution, where the soil sample is sieved and then analysed, in terms of weight (ASTM International, 2014a), to determine the content in particle sizes of the soil, which then is classified according gradation characteristics and particle size based on specifications established in the Unified Soil Classification System, or *USCS* (Das, 2010). The main properties necessary for later use were the estimation of the particle size below which 60%, 50%, 30% and 10% of the soil weight is present, commonly known as D_{60}, D_{50}, D_{30}, D_{10}. The value of D_{50} is representative of the mean particle size, whereas D_{60} and D_{10} are used to estimate the uniformity index C_u, and D_{60}, D_{30} and D_{10} are used to estimate the curvature index C_c (see Equations 2.1 and 2.2). Both C_u and C_c are used to establish if the soil is well or poorly graded, where well graded sands (SW) and gravels (GW) are defined by meeting $C_u > 4$ and $1 < C_c < 3$. If these criteria are not met, gravels (GP) and sands (SP) are classified as poorly graded. In addition to this classification, depending on the amount of fines present, another term is appended depending on the properties of the soil which passes the No. 200 sieve size. For the specific case of Ottawa F-65 sand, Parra (2016), El Ghoraiby, Park, et al. (2017), and Vasko et al. (2014) specified a mean particle size of $D_{50} \approx 0.20mm$, with average values of C_u and C_c of 1.61 and 0.96, classifying the sand as a uniform SP-sand with a negligible fines content of $\approx 0.17\%$ (also see gradation curve in Figure 2.1). Specifically, for the analysis of *CUDSS* test databases from Parra (2016) and El Ghoraiby and Manzari (2018), Table 2.1 summarises the magnitudes defined for all previously mentioned gradation properties. In the case of El Ghoraiby and Manzari (2018) gradation properties were assumed equal to those determined in El Ghoraiby, Park, et al. (2017).

$$C_u = \frac{D_{60}}{D_{10}} \tag{2.1}$$

$$C_c = \frac{\left(D_{30}\right)^2}{D_{10} \cdot D_{60}} \tag{2.2}$$

Database	USCS	D_{10} [mm]	D_{30} [mm]	D_{50} [mm]	D_{60} [mm]	C_u [-]	C_c [-]
PB2016	SP	0.140	0.170	0.200	0.220	1.610	0.960
EG2018	SP	0.136	0.174	0.210	0.235	1.728	0.947

Table 2.1: Gradation characteristics of Ottawa F-65 sand used to characterise samples from Parra (2016) and El Ghoraiby and Manzari (2018)

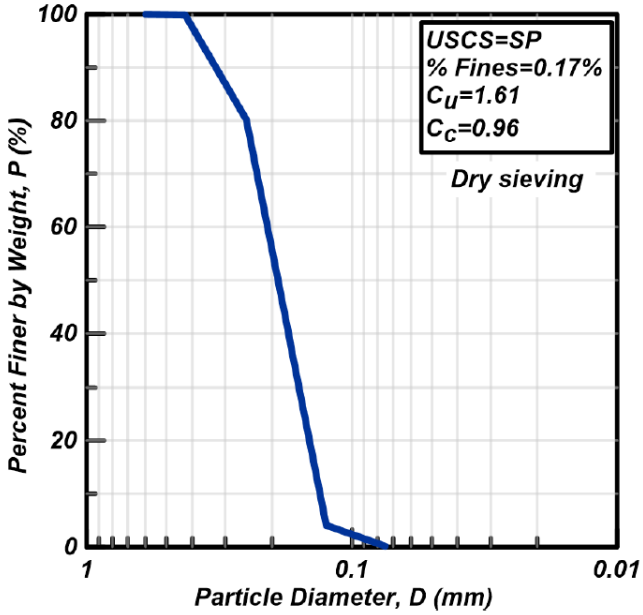

Figure 2.1: Gradation curve of Ottawa F-65 sand from Parra (2016)

2.1.2 Specific gravity

According to Parra (2016), Ottawa F-65 sand is a quartzitic (99.7%) sand with sub-rounded to rounded grains with a specific gravity of 2.65 (established as a mean value of two tests performed by ASTM International (2014b) standards). Several tests to obtain the specific gravity were also performed by El Ghoraiby, Park, et al. (2017), obtaining an mean value of, also, 2.65 (averaged from 30 measurements). Additionally, Parra (2016) compared more values obtained for G_s by different researchers (Cooper Lab, 2013; Vasko et al., 2014), yielding values for G_s of 2.673 and 2.648, respectively. Given the number of performed tests and the very close values yielded by different researchers, as well as suggested values in literature, the specific gravity was set at 2.65 for both databases.

2.1.3 Maximum and minimum void ratios

According to Kutter et al. (2019, in press), the maximum and minimum void ratios (e_{max} and e_{min}) have a significant effect on the cyclic behaviour of sands, which is why it is very important to obtain values with a reasonable degree of reliability. Values for e_{max} and e_{min} ranged from 0.745 to 0.833 and 0.492 to 0.581, respectively, and were calculated by determining the minimum and maximum dry densities of diverse Ottawa F-65 sand samples in various types of moulds, following the methods in ASTM International (2016) (Parra, 2016; Cooper Lab, 2013; Vasko et al., 2014), Ruffatto (2013) (Parra, 2016; Ruffatto, 2013; Vasko et al., 2014; El Ghoraiby and Manzari, 2018) and JIS 1224 Parra, 2016 testing methods and following Equations 2.3 and 2.4 in ASTM International (2014b), where ρ_w is the density of water at 20°C (1000 kg/m^3) and $G_s = 2.65$ (Parra, 2016; El Ghoraiby, Park, et al., 2017).

$$e_{max} = \frac{\rho_w \cdot G_s}{\rho_{d,min}} - 1 \tag{2.3}$$

$$e_{min} = \frac{\rho_w \cdot G_s}{\rho_{d,max}} - 1 \tag{2.4}$$

Figure 2.2 and Table 2.2 show a comparison between all the available values for e_{max} and e_{min}. For the benchmark calibration study of Ottawa F-65 sand in part II the PM4Sand model used the values obtained from Parra (2016). However, for further research or replication purposes (in case of lack of information), average values estimated in Table 2.2 are suggested. The reason behind choosing the void ratios from Parra (2016) was to maintain consistency within the sand samples used for the tests. Another reason why the definition of e_{max} and e_{min} is of vital importance was related to the position of the sample, in terms of initial relative state, relative to the steady-state line, distance denoted as the relative state parameter index ξ_R. Given that this parameter defines the level of contraction or dilation depending on changes in mean effective stress (p'), the correct definition of the void ratio range is crucial for adequately representing both contractive and dilative tendencies of the samples throughout each shearing cycle in cyclic and monotonic undrained behaviour.

Researcher	e_{max} [-]	e_{min} [-]
Cooper Lab (2013)	0.75	0.53
El Ghoraiby and Manzari (2018)	0.78	0.51
Parra (2016)	0.83	0.51
Ruffatto (2013)	0.83	0.58
Vasko et al. (2014)	0.75	0.49
Average	0.7865	0.5232

Table 2.2: e_{max} and e_{min} from different researchers.

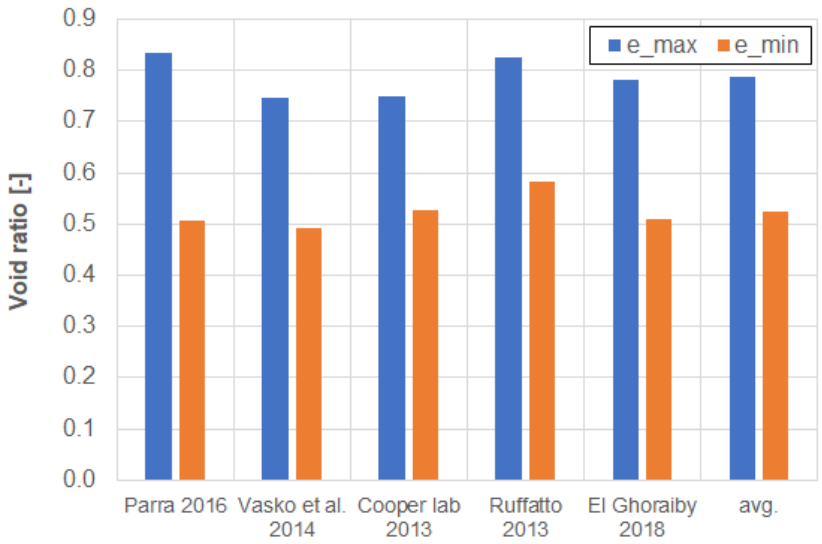

Figure 2.2: Comparison of mean maximum and minimum void ratios from Cooper Lab (2013), Parra (2016), Ruffatto (2013) and Vasko et al. (2014).

2.1.4 Hydraulic conductivity

Given that, for the benchmark case, perfectly undrained conditions were imposed by the boundaries at the soil element level in the Soil Test Facility in Plaxis, the hydraulic conductivity (k) parameter in the constitutive model was not yet important. However, this parameter becomes highly important when analysing conditions where boundaries do allow drainage. Even if for the case study no Ottawa F-65 sand was used, it was still deemed important to determine reference values for the hydraulic conductivity of this standardised sand, for loose and dense cases. For this

purpose, k-values for loose and dense scenarios were extracted from Cimini (2015), Parra (2016), and Vasko et al. (2014) and evaluated. Table 2.3 summarises these values. Additionally, both Parra (2016) and El Ghoraiby, Park, et al. (2017) established polynomial regression functions for the hydraulic conductivity based on initial void ratio (e_0), shown in Equations 2.8, 2.5, 2.6 and 2.7. Contrasting these regressions with measured hydraulic conductivities from Parra (2016), El Ghoraiby, Park, et al. (2017), and Vasko et al. (2014) and an additional function from Kozeny and Carman (1927), it was found that all three expressions defined by Parra (2016) were in accordance with measured values from Cimini (2015), whereas over-predicted magnitudes compared to those measured by Vasko et al. (2014) in loose and dense samples (see Figure 2.3). On the other hand, the linear regression proposed by El Ghoraiby, Park, et al. (2017) was a very good fit to measured loose and dense values from Vasko et al. (2014). These different fits gave reason to think that Vasko et al. (2014) and El Ghoraiby, Park, et al. (2017) performed their hydraulic conductivity tests in similar apparatuses, the same as for Parra (2016) and Cimini (2015). This was partially confirmed in Parra (2016), where it was argued that differences in trends could be attributed to tests being performed in different laboratory settings. Lastly, the expression given by Kozeny and Carman (1927) severely overestimated the magnitudes of hydraulic conductivity when contrasting the trend to measured values (at least within the range of void ratio relevant for Ottawa F-65 sand). As for the differences between the three proposed regressions by Parra (2016), differences were negligible within the void ratio range within which they were developed. Therefore, it was deemed best to use the individually developed linear regressions for the estimation of individual hydraulic conductivities in PB2016 and EG2018 databases, respectively, as both used different equipment for the measurements and both are statistically relevant for each database.

Researcher	$\rho_{d,loose}$ [kg/m^3]	k_{loose} [m/s]	$\rho_{d,dense}$ [kg/m^3]	k_{dense} [m/s]
Cimini (2015)	-	-	1654.0	$1.7 \cdot 10^{-4}$
Parra (2016)	1480.0	$2.2 \cdot 10^{-4}$	1722.0	$1.6 \cdot 10^{-4}$
Vasko et al. (2014)	1537.0	$1.64 \cdot 10^{-4}$	1617.0	$1.18 \cdot 10^{-4}$
Average	1508.5	$1.92 \cdot 10^{-4}$	1669.5	$1.39 \cdot 10^{-4}$

Table 2.3: k_{loose} and k_{dense} from different researchers.

$$k = \frac{1}{4430}(e_0 + 0.16), \ [m/s] \tag{2.5}$$

$$k = \frac{1}{2830}\left(\frac{e_0^2}{1+e_0} + 0.26\right), \ [m/s] \tag{2.6}$$

$$k = \frac{1}{3090}\left(\frac{e_0^3}{1+e_0} + 0.39\right), \ [m/s] \tag{2.7}$$

$$k = \frac{1}{100}(0.0207 \cdot e_0 - 0.0009), \ [m/s] \tag{2.8}$$

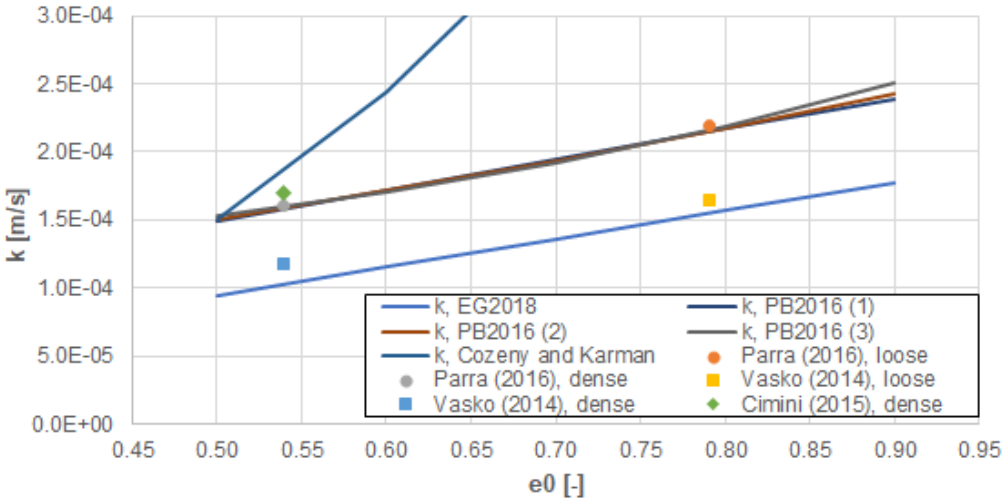

Figure 2.3: Comparison of hydraulic conductivity trends from different sources

2.1.5 Shear wave velocity, small-strain shear modulus and modulus coefficient

The adequate estimation of the small-strain shear modulus (G_{max}) was a crucial step in providing the PM4Sand constitutive model and adequate stress-strain performance. As mentioned in Boulanger and Ziotopoulou (2017), the normalised small-strain shear modulus coefficient (G_0), on of the primary model parameters in PM4Sand, can be estimated with penetration-based correlations (using either the normalised blow count, $(N_1)_{60}$, or normalised cone resistance, q_{c1N}, obtained from Standard Penetration Tests, SPT and Cone Penetration Tests, CPT, respectively) or, more preferably, with shear wave velocity (V_s) measurements, as these are directly related to G_{max} through the relationship shown in Equation 2.9. When looking at measurements of V_s, several authors like Andrus and Stokoe (2000), Huang et al. (2017), and Menq (2003) have demonstrated that the intrinsic physical properties that define the magnitude of V_s are mainly the soil type and the in-situ porosity (η) and relative density (D_{R0}) (see Figure 2.4a). However, measurements of V_s were also highly dependent on the mean effective confinement stress (p'_c) (Huang et al., 2017) (see Figure 2.4b). Therefore, to be able to compare values of V_s in different deposits, it became necessary to apply an overburden correction factor C_V defined by Andrus and Stokoe (2000) in Equation 2.11, converting V_s to its normalised value at 1 atm: V_{s1} (shown in Equation 2.10).

$$G = \rho_d \cdot V_s^2 \tag{2.9}$$

$$V_{s1} = C_V \cdot V_s \tag{2.10}$$

$$C_V = \left(\frac{p_a}{\sigma'_{vc}}\right)^{0.25} \tag{2.11}$$

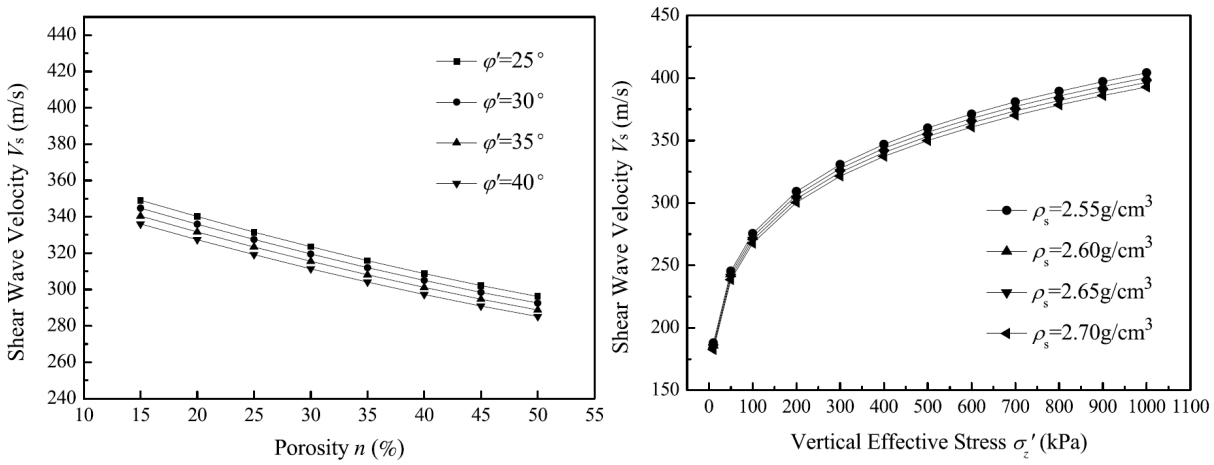

(a) Dependence on porosity (b) Dependence on confinement pressure

Figure 2.4: Shear wave velocity dependence on porosity (a) and confinement pressure (b) (Huang et al., 2017)

Over the last decades, many researchers (Baldi, Bellotti, Ghionna, Jamiolkowski, and Lo Presti, 1989; Rix and Stokoe, 1991; Robertson, Woeller, et al., 1992; Fear and Robertson, 1995; Hegazy and Mayne, 1995; Andrus and Stokoe, 2000; Andrus, Piratheepan, et al., 2004; Andrus, Hayati, et al., 2009) have proposed many relationships correlating penetration resistance (be that $(N_1)_{60}$ or q_{c1N}) to V_{s1}, using additional specific intrinsic properties of the soil, for Holocene, Pleistocene and Tertiary sands. However, in this case, in order to apply these correlations to a laboratory-reconstituted sand, it is important to have in mind the range of applicability of the proposed correlations. Specifically, the applicability of the correlation age-wise. Given that all correlations used in-situ measurements of Holocene, Pleistocene and Tertiary sand deposits, they cannot be directly applied to a newly-reconstituted sand samples without any modifications, as the estimated shear wave velocity magnitudes will be overestimated, especially in denser samples. For example, Andrus, Hayati, et al. (2009) proposed the correlation shown in Equation 2.12, where I_c is the soil behaviour type index specified in Robertson (2010), to estimate in-situ V_{s1} magnitudes in Holocene and Pleistocene Sands and, when comparing this correlation with measured V_{s1} values in EG2018, seen in Figure 2.5. As can be seen, the relationship by Andrus, Hayati, et al. (2009) overestimated the measurements taken at a vertical confinement pressure approximately equal to the atmospheric pressure (p_a), which gives reason to think that the correlation might have to be corrected with an age-factor for newly reconstituted sands[2]. To put this into a better perspective, the proposed V_{s1}-relationships by Andrus and Stokoe (2000) and Boulanger and Ziotopoulou (2017) (see Equations 2.13 and 2.14) were also compared in Figure 2.5, where greater proximity to the experimental values was observed (transformation from q_{c1N} to an equivalent $(N_1)_{60}$ was performed using the Andrus, Hayati, et al., 2009 equivalency shown in Equation 2.16 for Holocene sands) . Although not explicitly mentioned in Boulanger and Ziotopoulou (2017), the correlation plotted in Figure 2.5 showed that they might have been adapted for very young sand deposits. Therefore, for the purposes of characterising Ottawa F-65 sand for the later use in the benchmark calibration study in part II, the age-dependent-q_{c1N} correlation presented in Andrus, Hayati, et al. (2009) was used to estimate V_{s1}-magnitudes (shown in Equation 2.15, which in turn were used to estimate the G_0-magnitudes for the calibration of the PM4Sand model. For the age correction, a value of $t = 1$ day was used to represent newly-constituted laboratory samples.

[2]It was later found that, indeed, an age-correction factor needed to be applied for newly reconstituted sand samples, such as was done in Armstrong (2018) and for the estimation of the cyclic resistance ratios (CRR) of the layers in the practical case study.

$$V_{s1} = 17.2\left(q_{c1N}\right)^{0.396}\left(I_c\right)^{1.006} \tag{2.12}$$

$$V_{s1} = 93.2\left[(N_1)_{60}\right]^{0.231} \tag{2.13}$$

$$V_{s1} = 85\left[(N_1)_{60} + 2.5\right]^{0.25} \tag{2.14}$$

$$V_{s1} = \left[5.13\log_{10}(t) + 58.5\right] \cdot {q_{c1N}}^{0.231} \tag{2.15}$$

$$(N_1)_{60} = 0.263\left(q_{c1N}\right)^{0.913} \tag{2.16}$$

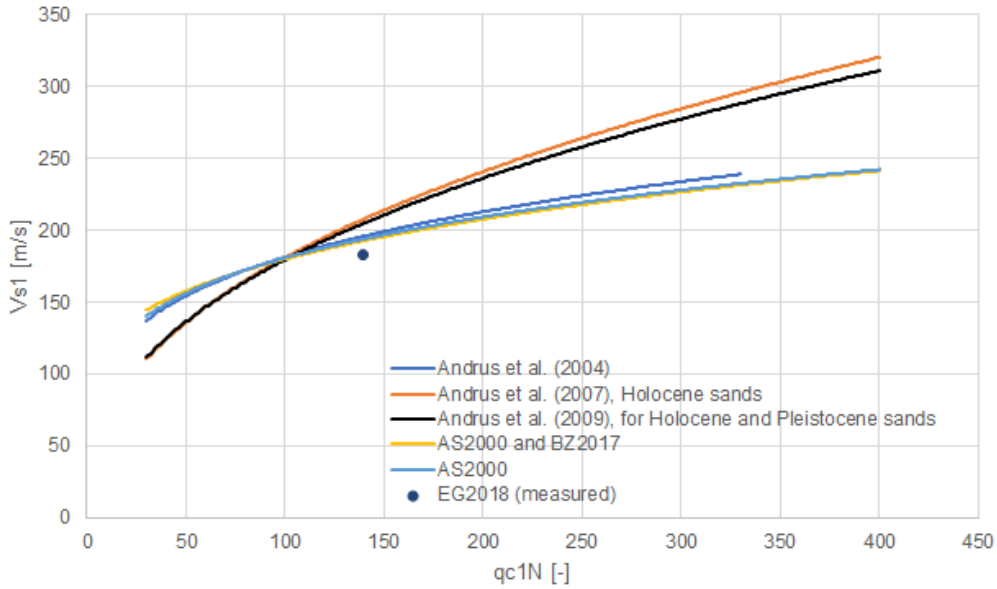

Figure 2.5: Comparison of several V_{s1}-correlations with measured values in EG2018

Considerable effort was put into determining which correlations were most appropriate for calculating V_s (through V_{s1}), as it is directly proportional, to the square root G_{max} (see Equation 2.9), which is used to determine G_0 through Equation 2.17. This would prove most useful in subsequent chapters when trying to determine the small-strain properties of cohesionless deposits in the case study, as V_s would be available for the determination of G_0. Another reason why it was important to establish which V_s-based correlations were adequate for use in the benchmark calibration process was to contrast resulting G_0 values to those obtained through the penetration-based correlation shown in Equation 2.18, proposed by Boulanger and Ziotopoulou (2017). Figures 2.6a and 2.6b show a comparison between calculated magnitudes of G_0 for dense sands from EG2018. Three types of estimations of G_0 were compared: those obtained through measured values of V_s, calculated values of V_{s1} and estimated values of $(N_1)_{60}$, using Equations 2.14 and 2.18, respectively for the latter two. As can be seen, for a confinement pressure of 40 kPa, the correlation proposed by Boulanger and Ziotopoulou (2017) underestimated G_0 values for dense samples, decreasing in difference with increasing relative density, whereas at 100 kPa, it overestimated G_0 values, being almost equal for the smallest shown density and increasing in difference towards the highest shown D_{R0}. As for the G_0-values estimated through the V_{s1}-correlation, Figure 2.6 shows smaller deviations from measured values (compared to the $(N_1)_{60}$-correlation at a confinement pressure of 40 kPa, reducing in variation when increasing in relative density), whereas at 100 kPa, the G_0-values are overestimated in a greater proportion than the $(N_1)_{60}$-correlation (increasing in variation with increasing relative density). In terms of percentage, shown in Figures 2.6c and 2.6d, the V_{s1}- and $(N_1)_{60}$-correlations underestimated G_0-values by approximately 24% and 15%, respectively, in dense samples confined at 40 kPa,

whereas in dense samples confined at 100 kPa, both correlations overestimated G_0-values by approximately 17% and 28%, respectively. Given these results, the trends implied that, for confinement pressures lower than 100 kPa, the $(N_1)_{60}$-correlation proposed by Boulanger and Ziotopoulou (2017) is more accurate, contrary to samples confined at pressures of 100 kPa or greater, where the modified correlation for V_{s1} is more accurate. Unfortunately, no direct measurements of V_s were available for loose or dense samples in PB2016 and, therefore, these trends could not be confirmed for loose sands or for confinement pressures greater than 100 kPa.

$$G = G_0 \cdot p_a \sqrt{\frac{p}{p_a}} \tag{2.17}$$

$$G_0 = 167\sqrt{(N_1)_{60} + 2.5} \tag{2.18}$$

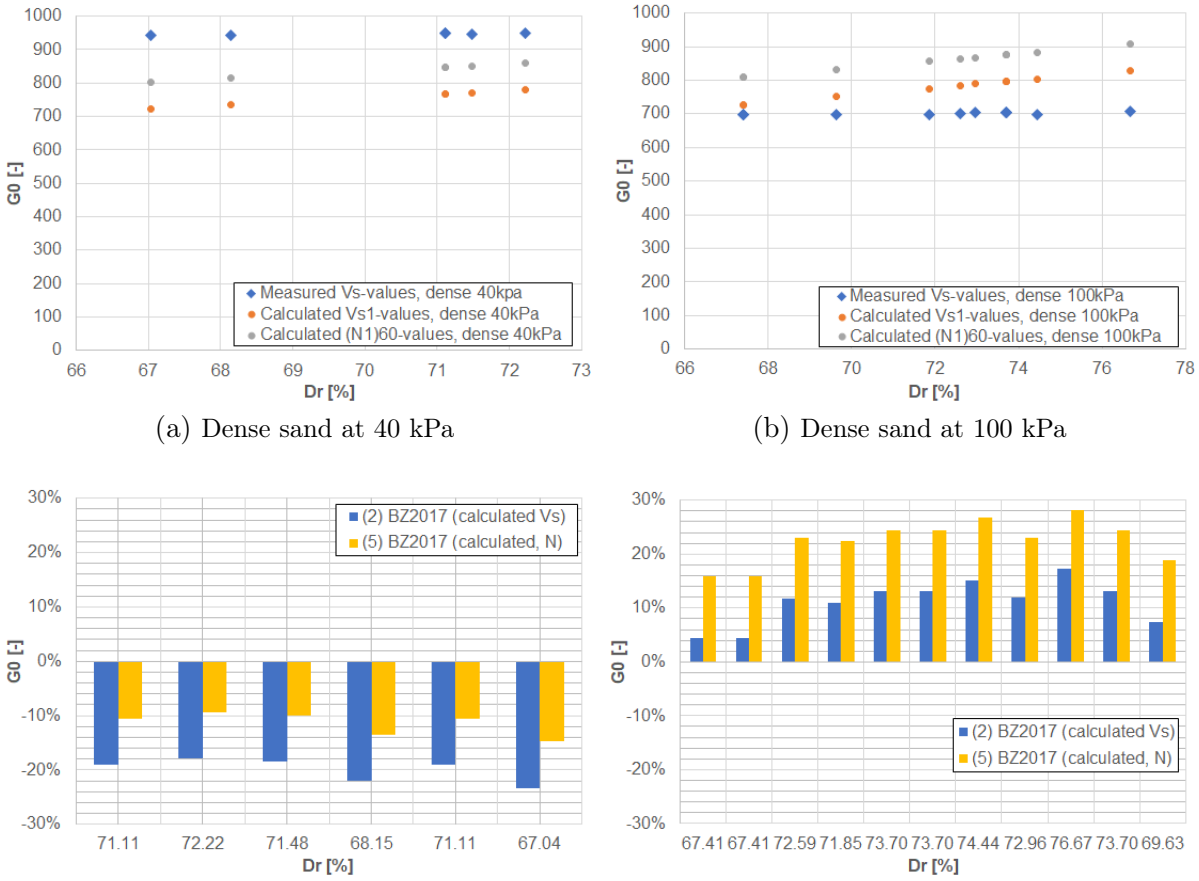

(a) Dense sand at 40 kPa

(b) Dense sand at 100 kPa

(c) Dense sand at 40 kPa

(d) Dense sand at 100 kPa

Figure 2.6: Comparison of estimated G_0-values for dense sands in EG2018 at 40 kPa and 100 kPa

So far, the characterisation of Ottawa F-65 sand has defined values and correlations for the estimation of the following physical properties:

- Grain size distribution properties
- Specific gravity
- Maximum and minimum void ratios
- Hydraulic conductivity
- Shear wave velocity

- Small-strain shear modulus and modulus coefficient

Now, section 2.3 finished the characterisation of Ottawa F-65 sand by defining the steady-state (or critical-state) friction angle (phi_{cv}), which was obtained through monotonic undrained direct simple shear ($MUDSS$) tests in Parra (2016), as well as Bolton's parameters (R and Q) for the definition of the steady-state line, which played a crucial role in the behaviour of undrained monotonic and cyclic behaviour of sands.

2.2 Direct simple shear testing

Before moving on to explaining the undrained monotonic and cyclic behaviour of saturated sand using Ottawa F-65 sand as reference, it was necessary to specify the testing methodology that was employed in databases from Parra (2016) and El Ghoraiby and Manzari (2018). Figure 2.7 shows a typical setup of a direct simple shear (DSS) test, where a soil sample is encased in a membrane which goes along the internal boundaries of the test apparatus. The confining rings allow for both lateral confinement of the soil and lateral movement, which induces a shearing in the soils sample. At the start of testing, be that for a $MUDSS$ or a cyclic undrained direct simple shear ($CUDSS$) test, the sample is saturated and then sealed with the membrane, after which an external normal force is applied on the top cap to generate a specific vertical effective overburden pressure (σ'_{v0}) inside the sample after consolidation has finished. After the desired confinement pressure is achieved, the desired monotonic or cyclic shear force is applied on the top cap.

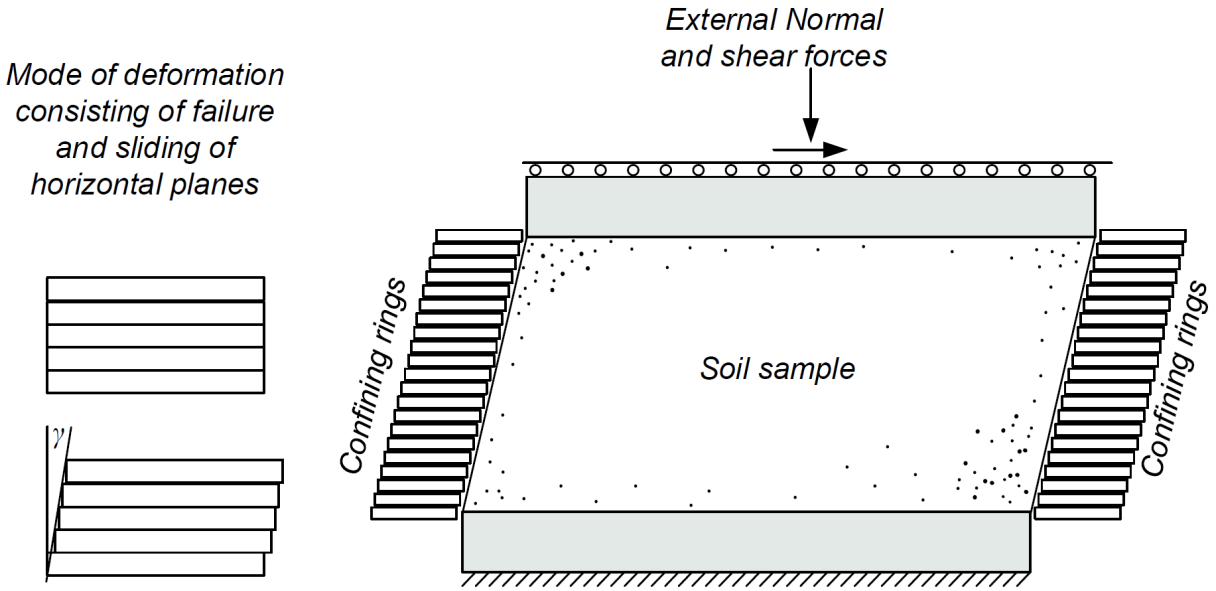

Figure 2.7: Direct simple shear test and primary mode of deformation (Klar et al., 2019)

The basic measurements that are taken from the test over the entire duration of the test are

- the experienced displacement at the top cap, which is transformed to shear strain (γ) with the use of the sample height,
- the normal force exerted on the sample, which is transformed to vertical overburden stress with the use of the sample radius,
- the shear force exerted on the sample, which is also transformed to shear stress with the use of the sample radius,

- the pore pressures inside the sample, which is usually measured at approximately the centre of the domain.

Based on these measurements monotonic and cyclic undrained behaviour can be plotted and analysed.

2.3 Undrained monotonic behaviour

The study of monotonic undrained behaviour is particularly useful when trying to predict the behaviour of an undrained sand subjected to large shear strains in one predominant direction, such as during landslides or pile-driving. For this particular case, and as mentioned later in chapter 4, the PM4Sand model was defined to be critical-state compatible, which raises the need to study the behaviour of the soil one wishes to calibrate when shearing under constant-volume conditions. In undrained monotonic loading, volumetric strains remain, in theory, zero. Experimental results confirm this but it does come with some variation, making volumetric strains close to zero at all times. This, however, does not mean that lateral and axial strains remain constant, as only their cumulative sum must remain zero. Since the volumetric strains remain zero, no densification occurs and the relative density and void ratio remain the same (some local changes may occur, but the average of the entire specimen is constant). When shearing very loose samples at moderate and high confinement stresses, post-peak softening can be experienced, followed by strain hardening toward the critical state condition, whereas at low confinement stress, this post-peak behaviour is absent. Due to the undrained and loose nature of the sand, the sand experiences contractive behaviour, generating positive pore water pressures, this decreases p'. After this, and at strains of 10% to 15%, the samples experience dilative behaviour, making the pore water pressure increments negative. In the case of dense sands, the stress path does not reach a minimum, but tend to have a very short contractive part and then start to dilate towards the critical state.

2.3.1 The steady-state line

Section 2.1.3 showed that the correct definition of e_{max} and e_{min} was crucial for the adequate estimation of the relative density of the undrained monotonic samples with which the steady-state line is fitted. The appropriate fit of the steady-state curve, adapted by Boulanger (2003) and originally defined by Bolton (1986) through Equation 2.19

$$D_R = \frac{R}{Q - \ln\left[\frac{100(1+2K_0)\sigma'_{vc}}{3p_a}\right]} \tag{2.19}$$

is extremely important as it will define the optimal values of constitutive model parameter R, which will define the moment of phase transformation during cyclic loading and, therefore, determine the evolution of pore water pressures as well as deformation. The value of Q, as proposed by Bolton (1986), was maintained at its original value of 10.0, representing soils mainly of quartzitic grain properties, as Ottawa F-65 sand is. For this part, only *MUDSS* samples from Parra (2016) which reached or were close to the steady-state were used for the optimisation of R. According to Parra (2016) and based on the study of the test results, only 3 out of 14 *MUDSS* tests reached or were close to the steady-state: Tests 1, 4 and 5 (03, 08 and 06, are the original test IDs in Parra, 2016). Figure 2.8 shows the fitting of the steady-state line given different values for R (shown in Table 2.5). The steady-state characteristics of the *MUDSS* used to fit the data are given in Table 2.4 (σ'_{vc} and e_{cs}), as well as 2 values for D_R ($D_{R1,cs}$ and $D_{R2,cs}$) at steady state. $D_{r1,cs}$ (shown in Figure 2.8 in circular markers) was calculated using the provided minimum and maximum void ratios by Parra (2016) and $D_{R2,cs}$ (shown in Figure 2.8 in square

markers) was calculated using the averaged values from Table 2.2 in section 2.1.3. Both sets of values of relative density were provided to illustrate the vita importance of the definition of e_{max} and e_{min} and how that affects the optimisation of the regression parameter R. As can be seen, the use of set 1 provided a value of $R = 1.4$, whereas set 2 provided a value of $R = 1.19$, shifting the critical-state line upwards and reducing the loose-of-critical region of the sand, reducing overall contractive shearing behaviour during cyclic loading in the model. This has a direct impact on the capacity of the model to accumulate pore pressures and, therefore, predicting liquefaction at the appropriate number of shearing cycles.

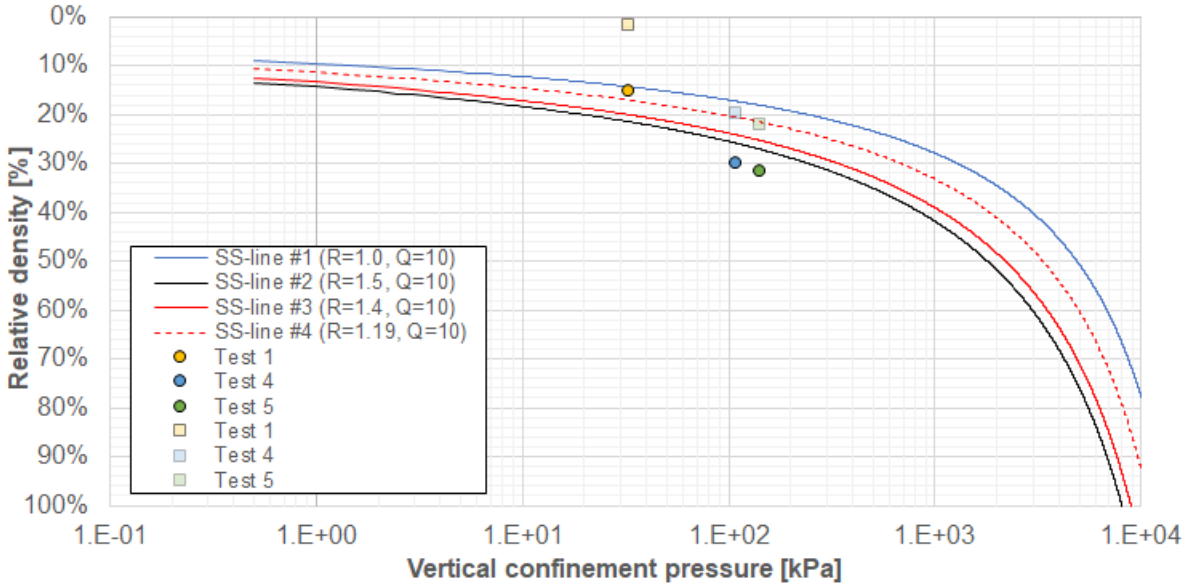

Figure 2.8: Comparison of steady-state lines, according to Boulanger (2003), fitted to *MUDSS* samples which have reached or were close to reaching the steady-state.

MUDSS test	$\sigma'_{v,cs}$ [-]	e_{cs} [-]	$D_{R1,cs}$	$D_{R2,cs}$
01	32.45	0.7818	15.07%	1.78%
04	108.50	0.7341	29.96%	19.88%
05	142.40	0.7285	31.72%	22.02%

Table 2.4: Sets of MUDSS samples which reached or were close to the steady state used for fitting the steady-state line defined by Boulanger (2003).

Steady-state line	R [-]	Q [-]
Bolton (1986)	1.0	10.0
Boulanger and Ziotopoulou (2017)	1.5	10.0
Fit 1	1.4	10.0
Fit 2	1.19	10.0

Table 2.5: Fitted values for R.

Having evaluated this situation, this research came to the conclusion that, for purposes of calibrating *CUDSS* tests belonging to a specific database (e.g. PB2016, EG2018), e_{max} and e_{min} values will be defined as those specified by the author of that specific database. Given that the

calibration process was only performed with 2 databases (El Ghoraiby and Manzari, 2018; Parra, 2016), only those void ratio sets were used in subsequent chapters. As for the calibration of the constitutive model for the case study, suggested e_{max} and e_{min} values of 0.8 and 0.5, respectively, as well as R and Q values of 1.5 and 10.0, will be used as specified in Boulanger and Ziotopoulou (2017) unless site-specific laboratory data is available. Lastly, for the calibration of *CUDSS* tests from Parra (2016), an R value of 1.4 will be assumed, leaving Q at its default value. As for the calibration of *CUDSS* tests from EG2018, given that there was no available data with which to optimise the steady-state line parameter R, the default value of 1.5, suggested by Boulanger and Ziotopoulou (2017) will be used.

2.3.2 The steady-state friction angle

The model explicitly requires the definition of ϕ_{cv}, as a secondary model parameter, as well as factors defining the shape of the steady-state line which will define the contraction and dilation ranges during cyclic shearing. Therefore, *MUDSS* tests from Parra (2016), were used in the determination of both ϕ_{cv} and the steady-state line (in this particular case, only those tests which were able to reach the steady-state were used). Vasko et al. (2014) also performed monotonic undrained *TXC* tests on Ottawa F-65 sand and explored the tendency towards the steady-state. However, that study was not considered in this work given the different innate stress-state differences induced on the soil by a *DSS* and a triaxial test setup (Parra, 2016; Powrie, 2004; Wijewickreme et al., 2013). As mentioned before, ϕ_{cv} was determined based on *MUDSS* tests through means of graphical approximation. The stress paths of all *MUDSS* were plotted in normalised and absolute σ'_{vc}-τ space in order to approximate the steady-state line through a line running through the origin (since the effective cohesion c' in cohesionless soils is zero). Figure 2.9 shows the steady-state lines in stress space for the recommended and fitted constant volume friction angles ϕ_{cv} of 33° (Boulanger and Ziotopoulou, 2017) and 30°. The fitted value of $\phi_{cv} = 30°$ was confirmed by the research performed by Parra (2016).

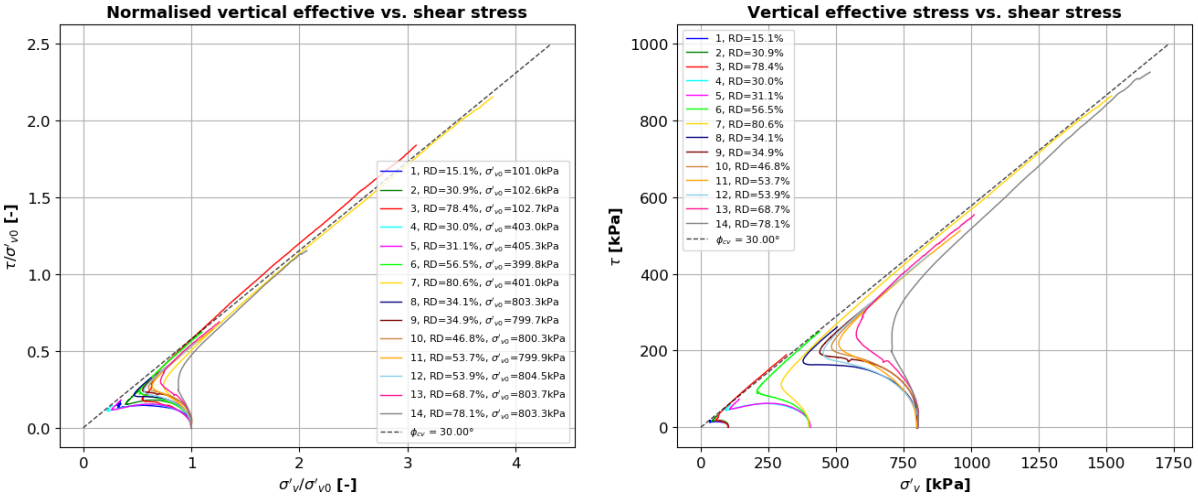

Figure 2.9: Determination of ϕ_{cv}

2.4 Undrained cyclic behaviour

The undrained cyclic behaviour of Ottawa F-65 sand, as most saturated saturated sands, has very distinct types of behaviour when sheared under different conditions. The undrained cyclic behaviour of Ottawa F-65 sand mainly depended on the following parameters:

1. Initial relative density and small-strain shear modulus (D_{R0}, G_{max})

2. Effective mean/vertical confinement/consolidation pressure (p'_c / σ'_{vc})

3. Magnitude of cyclic load (CSR)

4. Duration of cyclic loading

5. Presence of initial static shear stress/strain ($\alpha \neq 0$)

Under cyclic conditions, be that drained or undrained, a dense sand, sheared at a high CSR will behave differently compared to a loose sand sheared at a low CSR, or compared to a dense sand confined at a greater pressure or with presence of an initial static shear stress/strain. Therefore, it was important to properly study the effects of all previously mentioned points, which was one of the aims of this research work (with the exception of analysing the effect of initial static shear stress/strain, point 5, given that the case study evaluated only involved level-ground conditions and the inclusion of pre-shear would have extended the benchmark case significantly). Therefore, this section contains a general analysis of the effects of points 1 through 4 on the undrained cyclic behaviour of Ottawa F-65 sand using *CUDSS* tests performed in Parra (2016) and El Ghoraiby and Manzari (2018).

2.4.1 Effect of initial relative density

One of the most important factors determining the cyclic resistance of sands in cyclic undrained shearing is the initial relative state in terms of density. This, as seen earlier, depends on the grain type, method of grain deposition and, partially, confinement stress, all of which determine the natural state of e_0 of the soil relative to its boundaries e_{max} and e_{min}. The reason why "partially" is added to the effect of confinement stress is that deposits can have a wide range of in-situ relative densities under a low or high confinement stresses (as seen in the relative density distributions obtained for varied confinement stresses in Parra, 2016). However, as shown in Wu et al. (2004), there is a minimum relative density that can be achieved in loose sands when confined under large pressures. What can be implied is that, the larger the confinement pressure, the greater the minimum relative density that can be achieved will be. Having said this, Figure 2.10 compares the effect of relative density on pore pressure evolution and stress-strain behaviour in *CUDSS* tests confined at low and intermediate pressures[1]. As can be seen, the increase in density significantly increases the cyclic resistance of Ottawa F-65 sand when sheared at approximately the same CSR and σ'_{vc}, delaying the accumulation of pore pressures at a given moment in time or given number of shearing cycles. This effect is visible at low and intermediate confinement pressures, but it appears less notorious in *CUDSS* samples confined at 100 kPa. This could mean that relative density has a decreasing effect on cyclic resistance with increasing confinement stress.
This decreasing effect can be viewed from the perspective of stress-strain behaviour in Figure 2.10, where greater cyclic resistance is experienced from Figure 2.11a to 2.11b compared to from Figure 2.11c to 2.11d. Another aspect seen in Figure 2.10 is that an increase in relative density does not necessarily increase the shear stiffness of the sand, but it allows the sand, through the increased cyclic resistance, to reduce the magnitude of strain experienced up to a given number of shearing cycles.

[1]It is worth mentioning that, given the highly contractive and weak nature of loosely-compacted soils, there is a maximum magnitude of CSR beyond which it can be expected that the soil will collapse almost immediately. Therefore, some databases do not include the shearing of loosely-packed soils at a high CSR (higher than 0.12, according to results in PB2016), because little relevant information can be extracted from such cases. As for denser soils, the study of the effect of high $CSRs$ (e.g. up to 0.228, as performed in PB2016) becomes possible, as the soil structure is more resistant, as well as relevant, as large earthquake magnitudes measured at close proximity could register very high cyclic shear stresses, equivalent to high $CSRs$ (despite the short duration it may have). Furthermore, the evaluation of the effect of low $CSRs$ in dense sands may not be critical, as the cyclic resistance may be far greater, but relevant data still can be extracted, even if it is just for the sake of comparison with loose sands.

2.4.2 Effect of effective vertical confinement pressure

Another important factor affecting the cyclic resistance of sands is the effective vertical (or mean) confinement pressure, denoted here as σ'_{vc}. Taking as reference Figures 2.10 and 2.11[2], it can be seen that, when comparing *CUDSS* tests sheared at approximately the same cyclic shear stress amplitudes, the cyclic resistance of loose sands increased with increasing σ'_{vc}, and it decreased in the case of dense sands. The former finding, related to the loose *CUDSS* tests in Parra (2016), raised some questions as, according to the overburden stress factor proposed by Idriss and Boulanger (2008) and the data used to obtain this relationship, it was expected that the cyclic resistance in both loose and dense sands were to decrease with increasing confinement stress, which was not observed (also described in Tziolas, 2019). This could be the result of particular effects due to the grain size distribution of Ottawa F-65 sand, or it could be that the cyclic resistance of loose sands under varying confinement pressure is dependent on something else.

2.4.3 Effect of cyclic stress ratio

When comparing the effect of overburden stress, relative density and *CSR* on the cyclic resistance of a saturated sand, the *CSR*-magnitude is a direct indicator the cyclic strength of a sand. Given any initial relative density and confining stress, the greater the magnitude of the *CSR*, the lower the cyclic strength of the soil will be. This is quantitatively visible in the proposed exponential behaviour of the cyclic resistance of soils, proposed by Idriss and Boulanger (2008), shown in Equation 2.20. Figure 2.12 shows the effect of increasing *CSR* in loose and dense sands at 100 kPa confinement stress and at comparable relative densities, confirming that, in both loose and dense sands, the cyclic resistance decreases with increasing *CSR*. The effect of the magnitude of *CSR* increased dramatically when the sample was sheared at magnitudes of approximately 0.09 and above, which is consistent with the exponential formulation in Equation 2.20 (seen in absolute units; semi-logarithmic space smooths the exponential curve and this behaviour is harder to notice). Furthermore, another important effect that *CSR* has on dense specimens in terms of pore pressure evolution is the rate of dilation present during each cycle.

$$CRR = a \cdot N^{-b} \tag{2.20}$$

This is clearly present when observing loose and dense samples in Figures 2.12 and 2.13, where a greater shear stress amplitude generates the development of greater shear strains, creating larger dilative and contractive intervals during cyclic mobility. In dense sands, the increase in dilation and contraction causes the pore pressure ratio to fluctuate as much as 15%, 25% and 35% at low, intermediate and high *CSRs*, respectively, relative to its peak cycle r_u-magnitude experienced up to or after liquefaction has commenced. As for loose sands, this dissertation can only ascertain the quantitative effect of *CSR*-magnitude for low o intermediate amplitudes of cyclic shear stress. As shown in Figure 2.14, the variation of *CSR* generated r_u-fluctuations of approximately 15%, 20% and 25% at *CSRs* of 0.080, 0.095 and 0.115 in dense sands, whereas in loose sands fluctuations were about 5% smaller at equivalent *CSRs* compared to their denser counterparts. This is not entirely definitive, but it could be implied that in loose sands sheared at low to intermediate *CSR* magnitudes, its effect on the dilation-contraction intervals, and the accompanied r_u-fluctuations, is not as large as in dense sands sheared within the same range of *CSR*.

[2]No figure for dense sands confined at 400 kPa was included in this comparison to maintain comparable levels of CSR, since no dense sample in Parra (2016) at this confinement pressure was sheared below a *CSR* of 0.170.

2.4.4 Effect of duration of cyclic loading

Compared to the previously-mentioned factors affecting cyclic undrained behaviour of cohesionless soils, the duration of the cyclic load is the most important factor when it comes to the study of liquefaction. Based on what is presented in literature and what has been observed in (check which to put)(the analysed database from Parra (2016)), it can be stated with certainty that

uncemented sands at any relative density and sheared at any overburden pressure or cyclic shear stress can reach liquefaction if the cyclic load is applied during a long-enough period of time under undrained conditions.

This can be observed in Figures 2.10a and 2.10b or Figures 2.10d and 2.10d, where loose sands are seen to reach liquefaction relatively "fast" compared to their equivalent dense samples. This shows that even dense sands, when sheared long enough under undrained conditions and low *CSR*, can liquefy. Now, it stands to reason that, given the greater cyclic strength of a dense sand sheared at specific conditions, compared to its equivalent loose counterpart, dense sands will be less prone to liquefy during low-magnitude earthquakes due to usual duration of the seismic events, which usually last up to 60 seconds. However, extraordinary seismic events might provide an event with a long-enough duration to force denser sands to loose enough strength to be able to liquefy.

2.4.5 Effect of sample disturbances or accidental biases

In some cases, even if testing protocols have been followed to the letter, unintentional sample disturbances are introduced when setting up the test. Some sample disturbances may include:

- Uneven preparation of the sample either through air pluviation or dry funnel deposition, which increases the heterogeneity of the soil and, therefore, increasing the possibility of localised strength reduction within ht sample during shearing, leading to lower or higher cyclic strengths than expected.
- Introduction of initial static shear stress or deformation when sealing the sample volume and applying the confinement pressure, which may cause the development of excessive or reduced shear strains during shearing due to an unintentionally-induced bias.
- Inability to maintain constant-volume shearing conditions, which would allow for net volumetric strains to occur, altering the development of pore pressures under fully-undrained conditions. As seen in EG2018, not maintaining constant-volume boundary conditions may allow dilation to induce net volumetric expansion, reducing pore pressure accumulation within the sample.

The reason why a subsection was dedicated to explaining the possible causes and effects of unintentional biases when performing *CUDSS* tests, was because some unusual stress path and stress-strain behaviour was identified in some tests belonging to the EG2018 database. This was particularly visible in the stress paths of some of the *CUDSS* tests performed in EG2018, where different approaches towards the critical state can be evidenced normalised stress space (a comparative example between samples from PB2016 and EG2018 is shown in Figure 2.15). For example, the positive liquefaction loops present in Figure 2.15b describe a larger dilation rate compared to the negative liquefaction loops; the asymmetry being clearly visible when comparing it to the sheared sample in Figure 2.15a. This can be confirmed when observing the evolution of pore pressures in Figure 2.15d where greater effective stress is recovered during the intervals of greater dilation on the positive side, which is contrary to what happens to the sample in Figures 2.15a 2.15c, where dilation rates are equally distributed along both axes. This unintentionally-introduced bias may also be visually present in the stress-strain behaviour of the *CUDSS* sample

from EG2018 in Figure 2.15f, as the locus of the stress-strain curve has been shifted downward, compared to the sample shown from PB2016. Biases such as this one not only alter the shape of the stress path or the stress-strain behaviour, but also affect the triggering of liquefaction. This can be viewed easier in Figure 2.15d, where the apparent bias caused the sample to still accumulate net pore water pressure while at the same time exhibiting cyclic mobility. This meant that initial liquefaction could have happened much earlier than $r_u = 1.0$, or even 0.9. While peak values of r_u have been documented in Boulanger, Seed, et al. (1991) in samples with pre-existing initial static shear stress, and indeed happens in *CUDSS* samples from El Ghoraiby and Manzari (2018), no explanation for the progressive accumulation of pore water pressure up to stable cyclic mobility has been found. Therefore, the explanation given here that this bias is due to the presence of an unintentionally-introduced disturbance in the sample prior to shearing is not conclusive but offers a plausible view of the phenomenon and the inability of constitutive models to capture its essence, as will be demonstrated in Part II.

2.5 Preliminary conclusions regarding the cyclic undrained behaviour of Ottawa F-65 sand

- Critical state parameters such as R, Q and $\phi_c v$ were optimised based on *MUDSS* tests.
- As found in section 2.4.2, the cyclic resistance of loose and dense Ottawa F-65 sand samples with increasing overburden pressure tended to increase and decrease, respectively. For dense sands, the observed behaviour was aligned with findings in literature, as well as the K_σ formulation presented by Idriss and Boulanger (2008), which reduces *CRR* with increasing confinement pressure. However, in the case of loose sands, the increase in cyclic resistance contradicted the established $K - \sigma$ effect. This effect was also found in Fraser River sand (Sriskandakumar, 2004; Naesgaard, 2011), where for a given cyclic stress ratio, liquefaction resistance increased with confining pressure. This was believed to be caused due to stress densification at the application of the confinement pressure during the test setup (Naesgaard, 2011). Furthermore, it could be proposed that there is a relative density threshold beyond which cyclic resistance decreases, and below which it increases, with increasing confinement pressure.
- Some CUDSS tests show decreasing pore pressure evolution once cyclic mobility was reached. This could be explained by imperfect boundary conditions during testing. Either constant volume conditions were not maintained or load was not maintained constant or normal load was reduced, causing an overall reduction in pore pressures generated (allowing volume expansion).
- It was worth mentioning that laboratory *CUDSS* test measurements are not perfect and is a factor to consider when analysing the variability of cyclic resistance under equivalent soil samples. Data may have been measured in a location where fully undrained conditions were not present or too close to the edge of the sample, incorporating boundary effects.

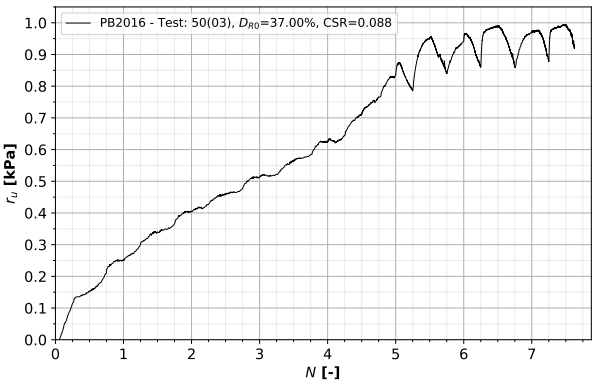

(a) PB2016, loose sand: D_{R0}=37.0%, σ'_{vc}=50 kPa, CSR=0.088

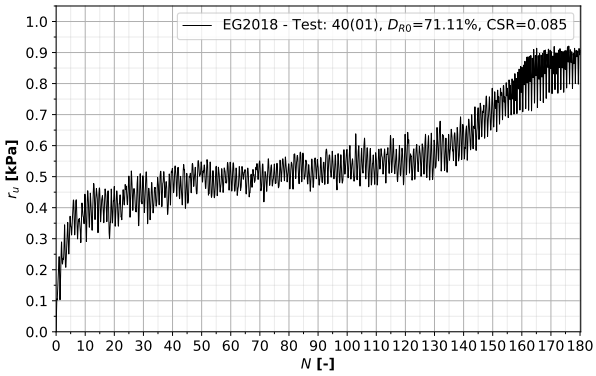

(b) EG2018, dense sand: D_{R0}=71.1%, σ'_{vc}=40 kPa, CSR=0.085

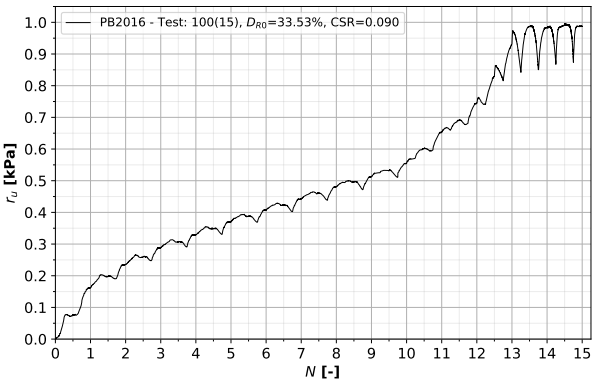

(c) PB2016, loose sand: D_{R0}=33.5%, σ'_{vc}=100 kPa, CSR=0.090

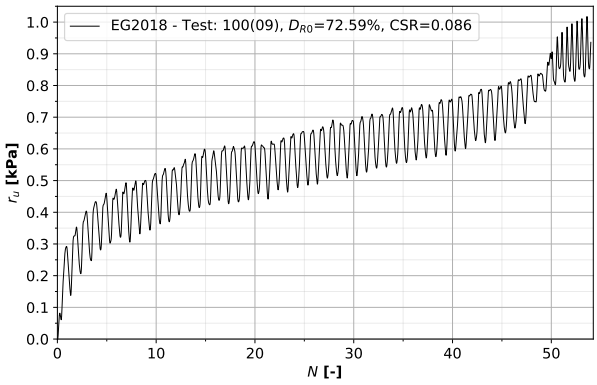

(d) EG2018, dense sand: D_{R0}=72.6%, σ'_{vc}=100 kPa, CSR=0.086

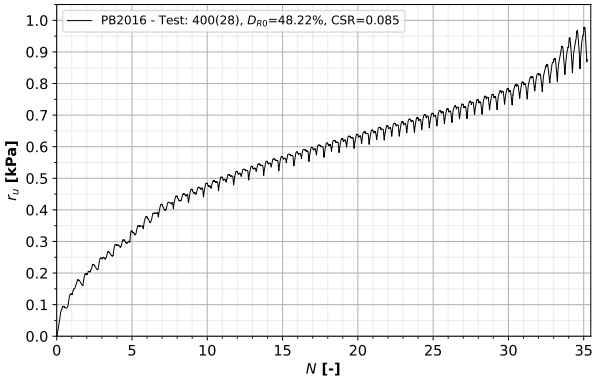

(e) PB2016, loose sand: D_{R0}=48.2%, σ'_{vc}=400 kPa, CSR=0.085

Figure 2.10: Effect of σ'_{vc} on cyclic resistance in terms of pore water pressure evolution in *CUDSS* test samples from Parra (2016) and El Ghoraiby and Manzari (2018)

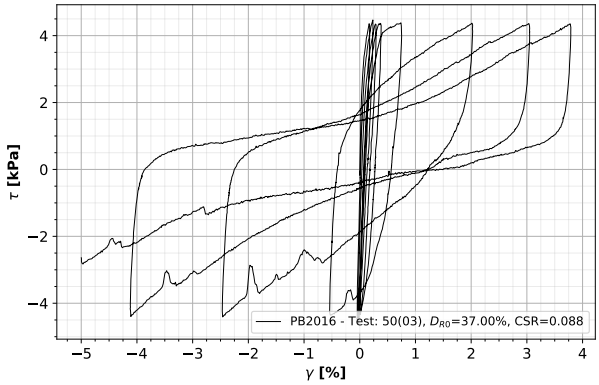

(a) PB2016, loose sand: D_{R0}=37.0%, σ'_{vc}=50 kPa, CSR=0.088

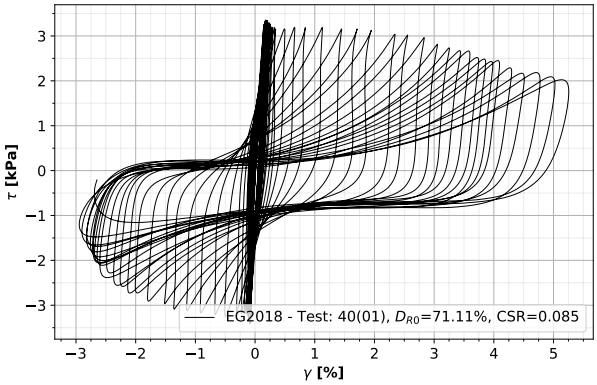

(b) EG2018, dense sand: D_{R0}=71.1%, σ'_{vc}=40 kPa, CSR=0.085

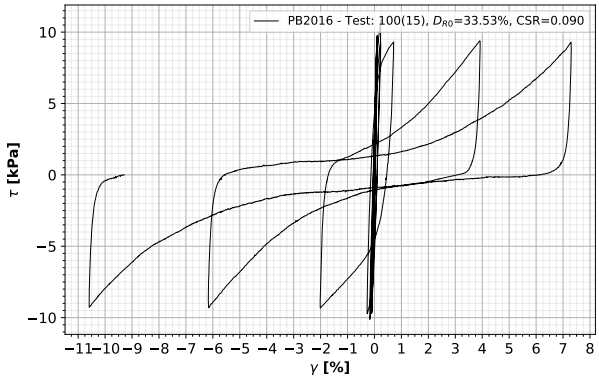

(c) PB2016, loose sand: D_{R0}=33.5%, σ'_{vc}=100 kPa, CSR=0.090

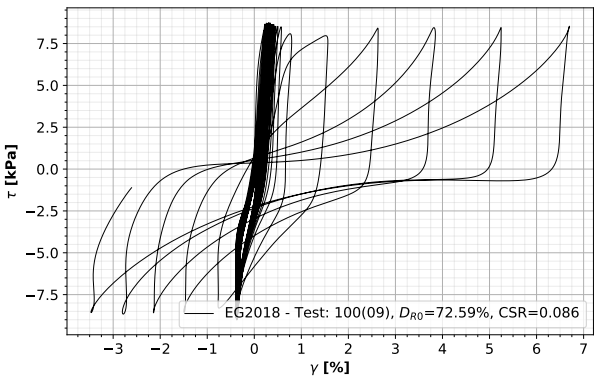

(d) EG2018, dense sand: D_{R0}=72.6%, σ'_{vc}=100 kPa, CSR=0.086

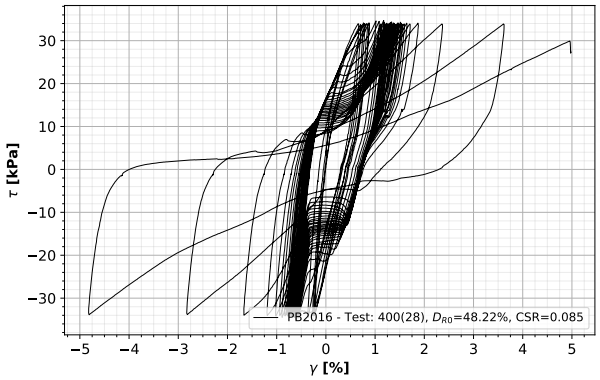

(e) PB2016, loose sand: D_{R0}=48.2%, σ'_{vc}=400 kPa, CSR=0.085

Figure 2.11: Effect of σ'_{vc} on cyclic resistance in terms of stress-strain behaviour in *CUDSS* test samples from Parra (2016) and El Ghoraiby and Manzari (2018)

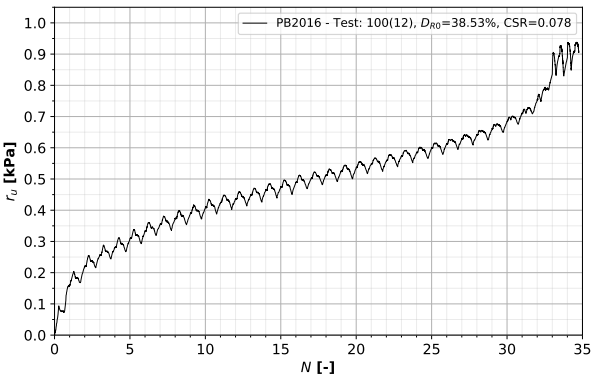

(a) PB2016, loose sand: D_{R0}=38.5%, σ'_{vc}=100 kPa, CSR=0.078

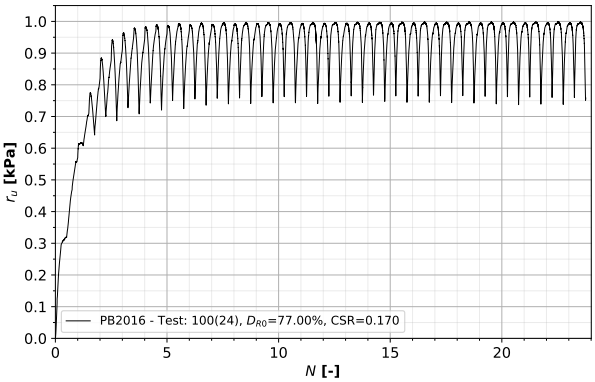

(b) PB2016, dense sand: D_{R0}=77.0%, σ'_{vc}=100 kPa, CSR=0.170

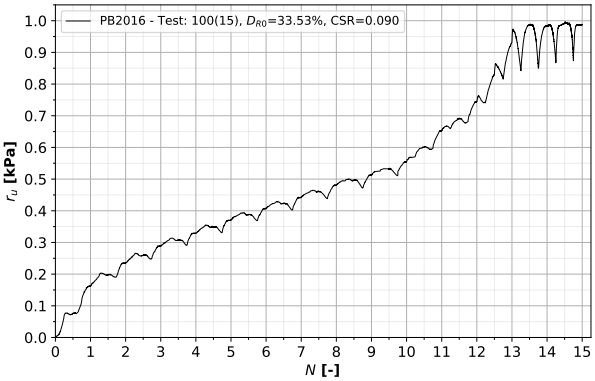

(c) PB2016, loose sand: D_{R0}=33.5%, σ'_{vc}=100 kPa, CSR=0.090

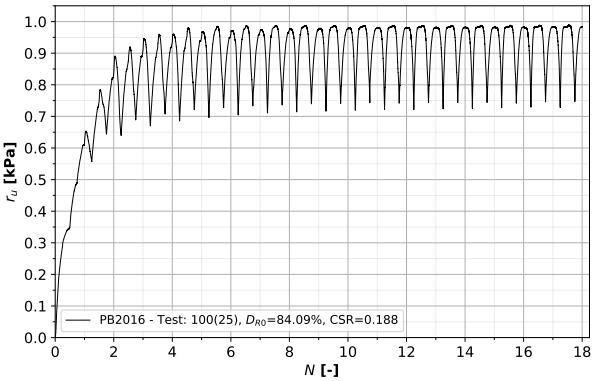

(d) PB2016, dense sand: D_{R0}=84.1%, σ'_{vc}=100 kPa, CSR=0.188

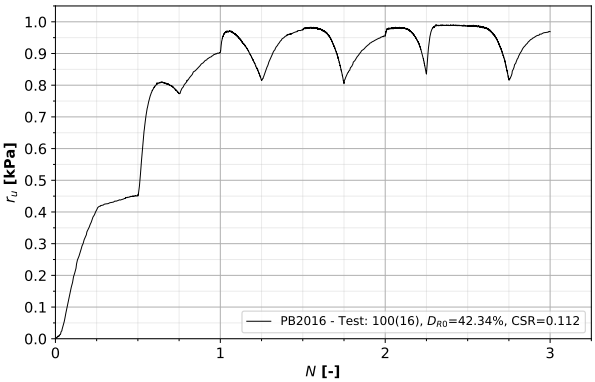

(e) PB2016, loose sand: D_{R0}=42.34%, σ'_{vc}=100 kPa, CSR=0.112

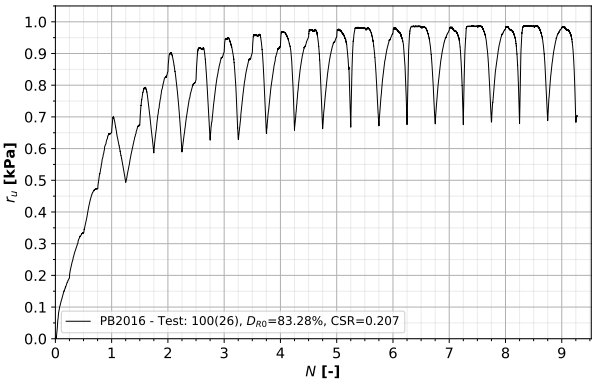

(f) PB2016, dense sand: D_{R0}=83.1%, σ'_{vc}=100 kPa, CSR=0.207

Figure 2.12: Effect of *CSR* on cyclic resistance in terms of pore water pressure evolution in *CUDSS* test samples from Parra (2016) (loose samples sheared at low to intermediate *CSRs* and dense samples sheared at high *CSRs*)

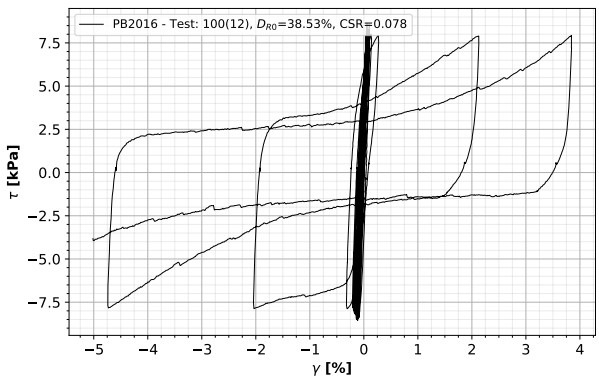

(a) PB2016, loose sand: D_{R0}=38.5%, σ'_{vc}=100 kPa, CSR=0.078

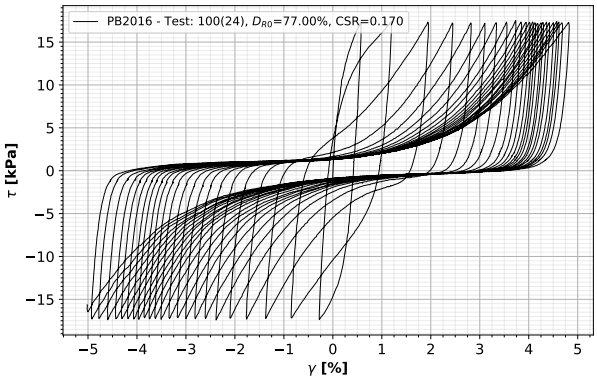

(b) PB2016, dense sand: D_{R0}=77.0%, σ'_{vc}=100 kPa, CSR=0.170

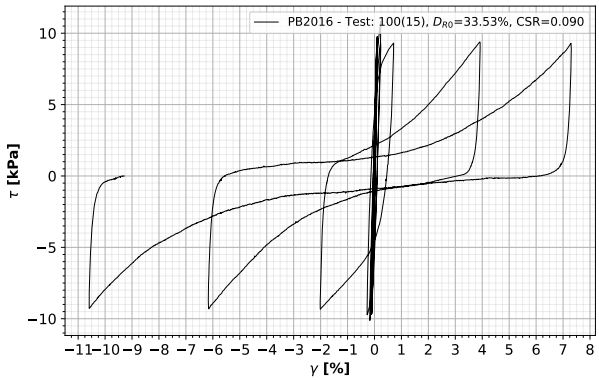

(c) PB2016, loose sand: D_{R0}=33.5%, σ'_{vc}=100 kPa, CSR=0.090

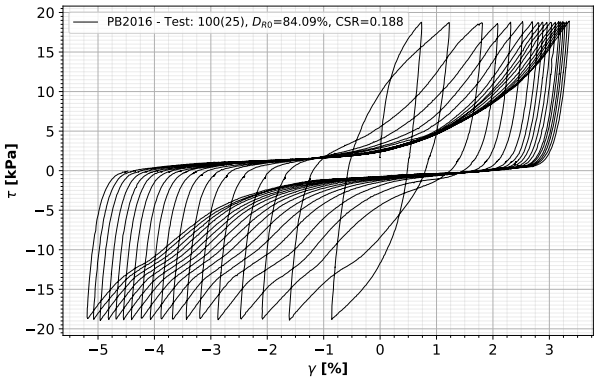

(d) PB2016, dense sand: D_{R0}=84.1%, σ'_{vc}=100 kPa, CSR=0.188

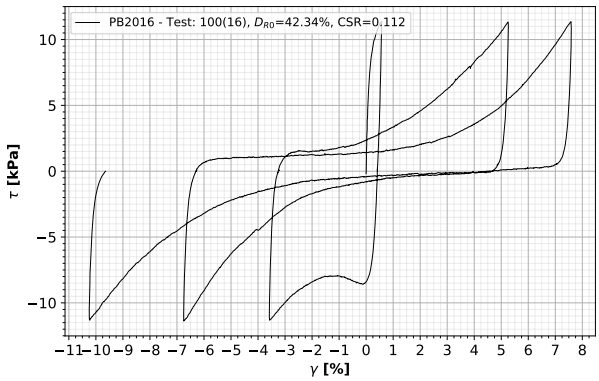

(e) PB2016, loose sand: D_{R0}=42.34%, σ'_{vc}=100 kPa, CSR=0.112

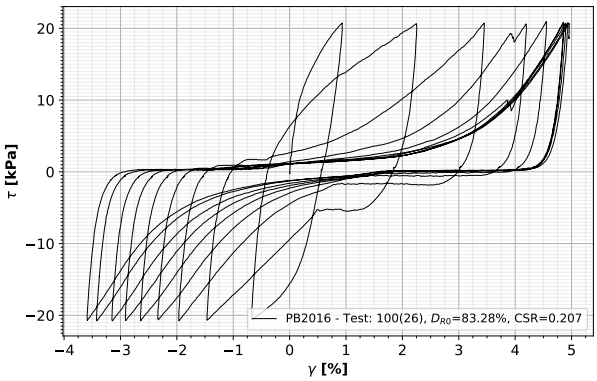

(f) PB2016, dense sand: D_{R0}=83.1%, σ'_{vc}=100 kPa, CSR=0.207

Figure 2.13: Effect of *CSR* on cyclic resistance in terms of stress-strain behaviour evolution in *CUDSS* test samples from Parra (2016) (loose samples sheared at low to intermediate *CSRs* and dense samples sheared at high *CSRs*)

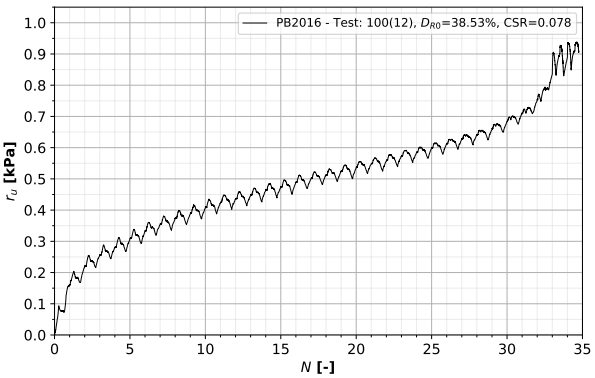

(a) PB2016, loose sand: D_{R0}=38.5%, σ'_{vc}=100 kPa, CSR=0.078

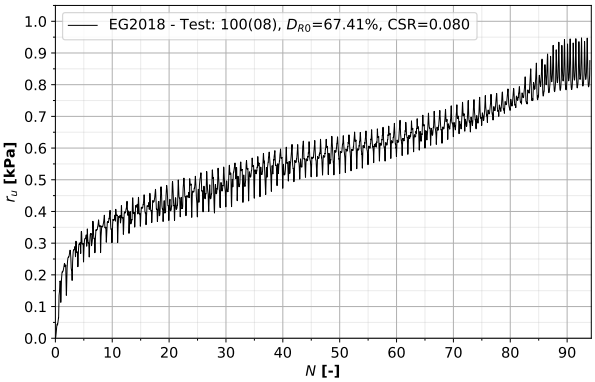

(b) EG2018, dense sand: D_{R0}=67.4%, σ'_{vc}=100 kPa, CSR=0.080

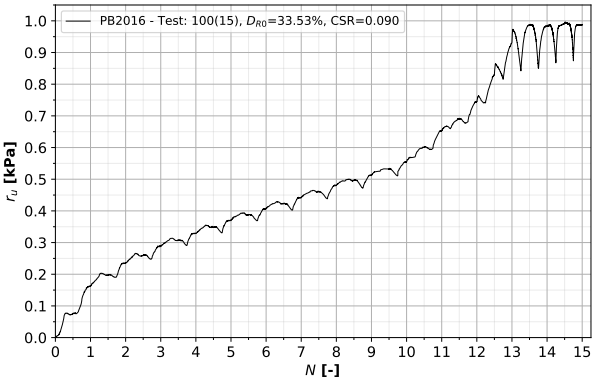

(c) PB2016, loose sand: D_{R0}=33.5%, σ'_{vc}=100 kPa, CSR=0.090

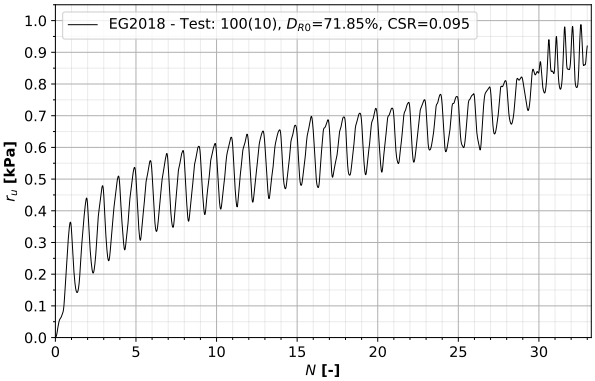

(d) EG2018, dense sand: D_{R0}=71.9%, σ'_{vc}=100 kPa, CSR=0.095

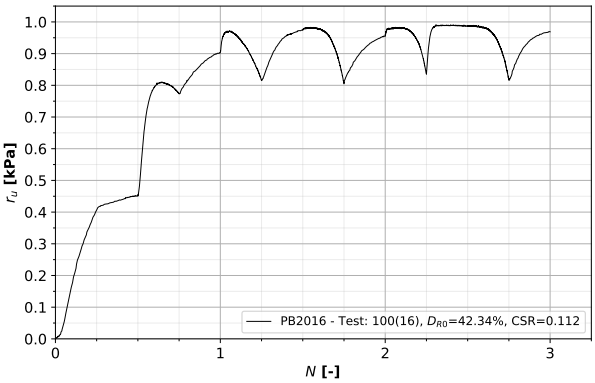

(e) PB2016, loose sand: D_{R0}=42.34%, σ'_{vc}=100 kPa, CSR=0.112

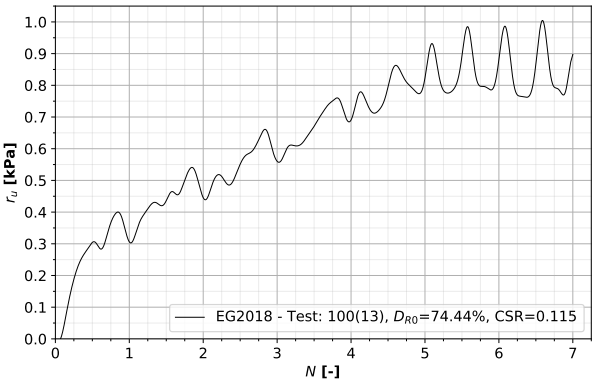

(f) EG2018, dense sand: D_{R0}=74.4%, σ'_{vc}=100 kPa, CSR=0.115

Figure 2.14: Effect of *CSR* on cyclic resistance in terms of pore water pressure evolution in *CUDSS* test samples from Parra (2016) and El Ghoraiby and Manzari (2018) sheared within a low to intermediate range of *CSRs*.

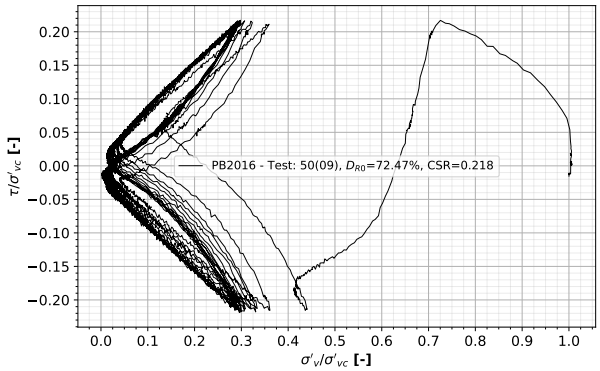

(a) Parra (2016), stress path

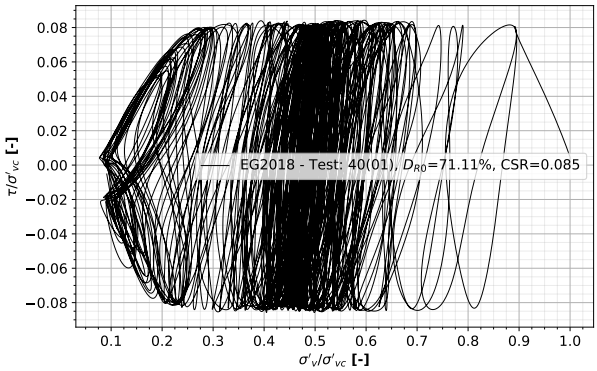

(b) El Ghoraiby and Manzari (2018), stress path

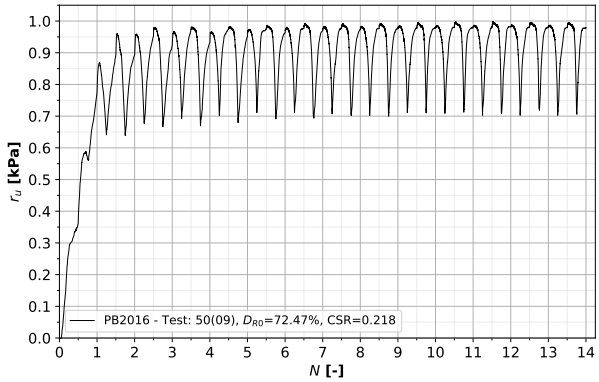

(c) Parra (2016), pore pressure evolution

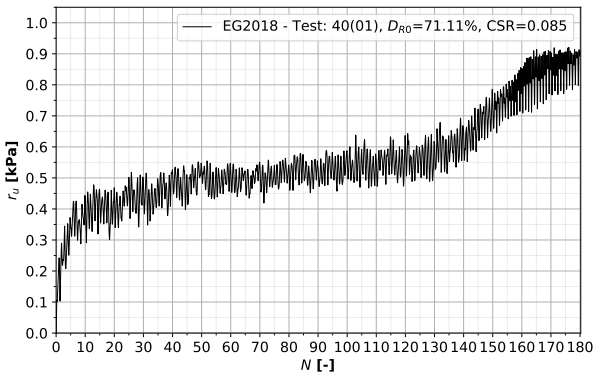

(d) El Ghoraiby and Manzari (2018), pore pressure evolution

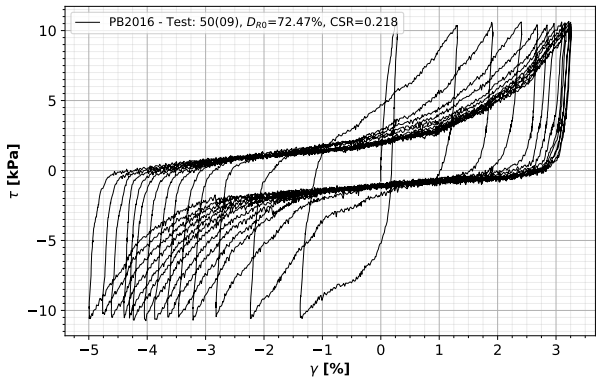

(e) Parra (2016), stress-strain behaviour: $\sigma'_{vc} = 50$ kPa, $CSR = 0.221$

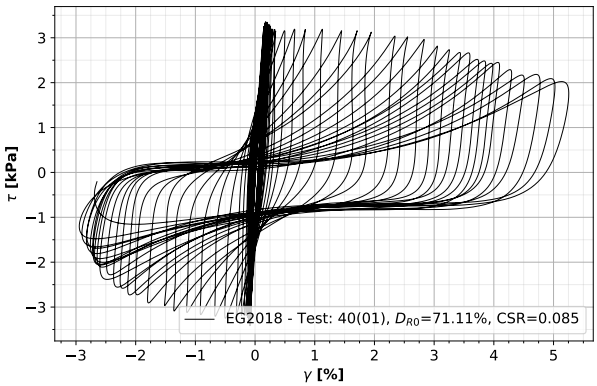

(f) El Ghoraiby and Manzari (2018), stress-strain behaviour: $\sigma'_{vc} = 40$ kPa, $CSR = 0.140$

Figure 2.15: Effect of apparent unintentionally-introduced bias in *CUDSS* test sample from El Ghoraiby and Manzari (2018) compared to a *CUDSS* test sample with no apparent bias from Parra (2016)

Chapter 3

Evaluation of liquefaction-triggering criteria

Since the phenomenon of liquefaction depends on excess pore pressure accumulation, strength degradation and deformation evolution in a saturated soil, many researchers (Armstrong, 2018; Idriss and Boulanger, 2008; Sriskandakumar, 2004) have proposed numerous definitions of liquefaction over the last decades (see Table 3.1). These, however, be it based on pore pressure (r_u), shear strain accumulation (γ) or energy capacity (Wu et al., 2004; Obermeier et al., 2001), usually only based liquefaction-triggering criteria on a single factor instead of on 2 or all 3 of them, leading to confusion. This confusion only increases when intentionally broad definitions of liquefaction are presented by institutions like ASCE and the NRC which do not mention any quantitative criteria by which liquefaction can be defined (Wu et al., 2004). Similarly, educational institutions, like University of California, at Berkeley, which defines liquefaction as a "significant reduction of strength and stiffness of a soil, principally as a result of pore pressure increase and corresponding reduction in effective stress" (extracted from Wu et al., 2004) still use definitions which only relate to one parameter and do not view liquefaction in a holistic manner. For example, one of the most commonly found explanations for why an r_u-based liquefaction-triggering criterion was more popular over a γ-based on in the past was because it was thought that excessive soil deformation was a direct consequence of strength loss during the liquefaction process. This misconception was debunked thanks to new developments over the past decades and now it has been accepted that shear deformations and pore pressure accumulation are closely interrelated (Wu et al., 2004). Furthermore, shear strain thresholds have now gained popularity when analysing liquefaction potential, as it allows the quantitative evaluation of the seismic performance of a specific soil, a feature lacking in r_u-based liquefaction-triggering criteria. Therefore, it was of great interest to jointly evaluate the relationship between thresholds in r_u and γ during the process of liquefaction in cohesionless soils subjected to diverse initial states and shearing conditions. This process would shed light on the behaviour of liquefaction-onset in sands when subjected to earthquakes and could be used to improve the calibration of liquefaction-triggering models, such as PM4Sand, as well as the accuracy of liquefaction potential analyses. To perform this adequately, r_u- and γ-thresholds had to be selected to evaluate liquefaction behaviour. These were determined based on recommendations found in literature, as well as available information found in the analysed *CUDSS* test databases (PB2016 and EG2018) in this dissertation. For purposes of this dissertation, only the *CUDSS* tests on Ottawa F-65 sand from Parra (2016) and El Ghoraiby and Manzari (2018) were used as reference for this analysis.

Reference	Used sand	Types of cyclic test	γ-based [%]		r_u-based [-]
			SA	DA	
NRC (1985)	unknown	TXC	2.50	none	none
Sriskandakumar (2004)	Fraser river	multiple	2.50 (TXC) 3.75 (DSS)		none
Wu et al. (2004)	Monterrey	DSS	3.00	6.00	0.85 0.90 0.92 0.94 0.96
Idriss and Boulanger (2008)	general	multiple	3.00	none	1.00
Vasko et al. (2014)	Ottawa F-65	TXC	none	5.00	1.00
Parra (2016)	Ottawa F-65	DSS	3.00	none	none
El Ghoraiby et al. (2017)	Ottawa F-65	TXC	2.50	none	none
El Ghoraiby and Manzari (2018)	Ottawa F-65	DSS	none	1.50 3.50 7.50	none
Armstrong (2018)	Ottawa F-65	TXC	none	none	0.95
Morales and Ziotopoulou (2018)	Ottawa F-65	DSS	3.00	none	none
Ziotopoulou et al. (2018)	Ottawa F-65	multiple	none	5.00	none
Ziotopoulou et al. (2019)	Ottawa F-65	multiple	2.50	none	none

Table 3.1: Shear strain- and pore pressure-based liquefaction-triggering criteria found in literature

3.1 Liquefaction-triggering analysis in loose and dense sands using *CUDSS* tests on Ottawa F-65 sand

For the analysis of liquefaction-onset behaviour in terms of pore pressure and shear strain accumulation, this section evaluated different liquefaction-triggering markers to identify the triggering of liquefaction in *CUDSS* tests of loose and dense Ottawa F-65 sand samples, sheared at different *CSRs* and confined at different pressures. The liquefaction-triggering markers were defined based on pore pressure ratio (strength reduction) r_u (0.80, 0.85, 0.90, 0.95 and 0.98) and shear strain accumulation γ (1%, 3% and 5%), where the aim was to identify their relationship to each other, if any, and establish which markers are appropriate to use under specific initial relative state and shearing conditions (see Figure 3.1 to visualise this concept in a loose and dense sand samples). The r_u-thresholds at 95% and 98% were defined based on suggested values found in literature (Armstrong, 2018; Idriss and Boulanger, 2008; Wu et al., 2004), whereas the ones at 80% and 85% were defined mostly as control markers (but were also found as markers in Wu et al., 2004), more than indicators of liquefaction-triggering. Lastly, the r_u threshold at 90% (also evaluated in Wu et al., 2004) was defined as a conservative value for identifying the triggering of liquefaction based on r_u results from different cyclic *TXC* and *DSS* test databases (El Ghoraiby, Park, et al., 2017; El Ghoraiby and Manzari, 2018; Parra, 2016). Furthermore, no threshold at 100% was defined since most of the analysed *DSS* tests did not reach the theoretical

value for liquefaction. However, it is worth mentioning that, after looking and comparing results obtained from undrained cyclic *TXC* and *DSS* tests, it seems that $r_u = 1.0$ conditions are more commonly achieved in a triaxial setting compared to a *DSS* one, as evidenced in El Ghoraiby, Park, et al. (2017), El Ghoraiby and Manzari (2018), and Vasko et al. (2014). As for the γ liquefaction-triggering markers, the 3% threshold was selected based on typical values used to present cyclic resistance curves (such as in Idriss and Boulanger, 2008; Ziotopoulou, Montgomery, Parra, et al., 2018; Parra, 2016; Boulanger, Seed, et al., 1991) and the 1% and 5% thresholds were based on presented values in Parra (2016), El Ghoraiby and Manzari (2018), and Wu et al. (2004), as well as to have an adequate range of deformation behaviour to compare to th r_u-based liquefaction-triggering criteria.

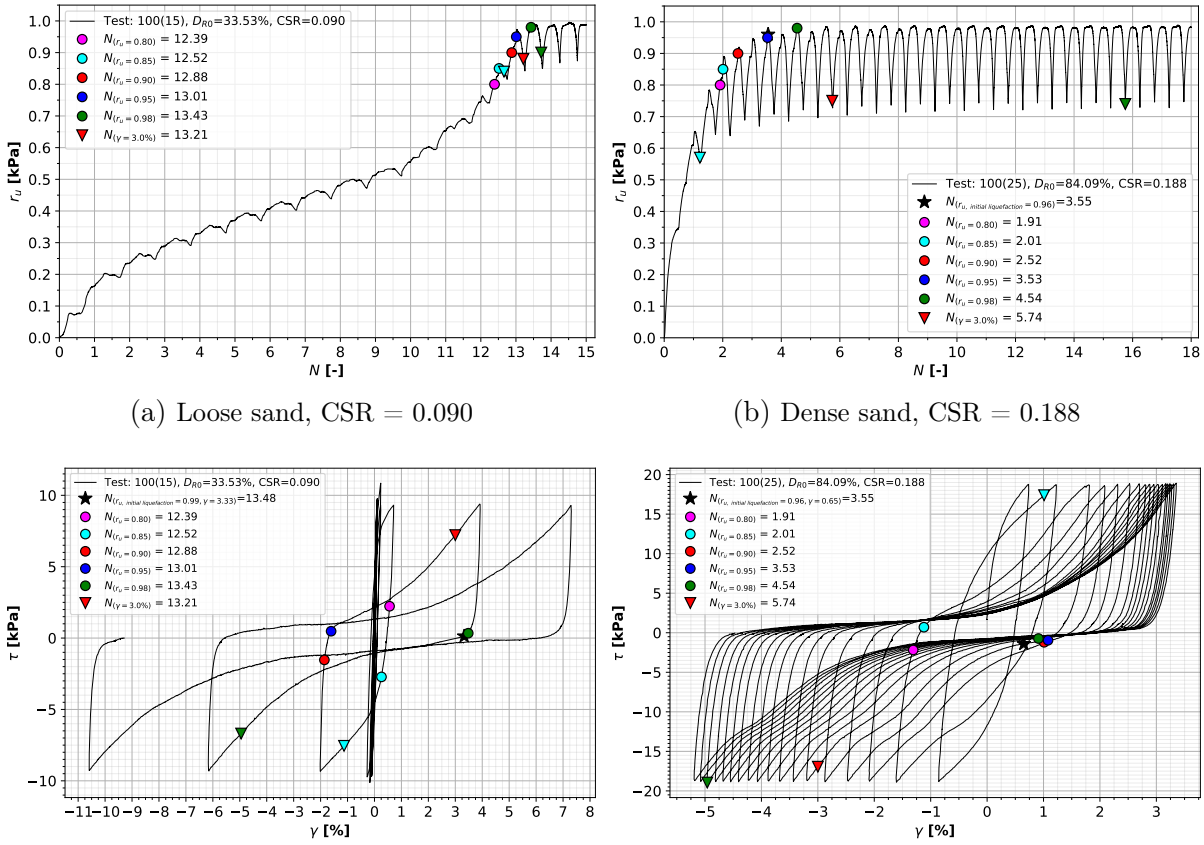

(a) Loose sand, CSR = 0.090

(b) Dense sand, CSR = 0.188

(c) Loose sand, CSR = 0.090

(d) Dense sand, CSR = 0.188

Figure 3.1: Illustration of identification of r_u and γ liquefaction-triggering markers in loose (a, c) and dense (b, d) Ottawa F-65 sand samples from Parra (2016) in terms of pore pressure accumulation and stress-strain behaviour

In the interest of replicability of this part of the research and before delving into the liquefaction-triggering analysis, it is worth mentioning the procedure used to identify the above-mentioned liquefaction-triggering markers, for both r_u and γ, within laboratory test results. For the case of $\gamma = 1\%$, a hard threshold was defined. Given that it was the first strain threshold and that normally this would not be viewed as excessive deformations, no flexibility in terms of reducing the threshold to a value $\approx 1\%$ was allowed when identifying this liquefaction trigger in the *CUDSS* tests. On the other hand, the γ-markers at 3% and 5% were defined as flexible, allowing values of γ which were very close, but not equal to, the threshold to be counted as having reached it. The reason behind this decision was to provide some flexibility around the identification of liquefaction-triggering markers when magnitudes of accumulated shear strains came close to the

pre-set thresholds. This meant that the identification of cycles to γ-liquefaction-triggering markers were defined as follows. The same concept was applied for the identification of r_u-markers in loose and dense samples in Parra (2016). Fixed thresholds were defined at $r_u = 0.80$ and $= 0.85$ given that most of the samples were able to reach these thresholds without problems. However, beyond these thresholds, some samples reached peak r_u values lower than 0.98, 0.95 or even 0.90, especially in dense samples due to their dilative tendencies. For this reason, it was decided that the r_u-thresholds at 0.80 and 0.85 should be fixed and those at 0.90, 0.95 and 0.98 should be flexible. In summary, the identification of the r_u- and γ-liquefaction-triggering markers followed the conditions below.

- Fixed thresholds: $r_u = 0.80,\ 0.85$ and $\gamma = 1\%$
- Flexible thresholds: $r_u \approx 0.90,\ 0.95,\ 0.98$ and $\gamma \approx 3\%,\ 5\%$

Test	σ'_{vc} [kPa]	D_{R0} [%]	$CSR_{measured}$ [-]	N_{total} [-]
40(01)	40	71.11	0.085	180
40(02)	40	72.2	0.096	41
40(03)	40	71.5	0.110	25
40(04)	40	68.2	0.120	16
40(05)	40	71.1	0.130	11
40(06)	40	67.0	0.140	11
100(07)	100	67.4	0.076	125
100(08)	100	67.4	0.080	94
100(09)	100	72.6	0.086	54
100(10)	100	71.9	0.095	33
100(11)	100	73.7	0.105	14
100(12)	100	73.7	0.105	15
100(13)	100	74.4	0.115	7
100(14)	100	73.0	0.120	7
100(15)	100	76.7	0.125	6
100(16)	100	73.7	0.130	6
100(17)	100	69.6	0.150	4

Table 3.2: *CUDSS* tests from El Ghoraiby and Manzari (2018)

Having defined the liquefaction-triggering markers by which liquefaction-onset behaviour will be studied, and as mentioned in the beginning of the chapter, *CUDSS* tests on Ottawa F-65 sand from Parra (2016) and El Ghoraiby and Manzari (2018) were used as reference (the initial state and cyclic testing conditions of all tests from both databases are shown in Tables 3.3 and 3.2). In order to properly analyse the effect of confinement pressure and *CSR* on the behaviour of liquefaction onset in loose and dense sands, it was necessary to group *CUDSS* tests so that they shared a comparable standard given their individual D_{R0}-values, *CSRs* and confinement pressures. For this purpose, 6 combinations of *CUDSS* tests from both databases were constructed to evaluate the onset of liquefaction with varying *CSR* or varying confinement stress. In the cases where both loose and dense samples were available for a given confinement stress (50, 100 and 400 kPa), the tests were presented together in the same graph. Additionally, given that loose and dense samples in PB2016 did not share common *CSRs*, groups were formed between samples from

Parra (2016) and El Ghoraiby and Manzari (2018) where possible. Otherwise, both loose and dense samples were compared within their own ranges of *CSR*. Figures 3.5, 3.6, 3.7, 3.8, 3.9 and 3.10 plot the cycles (Y-axis) to all proposed pore pressure ratios r_u (X-axis) as discrete points, in addition to the cycles to proposed single amplitude accumulated γ-thresholds as horizontal lines. The graphs were structured in a way that presented loose samples (where available) on a first row, followed by dense samples in a second row, both rows presenting a constant Y-axis range (where practically feasible) in order to visualise the cyclic strength degradation with increasing *CSR*. The number of columns varied from 3 to 4 depending on the number of tests available for each confinement pressure and the range in r_u was fixed to only show the liquefaction-triggering markers of interest.

Test	σ'_{vc} [kPa]	D_{R0} [%]	$CSR_{measured}$ [-]	N_{total} [-]
50(01)	50	38.69	0.075	26.8
50(02)	50	46.41	0.084	15.0
50(03)	50	37.00	0.088	7.6
50(04)	50	37.53	0.104	5.1
50(05)	50	68.75	0.180	26.8
50(06)	50	69.81	0.182	18.1
50(07)	50	65.68	0.186	12.6
50(09)	50	72.47	0.218	14.0
50(10)	50	77.5	0.220	15.0
100(12)	100	38.53	0.078	34.8
100(13)	100	46.50	0.092	5.5
100(14)	100	39.41	0.092	5.1
100(15)	100	33.53	0.090	15.0
100(16)	100	42.34	0.112	3.0
100(24)	100	77.00	0.170	23.8
100(25)	100	84.09	0.188	18.0
100(26)	100	83.28	0.207	9.3
400(28)	400	48.22	0.085	35.2
400(30)	400	48.16	0.089	17.0
400(31)	400	41.47	0.094	8.1
400(32)	400	37.33	0.114	9.6
400(33)	400	90.63	0.170	22.3
400(35)	400	82.53	0.185	6.2
400(36)	400	83.41	0.194	2.0
400(37)	400	81.88	0.228	1.65

Table 3.3: *CUDSS* tests from Parra (2016)

The 6 groups analysed in this chapter were constructed to compare the evolution of the previously proposed r_u- and γ-markers in loose and dense sands when sheared in progressively increasing *CSRs* at a fixed confinement stress. A separate analysis of loose and dense sands for each of the confinement pressures was performed and, where possible, *CSR* levels between

loose and dense samples were matched. Additionally, the resulting identifications of liquefaction-triggering criteria within one group of the experimental tests were cross-referenced with other groups to help define consistent liquefaction-triggering markers based on r_u and γ for loose and dense samples sheared at different ranges of *CSR* and at varying confinement stresses. The *CUDSS* groups were defined as follow.

Group 1: 6 *CUDSS* tests from EG2018 were used. Only dense samples at 40 kPa confinement pressure and sheared within a *CSR* range of 0.085 to 0.140 (low to high) were analysed. Specifically, tests 40(01), 40(02), 40(03), 40(04), 40(05) and 40(06) from EG2018 were compared. No loose samples were available at this confinement pressure.

Group 2: 8 *CUDSS* tests from PB2016 were used. Both loose and dense samples at 50 kPa confinement pressure and sheared within *CSR* ranges of 0.075 to 0.104 (low to intermediate) and 0.180 to 0.218 (high), respectively. Specifically, loose tests 50(01), 50(02), 50(03), 50(04), and dense tests 50(05), 50(06), 50(07) and 50(09) from PB2016 were compared. Since the *CSR* ranges do not overlap, loose and dense sample comparisons are not directly comparable. However, individual group comparisons are still perfectly valid within their own *CSR* ranges and loose and dense samples were qualitatively compared.

Group 3a: 6 *CUDSS* tests from PB2016 were used. Both loose and dense samples at 100 kPa confinement pressure and sheared within *CSR* ranges of 0.078 to 0.112 (low to intermediate) and 0.170 to 0.207 (high), respectively. Specifically, loose tests 100(12), 100(15), 100(16), and dense tests 100(24), 100(25) and 100(26) from PB2016 were compared. Similar to Group 2, Group 3a did not have comparable *CSR* ranges between loose and dense samples, so a qualitative comparison was made between the two general states of sand.

Group 3b: 8 *CUDSS* tests from PB2016 and EG2018 (4 each) were used. Both loose (from PB2016) and dense (from EG2018) samples at 100 kPa confinement pressure and sheared within *CSR* ranges of 0.078 to 0.112 (low to intermediate) and 0.076 to 0.115 (low to intermediate), respectively. Specifically, loose tests 100(12), 100(15), 100(13) and 100(16) from PB2016, and dense tests 100(07), 100(09), 100(10) and 100(13) from EG2018, respectively, were compared. In this particular case, *CSR* ranges and individual values for each tests were selected in a way so that a direct quantitative comparison between loose and dense sands could be performed.

Group 3c: 8 *CUDSS* tests from EG2018 were used. Only dense samples at 100 kPa confinement pressure and sheared within a *CSR* range of 0.080 to 0.150 (low to high) were analysed. Specifically, tests 100(08), 100(09), 100(10), 100(11), 100(13), 100(15), 100(16) and 100(17) from EG2018 were compared. No loose samples were available at this confinement pressure.

Group 4: 8 *CUDSS* tests from PB2016 were used. Both loose and dense samples at 400 kPa confinement pressure and sheared within a *CSR* range of 0.085 to 0.114 (low to intermediate) and 0.170 to 0.228 (high), were analysed. Specifically, loose tests 400(28), 400(30), 400(31), 400(32), and dense tests 400(33), 400(35), 400(36), 400(37) from PB2016 were compared. Similar to Group 2 and 3a, Group 4 did not have comparable *CSR* ranges between loose and dense samples, so a qualitative comparison was made between the two general states of sand.

In addition to the 6 groups established above, 3 more groups (5a, 5b and 6) combining *CUDSS* from both PB2016 and EG2018 were used to evaluate the effect of confinement pressure on loose and dense samples. Groups 5a to 6 were constructed to compare the evolution of the previously proposed r_u- and γ-markers in loose and dense sands when sheared in progressively increasing σ'_{vc} at equivalent magnitudes of *CSR* between loose and dense sands (where possible). A combined analysis of loose and dense samples from PB2016 (sheared at an equivalent *CSR*) was

performed to compare the effect of confinement pressure on the behaviour of liquefaction-onset. Additionally, a similar analysis was performed with dense sand samples from EG2018. Group 5a consisted of 6 *CUDSS* tests from PB2016, where both loose and dense samples sheared at equivalent *CSRs* were analysed under confinement pressures of 50 kPa, 100 kPa and 400 kPa (low to high). Specifically, loose tests 50(03), 100(15), 400(31), and dense tests 50(07), 100(25) and 400(35) from PB2016 were compared. Group 5b included 6 *CUDSS* tests from PB2016, where both loose and dense samples sheared at equivalent *CSRs* were analysed under confinement pressures of 50 kPa, 100 kPa and 400 kPa (low to high). This group is almost identical to Group 5a, with the slight difference that, instead of tests 100(15) and 400(31), tests 100(14) and 400(30) were selected to have another comparable *CSR* set between loose and dense samples. Lastly, Group 6 included 8 *CUDSS* tests from EG2018, where only dense samples sheared at equivalent *CSRs* were analysed under confinement pressures of 40 kPa and 100 kPa (low to intermediate). Specifically, samples confined at 40kPa 40(01), 40(02), 40(04), 40(05), and confined at 100kPa 100(09), 100(10), 100(14), 100(16) were compared.

The next sections described the behaviour of the onset of liquefaction in relation to the selected r_u- and γ-based markers when analysing select *CUDSS* tests grouped according to Group 1 to 6. The effect of CSR and confinement pressure on the behaviour of liquefaction-onset in terms of r_u and γ in loose and dense samples was analysed simultaneously. It is worth mentioning that, even if separate groups were built for this analysis, all *CUDSS* groups will provide insight on the effect of both *CSR* and confinement pressure on liquefaction behaviour.

3.1.1 Preliminary remarks on *CUDSS* test groups

When comparing dense samples confined at 40 kPa and 50 kPa and sheared at diverse cyclic shear stress amplitudes from Group 1 and 2, the difficulty of *CUDSS* tests performed by El Ghoraiby and Manzari in reaching r_u-values ≥ 0.90 stands out. The reason for this could be threefold: Either the boundary conditions in the *CUDSS* tests confined at 40 kPa were not able to generate fully undrained conditions throughout shearing[3], limiting the accumulation of pore pressures to ≈ 0.90, transducers which measured the pore pressures in the centre of the sample did not capture the build up in water pressure adequately, or samples sheared at very low confinement stresses (smaller than 50 kPa) do, in fact, exhibit liquefaction with a peak value of r_u. Unfortunately, given that only one set of dense samples confined at 40 kPa was available, the explanation to this behaviour could not be confirmed.

3.1.2 Effect of *CSR* on the behaviour of liquefaction in loose and dense sands

As mentioned earlier, this subsection covered the analysis of the effect of *CSR* on liquefaction behaviour on the basis of the constructed groups 1 to 4. Therefore, this part of the report was subdivided accordingly. Lastly, it was important to define, according to the loose and dense *CUDSS* tests observed in both databases, what ranges of *CSR* could be defined as low, intermediate, high or very high. Therefore, the following delimitations were defined:

- **Low range**: *CSRs* values up to 0.09. This limit was set based on the increased cyclic strength reduction experienced in both loose and dense samples when sheared at a $CSR > 0.09$.

[3]Some tests, in both PB2016 and EG2018, exhibited drops in r_u during cyclic mobility, which could be explained by the inability of maintaining proper undrained conditions during dilative shearing throughout cyclic mobility. This, however, is not present in samples confined at 40 kPa, where cyclic mobility is reached in the usual manner, staying at a constant average r_u after liquefaction has occurred. Therefore, the analysis of individual N-r_u curves, in the authors opinion, did not show any sign of alteration in the boundary conditions after liquefaction occurred. Nevertheless, it could be that the imperfect boundary conditions were present all throughout shearing.

- **Intermediate range**: *CSRs* values between 0.09 and 0.120. The upper limit was defined based on the cyclic resistance exhibited by loose samples at confinement pressures of 50 kPa, 100 kPa and 400 kPa. Even though these loose samples in Parra (2016) were only sheared up to a $CSR = 0.114$, the cyclic strength of the loose sample at 400 kPa confinement still showed some cyclic resistance. This gave reason to extend the upper limit to what could be defined as an intermediate range of *CSR*, so that all loose samples are able to fail when sheared at a low or intermediate *CSR*. This may seem arbitrary but it is reasonable to assume that the cyclic strength of loose sands subjected to high *CSRs* is virtually negligible, so it was pertinent, at least for this dissertation, to assume this upper limit.

- **High range**: *CSRs* values between 0.120 and 0.190. The upper limit was defined based on the reduced cyclic resistance exhibited in dense samples from Parra when sheared at $CSR \approx 0.190$.

- **Very high range**: *CSRs* values greater than 0.120. No upper limit was set for this range, as dense samples from Parra confined at low pressure exhibited remarkable cyclic resistance in terms of reaching 5% *SA* accumulated shear strains when sheared at $CSRs > 0.20$.

Analysing the effect of increasing *CSR* on dense Ottawa sand subjected to 40 kPa confinement (Group 1)

Dense Ottawa sand samples confined at 40 kPa showed typical cyclic behaviour in terms of shear strain accumulation, reaching the γ-thresholds in a spaced out manner with cycle-differences between the 3% and 5% markers ranging from approximately 7 and 11 to 2 and 3, for samples sheared at low and high *CSRs*[4], respectively (see Figure 3.5 and Figure 3.2 contrast between loose and dense samples in terms of reaching deformation thresholds). However, the dense samples had difficulty reaching r_u-values ≥ 0.90, and some cases even > 0.85 (which was the case of tests 03 and 04 from EG2018). This condition was described in section 3.1.1 and it could be proposed that these values are flawed. However, since no additional tests were performed at those conditions, the analysis assumed them as correct and proceeded with caution. Furthermore, tests reached r_u-values of ≈ 0.90 at approximately the same time that accumulated shear strains reached the threshold of $\gamma = 3\%$. Tests sheared at a $CSR \geq 0.12$ exhibited smaller peak r_u-values at ≈ 0.85, closely anticipated or followed by the activation of the $\gamma = 5\%$ threshold. The sample sheared at a *CSR* of 0.13 managed to reach a peak r_u-magnitude of 0.90 at the same deformation conditions as tests 03 and 04, whereas the sample sheared at a *CSR* of 0.14 reached $r_u = 0.90$ at approximately the same moment as $\gamma = 3\%$, reaching $r_u = 0.95$ at approximately 5% shear strains. In summary, the behaviour of liquefaction in 50% of the tests (those sheared at low and high *CSRs*) exhibited the activation of $r_u = 0.90$ and $\gamma = 3\%$ at approximately the same number of cycles (within a 3-cycle difference in test 01, sheared at a low *CSR*, and within a 1-cycle difference in tests 02 and 06, sheared at a low and high *CSR*). The other 50% of tests (03, 04 and 05) exhibited varied behaviour, activating $r_u = 0.85$ and $\gamma = 5\%$ markers in tests 40(03) and 40(04) (within a 2-cycle difference), as well as $r_u = 0.85$ and $\gamma = 3\%$ markers in tests 40(05) (within a 1-cycle difference) at approximately the same moment. These last results put in question whether it would be better to pair $r_u = 0.85$ or 0.90 with $\gamma = 3\%$ to define the liquefaction-state in dense sands confined at 40 kPa. However, differences between $r_u = 0.85$ and 0.90 were not too large (approximately 3 cycles at most in the previously-mentioned tests), which could be attributed to the intrinsic variability in tests like these and not to the liquefaction-triggering mechanism at these shearing conditions. Therefore, it could be concluded that, for dense sands confined at 40 kPa and sheared at *CSRs* between 0.085 and 0.140, the state of liquefaction can be approximated conservatively by using $r_u \approx 0.90$ and $\gamma = 3\%$, providing a consistent two-parameter-based threshold which can also describe the seismic performance of

the sand.

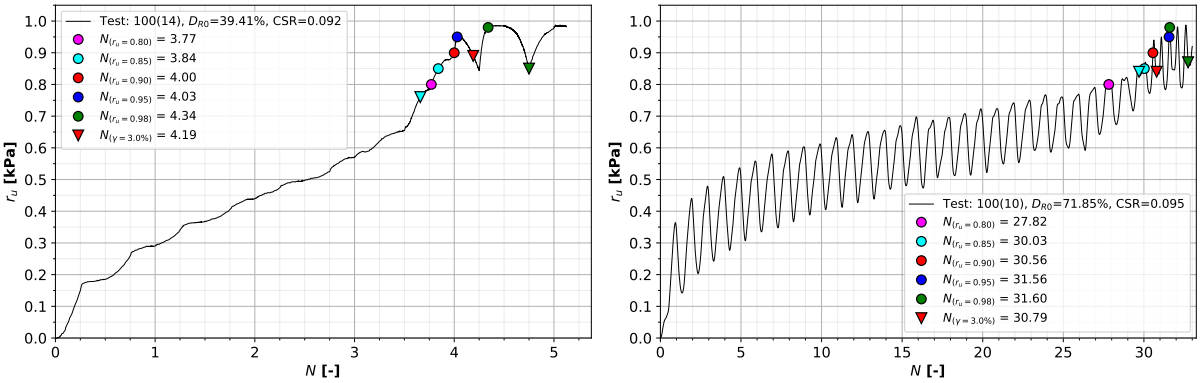

(a) PB2016: Loose sand, CSR = 0.092 (b) EG2018: Dense sand, CSR = 0.095

Figure 3.2: Comparison of triggering of γ-thresholds in loose and dense samples confined at 100 kPa and sheared at a comparable *CSR*

Analysing the effect of increasing *CSR* on loose and dense Ottawa sand subjected to 50 kPa confinement (Group 2)

When observing Figure 3.6, which presents loose and dense samples sheared at different *CSR* ranges at 50 kPa confinement, the behaviour of liquefaction-onset is defined clearly. The top row, showing loose sands sheared at low to intermediate *CSRs*, shows steadily decreasing cyclic strength with increasing *CSR*, where all r_u-markers are activated in a progressive manner, separated at most by 1 shearing cycle, before or at the same time as the $\gamma = 3\%$ threshold was activated. The bottom row, showing dense sands sheared at high to very high *CSRs*, however, does not show with clarity the steady decrease in cyclic strength with increasing *CSR* in terms of r_u. This could be attributed to the range of *CSR* the samples were subjected to, as r_u-values in dense samples confined at 40 kPa and shown in Figure 3.5, described above, also showed little degradation when sheared at high *CSRs*. However, the degradation was evident through the γ-markers, which steadily showed a degradation in cyclic resistance with the exception of test 50(09), which got a greater cyclic resistance due to a greater initial relative density of 72.5%, compared to the average of 68.1%. Here, the usefulness of defining liquefaction based on 2 parameters is evident, as dense sands might reach values of r_u close to 1.0 quickly, but the development of shear strains, indicator of seismic performance, need some time to develop due to the dense packing of these types of sands. Here, the $\gamma = 1\%$ threshold is reached almost immediately after the start of shearing, followed by the $\gamma = 3\%$ marker within a decreasing cycle-difference of 4 to 2.5, and lastly reaching the $\gamma = 5\%$ threshold after 22 to 8 cycles (decreasing with increasing *CSR*). Having analysed the liquefaction-onset in loose and dense sands confined at 50 kPa, it can be concluded that, for loose sands, the liquefaction-state can be approximated by both $r_u = 0.98$ and $\gamma = 3\%$, within a low to intermediate *CSR* range, whereas for dense sands sheared within high and very high *CSR* ranges, the state of liquefaction can be approximated in a conservative manner by $r_u = 0.95$ and $\gamma = 3\%$. It could be argued that $r_u = 0.98$ would be better suited to describe the state of liquefaction given that samples 50(06), 50(09) and 50(10) reached $r_u = 0.98$ before reaching $\gamma = 3\%$. However, a middle ground was considered, since the intrinsic variability

[4]In general, the spacing between the activation of γ-thresholds at 3% and 5% seem consistent with behaviour exhibited in dense samples when cyclically sheared in undrained conditions at any confinement pressure. However, as will be seen later in this section, the separation between those markers is usually much larger. Therefore, stress-strain behaviour might not be representative due to induced biases either at the preparation stage or due to issues in maintaining proper undrained boundary conditions.

could allow liquefaction at lower values of r_u, such as those seen in tests 50(05) and 50(07) (see Figure 3.3), therefore establishing a $r_u = 0.95$ as a conservative representation for the description of liquefaction in dense sands based on strength loss.

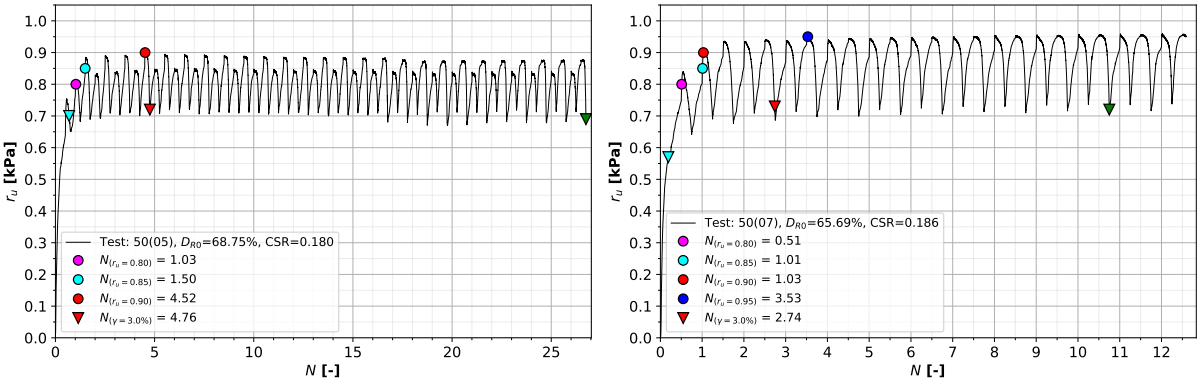

(a) Dense sand, CSR = 0.180 (b) Dense sand, CSR = 0.186

Figure 3.3: Outlying test results in dense Ottawa F-65 sand *CUDSS* tests confined at 50 kPa from PB2016

Analysing the effect of increasing *CSR* on loose and dense Ottawa sand subjected to 100 kPa confinement (Groups 3a, 3b and 3c)

Group 3a compared the liquefaction-onset behaviour in loose and dense sands confined at 100 kPa from Parra (2016) when sheared at low to intermediate and high to very high *CSRs*, respectively (see Figure 3.7). The top 3 figures show a standard decrease in cyclic resistance in loose samples, with increasing *CSR*, where all three γ-markers are activated very closely together with the r_u-markers. As is common in loose samples sheared at low to intermediate *CSRs*, accumulation of shear strains started to reach the specified thresholds when r_u started to get close to unity. All of the proposed markers for both r_u and γ were activated within a 2-cycle range for all loose samples analysed, slightly more concise than their loose counterparts confined at 50 kPa (see Figure 3.6). These almost identical behaviours had some slight variations but it could be argued that, for loose samples, the choice of liquefaction-triggering criterion for a liquefaction analysis could be anyone's choice, as they all fall within a very narrow range of cycles-to-activation. Nevertheless, it was concluded that the liquefaction-state in loose samples, sheared at low to intermediate *CSRs*, could be accurately described by r_u- and γ-markers at 0.95 and 3%, respectively, as they occurred at the same moment, within a half-cycle difference at the most, with the exception of test 100(12), where r_u-markers > 0.90 were not reached either because cyclic mobility was not allowed to continue for long, or because of imperfect boundary conditions during testing, which could have allowed for changes in volume during shearing, leading to partially drained conditions. As for the dense samples in the bottom row, liquefaction-onset behaviour showed the activation of all r_u-markers before the triggering of the $\gamma = 3\%$ marker in samples sheared up to a *CSR* of 0.188, whereas sample 100(26), sheared at $CSR = 0.207$, triggered the threshold at $\gamma = 3\%$ before r_u-markers at 0.95 and 0.98. Given that only 3 dense samples at 100 kPa from Parra (2016) were analysed, no conclusions could be extracted as to whether this deviation was part of the intrinsic variability of *CUDSS* tests when sheared at such high *CSRs* or part of the actual liquefaction behaviour. Therefore, based on what can be seen in Figure 3.7, the tests exhibit the usual type of shear strain accumulation evidenced in dense sands, which was fast activation of the $\gamma = 1\%$ threshold (within the $2^n d$ cycle in all three tests), followed by the activation of all r_u-markers before reaching the $\gamma = 3\%$ threshold (within 4 to 4.5 cycles in tests 24 and 25, and

1 cycle in test 26, which could be associated to the very high *CSR* or excessive local shearing associated with the intrinsic variability of soil), after which the $\gamma = 5\%$ threshold was activated with a cycle-lag of 18, 11 and 7, respectively for each test and *CSR* shown. This shows that in dense samples at 100 kPa, the number of cycles needed to reach the specified γ-markers reduced with increasing *CSR*, which was consistent with other dense samples of similar D_{R0} confined at different pressures. Having said this, it can be proposed that the liquefaction-state in dense sands sheared at high to very high *CSRs* is conservatively described by markers $r_u = 0.95$ and $gamma = 3\%$. It could be argued that $r_u = 0.98$ could better represent the state of liquefaction for this specific scenarios, but $r_u = 0.95$ was chosen because of the variability in test 100(26). Also, the differences between cycles to $r_u = 0.95$ and $\gamma = 3\%$ in all three tests were less than 3 cycles in tests 100(24) and 100(25), which were small compared to the total number of shearing cycles needed to reach $\gamma = 5\%$.

Next, Group 3c, shown in Figure 3.9, compared the behaviour of liquefaction-onset in dense samples from El Ghoraiby and Manzari (2018) at a confinement pressure of 100 kPa and sheared at low to high *CSRs*. When comparing the results obtained here with those obtained from samples sheared at high *CSRs* from PB2016 in Group 3a, shown in Figure 3.7, an unusually closely-spaced activation of the γ-thresholds was observed. After analysing the stress path and the stress-strain behaviour of each individual test and qualitatively comparing the observed behaviour to other databases (El Ghoraiby, Park, et al., 2017; Sriskandakumar, 2004), aside from PB2016, it was concluded that shear-strain-accumulation behaviour experienced by these tests was abnormal (see Figure 3.4), as accumulation of shear strains (between γ-thresholds at 3% and 5%) in dense sands usually involves more time and number of shearing cycles (mostly $\Delta N > 7$, according to observations). A possible explanation could be the presence of unintentionally introduced biases in the form of local deformations before the start of the tests. Another explanation could be that, during shearing, as discussed before in section 3.1.1, proper constant-volume boundary conditions were not maintained, causing the sample to locally reduce its relative density due to volumetric expansion during dilation, accelerating the accumulation of shear strains[5]. Therefore, in terms of γ-thresholds, the activation of the 5% threshold in these tests could not be considered to accurately describe liquefaction-state conditions for dense Ottawa F-65 sand. However, the γ threshold at 3% was accepted as valid, as trends in activation were consistent with those found in dense samples from Parra (2016). As for liquefaction behaviour in terms of r_u, the shown trends are consistent with those found by Parra (2016). According to this thorough analysis, it was concluded that the state of liquefaction in dense sands, confined at 100 kPa and sheared at low to high *CSRs*, could be approximated by the liquefaction-triggering markers $r_u = 0.90$ or 0.95 and $\gamma = 3\%$, considering the *CUDSS* tests from El Ghoraiby and Manzari (2018). The option between $r_u = 0.90$ was given for conservative reasons, as *CUDSS* samples sheared beyond 0.115 had difficulties in reaching $r_u = 0.95$. However, considering the trends in r_u-evolution in cyclic behaviour of dense sands and the *CUDSS* samples sheared at low *CSRs*, $r_u = 0.95$ could also be used. In any case, the differences in cycles-to-activation between r_u 0.90 and 0.95 in *CUDSS* tests in EG2018 were minimal (usually lower than 3 cycles). Lastly, loose and dense samples at equivalent *CSRs* were compared within low and intermediate ranges of *CSR*. This was possible by contrasting loose and dense *CUDSS* tests from Parra (2016) and El Ghoraiby and Manzari (2018), respectively, as they had overlapping *CSR* ranges at which the samples were sheared, shown in Figure 3.8. It was clear that, for a given *CSR*, dense samples had a greater cyclic resistance, both in terms of r_u and γ. However, the effect of relative density on cyclic resistance reduced with increasing *CSR*. This reducing effect affected both r_u- and γ-markers equally, although the effect on the 5% shear strain-threshold could not be confirmed due to the inconsistencies described earlier. Besides this, the only additional difference (without taking into account the issue of the 5% shear-strain threshold) could be that r_u markers in dense samples tended to activate in a more spaced-out manner, as can be seen in samples sheared at $CSRs \approx 0.095$. However, this isolated

event could be explained by the intrinsic variability in cyclic shearing of sands and, therefore, this condition could not be confirmed and was not included in the conclusions. Considering these observations, no new insight related to the behaviour of liquefaction-onset in dense sand was found and, therefore, the comparison of the *CUDSS* tests in Group 3b did not disagree with the proposed r_u- and γ-based liquefaction-triggering markers.

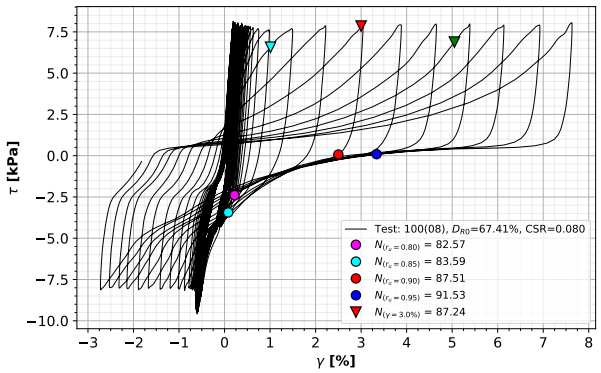

(a) El Ghoraiby and Manzari (2018): Dense Ottawa F-65 sand, 100 kPa confinement, CSR = 0.180, DSS

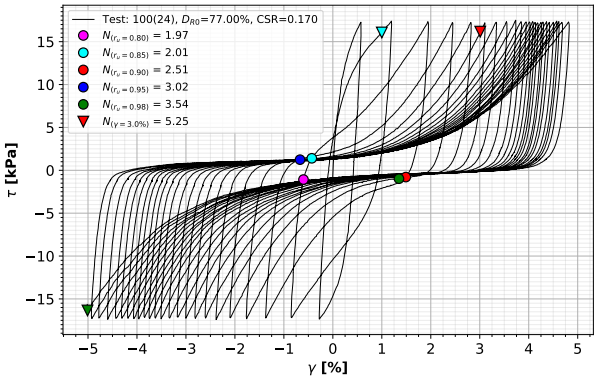

(b) Parra (2016): Dense Ottawa F-65 sand, 100 kPa confinement, CSR = 0.186, DSS

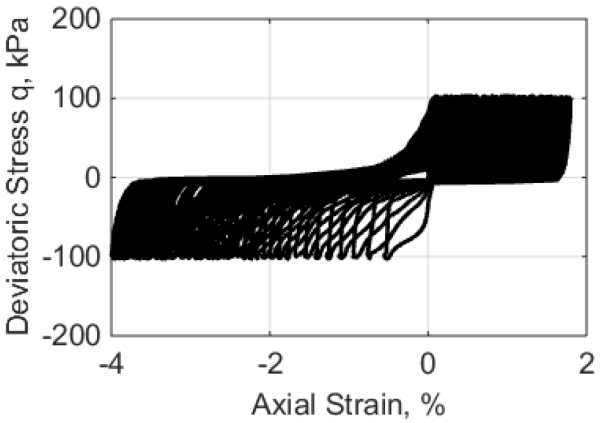

(c) El Ghoraiby, Park, et al. (2017): Dense Ottawa F-65 sand, 100 kPa confinement, CSR = 0.50, TXC

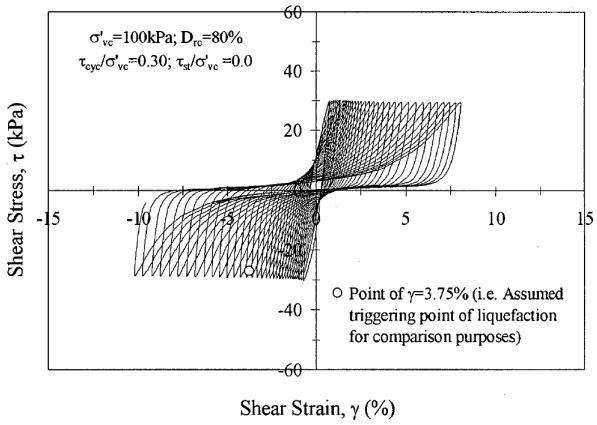

(d) Sriskandakumar (2004): Dense Fraser River sand, 100 kPa confinement, CSR = 0.30, DSS

Figure 3.4: Abnormality of stress-strain behaviour in dense *CUDSS* tests from El Ghoraiby and Manzari (2018) compared to typically observed cyclic stress-strain behaviour in dense sands in Parra (2016), El Ghoraiby, Park, et al. (2017) and Sriskandakumar (2004)

Analysing the effect of increasing *CSR* on loose and dense Ottawa sand subjected to 400 kPa confinement (Group 4)

As the last part of this section, the effect of *CSR* on loose and dense sands confined at 400 kPa was analysed through Group 4, shown in Figure 3.10. The top row shows a progressive increase in r_u-markers, closely-spaced, in simultaneity with the activation of, mostly, γ 3% and 5% thresholds. Results showed that loose sands sheared at low *CSRs* reached the 1% shear strain-threshold much earlier than the rest of the markers, approximately 27 to 8.5 cycles earlier, for samples sheared at a *CSR* of 0.085 and 0.089, respectively, reaching commonly exhibited

[5]This inconsistency was partially observable in dense samples confined at 40 kPa from El Ghoraiby and Manzari (2018).

shear-strain-accumulation behaviour in most loose sands when sheared at $CSRs > 0.090$. This difference could be attributed to the high confinement stress, and relative high cyclic stress, the dense sand is subjected to during shearing. However, it can also be seen that the activation of the $\gamma = 1\%$-threshold was consistent throughout the evaluated tests, suggesting that, given the high confinement stress and irregardless of the *CSR* (within a low to intermediate range), this threshold will be activated at a given number of cycles (in this case it was between $6^t h$ and $8^t h$ cycle). Furthermore, it was observed that, for samples sheared at a *CSR* below 0.089, r_u-markers at 0.90 and 0.95 were activated at almost the same cycles as $\gamma = 3\%$, whereas for samples sheared at a $CSR/geq0.089$, the activation of γ-threshold at 3% was in tune with almost all r_u-markers. After the activation of $\gamma = 3\%$, the threshold at $\gamma = 5\%$ was reached almost immediately after, with differences of 1 cycle, at most (in the case of test 28). Therefore, considering all previously described observations, it was concluded that the state of liquefaction for loose samples confined at 400 kPa and sheared within a low to intermediate *CSR* range could be accurately described by $r_u = 0.95$ and $\gamma = 3\%$. For samples sheared at *CSRs* larger than 0.085, it could be argued that marker $r_u = 0.85$ would be a better combination. However, the differences between shearing cycles to all r_u-markers was basically negligible for samples sheared at $CSRs \geq 0.089$, making it of little relevance which r_u value was specifically chosen, contrary to what was observed in test 400(28), where there was a more noticeable difference.

As for the dense samples sheared at high to very high ranges of *CSR* and shown in the bottom row of Figure 3.10, liquefaction-onset behaviour varied somewhat both in terms of r_u and γ. For instance, $\gamma = 1\%$ was reached within the first quarter-cycle in all samples given the high cyclic stresses applied in a densely packed sand. After that, $\gamma = 3\%$ was reached first in all evaluated tests, with decreasing cycle-differences as *CSRs* increased, consistent with cyclic behaviour of densely-packed soils. The activation of the $\gamma = 3\%$ threshold, however, and contrary to the behaviour experienced in loose sands at the same confinement pressure, was very closely followed by $r_u = 0.80$ and $r_u = 0.85$, increasing in proximity with all following r_u-markers as *CSR* increased. As for the activation of the $\gamma = 5\%$ marker, a lot of variation was observed, as it at times was reached even before the activation of $r_u = 0.80$ (test 36), immediately following the activation of $\gamma = 3\%$ or with some lag. However, from what has been observed in dense sands at this confinement pressure, the almost simultaneous activation of the liquefaction-triggers at $r_u = 0.85$ and $\gamma = 3\%$ was consistent throughout the evaluated tests. Therefore, it was concluded that the state of liquefaction in dense sands confined at 400 kPa was best described by $r_u = 0.80$ and $\gamma = 3\%$. If more flexibility was needed for samples sheared at greater *CSRs*, a magnitude between 0.85 and 0.90 could also be used to represent, in combination with $\gamma = 3\%$, the state of liquefaction in terms of r_u in dense samples sheared at a $CSR > 0.185$.

3.1.3 Effect of confinement pressure on liquefaction onset in loose and dense sands

After analysing the effect of *CSR* on the liquefaction-onset behaviour of loose and dense sands confined at fixed confinement pressures, it was of interest to perform a cross-referenced comparison of loose and dense *CUDSS* tests sheared at comparable *CSR* but with varying confinement pressures. This was tackled by comparing the *CUDSS* tests in groups 5a, 5b and 6, shown in Figures 3.11, 3.12 and 3.13. When comparing loose samples from PB2016 at an equivalent *CSR* of 0.090 over confinement pressures of 50, 100 and 400 kPa, it could be clearly seen that, with increasing confinement, there was an increase in cyclic resistance both relative to r_u- and γ-values. As for the dense samples, a general reduction in cyclic resistance was experienced with increasing confinement pressure (when analysed at equivalent *CSRs*).

3.2 Discussion and preliminary conclusions regarding liquefaction-onset in loose and dense Ottawa F-65 sand

After a thorough analysis of loose and dense samples sheared at diverse ranges of *CSR*, at different confinement pressures and from two different databases, quantitative measures for liquefaction-triggering criteria could be defined for specific and general types of sands sheared under different conditions. For each of the analysed sand groups, the following physically-consistent liquefaction-triggering criteria were defined to best represent a liquefied state.

Dense Ottawa F-65 sand confined at 40 kPa A quantitatively appropriate definition of a liquefied state in dense Ottawa F-65 sand when sheared within a low to intermediate *CSR* range and at 40 kPa (low) confinement could be approximated by liquefaction-triggering markers $r_u = 0.90$ and $\gamma = 3\%$.

Loose and dense Ottawa F-65 sand confined at 50 kPa For loose and dense Ottawa F-65 sands, confined at 50 kPa (low) and sheared within the *CSR* ranges specified, the state of liquefaction could be described by $r_u = 0.98$ and $\gamma = 3\%$, for loose sands, and $r_u = 0.95$ and $\gamma = 3\%$, for dense sands, respectively.

Loose and dense Ottawa F-65 sand confined at 100 kPa For loose and dense Ottawa F-65 sands, confined at 100 kPa (intermediate) and sheared within the *CSR* ranges specified, the state of liquefaction could be quantitatively approximated by $r_u = 0.95$ and $\gamma = 3\%$ for both loose and dense sands. Both the r_u- and γ-based liquefaction-triggering criteria were confirmed by both analysed databases.

Loose and dense Ottawa F-65 sand confined at 400 kPa For loose and dense Ottawa F-65 sands, confined at 400 kPa (high) and sheared within the *CSR* ranges specified, the state of liquefaction could be quantitatively approximated by $r_u = 0.95$ and $\gamma = 3\%$, for loose sands, and $r_u = 0.85$ and $\gamma = 3\%$, for dense sands, respectively.

Based on these results, a general set of liquefaction-triggering criteria for general types of sands sheared under various conditions was defined. For a cycle-difference tolerance of $\pm$ 2.5 cycles, $r_u = 0.95$ and $\gamma = 3\%$ were defined as appropriate liquefaction-triggering criteria which could be used for the calibration of cyclic undrained behaviour of general sands with Additionally, during the entire evaluation process of cyclic undrained shear tests of loose and dense sands, the following remarks and preliminary conclusions were found.

- Loose Ottawa F-65 sands exhibited increases in cyclic resistance with increasing confinement pressure, whereas dense samples showed the opposite trend. The increasing cyclic behaviour in loose sands could be attributed to particularities of Ottawa F-65 sand, but the trend was consistent in most of the *CUDSS* tests and was also confirmed in previous findings presented in chapter 2 and other by other researchers (Tziolas, 2019).

- At low to intermediate *CSRs*, loose sands at any confinement pressure and dense sands confined at high overburden pressures tended towards a net contractive behaviour, being very stiff while accumulating pore pressures. If the *CSR* was low to intermediate, the accumulation of shear strains also had a very stiff behaviour, which then increased rapidly once the pore pressures reached values close to $r_u \approx 1$.

- At low to intermediate *CSRs*, dense sands confined at low to intermediate overburden pressures tend to have a net dilative behaviour, where the accumulation of pore pressures is much slower due to the presence of greater dilative cycles during the shearing cycles. However, as mentioned above, these dilative tendencies tend to be suppressed when the confinement pressure is high enough.

- Loose and dense sands sheared at high *CSRs* tended to accumulate low-magnitude shear strains very fast, as well as pore pressures. In most cases, it was not even possible to shear loose sands at such high *CSRs* the denser samples were subjected to. In the case of dense sands, the application of high *CSRs* may generate a rapid accumulation of pore pressures, but larger shear strains ($\gamma \geq 3.0\%$) needed some time to develop.

- An important aspect to consider was the extrapolation of these findings towards a practical setting. By that, the question of whether these liquefaction-triggering criteria can be effectively used to identify liquefaction within an analysed soil profile appears, given that the ideal laboratory boundary conditions do not necessarily apply on-site. One of these questions was regarding the shear strain accumulation that soil experiences during shaking. There will be differences between shear strains developed in a single element and idealised environment compared to a practical situation, in that they may not be as large on-site as in laboratory tests, which creates a problem when trying to confirm liquefaction from a combined r_u- and γ-based approach. Therefore, a possible solution was to calibrate the model based on the before-mentioned liquefaction-triggering markers, but then evaluate liquefaction-triggering, in a practical setting such as a soil column, with a lower γ-threshold, as shear strains may not necessarily reach 3%. This threshold could be conservatively reduced to 2%, which was considered to be an indicator that the layer was, at least, close to liquefaction.

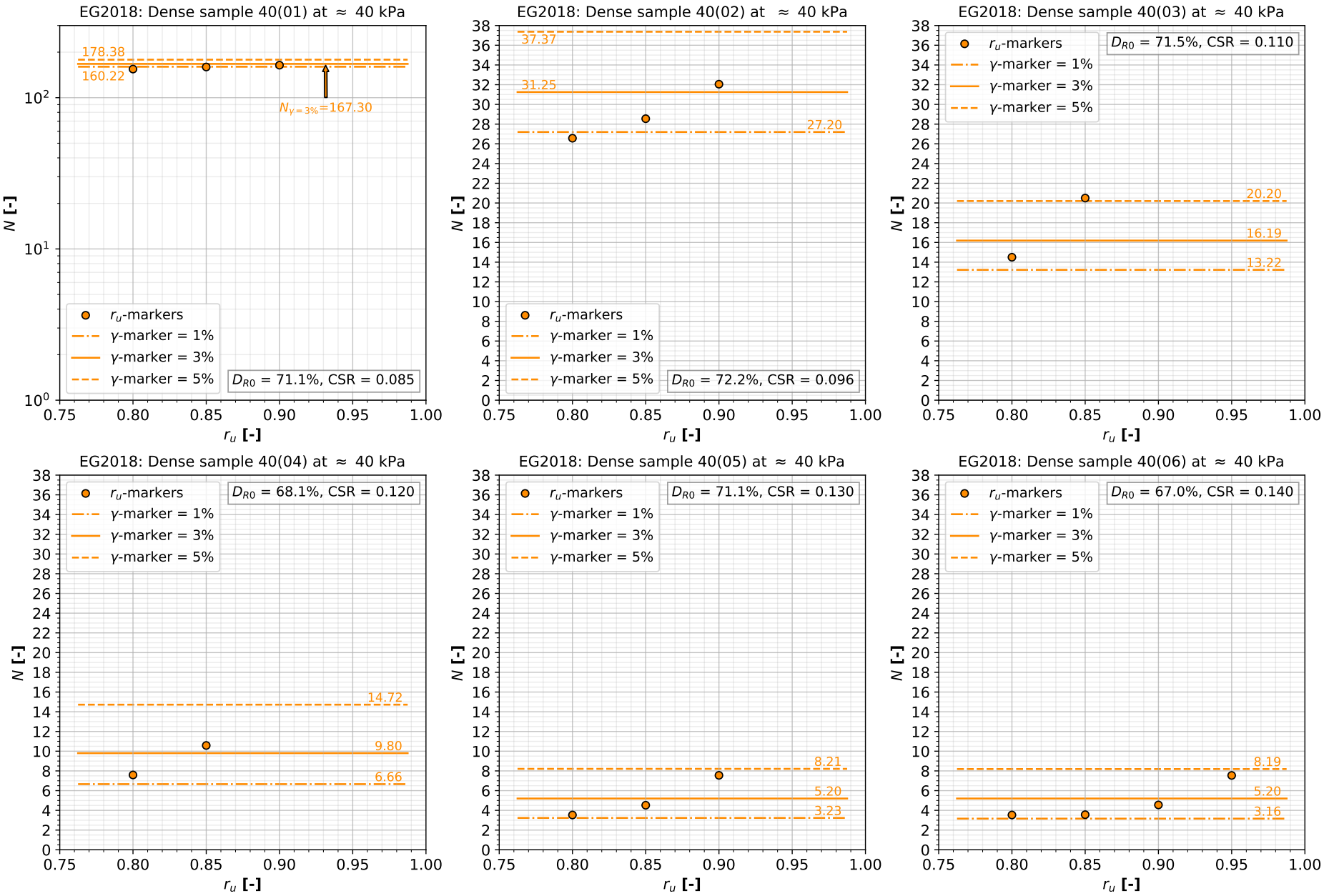

Figure 3.5: Group 1: Analysis of liquefaction onset in dense Ottawa F-65 sand *CUDSS* tests from El Ghoraiby and Manzari (2018) confined at 40 kPa and with increasing *CSR*

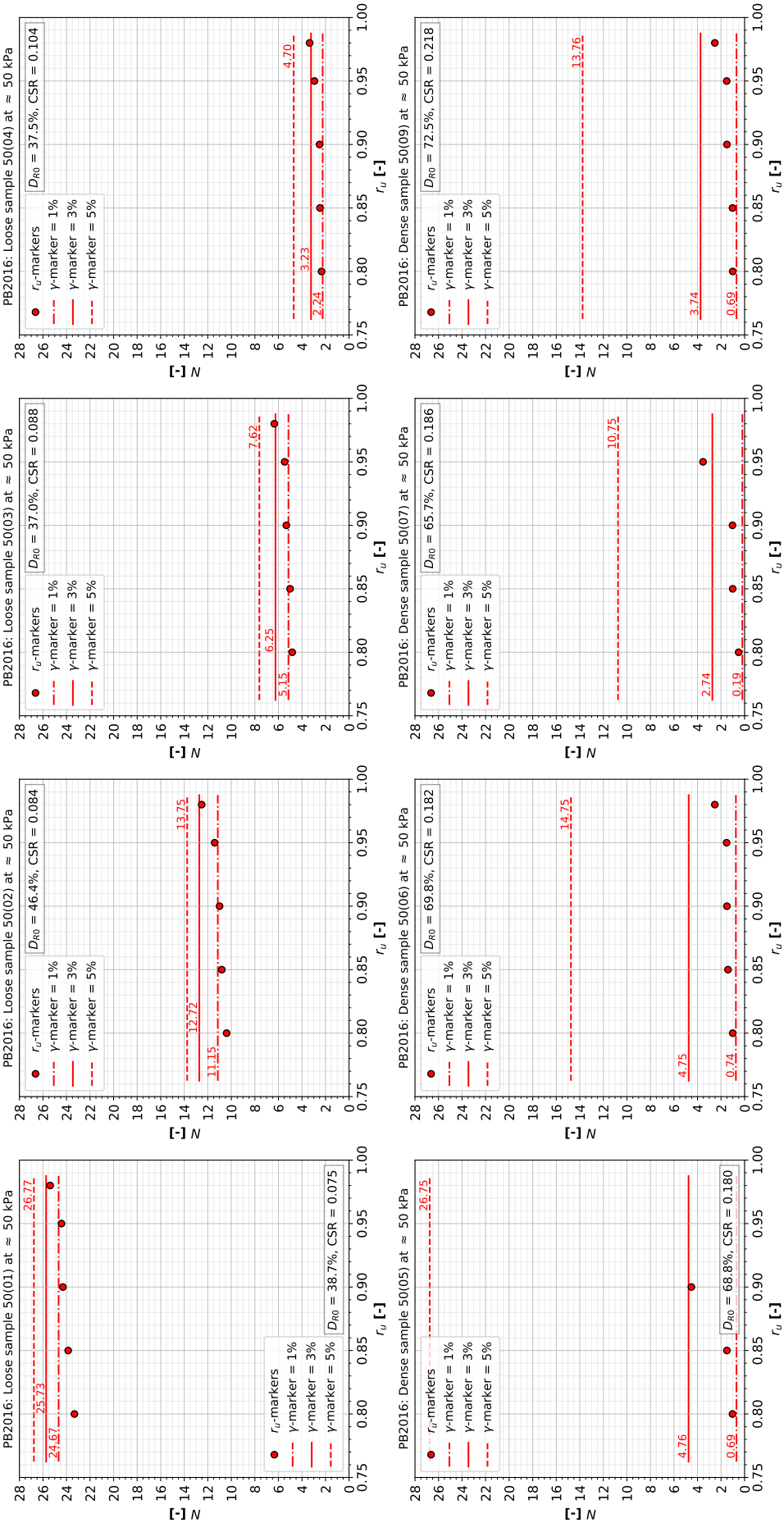

Figure 3.6: Group 2: Analysis of liquefaction onset in dense Ottawa F-65 sand *CUDSS* tests from Parra (2016) confined at 50 kPa and with increasing *CSR*

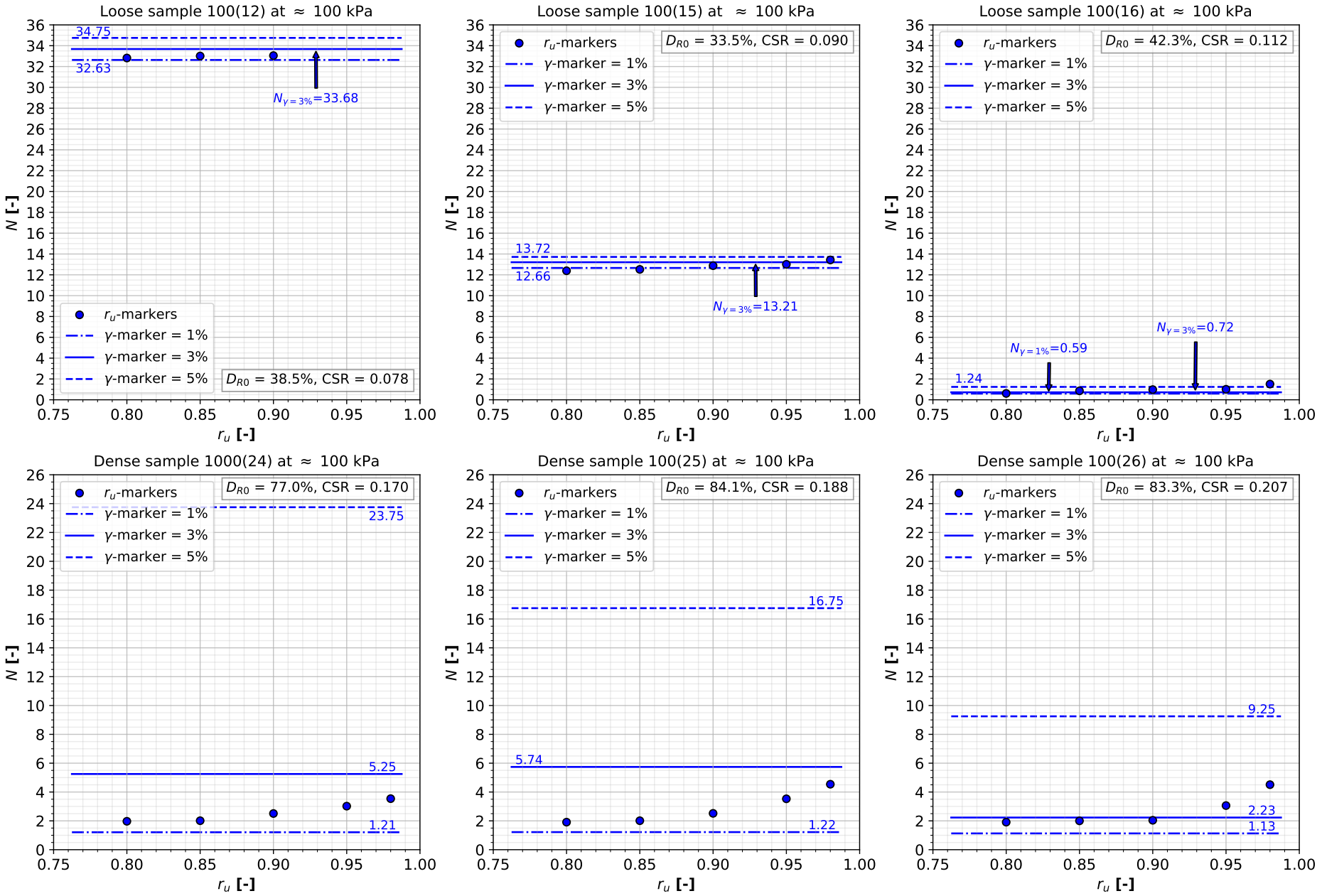

Figure 3.7: Group 3a: Analysis of liquefaction onset in loose and dense Ottawa F-65 sand *CUDSS* tests from Parra (2016) confined at 100 kPa and with increasing *CSR*

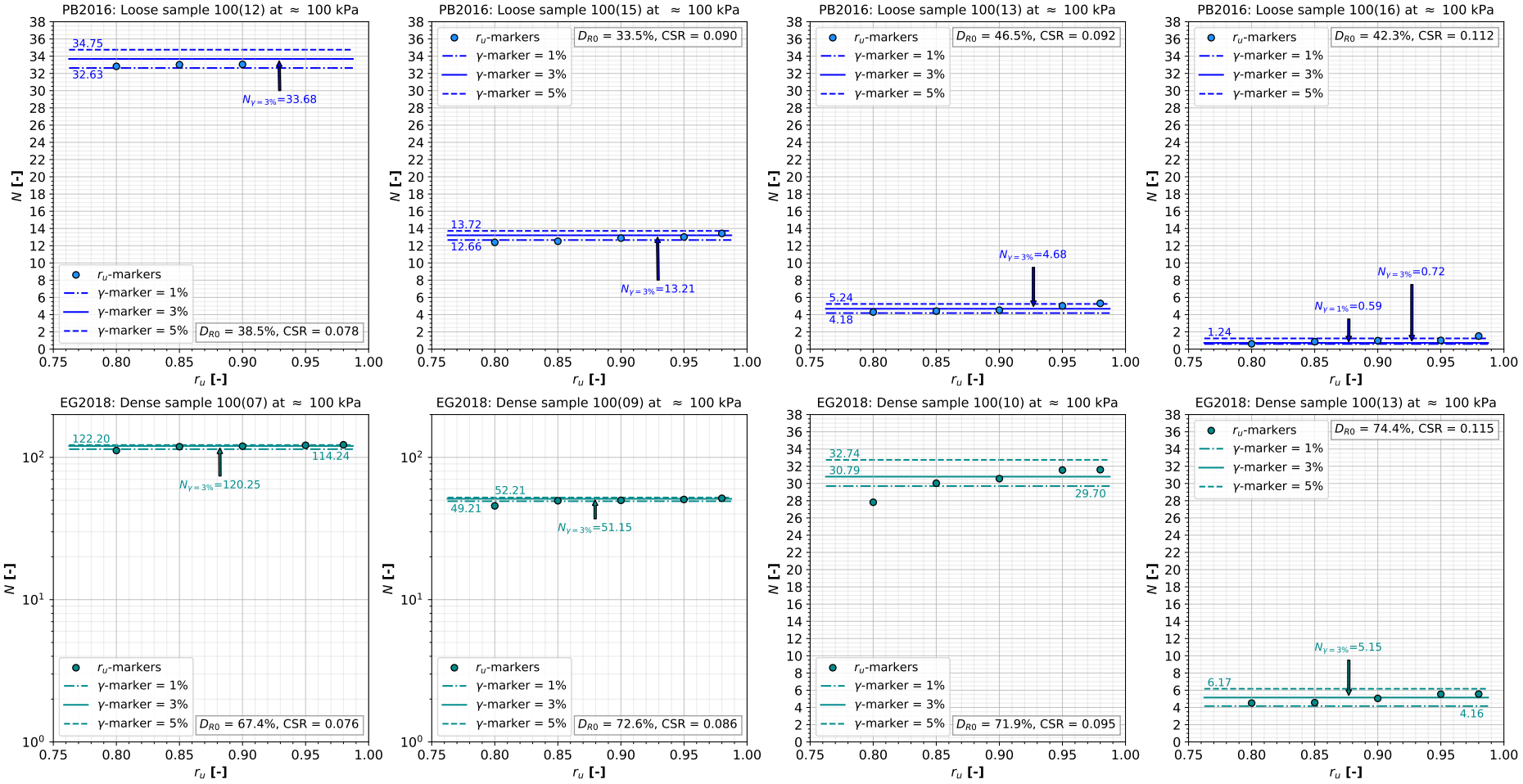

Figure 3.8: Group 3b: Analysis of liquefaction onset in loose and dense Ottawa F-65 sand *CUDSS* tests from Parra (2016) and El Ghoraiby and Manzari (2018), respectively, confined at 100 kPa and with increasing *CSR*

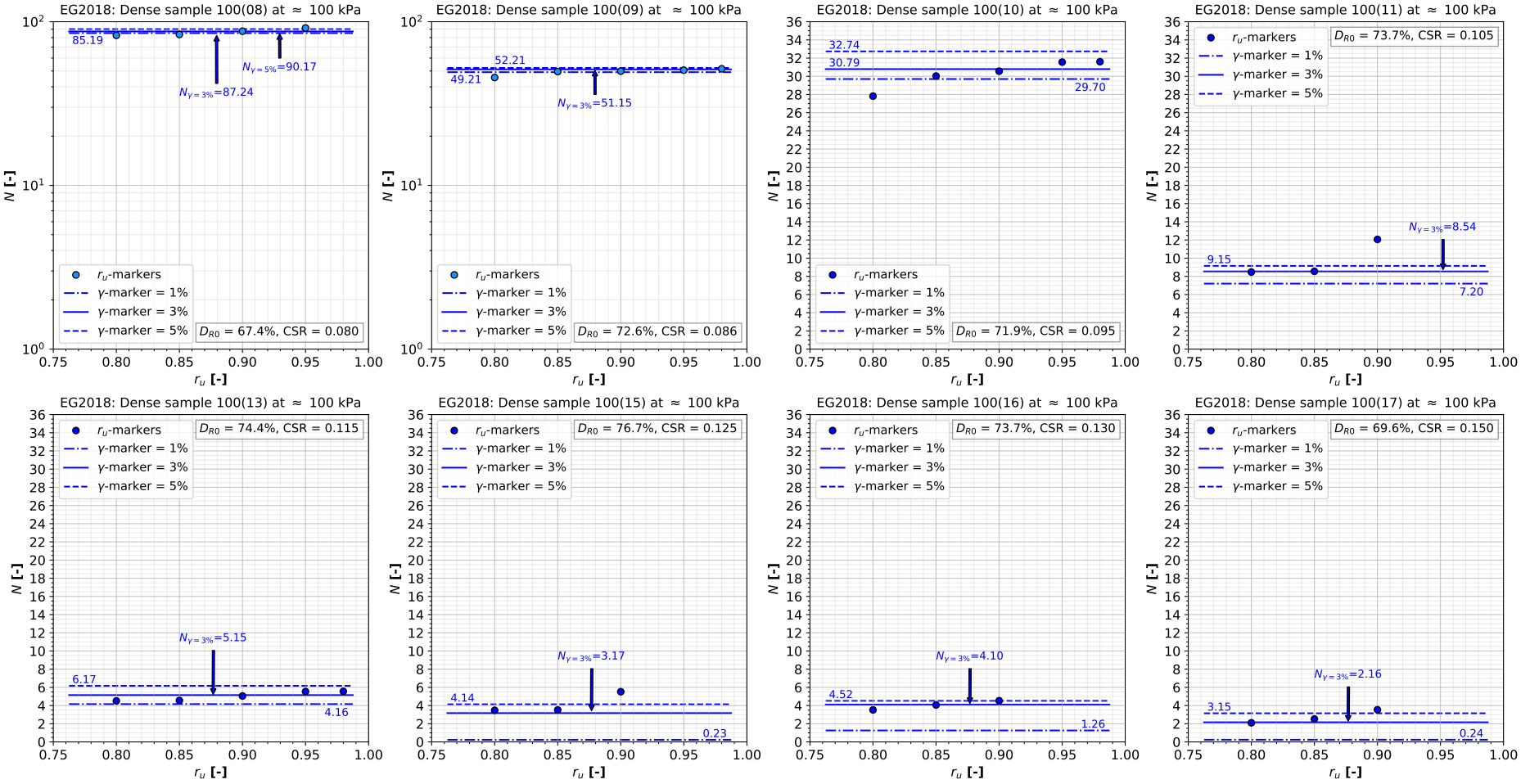

Figure 3.9: Group 3c: Analysis of liquefaction onset in dense Ottawa F-65 sand *CUDSS* tests from El Ghoraiby and Manzari (2018) confined at 100 kPa and with increasing *CSR*

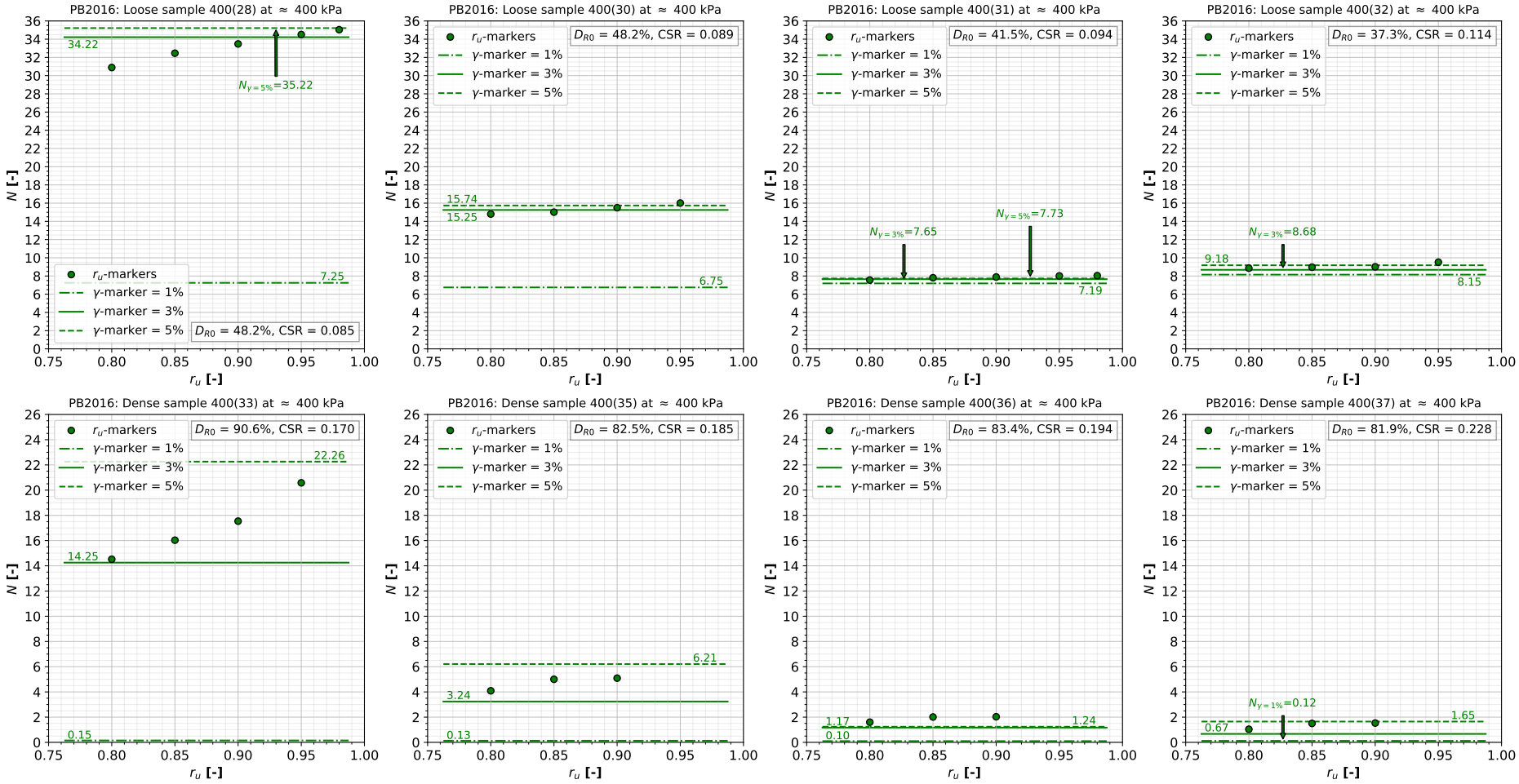

Figure 3.10: Group 4: Analysis of liquefaction onset in loose and dense Ottawa F-65 sand *CUDSS* tests from Parra (2016) confined at 400 kPa and with increasing *CSR*

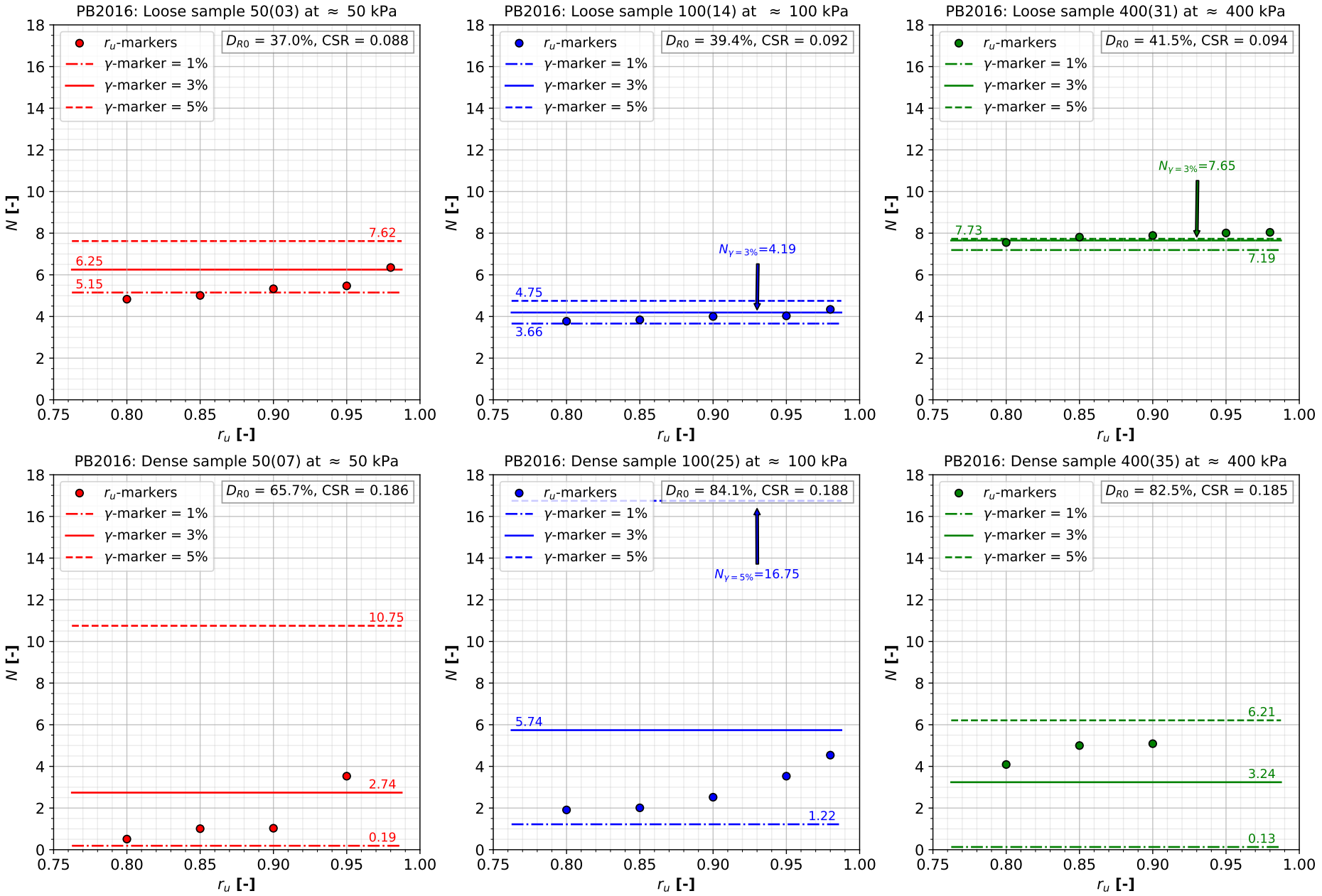

Figure 3.11: Group 5a: Analysis of liquefaction onset in loose and dense Ottawa F-65 sand *CUDSS* tests from Parra (2016) at equivalent *CSRs* and increasing confinement pressure

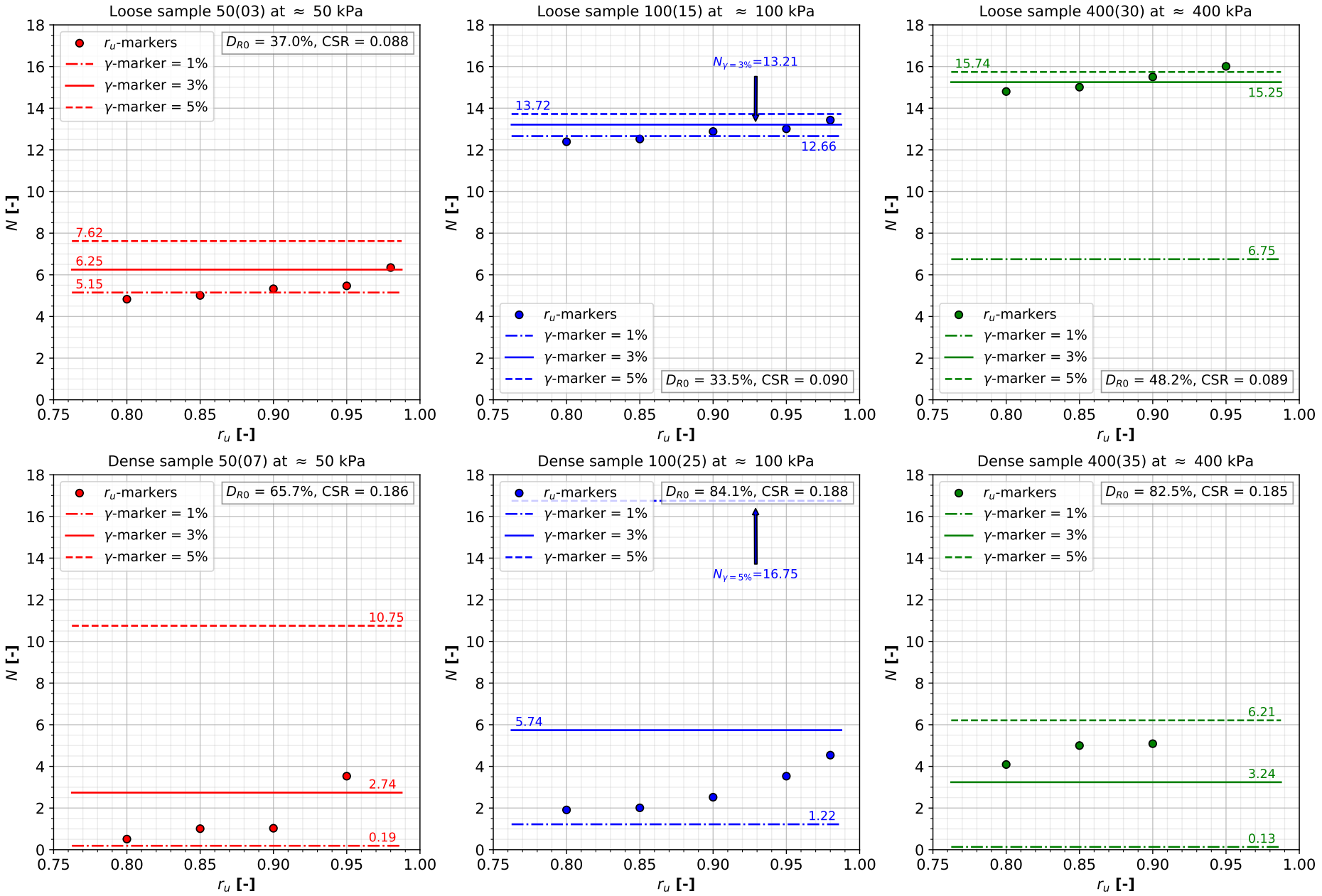

Figure 3.12: Group 5b: Analysis of liquefaction onset in loose and dense Ottawa F-65 sand *CUDSS* tests from Parra (2016) at equivalent *CSRs* and increasing confinement pressure

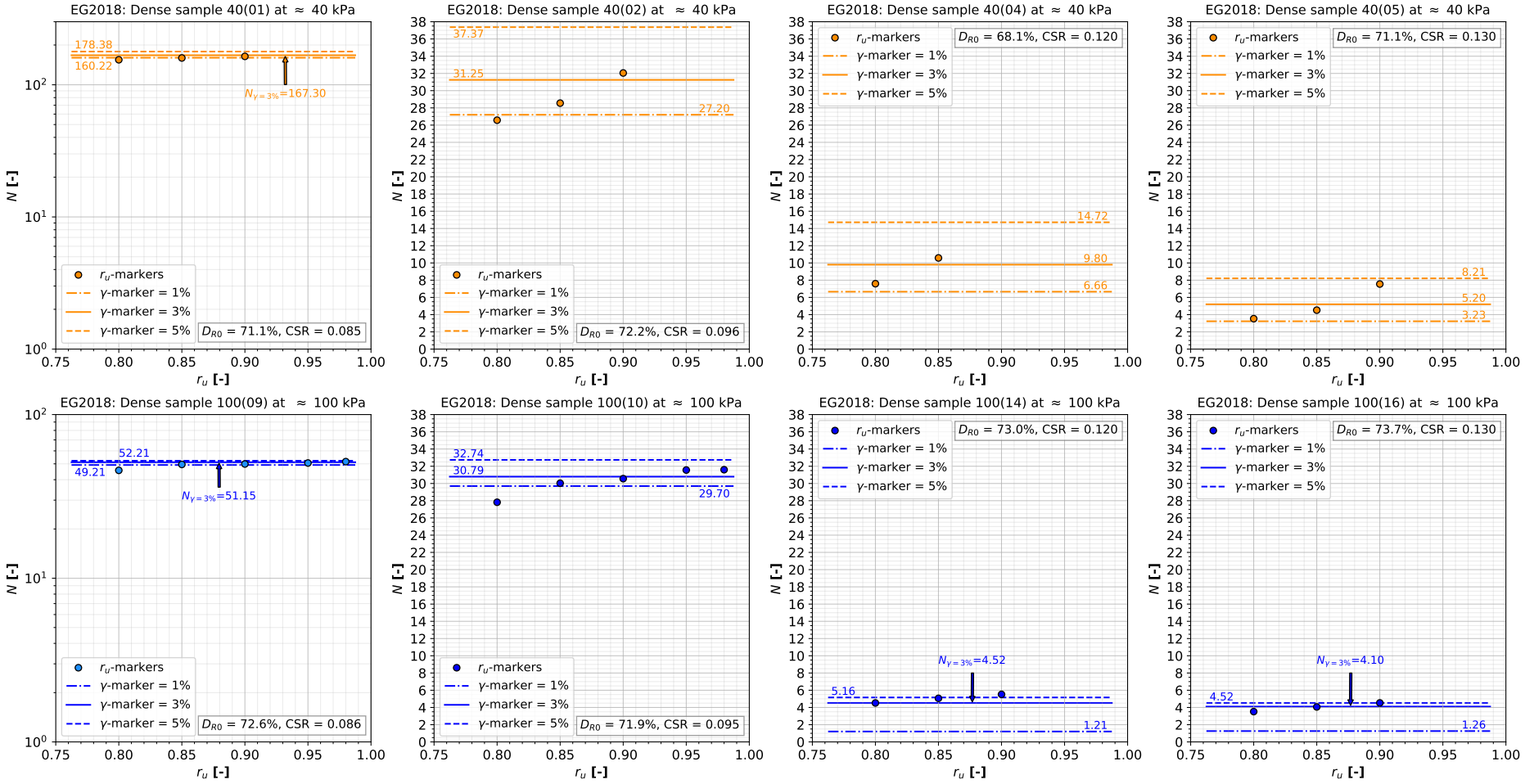

Figure 3.13: Group 6: Analysis of liquefaction onset in dense Ottawa F-65 sand *CUDSS* tests from El Ghoraiby and Manzari (2018) at equivalent *CSRs* and increasing confinement pressure

Chapter 4

The PM4Sand model

PM4Sand is a sand plasticity model for geotechnical earthquake engineering applications, which follows the basic framework of the stress-ratio controlled, critical state compatible and bounding surface plasticity model for sand presented by Dafalias and Manzari (2004). The last modifications included in the 3.1 version of PM4Sand were calibrations performed at the equation level in an attempt to better approximate experimental and case-history trends. According to Boulanger and Ziotopoulou (2017), some of the most important modifications, mostly related to improvements of the soil fabric, which is the grain structural state before and during shearing, included

- the modification of the process of formation/destruction of the fabric to make it dependent on plastic shear strains, instead of volumetric strains,
- the addition of fabric history and progressive fabric formation terms,
- the modification of the plastic modulus relationship by associating it the soil's fabric,
- the modification of dilatancy relationships for dependence on fabric history,
- the increase in control on volumetric contraction and dilative behaviour,
- the modification of the elastic modulus relationship to include dependence on stress ratio and fabric history,
- the reformulation of the model's steady state framework for it to be related to a relative state parameter index (Ξ_s),
- the simplification of the model to a plane-strain formulation,
- the improved modelling of post-liquefaction reconsolidation strains,
- the provision of default values for most primary parameters, among others.

Given that the intricacies of the constitutive formulation of the PM4Sand model are well described in Parra (2016) and that the purpose of this dissertation was not to analyse this formulation, but to determine its effectiveness in simulating cyclic undrained behaviour and identifying liquefaction under diverse initial state and shearing conditions, only relevant formulas and correlations were explicitly mentioned in this work[2]. In general, according to the results presented in Boulanger and Ziotopoulou (2017), the model provides reasonable approximations of cyclic undrained behaviour by only defining one set of parameters. However, as will be explained in part II and confirmed in other publications (Toloza, 2018; Tziolas, 2019), a single parameter set could not accurately describe cyclic undrained conditions over a range of shearing conditions, but were only valid under their specific initial and shearing conditions at which they were calibrated. Possible explanations for this issue were that the interactions between primary and some secondary model parameters were too complex for a single parameter set to be able to encompass a wide range of shearing conditions, or that the Plaxis implementation of the PM4Sand

model was too restrictive in its use of secondary model parameters. On a different note, given that accurate laboratory information available for calibration of constitutive models in design practice is limited, and that extraction of frozen undisturbed samples is prohibitively expensive, Boulanger and Ziotopoulou (2017) proposed that the PM4Sand model parameters be calibrated with the use of in-situ measurements and correlations, such as basic classification index tests (e.g. grain size distribution or disturbed samples), penetration resistance indexes, such as blow count (N), for SPT, and cone resistance (q_c), for CPT, and V_s. In addition to sampling disturbance effects, the identification of a representative sample from a highly heterogeneous soil domain is very difficult. Many samples would need to be extracted at different locations and depths and do so in a manner that remain undisturbed and could represent the in-situ conditions at their specific locations (Boulanger and Ziotopoulou, 2017).

In general, constitutive models used for geotechnical earthquake engineering applications need to approximate a broad mix of conditions within a single geotechnical structure. These could include strata of sand at different relative densities (loose or dense), confinement stresses, static shear stresses (previously sheared or not, depending on the loading conditions), drainage conditions and cyclic loading conditions, which PM4Sand approximates within a reasonable degree of accuracy. On the other hand, the same constitutive models are unlikely to be able to accurately describe both monotonic and cyclic, drained or undrained conditions under the same set of model parameters, which was the case with PM4Sand. This is due to the fact that design correlations stem from different sources and do not necessarily have physical consistence with each other (Boulanger and Ziotopoulou, 2017) (evidenced in part II when evaluating the normalised initial small-strain shear modulus, G_0), as some were based on a specific database of laboratory or case-history tests with a specific type of sand being tested. This lead to one of the limitations of the PM4Sand model, which cannot simultaneously simulate monotonic and cyclic behaviour with the same parameter set. Therefore, in order for a constitutive model to be useful in geotechnical earthquake engineering applications related to identifying liquefaction, such as is PM4Sand, its formulation must reasonably approximate the following.

1. Cyclic resistance ratio (CRR), commonly estimated based on SPT and CPT correlations, such as the one used in this dissertation (Idriss and Boulanger, 2014).
2. Dependence of CRR on the effective vertical overburden stress (σ'_{v0}) and the previously sustained static shear stress (α_s).
3. Accumulation of shear strains up to and after triggering of liquefaction.
4. Strength loss at and after the triggering of liquefaction, as well as the residual post-liquefaction strength.
5. Small-strain shear modulus, obtained through shear wave velocity measurements.
6. Shear modulus reduction and damping ratio relationships prior to liquefaction.
7. Drained monotonic shear strengths and stress-strain behaviour, such as peak friction angle (ϕ'_p).
8. Undrained monotonic shear strengths and stress-strain behaviour, to determine critical state friction angle for monotonic loading.
9. Volumetric strains during drained cyclic loading, which is suppressed during undrained loading and translates into pore water pressure generation.

Lastly, as Boulanger and Ziotopoulou (2017) intended with its creation, the PM4Sand model should provide an improved tool with which to identify the triggering of liquefaction in cohesionless soils subjected to earthquake loading. This particular part was investigated through a

[2]To view the complete formulation of the newest version of the PM4Sand model, please refer to Boulanger and Ziotopoulou (2017) or the following link: https://pm4sand.engr.ucdavis.edu/

benchmark calibration study using Ottawa F-65 sand, presented in part II, and a case study where semi-empirical correlations and a site response analysis using PM4Sand were compared and the effectiveness of the model was be evaluated (see part III). Both the benchmark calibration and practical case study were performed using the 2D implementation of the PM4Sand model in Plaxis (Vilhar et al., 2018), which was adapted for use with the finite element (*FEM*) method, compared to its original implementation with the finite difference (*FD*) method in FLAC, another commercially available numerical tool for geotechnical earthquake engineering applications, among other purposes.

4.1 Model input parameters

Given that this research has been performed using Plaxis 2D, only the available primary and secondary model parameters present in the user-defined model will be analysed. Based on the Plaxis 2D implementation (Vilhar et al., 2018), The model input parameters used in the PM4Sand model are grouped into a primary (3) and a secondary (9) set of parameters, with the addition of a post-shaking flag. All but the three primary model parameters (described below) have default values defined by Boulanger and Ziotopoulou (2017) selected to describe the general behaviour of quartzitic and cohesionless granular soils and may be modified depending on a range of criteria. If one compares the model parameters available for modification in the implemented versions of Plaxis and FLAC, it is immediately noticeable that FLAC provides much more freedom to the modeller in terms of shear availability of modifiable parameters (15, including primary and secondary model parameters). The Plaxis version limited the number of modifiable model parameters in order to provide simplicity in its use and, therefore, it can only be manipulated partially. However, according to Vilhar et al. (2018), the non-modifiable model parameters defined internally in the implemented model allow for the adequate representation of undrained cyclic behaviour, as shown when simulating the same test conditions as in Boulanger and Ziotopoulou (2017). Having said this, the primary input parameters include:

1. **Initial relative density $\mathbf{D_{R0}}$**. Defined by the initial void ratio e_0 (which must be defined in the general properties of the material model as well), can be estimated with the use of penetration- or shear wave velocity-based correlations (either $(N_1)_{60}$, q_{c1N} or V_{s1}). For CPT and SPT, Boulanger and Ziotopoulou (2017) suggested the correlation relating q_{c1N} and $(N_1)_{60}$ with D_R, respectively, proposed by Idriss and Boulanger (2008), shown in Equations 4.1 and 4.2, where the coefficients C_{dq} and C_d was estimated to be 0.9 by regression analysis.

$$D_R = 0.465\left(\frac{q_{c1N}}{C_{dq}}\right)^{0.264} - 1.063 \tag{4.1}$$

$$D_R = \sqrt{\frac{(N_1)_{60}}{C_d}} \tag{4.2}$$

   In principle, this input value should be determined by direct measurements of e_0 or through penetration-based correlations, and should represent the actual initial relative state of the sample. As will be seen in posterior chapters and as mentioned in Boulanger and Ziotopoulou (2017), the chose value may also be viewed as an apparent relative density rather than the strict meaning of D_R extracted from laboratory tests. However, many modellers consider that choosing a modified value of D_R defeats the purpose of a proper calibration (Armstrong, 2018), but Boulanger and Ziotopoulou (2017) only meant to provide the modeller with room for adjustment of the relative density parameter when calibrating the model. For example, a reduced D_{R0} magnitude compared to its original measurement may account for lower density values inside the soil sample or even represent the heterogeneous nature of soil within a 2-phase solid continuum used in finite element modelling.

2. **Small-strain shear modulus coefficient $\mathbf{G_0}$.** G_0 controls the magnitude of developed shear strains within the small-strain regime. Boulanger and Ziotopoulou (2017) proposed the penetration-based correlation in Equation 4.3 for the direct estimation of G_0. Otherwise, G_0 can also be estimated by shear wave velocity measurements or correlations based on penetration resistance, in combination with Equation 4.4.

$$G_0 = 167\sqrt{(N_1)_{60} + 2.5} \tag{4.3}$$

$$G = G_0 \cdot p_a \sqrt{\frac{p'_c}{p_a}} \tag{4.4}$$

3. **Contraction parameter $\mathbf{h_{p0}}$.** h_{p0} is perhaps the parameter which is most tricky to calibrate, as it defines the cyclic resistance of the soil in undrained cyclic behaviour and, for its adequate calibration, an adequate liquefaction-triggering threshold must first be defined (this will be discussed in chapter 3). Ideally, h_{p0} must be calibrated using *CUDSS* tests of the sand one wishes to model. However, since in most cases sample extraction is not feasible (especially for very deep deposits), the cyclic resistance must be estimated using semi-empirical correlations based on penetration resistance or shear wave velocity, such as the ones proposed by Idriss and Boulanger (2008) and Andrus, Hayati, et al. (2009), respectively.

The secondary input parameters were defined with default values and developed to reasonably reproduce physical trends in design correlations. They may be set at a default value but, where possible, these values could be confirmed and optimised by element loading calibrations. In total, Plaxis allows the modification of 9 secondary model parameters, which are:

4. **Maximum and minimum void ratios $\mathbf{e_{max}}$, $\mathbf{e_{min}}$.** These are set at their default values of 0.8 and 0.5 and they affect the computation of the relative state parameter index ξ_R and subsequently quantify the magnitude of contractive and dilative behaviour. According to Boulanger and Ziotopoulou (2017), refinement of these values may not be necessary as the calibration of the other parameters will have a much stronger effect. However, given that it affects the calculation of D_{R0}, it affects the overall behaviour of the stress-path and the shear strength of the model in stress-strain behaviour. Therefore, it is considered helpful, as magnitudes of e_{max} and e_{min} can vary significantly even for a single sand (see subsection 2.1.3), laboratory-estimation of these parameters should be performed.

5. **Bounding surface parameter $\mathbf{n^b}$.** This parameter controls the relative position of the bounding surface to the critical state surface, which in turn is dependent on the relative state index (defined by the state in density at a given point). Therefore, it affects the dilatancy of the model and the peak effective friction angles. The default value for n^b is 0.5.

6. **Dilatancy surface parameter $\mathbf{n^d}$.** This parameter controls the stress-ratio at which contraction transitions to dilation. A default value of 0.1 is set and produces a phase transformation angle slightly smaller than the constant volume friction angle, which is consistent with experimental data (Boulanger and Ziotopoulou, 2017).

7. **Steady-state friction angle $\phi_{\mathbf{cv}}$.** This angle defines the position of the critical state surface and is set at a default value of 33°.

8. **Poisson's ratio ν and atmospheric pressure $\mathbf{p_a}$.** The Poisson's ratio is set at its default value of 0.3, as suggested by Boulanger and Ziotopoulou (2017), consistent with values suggested by Kulhawy and Mayne (1990) for sand. The atmospheric pressure is assumed

to be equal to pressure of the atmosphere at sea level, being 101.3 kPa (also stated in Boulanger and Ziotopoulou, 2017).

9. **Critical state line parameters R** and **Q**. These values, in combination with the range in void ratio of a given sample, define the contractive and dilative behaviour of a sand during cyclic shearing. Default values for quartzitic sands, as recommended by Bolton (1986), are 1.0 and 10. However, Boulanger and Ziotopoulou (2017) suggested that R be increased to 1.5 to lower the steady-state line in order to better approximate typical results for direct simple shear loading. This value was confirmed (and later optimised) when describing the steady-state line of Ottawa F-65 sand in subsection 2.3.1.

10. **PostShake**. The activation of this flag at the end of the parameter menu reduces the post-shaking elastic shear modulus in order to increase reconsolidation strains after liquefaction has occurred during a seismic event. Given that a large part of the post-liquefaction reconsolidation process is governed by sedimentation effects, this modification was incorporated to try to simulate this effect. If the modeller wishes to evaluate this flag, two material models should be created, one defined for application during shaking and the other defined to only be activated after loading has ceased. In fact Boulanger and Ziotopoulou (2017) state that this flag should remain deactivated (value of 0) during the strong shaking portion of the simulation.

Part II

Benchmark calibration study using the PM4Sand model

Chapter 5

A unified calibration methodology

The benchmark calibration study of the PM4Sand model presented in the following chapters was performed with *CUDSS* tests presented in Parra (2016). Given the time constraints of this dissertation and the characteristics of the practical case study in part III, the study only included *CUDSS* tests which were not pre-sheared and were normally consolidated[1]. The principal aim of this exercise was to simulate the cyclic undrained behaviour, in a direct simple shear test setting, of *CUDSS* tests presented in Parra (2016) using the PM4Sand model. The objective of the calibration was to model cyclic undrained behaviour as accurately and as holistically as possible, in terms of liquefaction-triggering, stress-path and stress-strain behaviour. This part of the dissertation was of the utmost importance as an initial step to understand how to adequately implement the constitutive model when modelling potentially-liquefiable soils in a geotechnical earthquake engineering project and, therefore, was presented as a separate part. To this purpose, several calibration methodologies were studied and compared in terms of accuracy of stress-path and stress-strain behaviour and, most important of all, accuracy in predicting liquefaction-onset under diverse shearing conditions (as specified in *CUDSS* test databases from Parra). For example, Ziotopoulou, Montgomery, Parra, et al. (2018) and Ziotopoulou, Montgomery, Tsiaousi, et al. (2019) presented several calibration approaches to estimate the primary and some secondary model parameters of the PM4Sand model (h_{p0}, G_0, n^b and ϕ_{cv} among others), using both cyclic undrained *TXC* and *DSS* tests. Some of those calibration methodologies found in literature were presented below.

Calibration methodology A: The most used calibration methodology found in literature and used by modellers to calibrate the PM4Sand model in Ziotopoulou, Montgomery, Tsiaousi, et al. (2019) was, for a given D_{R0} and overburden pressure of the tested soil, to estimate G_0 with the $(N_1)_{60}$-based correlation proposed by Boulanger and Ziotopoulou (2017), when no data related of the small-strain properties of the sand were available, and iteratively vary the value of h_{p0} to fit a the cyclic resistance in stress-strain behaviour to a proposed liquefaction trigger (usually $\gamma = 3\%$, with 15 cycles to liquefaction). Afterwards, the same parameter set was used to check if the model could reproduce other other initial state and cyclic shearing conditions.

Calibration methodology B: Being a slight variation of calibration methodology A, the process started out with a correlation-calculated-value of G_0, which then was further calibrated based on the first shearing cycles within a *CUDSS* test. This same process was done for additional tests at different D_{R0} and then used to create a regression function to estimate G_0 at any given D_{R0}. This methodology was adopted by some modellers in Ziotopoulou, Montgomery, Parra, et al. (2018) and Ziotopoulou, Montgomery, Tsiaousi, et al. (2019). As for h_{p0}, its magnitude was calibrated based on the same process as in the calibration methodology A.

[1]Specification concerning Parra's *CUDSS* test database.

Calibration methodology C: A not so commonly used calibration methodology, calibration methodology C involved the calibration of G_0 using the axial strain accumulation rate (SAR). This methodology, used by *Fugro* in Ziotopoulou, Montgomery, Tsiaousi, et al. (2019), however, did not provide consistent measurements and the value of axial SAR increased with increasing CSR. This lead to the estimation of an average rate of SAR for the CSR range relevant for the centrifuge tests, which was equivalent to using the $(N_1)_{60}$-correlation with a multiplying factor of 0.80 for the value of D_{R0} in consideration. h_{p0} was calibrated the same as in calibration methodology A and B.

Calibration methodology D: This calibration methodology, used by Parra (2016) in PM4Sand calibrations performed in her doctoral thesis, involved calculating G_0 according to regression analyses performed on measured G_{max} values, starting out from the concepts laid out in Alarcón-Guzmán et al. (1989). The same as in calibration methodologies A, B and C, h_{p0} was iteratively adjusted to fit the cyclic resistance of the sand to a liquefaction-triggering marker (in this case, it was also $\gamma = 3\%$ at 15 cycles to liquefaction).

For all of the above-mentioned methodologies found in literature, the secondary model parameters e_{max}, e_{min} and ϕ_{cv} were optimised when relevant laboratory data was available (Ziotopoulou, Montgomery, Parra, et al., 2018; Ziotopoulou, Montgomery, Tsiaousi, et al., 2019). The published changes in ϕ_{cv} coincided with the suggested value by Parra (2016) of 30°. Additionally, the liquefaction-triggering threshold selected for the calibration of the cyclic resistance was also varied subjectively in different published articles, such as in Ziotopoulou, Montgomery, Tsiaousi, et al. (2019) where a shear strain threshold of 2.5% was selected for calibration, or in Armstrong (2018), where a pore pressure ratio threshold of 0.95 was selected (revisit Table 3.1 for a refresher on this situation). All the previously-mentioned calibration protocols present valid insights on how a liquefaction-identifying constitutive model can be calibrated with the use of either semi-empirical correlations or cyclic undrained laboratory tests specifically performed for the soil in question, as well as which liquefaction-triggering criteria are commonly used to define liquefaction. However, based on the liquefaction-onset analysis, based on the same *CUDSS* test database, performed in chapter 3, it was deemed necessary to try to determine whether it was possible for the PM4Sand model to be calibrated consistently with trends seen in loose and dense sands in terms of r_u and γ. For this purpose, a unified calibration methodology was proposed in this dissertation, which aimed to re-calibrate the PM4Sand model parameters, (mainly h_{p0} and D_{R0}) based on a combined r_u- and γ-based liquefaction-triggering approach. Based on the recommended choices for γ- and r_u-based liquefaction-triggering criteria presented in 3, it was decided that the unified calibration methodology, known from here on out as *CM2*, would attempt to calibrated the model based on reaching liquefaction-triggering markers at $r_u = 0.95$[2] and $\gamma = 3\%$, prioritising the latter criterion. The main reason behind attempting a combined liquefaction-triggering calibration approach was to provide the model with theoretical and practical consistency in the onset of liquefaction, defined by both strength loss and strain accumulation. Granted, as mentioned in Wu et al. (2004), it has already been observed that an r_u-based liquefaction-triggering criterion by itself is not appropriate to effectively represent the seismic performance of a soil, as it can be only measured in terms of shear strain. However, the use of a γ-based liquefaction-triggering criterion by itself is also not enough to represent liquefaction, as both are pore pressure and shear strain accumulation are intrinsically linked within the process of liquefaction (Wu et al., 2004).

Taking into account all the conditions described earlier, it was necessary to establish a calibration sequence before starting the benchmark calibration study, given that h_{p0} had a combined effect on pore pressure and shear strain evolution. Therefore, the calibration sequence proposed for *CM2* consisted in the following steps.

[2]In cases where the *CUDSS* test did not reach $r_u = 0.95$, $r_u = 0.90$ was used as a substitute.

Step 1: All secondary model parameters were defined based on their default values or on optimised values established from previous studies or characterisation tests. In this instance, optimised values obtained from chapter 2, in conjunction with default values, were used as starting secondary model parameter values. p_a and n^d were defined according to their default values (described in chapter 4) and the rest were defined based on values presented in Table 5.1.

Database	e_{max} [-]	e_{min} [-]	n^b [-]	ϕ_{cv} [°]	ν [-]	R [-]	Q [-]	PostShake
PB2016	0.83	0.51	0.5	30	0.3	1.4	10	0

Table 5.1: Optimised secondary constitutive model parameters for the calibration of the PM4Sand model using Ottawa F-65 sand.

Step 2: D_{R0} was set based on specified measurements in Parra (2016), as well as all *CUDSS* test conditions required: *CSR*, confinement stress, total number of cycles sheared during the test and K_0. G_0-magnitudes were defined based on D_{R0}-measurements, using the $q_{c1N,cs} - D_{R0}$ correlation proposed by Idriss and Boulanger (2008), in combination with the $q_{c1N,cs} - V_{s1,cs}$ correlation proposed by Andrus, Hayati, et al. (2009), which also considered the effect of ageing in sands (see Equations 5.1 and 5.2).

$$D_{R0} = 0.478(q_{c1N,cs})^{0.264} - 1.063 \tag{5.1}$$

$$(V_{S1})_{cs} = \left[5.13 \log_{10}(t) + 58.5\right] \cdot {q_{c1N,cs}}^{0.231} \tag{5.2}$$

As for h_{p0}, a preliminary magnitude was estimated based on experience: In general, h_{p0}-magnitudes for loose samples sheared at low *CSRs* were around the order of magnitude of 0.1, whereas for dense samples sheared at high *CSRs*, h_{p0}-magnitudes were between orders of magnitude of 0.001 and 0.01.

Step 3: Having defined the preliminary parameter set, the next step involved the calibration of n^b, which was performed by attempting to fit the model's stress path to the liquefaction cycles (butterfly loops) in stress space, as it directly modified the approach of the bounding line towards the steady-state line, affecting the r_u-minima which could be experienced during cyclic mobility. Normally, n^b should not deviate too much from its default value 0.5. In this benchmark study, n^b was left at 0.50, as calibrated values varied only slightly from its default value and both *CM1* and *CM2* were focused on trying to identify possible trends in h_p0 given different initial states and shearing conditions, which would have been significantly more difficult if the effect of n^b had to be considered too. Therefore, this step was considered to be optional, for future instances.

Step 4: Next, the contraction parameter h_{p0} was calibrated by fitting the model to the previously specified liquefaction-triggering markers. Here is where a distinction between calibration methodologies 1 and 2 must be made. *CM1*, being the original calibration methodology proposed by the creators of the PM4Sand model, focused on iteratively calibrating h_{p0} to fit the liquefaction-triggering marker $\gamma = 3\%$, while only keeping track of the triggering of marker $r_u = 0.95$. In the case of *CM2*, the methodology built on the h_{p0}-magnitude found in *CM1* and recalibrated the model by reducing D_{R0} and, at the same time, iteratively increasing h_{p0} to first fit the model to marker $\gamma = 3\%$, as well as obtain a more accurate triggering of liquefaction marker $r_u = 0.95$. At times, especially in very dense samples sheared at very high *CSRs*, D_{R0} had to be increased and h_{p0} reduced. This step effectively created 2 calibrated parameter sets, which were later evaluated and used as a basis for liquefaction hazard evaluation in the case study, presented in part III.

Having defined the calibration methodology used in this benchmark study, it is worth mentioning that, in some cases, not all types of behaviour was able to be adequately simulated. This was especially visible when performing the calibration of the *CUDSS* tests which sheared tests with a high initial relative density, as well as samples sheared at relatively high *CSRs*.

In total, 25 *CUDSS* tests were calibrated based on calibration methodologies *CM1* and *CM2*, following the steps described above. The main objective of the benchmark chapter was to try to determine possible trends in h_{p0} when calibrated against a wide range of initial state and shearing conditions. Table 5.2 shows the tests which were used for calibration in the benchmark study.

Test	σ'_{vc} **[kPa]**	**OCR [-]**	K_0 **[-]**	D_{R0} **[%]**	e_0 **[-]**	**CSR [-]**	**Cyclic shear stress [kPa]**	N_{total} **[-]**
50(01)	52.14	1.0	0.4286	38.69	0.706	0.075	3.91	26.8
50(02)	50.25	1.0	0.4286	46.41	0.682	0.084	4.22	15.0
50(03)	49.85	1.0	0.4286	37.00	0.712	0.088	4.39	7.6
50(04)	51.52	1.0	0.4286	37.53	0.710	0.104	5.36	5.1
50(05)	49.10	1.0	0.4286	68.75	0.610	0.180	8.84	26.8
50(06)	49.61	1.0	0.4286	69.81	0.607	0.182	9.03	18.1
50(07)	50.29	1.0	0.4286	65.68	0.620	0.186	9.35	12.6
50(09)	49.08	1.0	0.4286	72.47	0.598	0.218	10.70	14.0
50(10)	52.30	1.0	0.4286	77.5	0.582	0.220	11.51	15.0
100(12)	102.20	1.0	0.4286	38.53	0.707	0.078	7.97	34.8
100(13)	102.76	1.0	0.4286	46.50	0.681	0.092	9.45	5.5
100(14)	100.61	1.0	0.4286	39.41	0.704	0.092	9.26	5.1
100(15)	104.12	1.0	0.4286	33.53	0.723	0.090	9.37	15.0
100(16)	101.35	1.0	0.4286	42.34	0.695	0.112	11.35	3.0
100(24)	101.85	1.0	0.4286	77.00	0.584	0.170	17.31	23.8
100(25)	100.17	1.0	0.4286	84.09	0.561	0.188	18.83	18.0
100(26)	100.26	1.0	0.4286	83.28	0.564	0.207	20.75	9.3
400(28)	400.86	1.0	0.4286	48.22	0.676	0.085	34.07	35.2
400(30)	405.11	1.0	0.4286	48.16	0.676	0.089	36.05	17.0
400(31)	401.60	1.0	0.4286	41.47	0.697	0.094	37.75	8.1
400(32)	404.32	1.0	0.4286	37.33	0.711	0.114	46.09	9.6
400(33)	401.17	1.0	0.4286	90.63	0.540	0.170	68.20	22.3
400(35)	403.45	1.0	0.4286	82.53	0.566	0.185	74.64	6.2
400(36)	400.69	1.0	0.4286	83.41	0.563	0.194	77.73	2.0
400(37)	401.62	1.0	0.4286	81.88	0.568	0.228	91.57	1.65

Table 5.2: Initial state and shearing conditions for *CUDSS* tests from Parra (2016)

Chapter 6

Calibration of the PM4Sand model using *CUDSS* tests from PB2016

This chapter describes the calibration process and results of loose and dense Ottawa sand *CUDSS* tests from Parra (2016) confined at 50, 100 and 400 kPa and sheared at a wide range of *CSRs*. Since a large number of calibrations was performed, only the necessary information for illustrative purposes was presented. For this purpose, the calibration process for one loose and dense sample at each confinement stress was selected to illustrate the calibration process and explain the final trends obtained at the end of the benchmark study for this database. Tests 50(01), 50(06), 100(12), 100(24), 400(28) and 400(33) (shown in Figures 6.1 and 6.3) were selected and plotted in $N - r_u$-space and $N - \gamma$-space next to its calibrated PM4Sand models following *CM1* and *CM2* (shown in Figures) to allow an adequate understanding of how variations in h_{p0} and D_{R0} (see Table 6.1) would affect the accuracy of the calibrated model to experimental results.

Following the proposed structure of the unified calibration methodology described in chapter 5 and taking into consideration the optimised secondary model parameters from Table 5.1, the first step was to calculate the corresponding magnitudes of G_0 based on the specified D_{R0}-measurements for each test, as well as provide a preliminary h_{p0}-magnitude to start the iterative calibration process. Once those values were defined, the initial state and cyclic shearing conditions for each test were defined in the Soil Test Facility in Plaxis and h_{p0} was adjusted according to the established calibration sequence for both *CM1* and *CM2*. All calibrated parameters for the 6 tests presented in this chapter are shown in Table 6.1. In general terms, the calibration processes of loose samples sheared at low *CSRs* were the least cumbersome, while calibrating the dense and loose sand samples sheared at relatively high *CSRs* caused several problems, for which compromises had to be assumed at times. Such was the case of test 400(33), which due to its very high D_{R0} and relatively high *CSR* exhibited an unusual cyclic behaviour, characterised by mostly dilative tendencies during shearing, which allowed for a slow buildup or pore pressures, contrary to what one would expect at such high confinement pressures. In this particular case, the activation of the proposed liquefaction markers had to be modified, which was the way how most difficult cases were treated. In general, the PM4Sand model performed very well when calibrating loose sand samples sheared at low *CSRs* and at all three testing overburden pressures. Affinity of the model in terms of pore pressure and shear strain evolution to the experimental data was very good for tests 50(01) and 100(12), which represented loose samples, confined at 50 kPa and 100 kPa, sheared at low *CSRs*. While in the case of test 400(28), the model had more trouble replicating the evolution of pore pressures and shear strains all the way up to shortly before liquefaction was triggered. This meant that the greater the greater the absolute cyclic shear stress applied on the sample, the more difficulty PM4Sand had to provide and adequate fit to both pore pressure and shear strain evolution. As for possible trends in calibrated h_{p0} of loose samples, not much can be said besides that, with increasing overburden pressure, the magnitude

of h_{p0} increased to compensate for the increasing contractive behaviour the higher overburden pressures impose on a sand sample with a specific relative density. This means that, the greater the dilative tendencies of the sand during shearing, the smaller the h_{p0}-value had to be to match the specified cyclic resistance of the sample.

As for the model's affinity for dense samples it was clear that initial pore pressure evolution was an issue when samples were sheared at relatively high *CSRs*, where differences could reach up to 40% in r_u-magnitudes at a given cycle before liquefaction was reached[3]. However, cyclic mobility was reasonably well simulated, and liquefaction markers were activated at mostly the right moments. Furthermore, the same difficulties were evidenced when comparing the calibrated models with the experimental curves in terms of shear strain evolution. Here, dense sand behaviour was very hard to adequately simulate, as the *CUDSS* tests showed a kind of asymptotic exponential behaviour in shear strain evolution evolution envelopes in most of the evaluated tests. The important part to take away in these situations was that, in the case of dense sands, shear strain accumulation after initial liquefaction had occurred, was very slow compared to the common exponential growth of shear strains in loose samples after reaching liquefaction. That is why, when PM4Sand was calibrated following the steps of either *CM1* or *CM2*, excessive shear strains developed after the activation of the liquefaction-triggering markers. This inconsistency could be explained due to the effect of the linear increase in shear strains simulated by the PM4Sand model, which was not always consistent with experimental findings. This linear trend in shear strain accumulation was mostly consistent in loose samples confined at all analysed overburden pressures and sheared at low *CSRs*. In closing , caution is advised when trying to model very dense sands and shearing at high *CSRs*, as the accumulation of shear strains beyond 3% will be excessive in most dense sand cases.

Test	**Calibration methodology**	$\mathbf{D_{R0}}$ **[%]**	$\mathbf{h_{p0}}$ **[-]**	$\mathbf{G_0}$ **[-]**	$\mathbf{n^b}$ **[-]**
50(01)	1	38.69	0.232000	353.79	0.50
	2	38.69	0.232000	353.79	0.50
50(06)	1	69.81	0.01170	506.44	0.50
	2	71.00	0.00614	506.44	0.50
100(12)	1	38.53	0.495300	353.08	0.50
	2	38.53	0.495300	353.08	0.50
100(24)	1	77.00	0.002862	553.58	0.50
	2	74.00	0.007850	553.58	0.50
400(28)	1	48.22	0.503700	399.03	0.50
	2	48.22	0.503700	399.03	0.50
400(33)[4]	1	90.63	0.0109	636.65	0.50
	2	90.63	0.0148	636.65	0.50

Table 6.1: Calibrated constitutive model parameter sets for selected *CUDSS* tests from Parra (2016)

[3]It is worth mentioning that these large differences were only present over 1 to 2 cycles before liquefaction was reached. In terms of identifying liquefaction, the model still does its job relatively well. However, depending on what one wishes to analyse, be that stress-strain behaviour before or after liquefaction has been triggered, it is important to take these relatively high variations into consideration. Here, the researcher would enter the realm of smart-modelling, which would be the tailoring of the calibration objectives based on what parts of the stress-state one wishes to analyse. However, this is out of the scope of this dissertation.

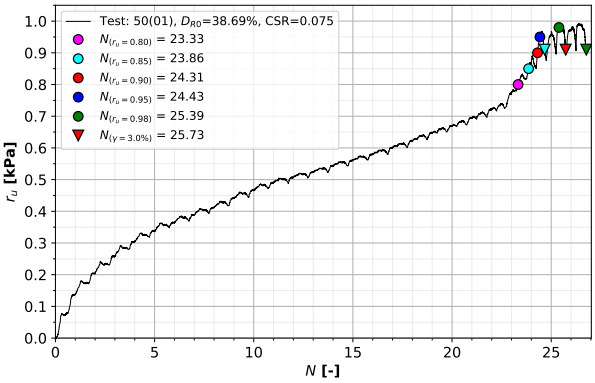

(a) Loose sand: 50 kPa, CSR = 0.075, $D_{R0} = 38.7\%$

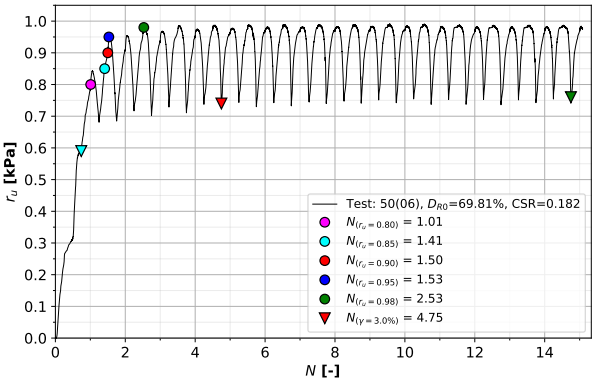

(b) Dense sand: 50 kPa, CSR = 0.182, $D_{R0} = 69.8\%$

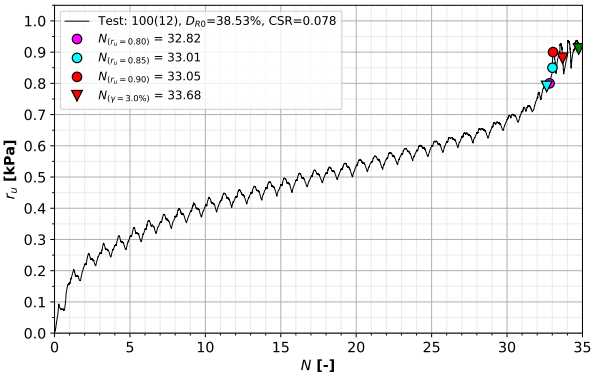

(c) Loose sand: 100 kPa, CSR = 0.078, $D_{R0} = 38.5\%$

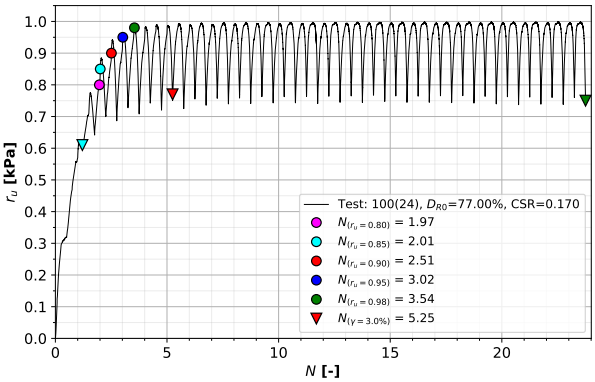

(d) Dense sand: 100 kPa, CSR = 0.170, $D_{R0} = 77.0\%$

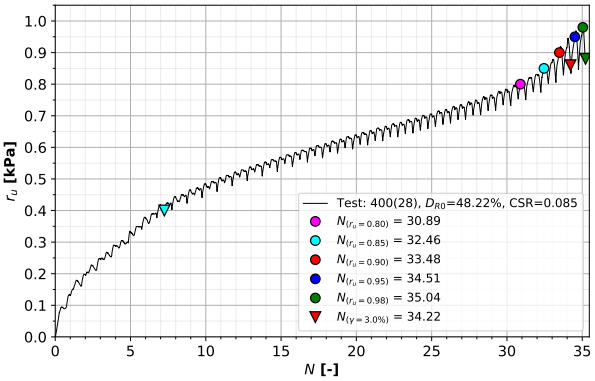

(e) Loose sand: 400 kPa, CSR = 0.085, $D_{R0} = 48.2\%$

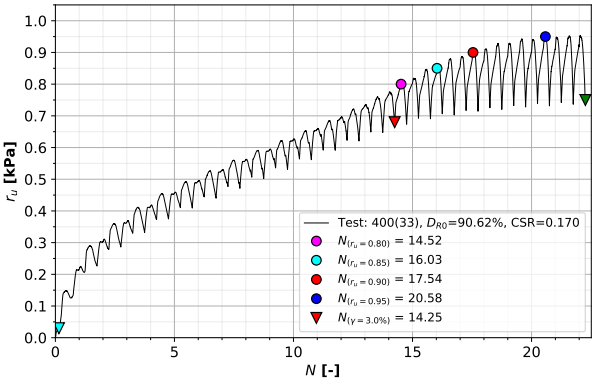

(f) Dense sand: 400 kPa, CSR = 0.170, $D_{R0} = 90.6\%$

Figure 6.1: $N - r_u$-evolution curves of selected loose and dense sands at 50, 100 and 400 kPa confinement pressures from PB2016, including liquefaction-triggering markers, to illustrate the calibration process

[4] *CUDSS* test 400(33) was quite tricky to calibrate given its very high relative density and *CSR*.

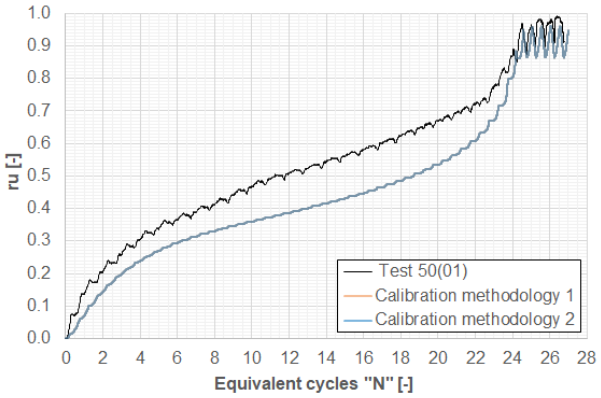

(a) Loose sand: 50 kPa, CSR = 0.075, $D_{R0} = 38.7\%$

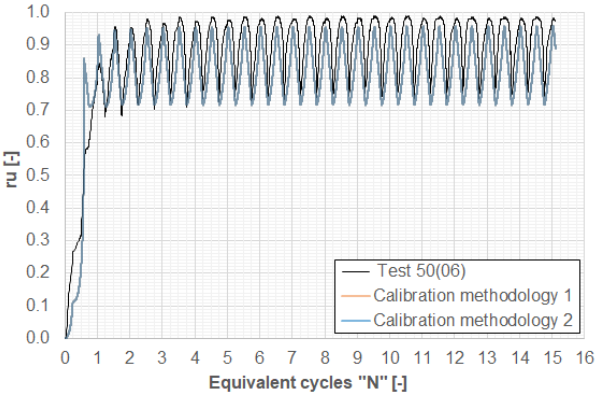

(b) Dense sand: 50 kPa, CSR = 0.182, $D_{R0} = 69.8\%$

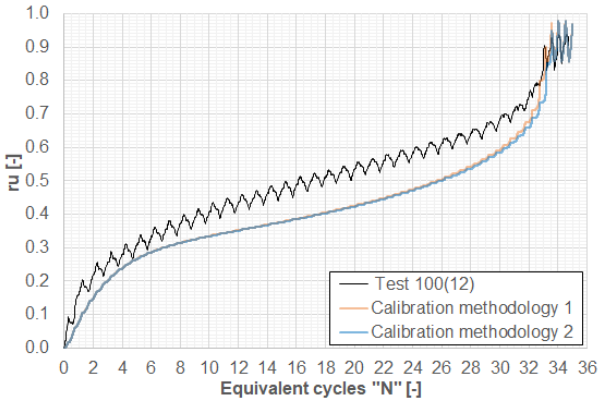

(c) Loose sand: 100 kPa, CSR = 0.078, $D_{R0} = 38.5\%$

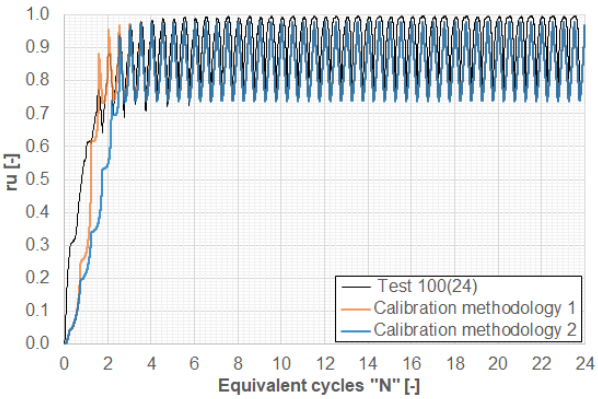

(d) Dense sand: 100 kPa, CSR = 0.170, $D_{R0} = 77.0\%$

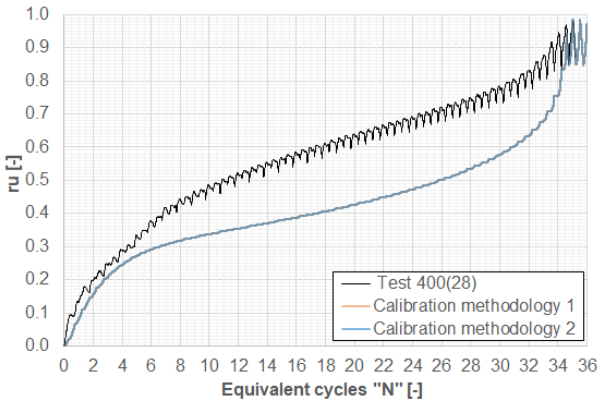

(e) Loose sand: 400 kPa, CSR = 0.085, $D_{R0} = 48.2\%$

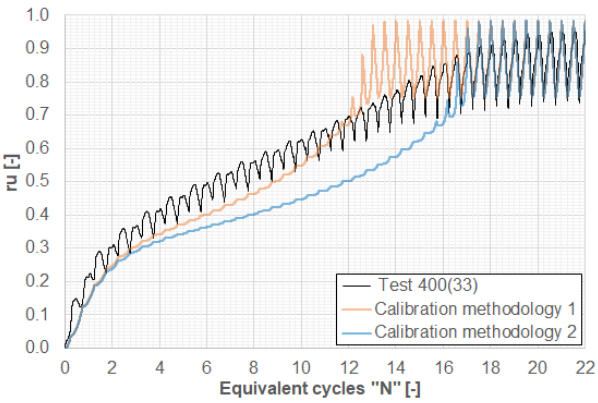

(f) Dense sand: 400 kPa, CSR = 0.170, $D_{R0} = 90.6\%$

Figure 6.2: Comparison of $N - r_u$-curves of selected loose and dense sands at 50, 100 and 400 kPa confinement pressures from PB2016 and calibrated model with *CM1* and *CM2*.

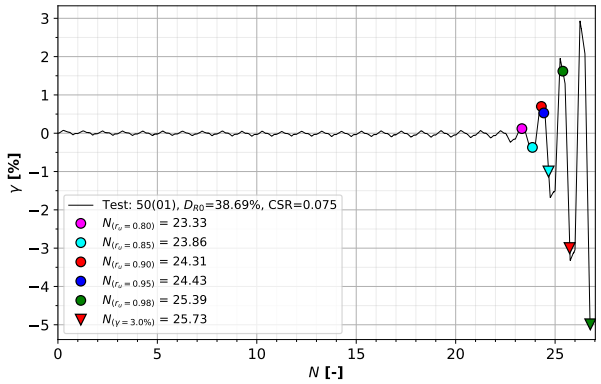

(a) Loose sand: 50 kPa, CSR = 0.075, $D_{R0} = 38.7\%$

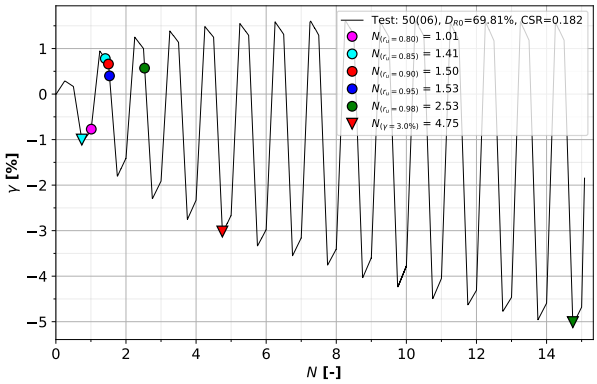

(b) Dense sand: 50 kPa, CSR = 0.182, $D_{R0} = 69.8\%$

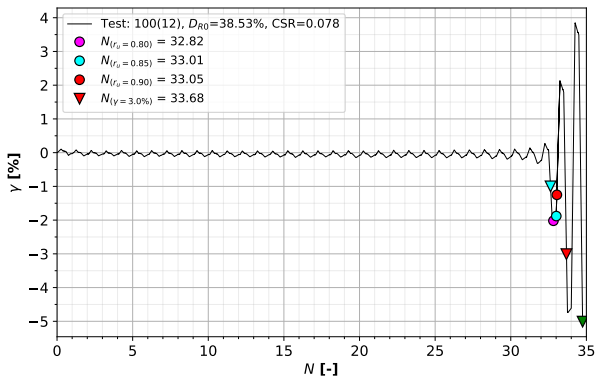

(c) Loose sand: 100 kPa, CSR = 0.078, $D_{R0} = 38.5\%$

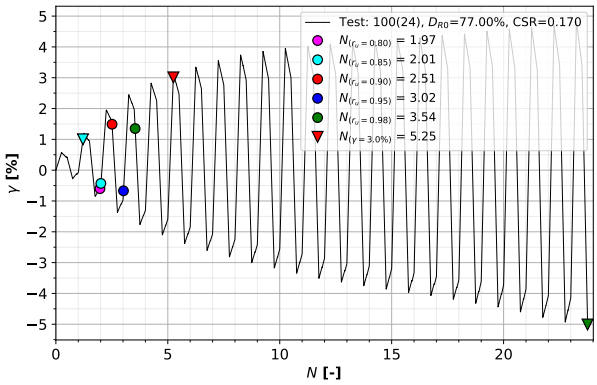

(d) Dense sand: 100 kPa, CSR = 0.170, $D_{R0} = 77.0\%$

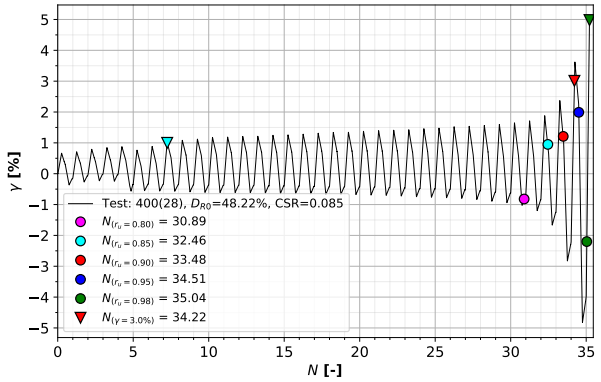

(e) Loose sand: 400 kPa, CSR = 0.085, $D_{R0} = 48.2\%$

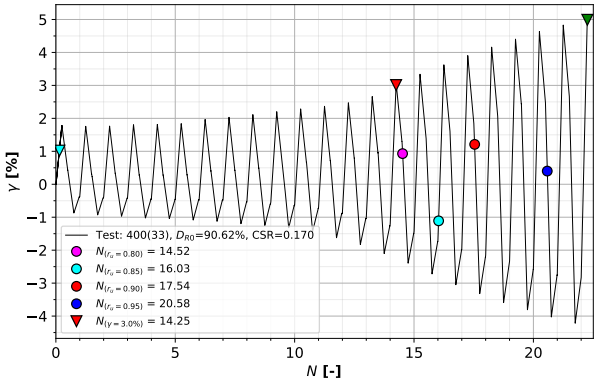

(f) Dense sand: 400 kPa, CSR = 0.170, $D_{R0} = 90.6\%$

Figure 6.3: γ-evolution curves of selected loose and dense sands at 50, 100 and 400 kPa confinement pressures from PB2016, including liquefaction-triggering markers, to illustrate the calibration process

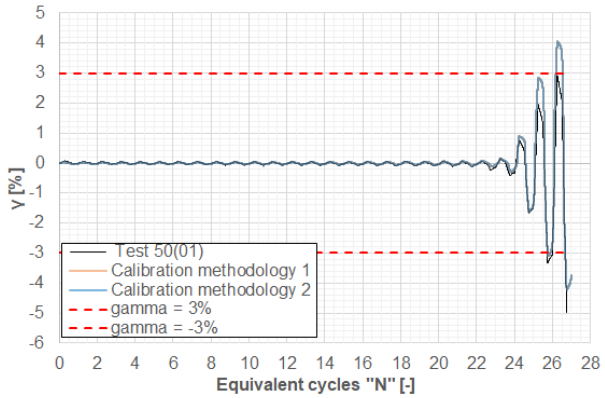

(a) Loose sand: 50 kPa, CSR = 0.075, $D_{R0} = 38.7\%$

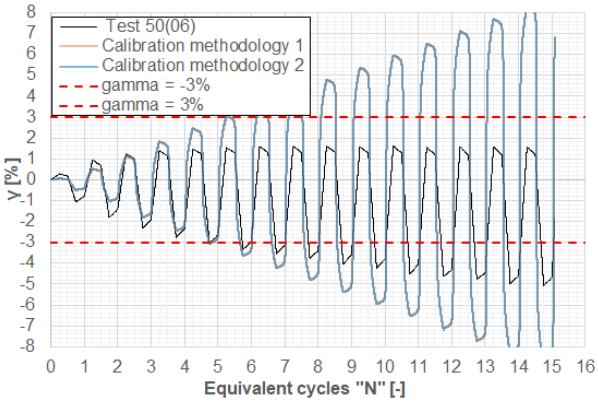

(b) Dense sand: 50 kPa, CSR = 0.182, $D_{R0} = 69.8\%$

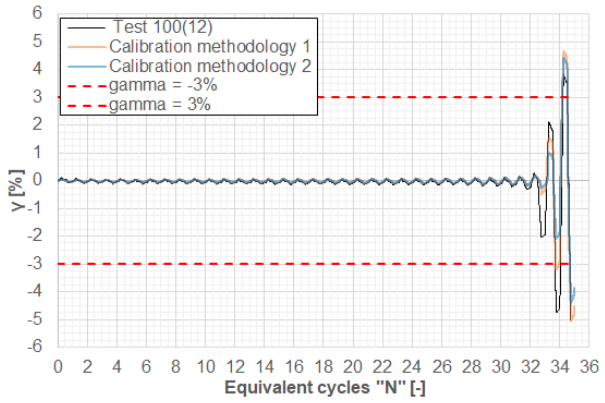

(c) Loose sand: 100 kPa, CSR = 0.078, $D_{R0} = 38.5\%$

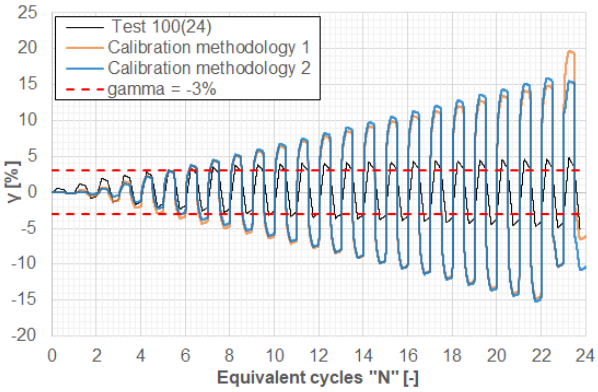

(d) Dense sand: 100 kPa, CSR = 0.170, $D_{R0} = 77.0\%$

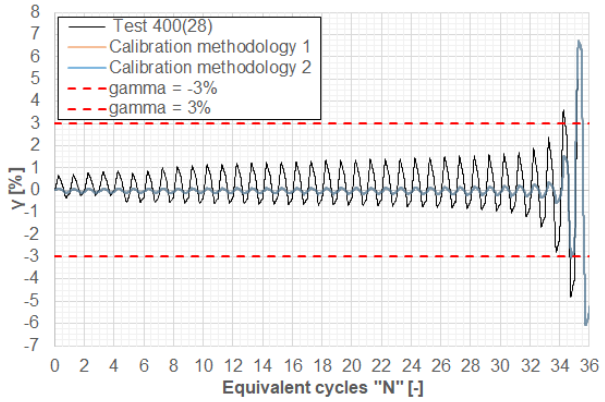

(e) Loose sand: 400 kPa, CSR = 0.085, $D_{R0} = 48.2\%$

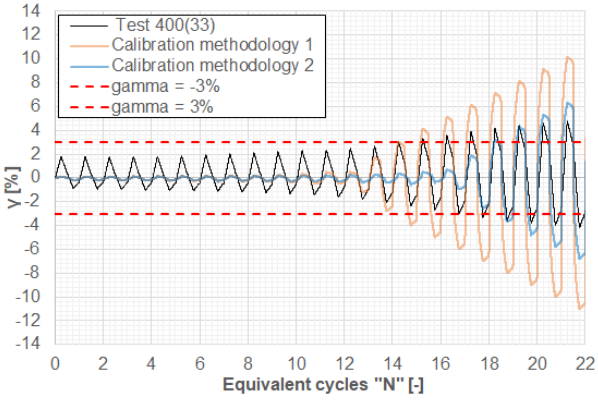

(f) Dense sand: 400 kPa, CSR = 0.170, $D_{R0} = 90.6\%$

Figure 6.4: Comparison of $N - \gamma$-curves of selected loose and dense sands at 50, 100 and 400 kPa confinement pressures from PB2016 and calibrated model with *CM1* and *CM2*

6.1 Discussion and preliminary conclusions regarding the benchmark calibration study

In all, the PM4Sand model simulated the cyclic behaviour of loose sands better, both in terms of pore pressure and shear strain evolution, compared to dense samples when sheared at relatively high *CSRs*. Caution should be employed in the use of parameter sets which were calibrated for the use with dense sands when sheared at high cyclic stresses. All calibrated dense samples at 50, 100 and 400 kPa were very cumbersome, as many compromises had to be implemented so that reasonable accumulation of shear strains occurred. What mostly happened was that, given the stiff behaviour of the PM4Sand model, the h_{p0} had to be reduced in a way which allowed proper triggering of $\gamma = 3\%$, which in turn caused the side-effect of excessive shear strain accumulation after a given number of cycles.

6.1.1 Parameter trends found

After the evaluation of the calibration characteristics of all *CUDSS* tests from PB2016, partial trends for h_{p0} were found with varying *CSR*, relative density and confinement pressure as shown in Figure 6.5. If one would observe the h_{p0}-magnitudes obtained for diverse *CSR*-magnitudes, no clear trend can be extracted. However, if one observed the values obtained from calibrated loose samples (values grouped towards the left), there was a slight reducing trend of h_{p0} with increasing *CSR*. This, of course was not clear, because all samples had different relative densities, which played a major role in the calibration of h_{p0}. This decreasing trend was less clear for dense samples, as the very high *CSR*-magnitudes generated very complex conditions during calibration and some compromises had to be introduced. Despite all this apparent chaos, a few conclusions could be extracted from the obtained calibrated sets, for both *CM1* and *CM2*:

- The PM4Sand model was not able to adequately reproduce cyclic undrained behaviour at different initial states and shearing conditions while only using a single parameter set. For each specified initial state and cyclic shearing conditions applied to the sand sample, a different material parameter set had to be derived.
- Differences between calibrated h_{p0}-values obtained for loose and dense sand samples reached up to 3 orders of magnitude, reducing towards intermediate *CSRs* and D_{R0}.
- The model parameters' interaction between each other is too complex to be able to derive a regression curve which would try to predict h_{p0}-values given certain initial conditions.
- The necessity for *CM2*-based model parameters became apparent when trying to model dense sands at low to intermediate overburden pressures and at intermediate to high *CSRs*, as those calibrated parameters showed greater affinity in terms of pore pressure and shear strain evolution, as well as the correct triggering of liquefaction. On the other hand, *CM1*- and *CM2*-based model parameters became equal when modelling loose sand at any given overburden pressure and when sheared at low *CSRs*. This meant that the holistic calibration methodology was explicitly needed to be able to adequately model sands which exhibited greater dilative behaviour. Sands which tended more towards contractive behaviour, be that through a low D_{R0} or high confinement pressure, did not need to have their model parameters updated to *CM2*.

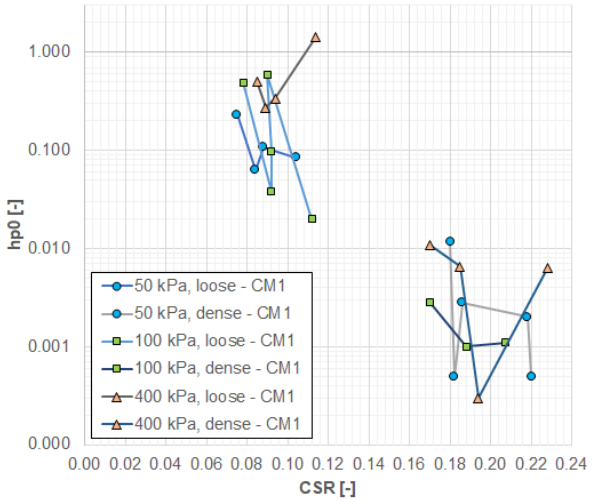

(a) Using *CM1*

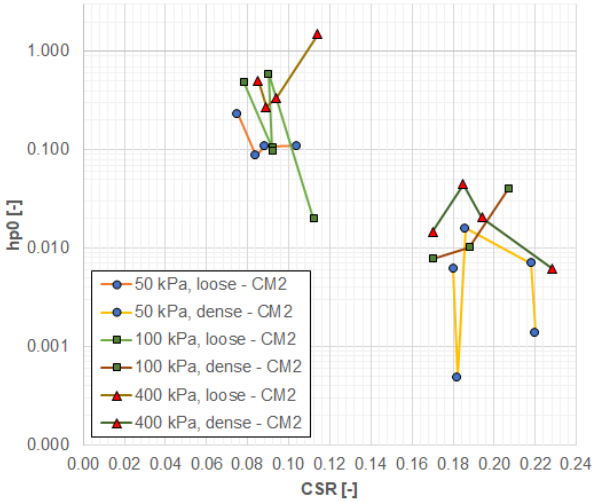

(b) Using *CM2*

Figure 6.5: h_{p0}-trends of all calibrated *CUDSS* tests from PB2016 using calibration methodologies *CM1* and *CM2*.

6.1.2 Limitations of the PM4Sand model

During the calibration process, several limitations of the PM4Sand model were identified.

- Pore water pressure evolution during early cycles could not be adequately modelled, especially in dense samples sheared at high *CSRs*, even by attempting to drastically modify D_{R0}. Possible explanations for this phenomenon are threefold: The first explanation was that, given the innate heterogeneity of soils and the imposed homogeneity of the 2-phase solid continuum used to model the soil element, greater local rearrangement of soil particles during the first cycles could have caused and accelerated growth in pore water pressure the initial cycles during testing, compared to the r_u-curve of the model. Also, the model has an elastic part which may overly stiffen the initial response of the model. The second explanation was related to the model parameters of the PM4Sand model, specifically some secondary and tertiary model parameters which cannot be modified in the user-defined implementation of PM4Sand in Plaxis. It could be that some of these parameter would need slight modifications so that initial pore water pressure evolution could be better approximated. However, this cannot be proven until future research and until Plaxis develops

a tool which would allow the modification of the internal secondary and tertiary model parameters. The third and less likely explanation was that measurements could have been compromised due to imperfect undrained (constant volume) conditions during shearing or by an imperfect location of the hydraulic sensors.

- The PM4Sand model had problems trying to model dense sand samples, as shown in previous subsections during the calibration process. This was most evident in the discordance present between the experimental and simulated pore water pressure evolution curves, where the model severely underestimated magnitudes of r_u.

- In some cases, PM4Sand had difficulties estimating peak r_u-magnitudes for specific tests and mostly overestimated the maximum pore pressure ratio in *CUDSS* tests. However, this discrepancy was attributed to the differences in boundary conditions between the simulated element and the actual *CUDSS* test.

- The PM4Sand model was not able to simulate different undrained shearing conditions in either loose or dense sands with a single parameter set. For different shearing conditions, the model needed a new set of parameters. This finding was also confirmed by research performed in Toloza (2018) and Tziolas (2019) and was analogous to what other liquefaction-simulating models, such as UBCSAND, where specific calibration sets had to be created for each shearing condition (Naesgaard, 2011). However, it is worth noting, as described in Naesgaard (2011), that an optimal model should be able to replicate different shearing conditions, which are not intrinsic properties or related to the initial state conditions of a soil (such as small-strain stiffness and relative density).

- Given that no single set of parameters can be used to describe different initial conditions within the sand domain, it was suggested that, for the practical case study, the soil domain be divided into sections where optimal parameter sets could be calibrated based on averaged zones. The main parameters for calibration would be the averaged D_{R0}-, σ'_{v0}- and G_0-magnitudes.

- In situations where D_{R0} and h_{p0} had to be modified to attempt to reach both liquefaction-triggering markers $\gamma = 3\%$ and $r_u = 0.95$ at their specified cycles, *CM2* induced a stiffer behaviour in the model when the stress-strain state was yet below the established liquefaction threshold. This stiffness, however, reduced dramatically once the model was close to reaching a liquefied state, and did so even faster than the original calibration methodology *CM1*. Therefore, if the *CUDSS* test had enough shearing cycles, one of the side-effects of using *CM2* was that it accumulated more strains, compared to a model calibrated with *CM1*, by the end of the test. This could lead to deformation incompatibilities when a specific soil is subjected to large earthquake durations and accelerations.

- An important aspect to take into account when using *CM2* was that it has not yet been validated against other experimental data, such as geo-centrifuge tests. It is of great importance that this method be validated using these experiments to determine its validity and its possible perks and shortcomings. This aspect could unfortunately not be included in this research due to time constraints and it is suggested that future research should cover this.

6.1.3 Remarks regarding the calibration process for PM4Sand

- Given that ϕ_{cv} is an intrinsic property of a sand with specific granulometric properties, no variation of the model parameter ϕ_{cv} was attempted during the benchmark calibration study using the PM4Sand model. Additionally, changes in ϕ_{cv} during the calibration

process would have brought further variation on the calibration and would only have complicated the determination of possible trends in h_{p0} and G_0. Therefore, the value of 30° suggested by Parra (2016) was deemed sufficiently accurate to describe the steady-state of Ottawa F-65 sand sheared under any conditions.

Part III

Practical case study

Chapter 7

Introduction to the case study

The chapters contained in this part of the dissertation present the practical application of the PM4Sand model in a 1D and 2D case study. For both parts of the case study, cohesionless layers which were vulnerable to liquefaction were modelled with PM4Sand, whereas all cohesive layers and cohesionless layers which were not prone to liquefy were modelled using the HSsmall model, a constitutive model capable of simulating cyclic undrained behaviour but without hysteretic behaviour[1]. Based on the preliminary conclusions obtained from parts I and II, two PM4Sand calibration methodologies (*CM1* and *CM2*) were tested and compared within a 1D liquefaction hazard analysis setting. The 1D soil column was subjected to a single earthquake signal scaled to beyond design conditions (explained in section 7.1), Umbria Marche, whose characteristics were described in section 7.1, and a thorough liquefaction hazard analysis was performed with the use of r_u- and γ-based time histories and profiles, with the aim of determining if the either of the calibration methodologies triggered liquefaction, in any of the vulnerable layers, in a physically-consistent way, as explained in chapter 3, and if the analysis would be able to discard a extreme seismic loading consequences, known as a cliff-edge scenario (explained in section 7.1), at the foundation level. Furthermore, the Idriss and Boulanger semi-empirical liquefaction analysis method was selected to calculate separate liquefaction hazard results in terms of safety factors and used for comparison with the numerically-obtained ones to determine if the PM4Sand model provided any significant differences. Given that this and other semi-empirical methods loose their applicability at depths greater than 15 m, this comparison was essential to establish if using numerical tools improved insights into site liquefaction hazard analyses, especially at great depths. Following this, the 1D soil column was extended to a 2D model which included a simplified structure representing a hypothetical critical facility. The 2D model was subjected to the same earthquake signal, where the objective was, with the use of only calibration methodology *CM2*, to evaluate if soil-structure interaction had any effect on the liquefaction hazard of the site. Within that same analysis, possible effects of structural load variations were evaluated as well.

7.1 Design philosophy of a critical facility and earthquake input motion

The design of critical facilities must comply with rigorous structural and geotechnical design criteria which exceed those of standard building codes and limit states. Additionally, a seismic hazard evaluation is required and, if necessary, seismic loading should be included in the structural and geotechnical design. According to several international standards and manuals (PEER, 2014; FEMA, 2007; ANVS, 2017; IAEA, 2010; IAEA, 2004), the seismic design of a

[1]Given that the scope of this dissertation involved only the study of the PM4Sand model, it was assumed that HSsmall was a common-enough constitutive model for general cyclic soil behaviour that no detailed explanation about the model was necessary within this dissertation.

critical facility needs to discard disproportionate increases in consequences related to a hazard level beyond that of the ultimate (ULS) and accidental limit state (ALS) design stages. This is known as the beyond design basis scenario, which has the aim of discarding excessive effects of seismic loading on the structure, also called cliff-edge effects. The seismic hazard and, especially, the potential effects of liquefaction are usually part of the beyond design basis analysis, where a beyond design basis earthquake ($BDBE$) can reach significant acceleration magnitudes, even in areas of low seismicity. Therefore, in areas where thick layers of alluvial deposits are present, as was the case with evaluated soil profile, performing a liquefaction cliff-edge assessment with only semi-empirical correlations is not sufficient, as their range of applicability is limited and critical facilities tend to be large structures which can influence seismic wave propagation within a large radius from the structure, affecting the cyclic resistance of the soil deposits up to significant depths. To supplement these shortcomings, the use of more advanced modelling methods to assess liquefaction hazard is needed, which is where the practical application of the PM4Sand constitutive model becomes relevant. For this purpose, a theoretical and simplified case of a typical critical facility was assumed for the liquefaction hazard analysis. Specifically, the effects of soil-structure interaction on the soil profile's overall liquefaction hazard were evaluated, considering the liquefaction of the foundation layer of the structure as a cliff-edge scenario.

Having defined the seismic hazard level that was evaluated in this dissertation, it was necessary to define the earthquake input motion that was going to be used for the site response and liquefaction hazard analyses. For this research, and given the more computationally-expensive 2D model, one earthquake signal compliant with $BDBE$-conditions was selected based on its duration and intensity to be used in both the 1D and 2D liquefaction hazard analyses. The scaled earthquake signal used was the Umbria Marche earthquake, which occurred in September of 1997 in the Perugia province of Italy. The background signal, originated from a normal type fault, had a duration of 14.91 seconds, an estimated moment magnitude of $M_w = 6.0$, a $PGA = 0.426g$, and was recorded at a seismographic station located between the towns of Gubbio and Piana. Figure 7.1a shows the ATH of the Umbria Marche $BDBE$-signal, where it can be seen that the signal, besides its short duration, was not particularly rich in frequency content. This was confirmed by a frequency content analysis shown in Figure 7.1b, where it can be observed that the signal had a distinct predominant frequency of 1.94 Hz within a frequency range of 0 Hz to 16 Hz but with scarce distribution. Given the very large acceleration magnitudes of the Umbria Marche $BDBE$ signal, it was expected that some of the layers would trigger liquefaction. However the when and the behaviour of the onset of the liquefaction-triggering parameters was still pretty much unknown before the analysis.

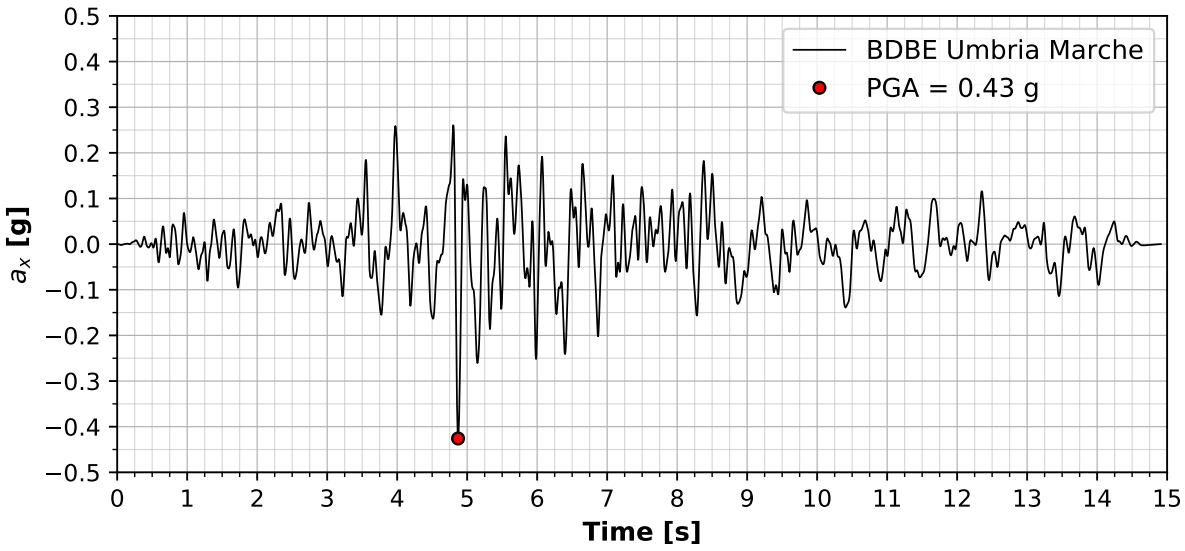

(a) Acceleration time-history

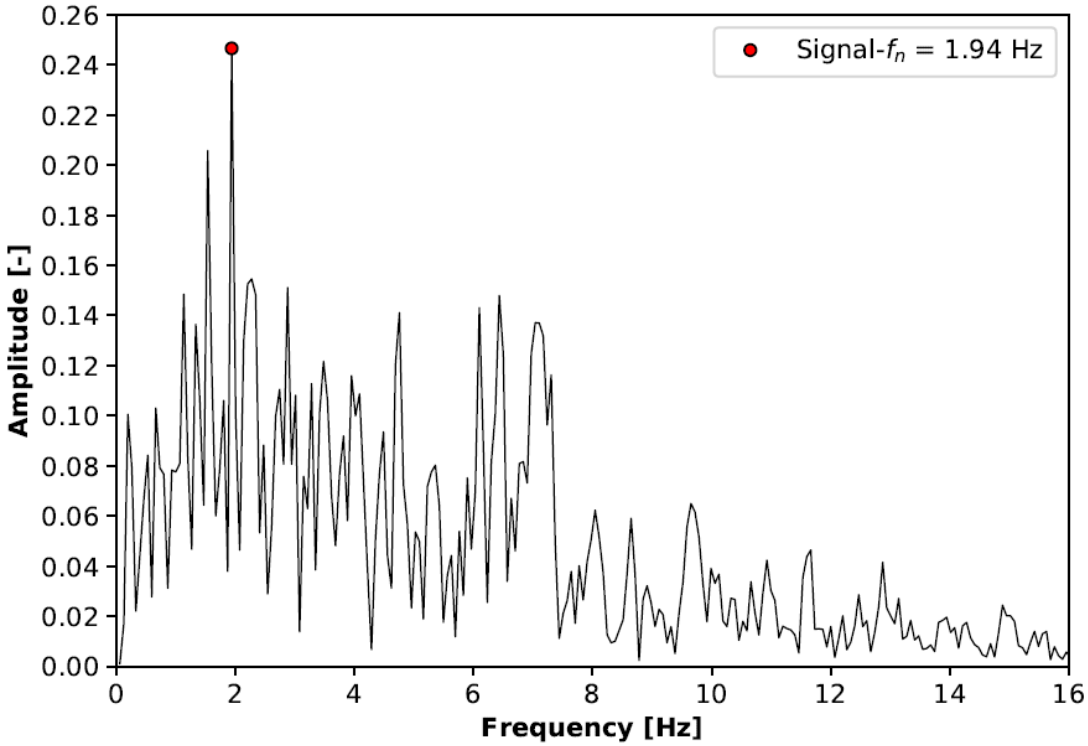

(b) Frequency content

Figure 7.1: Umbria Marche *BDBE* signal (scaled from original signal which occurred in September 1997)

7.2 Site characterisation

The description and characterisation of the soil layers present at the hypothetical project site were defined based on a single *CPTu*-profile, in addition to complementary borehole data and information from the V4 and V5 ground-motion models for the Groningen field (Bommer, Dost, et al., 2017a; Bommer, Edwards, et al., 2018). A q_c-based soil classification was performed with the specified definitions in Robertson (1990) and Robertson (2010), which was contrasted with the borehole data to establish the main soil types and particular characteristics. Then,

Groningen field formations were assigned to the established soil layers according to the V4 and V5 models in order to provide a consistent geological time setting. In total, 6 main sand layers were identified in the soil profile (as seen in Figure 7.2), interbedded with clay and peat layers, the former of which were further subdivided to account for adequate stress wave propagation and soil parameter averaging.

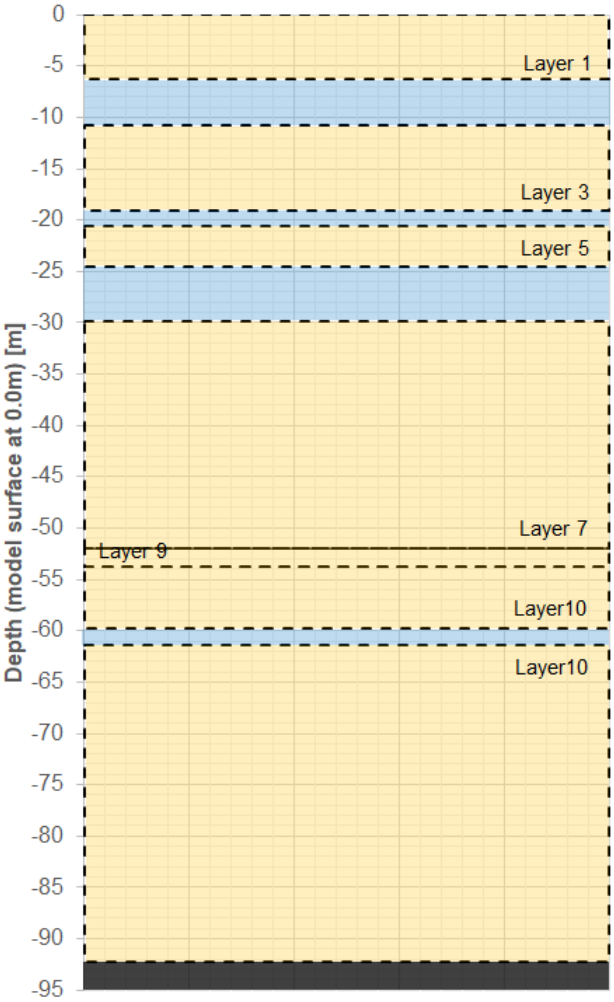

Figure 7.2: Generalised soil profile for case study

Tables 7.2 and 7.3 provide a general overview of the soil layers identified for the hypothetical project site of the critical facility, including geological designation, soil type, sub-layers, layer depths[2] and thicknesses and geological age. The general mechanical and physical soil properties, such as unit weights (UW), reference elastic secant, oedometer and unloading/reloading moduli (${E_{50}}^{ref}$, ${E_{oed}}^{ref}$ and ${E_{ur}}^{ref}$, effective friction angles (ϕ') and cohesion (c') magnitudes were extracted from NEN (2016), whereas V_s-magnitudes and index and relative state properties, such as the lateral earth pressure coefficient (K_0), overconsolidation ratio (OCR), C_u, D_{10}, D_{50} and plasticity index (PI) were extracted from the V4 and V5 models presented in Bommer, Dost, et al. (2017b) in accordance with the previously assigned layer designations. Furthermore, HSsmall-specific parameters such as the reference small-strain shear modulus (${G_0}^{ref}$) and the shear strain magnitude at 70% degradation of G_{max} ($\gamma_{0.7}$) were calculated based on the generic Mohr-Coulomb formulation found in PLAXIS (2019b) and material-specific correlations, respectively. The material-specific correlations used to determine $\gamma_{0.7}$ the sand, clay and peat layers

were those presented in Menq (2003), Darendeli (2001), Konstantinou et al. (2017), and Bommer, Dost, et al. (2017b), the latter two corresponding both to different types of peat. Figure 7.3 shows the small-strain shear modulus degradation curves constructed for all layers of the soil profile. All of the previously mentioned soil parameters were summarised in Tables 7.4 to 7.7. Lastly the determination of some additional soil characterisation parameters were discussed in greater detail.

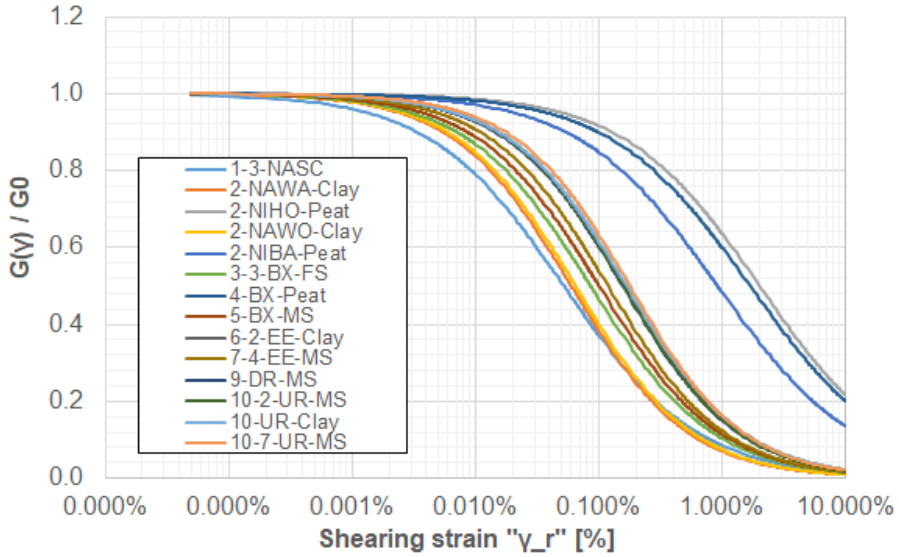

Figure 7.3: G_0 degradation curves for all soil profile sub-layers

7.2.1 Power of stress-level dependency m

The power of stress-level dependency m, was defined according to suggestions in PLAXIS (2019b), Soos (1990), Laera and Brinkgreve (2015a), and Laera and Brinkgreve (2015b). In general, exponent $m = 0.5$ and $m = 1.0$ were chosen for sands and soft soils, respectively. However, given that the considered soft soils were overconsolidated, slight reductions were applied to m, making it 0.8 and 0.6 for layers with $OCRs$ of 2 and 4, respectively, for clays and peats. In some cases, it was suggested that a modification of m should be applied for dynamic analyses, reducing m to 0.5 for all types of layers, making the overall response of the soil column somewhat stiffer. However, this modification was not evidenced in any previous site response analysis examples performed in Plaxis (Laera and Brinkgreve, 2015b; Laera and Brinkgreve, 2015a), which is why this option was not selected.

7.2.2 Fines content

Fines content percentages in each cohesionless layer were determined based on each layer description (from V4 model) and approximated to the lowest multiple of 5. This was a very generalised approximation, as it was more realistic to assume that fines content transitions in a more continuous from layer to layer. For example, if a clay or silt layer lies on top of a sand layer, it would be natural to assume that, due to age and the nature of deposition, that the transition zone between those two layers would have a greater fines content than the lower parts of the sand layer. In a more detailed study, such fines content transitions would be recommended.

[2]The depths of layer boundaries presented in Tables 7.2 and 7.3 were later transformed to equivalent depths for the 1D and 2D liquefaction potential analyses based on a surface level of 0.00 m, as seen in Tables 7.4, 7.5, 7.6, 7.7.

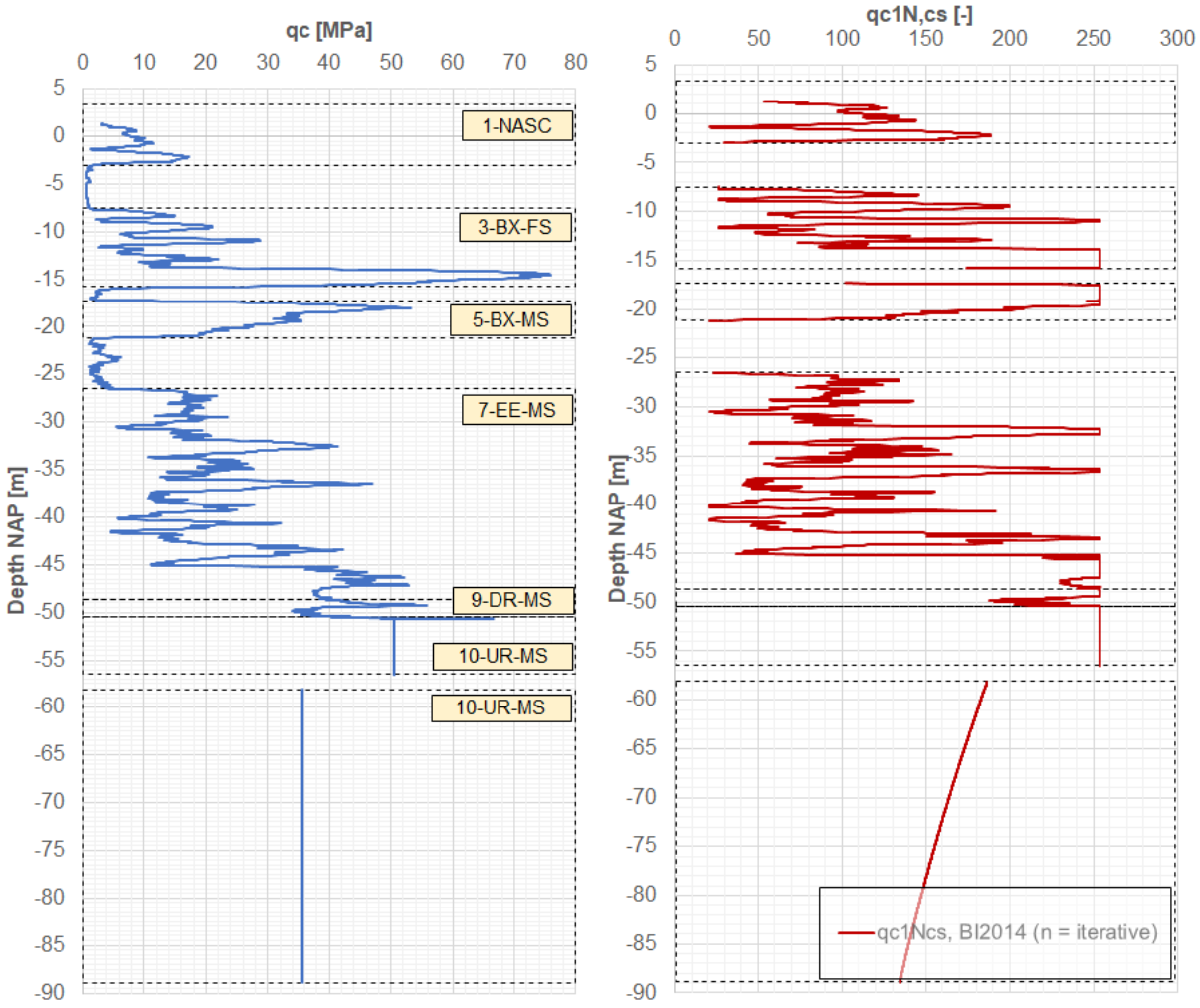

(a) q_c-profile (b) $q_{c1N,cs}$-profile

Figure 7.4: Transformation of q_c- to $q_{c1N,cs}$-magnitudes

However, the simplified approach was assumed in this instance as little information and time was available. Therefore, 5% of fines was assumed for all cohesionless layers except for layers 3-1- to 3-4-BX-FS, where a fines content of 10% was assumed. Based on these assumptions, the fines content correction could be estimated, as described by Equation 7.1, following the optimised version presented in Idriss and Boulanger (2014). However, to be able to use this correlation, the q_c soil profile had to first be overburden-stress-corrected with a D_R-dependent parameter C_N, modified from the original version in Salgado et al. (1997) as shown in Equation 7.2, leading to a normalised value of q_c, known as q_{c1N}, a resistance term commonly used in liquefaction studies. This was an iterative process which was easily performed using Excel's iterative feature (as suggested by Idriss and Boulanger, 2014). Based on these values, the q_c-profile was fines-corrected, which resulted in the fines-corrected cone penetration ($q_{c1N,cs}$)-profile which is shown in Figure 7.4.

$$q_{c1N,cs} = q_{c1N} + \Delta q_{c1N} = q_{c1N} + \left(11.9 + \frac{q_{c1N}}{14.6}\right) \exp\left(1.63 - \frac{9.7}{FC[\%]+2} - \left(\frac{15.7}{FC[\%]+2}\right)^2\right) \quad (7.1)$$

7.2.3 Estimation of e_{max}, e_{min} and D_{R0}

As described by many authors (e.g. Menq, 2003) the maximum and minimum limits for void ratio in a particular sand depend solely on the physical properties of the grain structure, such as the particle size, grain size distribution and compressibility, the latter being controlled by the presence of certain compressible minerals such as feldspar. However, given that only very limited data was available, it was decided to maintain the default values for e_{max} and e_{min} as presented by Boulanger and Ziotopoulou (2017), values which were needed for the calibration of the PM4Sand secondary model parameters. Next, several q_c-based D_{R0}-correlations were evaluated. Among them were correlations proposed by Jamiolkowski et al. (1985), Kulhawy and Mayne (1990), Baldi, Bellotti, Ghionna, Jamiolkowski, and Pasqualini (1986), Salgado et al. (1997), Idriss and Boulanger (2014), Robertson and Cabal (2015), and Youd and Idriss (1997). Upon evaluation of these correlations, great variations were evidenced, which would have over-complicated and introduced further error sources in the design process if implemented. Therefore, given that only the Idriss and Boulanger was proposed for the numerical analysis, the D_{R0} correlation specific to that method, shown in Equation 7.3. Based on the explanation provided in section 7.2.2, a D_{R0}-profile could be estimated based on q_{c1N}, shown in Figure 7.5. For the final D_{R0}-magnitudes of the cohesionless sub-layers, average magnitudes were calculated.

$$q_{c1N} = C_N q_c = \left(\frac{p_a}{\sigma'_{v0}}\right)^{1.338-0.249(q_{c1N})^{0.264}} \tag{7.2}$$

$$D_R = 0.478\big(q_{c1N,cs}\big)^{0.264} - 1.063 \tag{7.3}$$

7.2.4 Rayleigh damping ratios α and β

Rayleigh, or viscous, damping was added to the HSsmall model as a measure to create additional damping within the small-strain regime (Brinkgreve et al., 2007). This damping addition, next to the hysteretic damping term, which is frequency-independent, is associated to the velocity term in the dynamic equation and modifies the mass and stiffness matrices through the Rayleigh coefficients α and β, respectively. In contrast to hysteretic damping, Rayleigh damping is frequency-dependent and its coefficients must be calibrated based on the natural frequency of the system and the dominant load frequency (Brinkgreve et al., 2007). Plaxis 2D has a feature inside the definition of the HSsmall model where the user can specify equivalent single degree-of-freedom magnitudes for 2 target damping ratios ξ and frequencies with which the Rayleigh coefficients are calibrated. For the estimation of ξ, Laera and Brinkgreve (2015a) suggest that the same value between 0.5% and 2% should be used for both targets. For this case study, a value of 1% will be defined for ξ. Whereas, for the target frequencies, Hudson et al. (1994) suggested that the first frequency should be equal to the fundamental frequency of the whole soil model f_n (or column in case of 1D-*SRA*) and the second should be calculated by multiplying the fundamental frequency by a factor n, which is equal to the closest odd integer greater than the ratio between the predominant frequency of the input earthquake motion f_i and the fundamental frequency of the soil model. The fundamental frequency and the 2nd target frequency can be calculated using Equations 7.4 and 7.5, where V_s is averaged over all soil layers and H is the thickness of the entire soil model. For the conditions of the soil model, an average $V_s = 262.81$ m/s was estimated, leading to a natural frequency of the soil of $f_n = 0.69\ Hz$. Using a damping ratio of 1% and the natural frequency of the soil column, the Rayleigh damping ratios for the Umbria Marche signal were 0.07619, $5.594 \cdot 10^{-4}$.

$$f_{target1} = f_n = \frac{V_s}{4H} \tag{7.4}$$

$$f_{target2} = n(f_n),\ n = \text{closest odd integer greater than } \frac{f_i}{f_n} \tag{7.5}$$

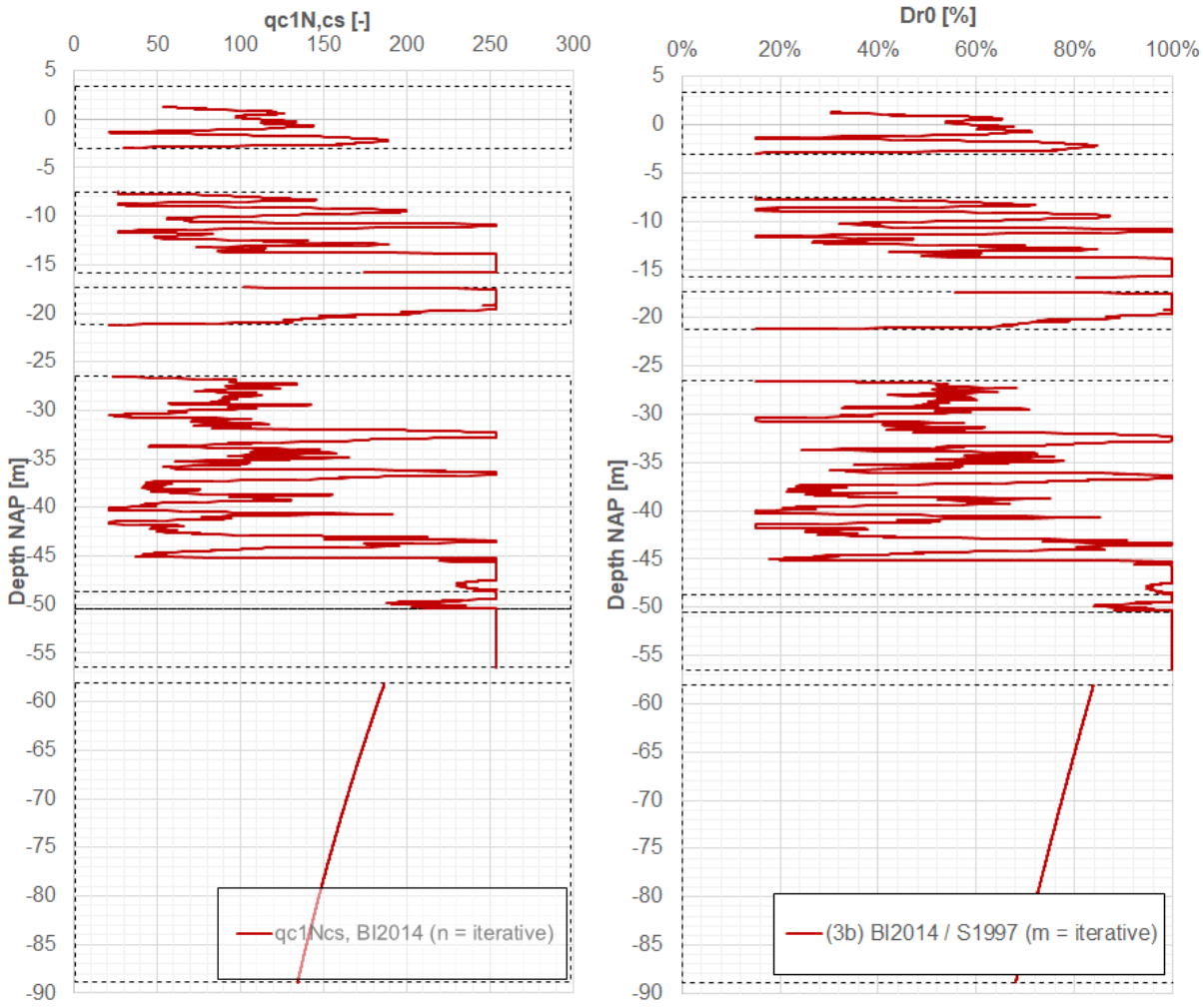

(a) $q_{c1N,cs}$-profile (b) D_{R0}-profile

Figure 7.5: $q_{c1N,cs}$- and calculated D_{R0}-profiles of the entire soil column domain

7.2.5 Cyclic resistance ratios

Based on the semi-empirical methods available, it was decided to use the $q_{c1N,cs}$-correlation proposed by Idriss and Boulanger (2014) to calculate the CRR-magnitudes for each liquefaction-vulnerable sub-layer. V_s- and $q_{c1N,cs}$-correlations by Andrus, Piratheepan, et al. (2004) and Andrus, Hayati, et al. (2009) were also evaluated but were deemed unreliable, especially the V_s-correlation. The $q_{c1N,cs}$-correlation by Robertson and Wride (1998) and Youd and Idriss (1997) was analysed as well and provided results very similar to Idriss and Boulanger's method but slightly less conservative, especially in the deeper regions where we were particularly interested in. Therefore, only the semi-empirical correlation proposed by Idriss and Boulanger was employed for the determination of the CRR-magnitudes for the calibration of the PM4Sand layers and for the semi-empirical and numerical comparison.

Idriss and Boulanger's CRR-correlation, presented in Equation 7.6, is dependent on $q_{c1N,cs}$ (specified in 7.2.2 and 7.2.3) and is a normalised correlation for a moment magnitude (M_w) of

7.5 and an effective overburden pressure (σ'_{v0}) of 1 atmosphere (101.3 kPa). Based on the $q_{c1N,cs}$-profile calculated in earlier sections, the CRR-profile was calculated and then overburden-stress corrected through factor K_σ (shown in Equation 7.7, which is a normalisation term analogue to C_N but for the application to CRR. Given that the PM4Sand model could not adequately model different shearing conditions with a single parameter set, K_σ-corrected CRR-magnitudes were needed. However, no magnitude scaling factor (MSF) was applied. This was explained in detail in section 7.3. Having said this, the obtained CRR-magnitudes were then capped at 0.6, value beyond which sand is assumed not to be able to liquefy (see Figure 7.6. The CRR-magnitudes were not magnitude-corrected (MSF) For the determination of the average magnitudes of CRR per layer, values greater than 0.6 were filtered and the criterion $\mu_{CRR} - \sigma_{CRR}$ was applied to obtain conservative CRR-values. The reason for the adoption of this calculation criterion was to try to approximate heterogeneous soil behaviour: Since failure in any material occurs through its weakest part, it would be unwise to assume a simple average of a certain soil property over a determined range of depth, especially if that property was the one analysed for failure conditions. Additionally, in the case of liquefaction, stress is expected to relocate towards adjacent lower-stress regions around a location which has liquefied, progressively expanding the area of soil which reaches liquefaction. Therefore, to try and simulate these conditions, a lower than average CRR was adopted.

$$CRR_{M_w=7.5,\sigma'_v=1atm} = \exp\left(\frac{q_{c1N}}{113} + \left(\frac{q_{c1N}}{1000}\right)^2 - \left(\frac{q_{c1N}}{140}\right)^3 + \left(\frac{q_{c1N}}{137}\right)^4 - 2.80\right) \tag{7.6}$$

$$K_\sigma = 1 - C_\sigma \ln\left(\frac{\sigma'_v}{p_a}\right) \leq 1.1 \tag{7.7}$$

$$C_\sigma = \frac{1}{37.3 - 8.27\left(q_{c1N,cs}\right)^{0.264}} \leq 0.3 \tag{7.8}$$

7.3 Calibration of liquefiable layers

Layers were calibrated according to suggestions from Boulanger and Ziotopoulou (2017) and Ziotopoulou, Boulanger, et al. (2012) where the $CRRs$ were calculated for a magnitude of $M_w = 7.5$ and for each of the layer's average overburden pressure (taken at the centre of each sub-layer). Given that the proposed $q_{c1N,cs}$-correlations by Idriss and Boulanger (2014) and Robertson and Wride (1998) gave very similar CRR-values for layers which were considered to be susceptible to liquefaction, it was decided that only the CRR-magnitudes calculated through Idriss and Boulanger's method were going to be used for the numerical analyses in 1D and 2D. Having established these conditions, the previously-obtained $q_{c1N,cs}$-profile was used to estimate the CRR-magnitudes at the centre of each layer, as well as the average D_{R0}-values of all cohesionless layers. Given that no additional data was available, e_{max}, e_{min}, n^b, n^d, ϕ_{cv}, R and Q were left at their default values, after which h_{p0} was fit to match liquefaction-triggering criteria specified in part II, them being $r_u = 0.95$ and $\gamma = 3\%$, after 15 equivalent uniform cycles, estimated for an earthquake magnitude of $M_w = 7.5$ as suggested in Idriss (1999) and Idriss and Boulanger (2008). Similar to the benchmark case study, calibration methodologies *CM1* and *CM2* were used to calibrate the PM4Sand layers.The reason why the calibration of the PM4Sand layers was performed using calculated CRR-values for the standardised moment magnitude of $M_w = 7.5$ (for all input motion scenarios) instead of calculating CRR-magnitudes specifically to each of the input signals' M_w was because the equivalent-uniform-cycle concept proposed by Idriss (1999) referred to the intrinsic cyclic resistance of a soil body to a given number of cycles: Irrespective of the stresses induced by a specific earthquake motion, a specific soil's cyclic resistance only depends on its intrinsic mechanical properties and its initial state.

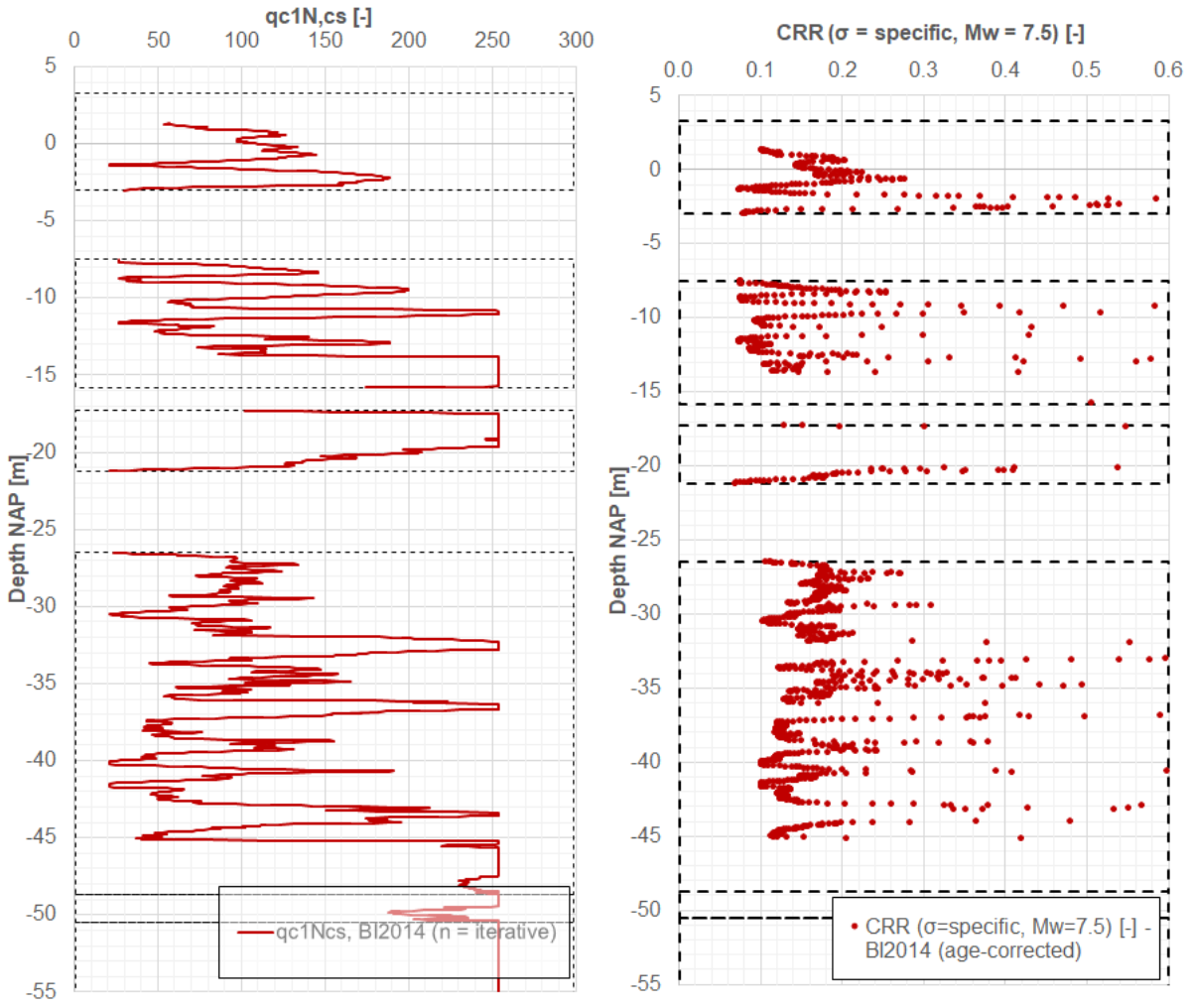

(a) $q_{c1N,cs}$-profile (b) CRR-profile

Figure 7.6: Calculated $q_{c1N,cs}$- and CRR-profiles of liquefiable layers

If a specific earthquake induces a certain magnitude of cyclic shear stress on the soil, it is only a matter of time (or equivalent uniform cycles), depending on the magnitude of M_w, until the soil reaches liquefaction (considering that there are enough conditions to consider there is undrained behaviour). Therefore, it was trivial whether the layers were calibrated to an earthquake magnitude of $M_w = 7.5$ or another, since the equivalent uniform cycles specified in Idriss (1999) would change accordingly. This approach was also used by researchers studying the effect of and onset of liquefaction through numerical modelling, like in Ziotopoulou, Boulanger, et al. (2012), among others. It is, however, important to mention that this procedure is only valid for calibrating the constitutive model behaviour of cohesionless soils using a liquefaction-capable material model and not when trying to evaluate the liquefaction potential of a soil profile using the simplified approach specified by Seed and Idriss (1971) in conjunction with any of the available CRR calculation methodologies, as was performed in section 8.3. Taking into account all of the above, the cohesionless layers of the model were calibrated based on CRR-magnitudes calculated using the methodology proposed by Idriss and Boulanger (2014). It is, however, worth mentioning that in order to calculate the average values of CRR for all layers, this research assumed that Idriss and Boulanger's $q_{c1N,cs} - CRR$ correlation was applicable at greater depths than those used in the updated database (Idriss and Boulanger, 2014) to create the correlation. Therefore, there was already at this early stage, an intrinsic error which must be compensated through future research but was put aside for purposes of this research. Having said this, cohesionless

layers from 1-3-NASC-MS to 7-5-EE-MS were calibrated based on calibration methodologies 1 and 2, specified in part II, at their average overburden pressure, D_{R0} and G_0. Calibration methodology 1 (*CM1*) followed the original calibration concept used by most researchers, which was to calibrate h_{p0} to reach the liquefaction-triggering marker $\gamma = 3\%$ at 15 uniform stress cycles, not taking into account the evolution of pore pressures, whereas calibration methodology 2 (*CM2)*, the one proposed in this research, focused on trying to reach liquefaction-triggering markers $\gamma = 3\%$ and $r_u = 0.95$ at approximately 15 uniform stress cycles. The new methodology, as explained in part II, prioritised reaching the $\gamma = 3\%$ marker first, at approximately 15 cycles, after which D_{R0} and h_{p0} were iteratively recalibrated to reduce the difference in cycles between the triggering of $\gamma = 3\%$ and $r_u = 0.95$. For this purpose, a maximum tolerance for ΔN between the triggering of $\gamma = 3\%$ and $r_u = 0.95$ was established at 2.5 cycles, based on the assumption the liquefaction can be quantitatively represented by those markers, which develop at approximately ± 2.5[1]. Cohesionless layers 1-1- and 1-2-NASC-MS and 7-6-EE-MS to 10-10-UR-MS were not included in the calibration process because they were either, above the specified ground water table, had a $CRR \geq 0.6$, or were too deep for any of the used earthquake signals to produce large-enough shear stresses to pose a significant liquefaction hazard. The latter is further explained in section 8.1. Table 7.1 presents the calibrated PM4Sand model parameters for all cohesionless layers used in the 1D and 2D numerical liquefaction potential analyses in chapters 8 and 9.

Layer	**$CRR_{M_w=7.5}$ [-]**	**D_{R0} [-]**		**h_{p0} [-]**		**G_0 [-]**
		(1)	(2)	(1)	(2)	
1-1-NASC-MS	above GWT	0.5209	0.5209	-	-	1306.91
1-2-NASC-MS	above GWT	0.5209	0.5209	-	-	944.32
1-3-NASC-MS	0.1199	0.5209	0.31	0.0305	1.5950	944.46
1-4-NASC-MS	0.1248	0.5645	0.32	0.0400	2.0500	1012.85
1-5-NASC-MS	0.1410	0.6369	0.35	0.0260	3.0000	1071.28
3-1-BX-FS	0.1005	0.4088	0.35	0.1275	0.2700	1200.80
3-2-BX-FS	0.1253	0.6694	0.40	0.0080	0.4500	1153.94
3-3-BX-FS	0.0940	0.5185	0.38	0.0295	0.1731	1109.36
3-4-BX-FS	0.1377	0.8796	0.55	0.0003	0.1440	1064.72
5-BX-MS	0.1703	0.8738	0.62	0.0030	0.1780	1032.57
7-1-EE-MS	0.1620	0.5063	0.5063	0.8500	0.8500	840.25
7-2-EE-MS	0.1552	0.5984	0.5063	0.2630	0.2630	792.59
7-3-EE-MS	0.1741	0.6335	0.6335	0.3040	0.3040	752.21
7-4-EE-MS	0.1292	0.4144	0.4144	1.0470	1.0470	717.43
7-5-EE-MS	0.1281	0.5090	0.5090	0.4050	0.4050	687.08
7-6-EE-MS to 10-10-UR-MS	no liquefaction hazard	-	-	-	-	-

Table 7.1: Calibrated primary PM4Sand model parameters based on CRR calculated with $q_{c1N,cs}$-correlation from Idriss and Boulanger (2014) and using both calibration methodologies

[1]This tolerance was based on detailed analysis of the *CUDSS* tests from Parra (2016), which showed that, for most loose and dense sands confined at 50, 100 and 400 kPa and sheared at low to high *CSRs*, that the difference between the triggering of $\gamma = 3\%$ and $r_u = 0.95$ could be approximated to ± 2.5. There were some exceptions to this rule, but $\Delta N = 2.5$ was established for all types of initial states for simplification purposes.

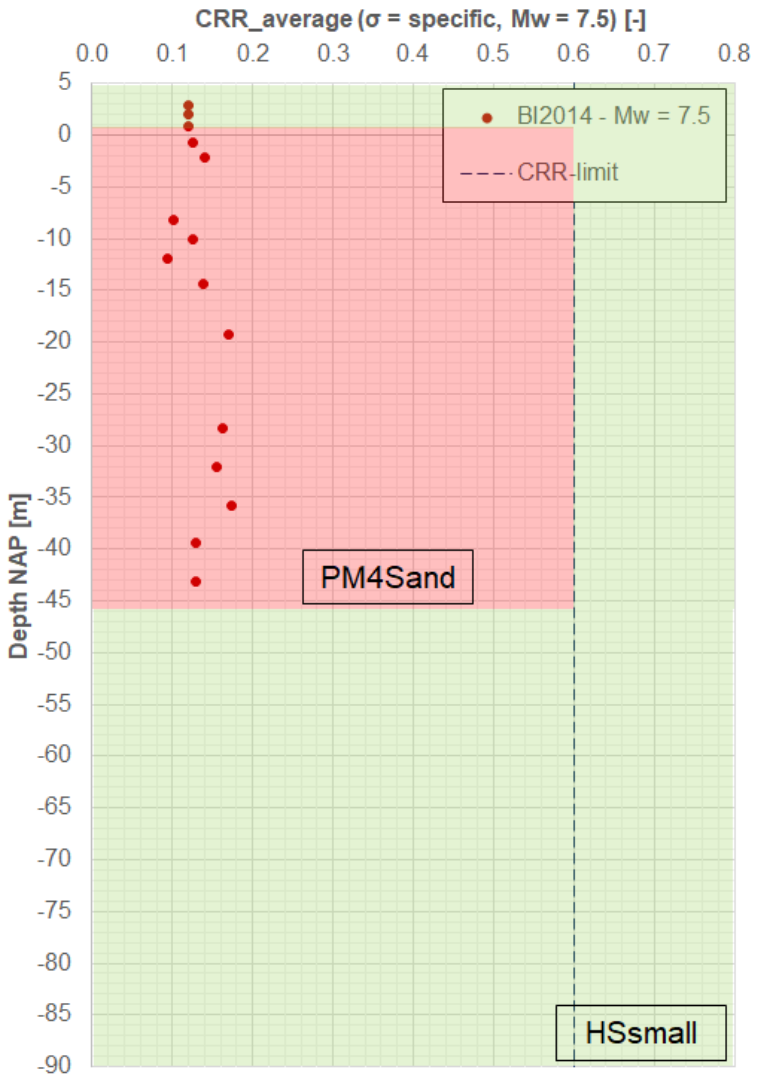

Figure 7.7: Zonification of PM4sand and HSsmall modelled regions and estimated CRR-magnitudes for calibration

To finish this section, *CM2* provided a holistic calibration approach both in terms of pore pressure and shear strain evolution, compared to *CM1*, which modified the cyclic behaviour of liquefiable layers in 1D and 2D. As mentioned in the preliminary conclusions of part II, the PM4Sand model could adequately model sands in loose states at various overburden pressures and sheared at relatively low to intermediate *CSRs*. However, it had difficulties modelling sands in dense states and sheared at intermediate to high *CSRs*. For sands falling within the former cases, *CM1* provided a good enough calibrated parameter set, which allowed liquefaction markers $\gamma = 3\%$ and $r_u = 0.95$ to be activated within the specified tolerance. Also falling within that category, were dense sand samples confined at high overburden stresses ($\geq$ 300 kPa and higher). As for dense sands confined at low to intermediate overburden pressures, *CM2* allowed the model to reach both liquefaction markers within the established ΔN tolerance. A possible explanation to these difference between results obtained by using *CM1* and *CM2* was that when soil properties, initial state and shearing conditions allowed for high dilative tendencies during cyclic shearing, PM4Sand would create a larger ΔN between the triggering of $\gamma = 3\%$ and $r_u = 0.95$. These dilative tendencies during shearing could be caused due to a high D_{R0} or low confinement pressure. The magnitude of ΔN between $\gamma = 3\%$ and $r_u = 0.95$ reduced when the behaviour of the PM4Sand model became more contractive, either through a lower

D_{R0}-magnitude or high overburden pressure. Therefore, it made sense that the calibration of shallow layers in the case study resulted in different material parameter sets, as they tended towards a dilative behaviour given their high D_{R0}-values and low to intermediate confinement pressures. This effect was reduced with increasing depth, as very deep layers, starting from 7-1-EE-MS downwards, experienced reduced dilative behaviour. These changes can be observed in Figures 7.8 and 7.9 where the calibrated models of layers 1-3-NASC-MS and 7-1-EE-MS can be observed for illustration purposes (to see complementary graphs of these and the remainder of the calibrated layers, refer to Figures 10.1 to 10.13). These layers represent dense sands confined at low and high confinement pressures. As described earlier, the calibrated *CM2*-model was obtained by iteratively reducing D_{R0} and recalibrating h_{p0} to try and match both the γ- and r_u-based liquefaction-triggering markers. Figure 7.10 shows the recalibration process of all calibrated layers, where D_{R0} and h_{p0} progressively reduce and increase, respectively, to lower ΔN below the acceptable tolerance level of 2.5 cycles.

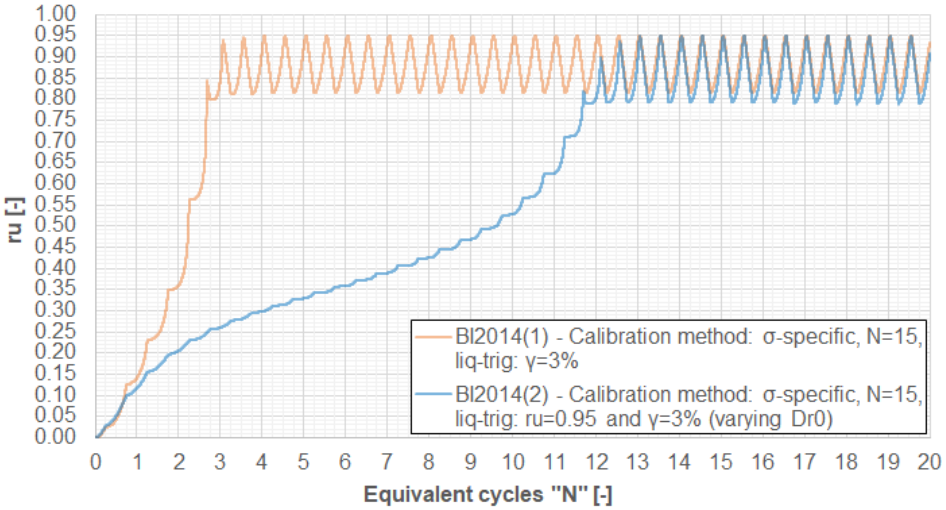

(a) Layer 1-3-NASC-MS

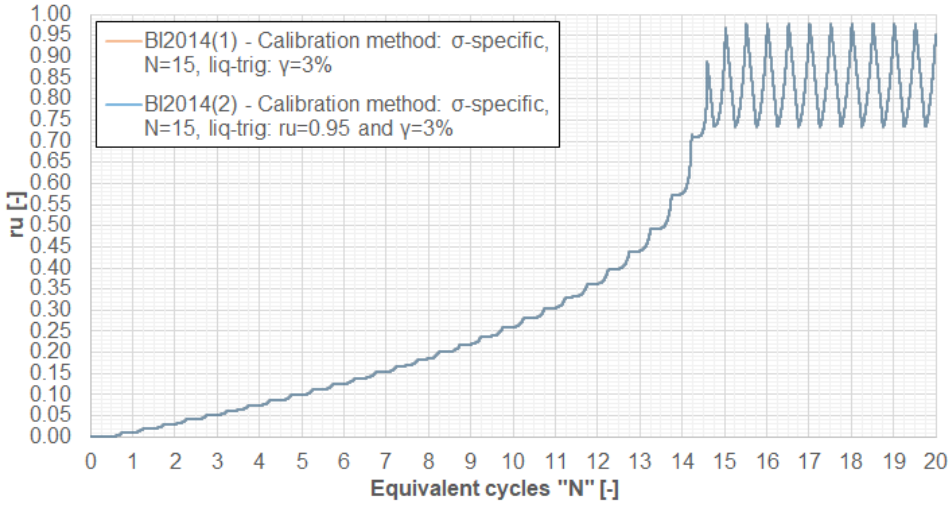

(b) Layer 7-1-EE-MS

Figure 7.8: Calibrated $N - r_u$ curves using calibration methodologies 1 and 2 of shallow and deep layers 1-3-NASC-MS and 7-1-EE-MS, respectively.

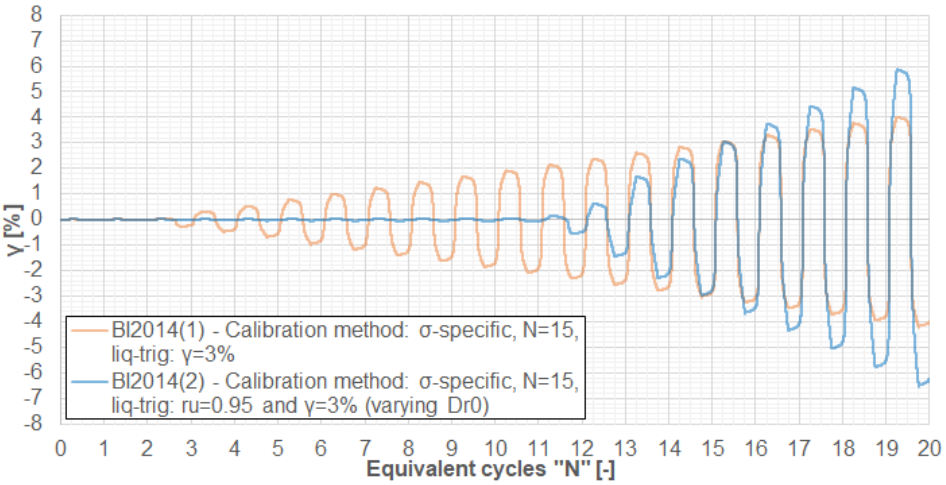

(a) Layer 1-3-NASC-MS

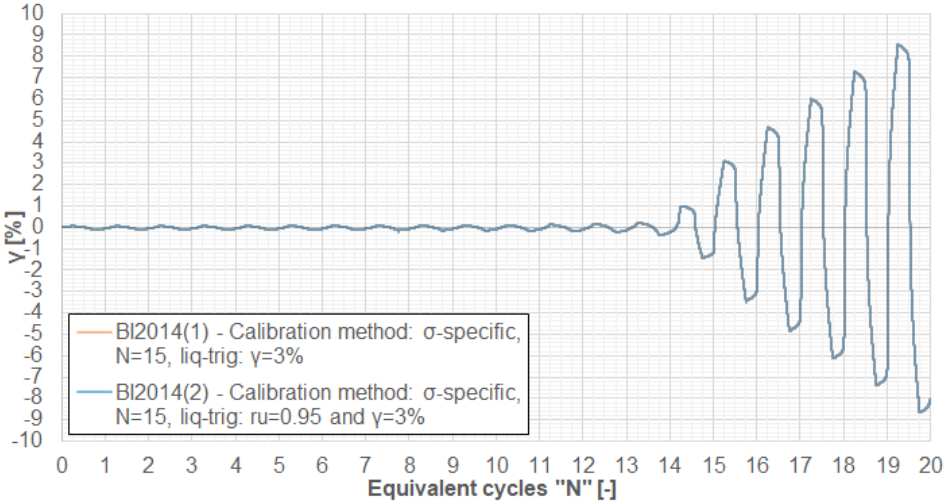

(b) Layer 7-1-EE-MS

Figure 7.9: Calibrated $N - \gamma$ curves using calibration methodologies 1 and 2 of shallow and deep layers 1-3-NASC-MS and 7-1-EE-MS, respectively.

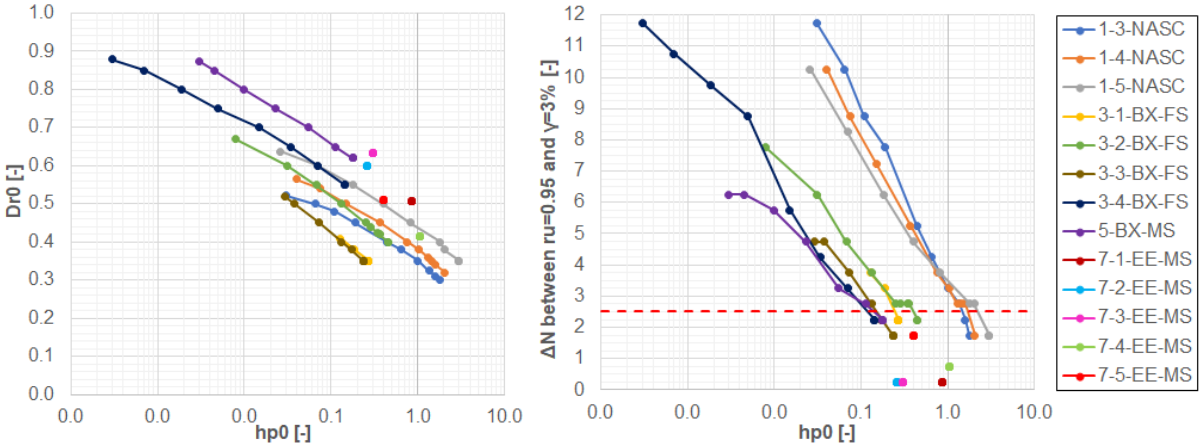

(a) Variation of D_{R0} and h_{p0}

(b) Variation of ΔN and h_{p0}

Figure 7.10: to obtain *CM2*-based calibrated parameters

Chronostratigraphy		Soil type	Abbrev.*	Sub-layers	Depth** [m]		
Formation	**Epoch**				**Top**	**Bottom**	**t**
Naaldwijk - Schoorl	Holocene	Medium sand	NASC-MS	1-1-NASC-MS	3.32	2.41	0.91
				1-2-NASC-MS	2.41	1.50	0.91
				1-3-NASC-MS	1.50	0.10	1.40
				1-4-NASC-MS	0.10	-1.40	1.50
				1-5-NASC-MS	-1.40	-3.00	1.60
Naaldwijk - Walcheren	Holocene	Clay	NAWA-Clay	2-NAWA-Clay	-3.00	-4.50	1.50
Nieuwkoop - Holland Peat	Holocene	Peat	NIHO-Peat	2-NIHO-Peat	-4.50	-5.00	0.50
Naaldwijk - Wormer	Holocene	Clay	NAWO-Clay	2-1-NAWO-Clay	-5.00	-6.20	1.20
				2-2-NAWO-Clay	-6.20	-7.40	1.20
Nieuwkoop - Basal Peat	Holocene	Peat	NIBA-Peat	2-NIBA-Peat	-7.40	-7.50	0.10
Boxtel	Late Pleistocene to early Holocene	Fine sand	BX-FS	3-1-BX-FS	-7.50	-9.00	1.50
				3-2-BX-FS	-9.00	-11.00	2.00
				3-3-BX-FS	-11.00	-13.00	2.00
				3-4-BX-FS	-13.00	-15.80	2.80
		Peat	BX-Peat	4-BX-Peat	-15.80	-17.30	1.50
		Medium sand	BX-FS	5-BX-MS	-17.30	-21.20	3.90
Eem	Late Pleistocene	Clay	EE-Clay	6-1-EE-Clay	-21.20	-22.90	1.70
				6-2-EE-Clay	-22.90	-24.60	1.70
				6-3-EE-Clay	-24.60	-26.50	1.90
		Medium sand	EE-MS	7-1-EE-MS	-26.50	-30.20	3.70
				7-2-EE-MS	-30.20	-33.90	3.70
				7-3-EE-MS	-33.90	-37.60	3.70
				7-4-EE-MS	-37.60	-41.30	3.70
				7-5-EE-MS	-41.30	-45.00	3.70
				7-6-EE-MS	-45.00	-48.70	3.70

Table 7.2: Soil layer descriptions at the hypothetical project site (*:Abbreviation; **: Relative to NAP)

Chronostratigraphy		Soil type	Abbrev.[2]	Sub-layers	Depth[3] [m]		
Formation	**Epoch**				**Top**	**Bottom**	**t**
Drente	Middle to late Pleistocene	Medium sand	DR-MS	9-DR-MS	-48.70	-50.50	1.80
Urk	Middle Pleistocene	Medium sand	UR-MS	10-1-UR-MS	-50.50	-53.50	3.00
				10-2-UR-MS	-53.50	-56.50	3.00
		Clay	UR-Clay	10-UR-Clay	-56.50	-58.10	1.60
		Medium sand	UR-MS	10-3-UR-MS	-58.10	-61.90	3.80
				10-4-UR-MS	-61.90	-65.70	3.80
				10-5-UR-MS	-65.70	-69.50	3.80
				10-6-UR-MS	-69.50	-73.30	3.80
				10-7-UR-MS	-73.30	-77.20	3.90
				10-8-UR-MS	-77.20	-81.10	3.90
				10-9-UR-MS	-81.10	-85.00	3.90
				10-10-UR-MS	-85.00	-88.90	3.90
Seismic base layer	-	Bedrock	SBL	SBL	-88.90	-	-

Table 7.3: Soil layer descriptions at the hypothetical project site (continued; *:Abbreviation; **: Relative to NAP)

[2]The presented abbreviations consist of a first part, defining the geological unit, which is the same as mentioned in Bommer, Dost, et al. (2017a), and a second part which define the type of soil.

[3]Relative to NAP. For the rest of the chapters, the depths were adjusted to a surface at 0.00 m for implementation in the model.

[4]Depths of model shifted based on a surface level at 0.00 m.

[5]UW: Unit weight; T: Top, B: Bottom

Sub-layers	Soil types	Depth[4] [m]		UW $\frac{kN}{m^3}$]		E_{50}^{ref} [kPa]	E_{oed}^{ref} [kPa]	E_{ur}^{ref} [kPa]	c'^{ref} [kPa]	ϕ' [°]	ψ' [°]	m [-]
		T.[5]	B.[5]	Dry	Sat.							
1-1-NASC-MS	Medium sand	0.00	-0.91	20.50	20.50	51250	51250	205000	0.00	33.75	0	0.5
1-2-NASC-MS	Medium sand	-0.91	-1.82	20.50	20.50	51250	51250	205000	0.00	33.75	0	0.5
1-3-NASC-MS	Medium sand	-1.82	-3.22	20.50	20.50	51250	51250	205000	0.00	33.75	0	0.5
1-4-NASC-MS	Medium sand	-3.22	-4.72	20.50	20.50	51250	51250	205000	0.00	33.75	0	0.5
1-5-NASC-MS	Medium sand	-4.72	-6.32	20.50	20.50	51250	51250	205000	0.00	33.75	0	0.5
2-NAWA-Clay	Clay	-6.32	-7.82	17.75	17.75	2875	1437.5	17250	1.50	22.50	0	0.8
2-NIHO-Peat	Peat	-7.82	-8.32	12.50	12.50	750	500	4500	3.75	15.00	0	0.8
2-1-NAWO-Clay	Clay	-8.32	-9.52	20.50	20.50	2875	1437.5	17250	1.50	22.50	0	0.8
2-2-NAWO-Clay	Clay	-9.52	-10.72	20.50	20.50	2875	1437.5	17250	1.50	22.50	0	0.8
2-NIBA-Peat	Peat	-10.72	-10.82	12.50	12.50	750	500	4500	3.75	15.00	0	0.8
3-1-BX-FS	Fine sand	-10.82	-12.32	20.50	20.50	51250	51250	205000	0.00	33.75	0	0.5
3-2-BX-FS	Fine sand	-12.32	-14.32	20.50	20.50	51250	51250	205000	0.00	33.75	0	0.5
3-3-BX-FS	Fine sand	-14.32	-16.32	20.50	20.50	51250	51250	205000	0.00	33.75	0	0.5
3-4-BX-FS	Fine sand	-16.32	-19.12	20.50	20.50	51250	51250	205000	0.00	33.75	0	0.5
4-BX-Peat	Peat	-19.12	-20.62	12.50	12.50	750	500	4500	0.00	33.75	0	0.6
5-BX-MS	Medium sand	-20.62	-22.57	21.00	21.00	92500	92500	370000	0.00	37.50	0	0.5

Table 7.4: Soil layer properties at the hypothetical project site

[e]

Sub-layers	Soil types	Depth[4] [m]		V_S [m/s]	G_0^{ref} [kPa]	$\gamma_{0.7}$ [-]	K_0^{nc} [-]	K_0 [-]	OCR [-]	k [m/s]	ν'_{ur} [-]	p^{ref} [kPa]	R_f [-]
		T.[5]	B.[5]										
1-1-NASC-MS	Medium sand	0.00	-0.91	122.10	151851.92	$7.743 \cdot 10^{-5}$	0.444	0.50	1.0	$3.240 \cdot 10^{-4}$	0.2	100	0.9
1-2-NASC-MS	Medium sand	-0.91	-1.82	136.61	109747.68	$1.275 \cdot 10^{-4}$	0.444	0.50	1.0	$3.240 \cdot 10^{-4}$	0.2	100	0.9
1-3-NASC-MS	Medium sand	-1.82	-3.22	154.23	109763.36	$1.585 \cdot 10^{-4}$	0.444	0.50	1.0	$3.240 \cdot 10^{-4}$	0.2	100	0.9
1-4-NASC-MS	Medium sand	-3.22	-4.72	172.83	117711.70	$1.824 \cdot 10^{-4}$	0.444	0.50	1.0	$3.240 \cdot 10^{-4}$	0.2	100	0.9
1-5-NASC-MS	Medium sand	-4.72	-6.32	189.41	124502.44	$2.042 \cdot 10^{-4}$	0.444	0.50	1.0	$3.240 \cdot 10^{-4}$	0.2	100	0.9
2-NAWA-Clay	Clay	-6.32	-7.82	162.92	44989.53	$2.119 \cdot 10^{-4}$	0.617	0.50	2.0	$1.331 \cdot 10^{-10}$	0.2	100	0.9
2-NIHO-Peat	Peat	-7.82	-8.32	83.90	18345.54	$6.066 \cdot 10^{-3}$	0.741	0.35	2.0	$1.331 \cdot 10^{-10}$	0.2	100	0.9
2-1-NAWO-Clay	Clay	-8.32	-9.52	168.81	45260.11	$2.214 \cdot 10^{-4}$	0.617	0.50	2.0	$1.331 \cdot 10^{-10}$	0.2	100	0.9
2-2-NAWO-Clay	Clay	-9.52	-10.72	173.13	45386.93	$2.285 \cdot 10^{-4}$	0.617	0.50	2.0	$1.331 \cdot 10^{-10}$	0.2	100	0.9
2-NIBA-Peat	Peat	-10.72	-10.82	145.86	14391.29	$2.680 \cdot 10^{-3}$	0.741	0.70	2.0	$1.331 \cdot 10^{-10}$	0.2	100	0.9
3-1-BX-FS	Fine sand	-10.82	-12.32	251.98	120857.58	$2.563 \cdot 10^{-4}$	0.444	1.00	1.0	$2.777 \cdot 10^{-5}$	0.2	100	0.9
3-2-BX-FS	Fine sand	-12.32	-14.32	255.93	116141.30	$2.727 \cdot 10^{-4}$	0.444	1.00	1.0	$1.965 \cdot 10^{-5}$	0.2	100	0.9
3-3-BX-FS	Fine sand	-14.32	-16.32	259.93	111654.33	$2.899 \cdot 10^{-4}$	0.444	1.00	1.0	$2.491 \cdot 10^{-5}$	0.2	100	0.9
3-4-BX-FS	Fine sand	-16.32	-19.12	264.14	107162.28	$3.090 \cdot 10^{-4}$	0.444	1.00	1.0	$1.222 \cdot 10^{-5}$	0.2	100	0.9
4-BX-Peat	Peat	-19.12	-20.62	148.12	15628.30	$4.905 \cdot 10^{-3}$	0.741	1.10	5.456	$1.331 \cdot 10^{-10}$	0.2	100	0.9
5-BX-MS	Medium sand	-20.62	-22.57	269.85	164833.33	$3462 \cdot 10^{-4}$	0.3912	1.00	1.0	$7.177 \cdot 10^{-5}$	0.2	100	0.9

Table 7.5: Soil layer properties at the hypothetical project site (continued)

Sub-layers	Soil types	Depth[4] [m]		UW $\frac{kN}{m^3}$]		E_{50}^{ref} [kPa]	E_{oed}^{ref} [kPa]	E_{ur}^{ref} [kPa]	c'^{ref} [kPa]	ϕ' [°]	ψ' [°]	m [-]
		T.[5]	B.[5]	Dry	Sat.							
6-1-EE-Clay	Clay	-22.57	-26.22	19.00	19.00	4000	2000	24000	4.75	22.50	0	0.6
6-2-EE-Clay	Clay	-26.22	-27.92	19.00	19.00	4000	2000	24000	4.75	22.50	0	0.6
6-3-EE-Clay	Clay	-27.92	-29.82	19.00	19.00	4000	2000	24000	4.75	22.50	0	0.6
7-1-EE-MS	Medium sand	-29.82	-33.52	20.50	20.50	60000	60000	240000	0.00	33.75	0	0.5
7-2-EE-MS	Medium sand	-33.52	-37.22	20.50	20.50	60000	60000	240000	0.00	33.75	0	0.5
7-3-EE-MS	Medium sand	-37.22	-40.92	20.50	20.50	60000	60000	240000	0.00	33.75	0	0.5
7-4-EE-MS	Medium sand	-40.92	-44.62	20.50	20.50	60000	60000	240000	0.00	33.75	0	0.5
7-5-EE-MS	Medium sand	-44.62	-48.32	20.50	20.50	60000	60000	240000	0.00	33.75	0	0.5
7-6-EE-MS	Medium sand	-48.32	-52.02	20.50	20.50	60000	60000	240000	0.00	33.75	0	0.5
9-DR-MS	Medium sand	-52.02	-53.82	20.50	20.50	60000	60000	240000	0.00	33.75	0	0.5
10-1-UR-MS	Medium sand	-53.82	-56.82	20.50	20.50	60000	60000	240000	0.00	33.75	0	0.5
10-2-UR-MS	Medium sand	-56.82	-59.82	20.50	20.50	60000	60000	240000	0.00	33.75	0	0.5
10-UR-Clay	Clay	-59.82	-61.42	20.50	20.50	7500	3750	45000	14.00	25.00	0	0.6
10-3-UR-MS	Medium sand	-61.42	-65.22	20.50	20.50	60000	60000	240000	0.00	33.75	0	0.5
10-4-UR-MS	Medium sand	-65.22	-69.02	20.50	20.50	60000	60000	240000	0.00	33.75	0	0.5
10-5-UR-MS	Medium sand	-69.02	-72.82	20.50	20.50	60000	60000	240000	0.00	33.75	0	0.5
10-6-UR-MS	Medium sand	-72.82	-76.62	20.50	20.50	60000	60000	240000	0.00	33.75	0	0.5
10-7-UR-MS	Medium sand	-76.62	-80.52	20.50	20.50	60000	60000	240000	0.00	33.75	0	0.5
10-8-UR-MS	Medium sand	-80.52	-84.42	20.50	20.50	60000	60000	240000	0.00	33.75	0	0.5
10-9-UR-MS	Medium sand	-84.42	-88.32	20.50	20.50	60000	60000	240000	0.00	33.75	0	0.5
10-10-UR-MS	Medium sand	-88.32	-92.22	20.50	20.50	60000	60000	240000	0.00	33.75	0	0.5
SBL	Bedrock	-92.22	-95.22	21.00	21.00	-	-	-	-	-	-	-

Table 7.6: Soil layer properties at the hypothetical project site (continued)

[e]

Sub-layers	Soil types	Depth[4] [m]		V_S [m/s]	G_0^{ref} [kPa]	$\gamma_{0.7}$ [-]	K_0^{nc} [-]	K_0 [-]	OCR [-]	k [m/s]	ν'_{ur} [-]	p^{ref} [kPa]	R_f [-]
		T.[5]	B.[5]										
6-1-EE-Clay	Clay	-22.57	-26.22	233.34	53837.29	$5.490 \cdot 10^{-4}$	0.617	1.30	5.721	$1.331 \cdot 10^{-10}$	0.2	100	0.9
6-2-EE-Clay	Clay	-26.22	-27.92	235.22	52885.08	$5.618 \cdot 10^{-4}$	0.617	1.30	5.789	$1.331 \cdot 10^{-10}$	0.2	100	0.9
6-3-EE-Clay	Clay	-27.92	-29.82	237.03	51907.55	$5.748 \cdot 10^{-4}$	0.617	1.30	5.861	$1.331 \cdot 10^{-10}$	0.2	100	0.9
7-1-EE-MS	Medium sand	-29.82	-33.52	267.70	117616.10	$3.671 \cdot 10^{-4}$	0.444	1.0	1.0	$6.456 \cdot 10^{-5}$	0.2	100	0.9
7-2-EE-MS	Medium sand	-33.52	-37.22	267.70	110943.98	$3.860 \cdot 10^{-4}$	0.444	1.0	1.0	$5.872 \cdot 10^{-5}$	0.2	100	0.9
7-3-EE-MS	Medium sand	-37.22	-40.92	267.70	105292.09	$4.039 \cdot 10^{-4}$	0.444	1.0	1.0	$5.694 \cdot 10^{-5}$	0.2	100	0.9
7-4-EE-MS	Medium sand	-40.92	-44.62	267.70	100424.39	$4.207 \cdot 10^{-4}$	0.444	1.0	1.0	$7.008 \cdot 10^{-5}$	0.2	100	0.9
7-5-EE-MS	Medium sand	-44.62	-48.32	267.70	100424.39	$4.366 \cdot 10^{-4}$	0.444	1.0	1.0	$6.499 \cdot 10^{-5}$	0.2	100	0.9
7-6-EE-MS	Medium sand	-48.32	-52.02	267.70	100424.39	$4.518 \cdot 10^{-4}$	0.444	1.0	1.0	$3.888 \cdot 10^{-5}$	0.2	100	0.9
9-DR-MS	Medium sand	-52.02	-53.82	287.21	101359.62	$5.618 \cdot 10^{-4}$	0.444	1.0	1.0	$3.936 \cdot 10^{-5}$	0.2	100	0.9
10-1-UR-MS	Medium sand	-53.82	-56.82	342.22	103243.44	$5.586 \cdot 10^{-4}$	0.444	1.0	1.0	$3.471 \cdot 10^{-5}$	0.2	100	0.9
10-2-UR-MS	Medium sand	-56.82	-59.82	347.11	103356.13	$5.719 \cdot 10^{-4}$	0.444	1.0	1.0	$3.519 \cdot 10^{-5}$	0.2	100	0.9
10-UR-Clay	Clay	-59.82	-61.42	324.07	68993.64	$5.934 \cdot 10^{-4}$	0.444	1.0	1.0	$1.331 \cdot 10^{-10}$	0.2	100	0.9
10-3-UR-MS	Medium sand	-61.42	-65.22	354.84	103529.10	$5.931 \cdot 10^{-4}$	0.444	1.0	1.0	$4.654 \cdot 10^{-5}$	0.2	100	0.9
10-4-UR-MS	Medium sand	-65.22	-69.02	360.41	103653.49	$6.085 \cdot 10^{-4}$	0.444	1.0	1.0	$4.768 \cdot 10^{-5}$	0.2	100	0.9
10-5-UR-MS	Medium sand	-69.02	-72.82	365.75	103770.94	$6.234 \cdot 10^{-4}$	0.444	1.0	1.0	$4.878 \cdot 10^{-5}$	0.2	100	0.9
10-6-UR-MS	Medium sand	-72.82	-76.62	370.88	103882.19	$6.379 \cdot 10^{-4}$	0.444	1.0	1.0	$4.987 \cdot 10^{-5}$	0.2	100	0.9
10-7-UR-MS	Medium sand	-76.62	-80.52	375.87	103989.00.1	$06.521 \cdot 10^{-4}$	0.444	1.0	1.0	$5.094 \cdot 10^{-5}$	0.2	100	0.9
10-8-UR-MS	Medium sand	-80.52	-84.42	380.74	104092.18	$6.661 \cdot 10^{-4}$	0.444	1.0	1.0	$5.200 \cdot 10^{-5}$	0.2	100	0.9
10-9-UR-MS	Medium sand	-84.42	-88.32	385.45	104190.57	$6.796 \cdot 10^{-4}$	0.444	1.0	1.0	$5.3054 \cdot 10^{-5}$	0.2	100	0.9
10-10-UR-MS	Medium sand	-88.32	-92.22	389.99	104284.59	$6.929 \cdot 10^{-4}$	0.444	1.0	1.0	$5.407 \cdot 10^{-5}$	0.2	100	0.9
SBL	Bedrock	-92.22	-95.22	21.00	21.00	430.00	-	-	-	-	-	-	-

Table 7.7: Soil layer properties at the hypothetical project site (continued)

Chapter 8

1D site response and liquefaction potential analysis

An equivalent one-dimensional *SRA* and *LPA* of the soil profile at a given project site is considered to be a necessary part of the preliminary study for the seismic resistant design of a structure, as site effects will modify the seismic signal which will reach the foundation and could create liquefiable conditions if saturated undrained conditions are present. Depending on the composition of soil layers, site effects involve the filtering, damping or amplification of certain frequencies, which then determine what frequency content of the signal that reaches the structure's foundation. To perform the site response analysis, a comprehensive site and laboratory investigation was needed to determine the physical, mechanical and hydraulic properties of all soil strata, including layers of weathered rock and the base rock layer itself (even beyond it if possible). Given the previously-hypothetical conditions of this project, the site characterisation made use of publicly-available data, as well as a single q_c-profile and borehole, all described in 7.2, which was considered enough to move on to perform the *SRA* and, one of the main objectives of this dissertation, the *LPA*. By the end of this chapter, preliminary conclusions were presented regarding the effect of two PM4Sand calibration methodologies (previously defined in section 7.3 and part II) on the onset of liquefaction in cohesionless layers. 3 methods of liquefaction hazard analysis were described and used to evaluate the presence of liquefied layers, consistent with experimental findings, mentioning the benefits of the proposed evaluation techniques in engineering practice. Lastly, beyond design basis conditions at the potential foundation level were evaluated in order to determine if cliff-edge conditions arose, and a simple comparison between numerically- and semi-empirically-obtained liquefaction hazard safety factors were compared to demonstrate the advantage and necessity of the use of advanced numerical models for the analysis of liquefaction. Overall, this chapter was divided into the following sections.

1. First, an undrained *SRA* without liquefaction analysis was performed using only the HSsmall constitutive model, so as to get a picture of the soil behaviour when subjected to the selected *BDBE* input signal defined in section 7.1.

2. Second, a fully-undrained[1] liquefaction hazard assessment was performed on the 1D model subjected to the Umbria Marhce *BDBE* signal. Here, HSsmall was used for the fine-grained soil layers, and cohesionless layers which did not have any liquefaction hazard, and PM4Sand was used to capture adequate cyclic undrained behaviour in coarse-grained soil layers and identify potentially liquefiable zones using r_u- and γ-based analysis techniques, congruent with findings from parts I and II. However, a lower γ-threshold was used to identify liquefaction triggering, which was explained in section 8.2.

3. Third, numerically-obtained liquefaction hazard results were compared to semi-empirically-obtained ones from 2 methods in terms of safety factors.

8.1 Site response analysis of the 1D soil column using only HSsmall

A 1D-simplified analysis can be performed when the soil layers and the bedrock surface are assumed to be horizontal and to extend to infinity. Additionally, upward-propagating seismic waves need to coincide with the shear waves propagating vertically from the seismic base layer Laera and Brinkgreve (2015a). This is justified by Snell's law of refraction, where successive refraction bend the seismic waves into a nearly vertical path. Therefore, a 1D-simplified model can consist of a slender soil column with the domain width equal to the width of a single finite element, given that appropriate boundary conditions are specified (Laera and Brinkgreve, 2015a).

8.1.1 Modelling conditions

When using Plaxis' dynamic calculation module, two construction stages had to be defined for the *SRA* of the slender soil column. The initial stage, defined with K_0-conditions, established a neutral in-situ stress state based on the provided unit weights, K_0- and OCR-values specified for each layer and the ground water table specified at the borehole level for the model. Suction was ignored and no time step was defined. For the modelling conditions of this stage, normally-fixed boundary conditions were used at the sides of the soil column, whereas fully-fixed and free boundaries were defined for the bottom and the top of the soil column, respectively. The second stage, defined as a fully-undrained dynamic analysis, was set to start from the initial stage and use the pore pressures calculated at the end of the first stage. Given that unaltered in-situ conditions were needed, displacements and small strains were reset to zero. Suction was ignored and a time step equal to the dynamic step time of the input motion was set, which was equal to 0.005. The earthquake input motions were defined as dynamic multipliers so that would be able to be assigned to a horizontal prescribed uniform displacement at the bottom of the *SBL*. The prescribed uniform displacement was multiplied by a factor of 0.5 m, instead of 1 m, so that only upward-propagating stress-waves were be induced in the model. This option essentially halved the input motion in order to account for refraction and reflection. As for the modelling conditions, a compliant-base boundary, in conjunction with a deactivated interface element, was defined for the bottom of the soil column, and tied-degrees-of-freedom boundary conditions were used at the sides, leaving the top of the model free. A compliant-base boundary condition ensures that reflected waves from layers above are absorbed and allows direct application of an input (upward propagating) *ATH* (PLAXIS, 2019a). Tied-degrees-of-freedom essentially connects nodes at either side of the soil columns, ensuring that both boundaries deform in an equal manner. This analysis option can be used for site response analysis as well as for dynamic soil-structure interaction analysis where the model bottom boundary is within a homogeneous layer of soil or bedrock with a high shear wave velocity. At least 1 m of bedrock is recommended, below which the compliant based boundary is applied (PLAXIS, 2019a; Laera and Brinkgreve, 2015b; Laera and Brinkgreve, 2015a). Lastly, the maximum steps and the Newmark α and β dynamic parameters were defined. The maximum number of calculation steps were defined based on the total dynamic time of the earthquake signal as well as the time step interval defined in the dynamic multiplier, which resulted in 2982 for the case of Umbria Marche. As for the dynamic parameters, PLAXIS (2019a) states that α and β can be defined as 0.3025 and 0.6 for a damped Newmark scheme.

[1]The fully-undrained designation was related to the type of dynamic analysis which was performed in Plaxis, as was a partially-drained option available. The latter was not presented, as the partially drained option provided significantly different results in terms of liquefaction hazard.

8.2 1D liquefaction hazard assessment with PM4Sand in Plaxis

Given that great importance was given to the calibration method of the PM4Sand model, this section first compared the effect of *CM1* and *CM2* on the onset of liquefaction at a local level through r_u- and γ-time histories in order to consistently identify liquefied regions based on both markers. Then, the overall liquefaction hazard of the soil column was evaluated in terms of profiles of maximum experienced pore pressures and shear strains, as well *PGA*- and *PGD*-magnitudes. Additionally, an *ATH*-based evaluation was used to complement the identification of liquefied layers in the soil column. For the first part, the soil profile's liquefaction hazard was preliminarily evaluated using *PGA*- and *PGD*-profiles, after which time histories of r_u and γ of all cohesionless layers, 1-NASC-MS, 3-BX-FS, 5-BX-FS and 7-EE-MS, were extracted at 3 locations (top, centre and bottom) from each of their sub-layers (1-3-NASC-MS to 7-5-EE-MS). This level of detail was deemed necessary at an academic level to evaluate the onset of liquefaction and the time-dependent effect of both calibration methodologies. All data extraction points were located as close to the centre of the soil column as possible, which was considered representative of each specific depth due to proper 1D wave propagation, which is explained further in the mesh sensitivity analysis in section 9.1. As far as preliminary expectations went, as demonstrated in part II and the calibration of the layers in section 7.3, some delays in pore pressure evolution in *CM2*-results were expected, relative to the ones from *CM1*. However, given that the PM4Sand model had limitations when modelling the shear strain evolution of dense sands under certain cyclic shearing conditions, it was not clear from the beginning whether *CM1* or *CM2* would yield greater magnitudes for an equivalent induced stress and duration of said stress. Nevertheless, it could already be anticipated that duration would play a major role in the evolution of, above all, post-liquefaction shear strains, which PM4Sand could not adequately model in dense sands. Having said this, the soil column was subjected to the Umbria Marche *BDBE* signal and evaluated both *CM1*- and *CM2*- in simultaneity, in terms of r_u and γ for each layer. Lastly, a modification in the γ-based liquefaction-triggering criterion of 3% had to be made, since practice often shows deformations experienced on-site may not be as large as those shown in laboratory testing. This same concept was applied in a modelling setting, where shear deformations in large domains may not be as large as those seen during single-element testing but could still exhibit flow or near-flow conditions. Therefore, the $\gamma = 3$ threshold was made flexible and a magnitude of $\gamma \geq 2\%$ was used to identify/confirm a liquefaction within the γ-time histories.

8.2.1 Liquefaction hazard in model when subjected to the Umbria Marche *BDBE* signal

This section analysed the triggering of liquefaction in all layers according to the previously established liquefaction-triggering criteria ($r_u = 0.95$ and $\gamma \geq 2\%$). Figure 8.1 provides an overview of the obtained *PGA*- and *PGD*-magnitudes for the *CM1*- and *CM2*-calibrated models after being subjected to the Umbria Marche *BDBE* signal. Contrasting *PGA*- and *PGD*-profiles of the *LPAs* to the ones obtained for the HSsmall-*SRA* was a good way to perform a preliminary assessment of the liquefaction potential of the soil profile, as a clear distinction in acceleration and differential deformation trends was present. For example, when isolating the results from *CM1* and *SRA* in Figure 8.1b, the shift in differential displacements from the cohesive to the cohesionless layers (the latter depicted within the dashed rectangles) was evident, as the soft layers between layers 1-NASC-MS and 3-BX-FS accumulated most of the deformations in the *SRA*, whereas differential deformations almost completely transferred from that location towards liquefied regions within layers 1-NASC-MS and 3-BX-FS, which can be identified by the large *PGD*-differences per depth[1]. Specifically, *PGD*-magnitudes indicated the presence of liquefied regions in sub-layers 3-1- and 3-3-BX-FS for both *CM1* and *CM2*, whereas this was not entirely clear in sub-layers 1-3- and 1-4-NASC-MS for either calibration methodology. When observing Figure 8.1a, greater differences can be observed between *CM1* and *CM2*, as well as

a distinct reduction in *PGA*-magnitudes from layer 7-EE-MS upwards compared to the *SRA* results. Diminution of acceleration magnitudes could be explained due to energy dissipation in liquefied layers, which in turn indirectly affected the upper and lower layers in a post liquefaction setting by filtering reflecting and refracting seismic waves. Furthermore, potentially liquefied regions could be identified by the large dispersion and differences of *PGA*-magnitudes per depth. The *CM1*-response confirmed the liquefaction of sub-layers 3-1- and 3-3-BX-FS but also indicated that layers 1-3- to 1-5-NASC-MS could have liquefied, whereas *CM2*-results only confirmed liquefaction in layer 3-1-BX-FS, leaving layer 3-3-BX-FS unclear. Based on these two data profiles, for both *CM1* and *CM2*, one could preliminarily identify which regions could have in fact liquefied. Nevertheless, a more detailed analysis of r_u- and γ-time histories and profiles was needed to confirm these findings[2].

[1]Figure 8.1b also shows a distinct deviation of deformations starting from sub-layer 7-5-EE-MS upwards between the *LPA* and *SRA* results which was caused due to the implementation of the PM4sand model in the upper cohesionless layers. This showed that the PM4Sand model response in areas which were not prone to liquefy (r_u-values in that region remained below 0.05 and shear deformations were also small) was less stiff compared to that of the HSsmall model.

[2]The following sections will make reference to figures in the Appendix, located at the back of this document. Given that a lot of information is presented, it is advised to view these graphs digitally, as it was at times difficult to fit some graphs within a single A4 page.

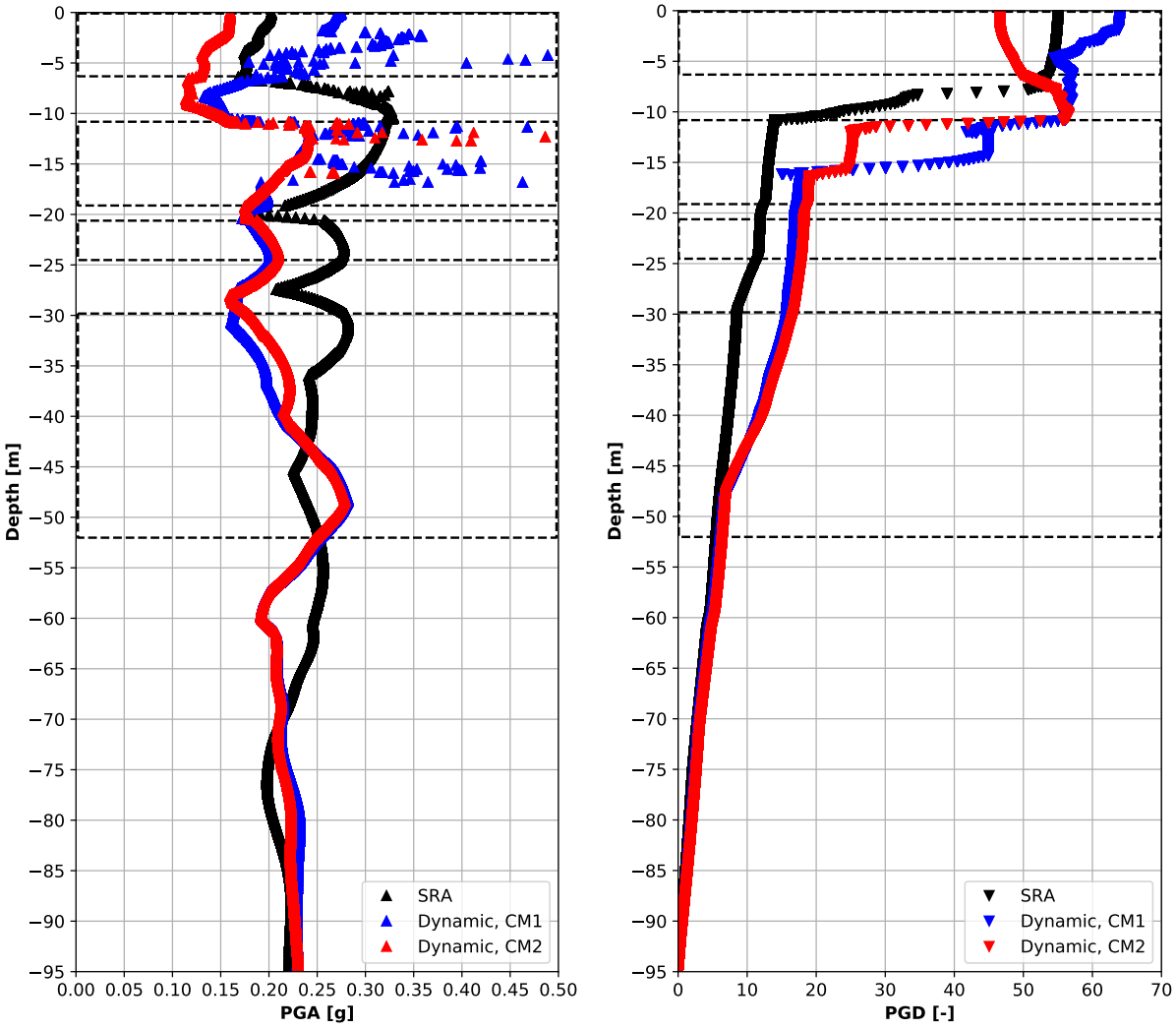

(a) Peak ground acceleration profile

(b) Peak ground displacement profile

Figure 8.1: Comparison of Umbria Marche *BDBE PGA*- and *PGD*-profiles in an *SRA* and *LPA* setting, using both *CM1* and *CM2* to calibrate the PM4Sand layers

Analysis of local r_u and γ time histories

Having preliminarily identified potential regions of liquefaction in layers 1-NASC-MS and 3-BX-FS, it was necessary to further evaluate the evolution of pore pressures and shear strains through r_u- and γ-time histories within these and the rest of the cohesionless layers. Layers 5-BX-MS and 7-EE-MS did not have had a significant risk of liquefaction, but they still were analysed for comparative purposes. When analysing layer 1-NASC-MS, the most relevant parts of the r_u-time histories were comprised within the first 6 seconds both in terms of r_u and γ responses over time, as Figure 8.2 presents (also refer to Figure 10.14 in the Appendix). It can be observed that *CM1* reached liquefaction in terms of r_u in all sub-layers in a progressive manner from shallowest to deepest location, starting at $t \approx 4.40s$ within sub-layer 1-3- and continuing with sub-layers 1-4- and 1-5-NASC-MS at $t \approx 4.80s$ and $t \approx 5.25s$, respectively[3].

[3]The progressive activation of liquefaction from shallowest to deepest was expected, as the calculated CRR-values of the layers increase with depth (in these situations). This behaviour, however, was not present entirely in *CM2*-results, as layer 1-4-NASC-MS reached greater r_u-magnitudes compared to the other sub-layers while having a lower greater CRR than layer 1-3-NASC-MS.

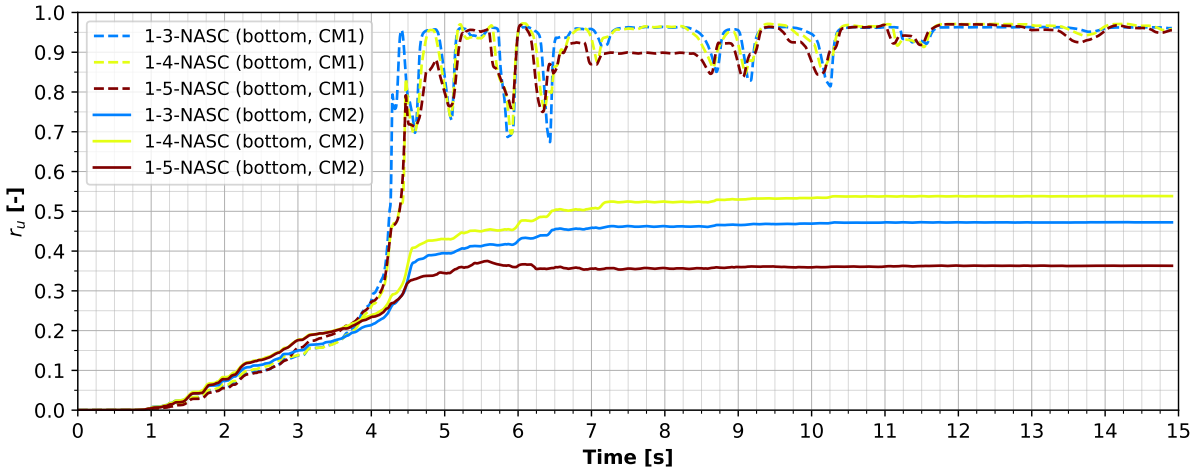

(a) r_u-evolution in all sub-layers of 1-NASC-MS

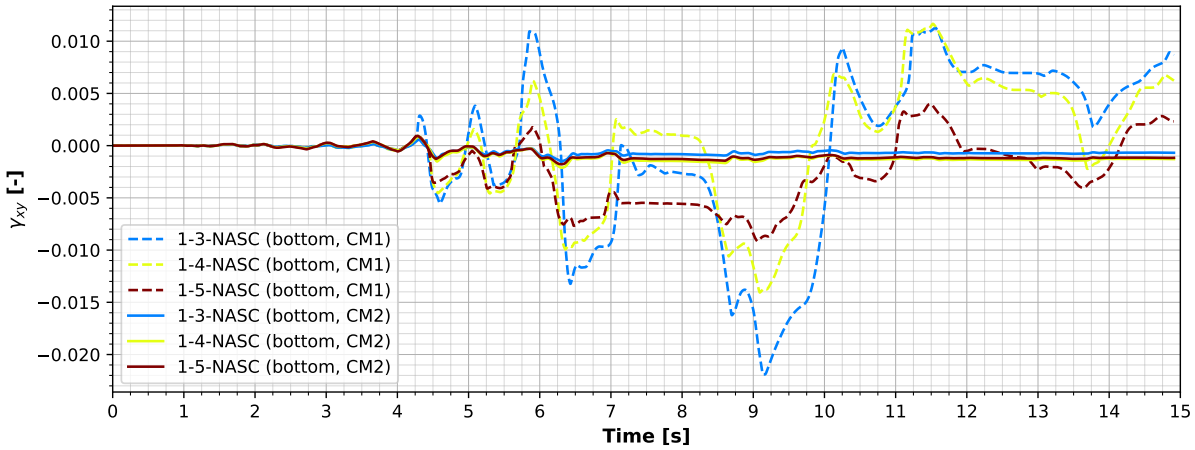

(b) γ-evolution in all sub-layers of 1-NASC-MS

Figure 8.2: r_u- and γ-time histories responses to the Umbria Marche *BDBE* signal at select points within layer 1-NASC-MS.

However, when analysing evolution of shear strains, one could observe that neither of the three sub-layers surpassed the $\gamma \geq 2\%$ threshold defined for the evaluation of liquefaction-triggering at approximately the same moment. Only layer 1-3-NASC-MS exceeded the 2%-mark, but at $t \approx 9.15s$, creating a $4.75s$-difference between the triggering of liquefaction based on r_u and γ, which was more than a 100% increase of the time it took for the model to activate the $r_u = 0.95$ marker. This difference was attributed to the earlier activation of $r_u = 0.95$ defined during the calibration of the sub-layer in section 7.3 (specifically, there was a 11.75-cycle difference), which caused the premature activation of the r_u-marker and created the inconsistency in the triggering of liquefaction for the *CM1*-results. In contrast, when observing the r_u- and γ-evolution over time of *CM2*, it can be evidenced that neither of the three sub-layers reached liquefaction conditions, and only maximum values of $r_u \approx 0.55$ and $\gamma \approx 0.25\%$ were reached within sub-layer 1-4-NASC-MS. This contrast in behaviour was expected, as the difference between the triggering of the r_u- and γ-markers was considerably smaller compared to *CM1* (1.75 cycles). This allowed *CM2* to maintain consistency in its results, unlike *CM1*, which inconsistency between r_u- and γ-time histories was not acceptable. Having said this, it must be concluded that, according to the established evaluation procedure, *CM1*-results were not consistent in identifying liquefaction in layer 1-NASC-MS, whereas *CM2* was consistent in discarding it, as both r_u- and γ-values in the latter remained below the established thresholds. Therefore, liquefaction, at the local level

in layer 1-NASC-MS, was discarded, even though there was still a moderate liquefaction risk present in the latter case (given that r_u-magnitudes reached up to 0.55).

Sub-layer	Location	Model	t to $r_u = 0.95$ [s]	t to $\gamma \geq 2\%$ [s]	Δt [s]
3-1-BX-FS	Top	CM1	4.80	5.75	0.90
		CM2	5.15	5.55	0.40
	Centre	CM1	5.15	5.75	0.60
		CM2	5.15*	6.85	1.70*
	Bottom	CM1	7.10	8.50	2.40
		CM2	6.10*	9.10	3.00*
3-3-BX-FS	Top	CM1	6.00	10.90	4.90
		CM2	-	-	-
	Centre	CM1	5.95	9.75	3.80
		CM2	13.75	-	-
	Bottom	CM1	5.90	9.30	3.40
		CM2	7.30	8.30	1.00

Table 8.1: Activation times of r_u- and γ-based liquefaction triggering criteria in layer 3-BX-FS in models *CM1* and *CM2* for Umbria Marche *BDBE* scenario (layers 3-2- and 3-4-BX-FS did not exhibit liquefaction)

Next, Figures 8.3 and 8.4 (also refer to Figure 10.15 in the Appendix) present select r_u- and γ-time histories of all sub-layers within 3-BX-FS for ease of inspection. In the case of *CM1*, all locations within sub-layers 3-1- and 3-3-BX-FS triggered liquefaction, whereas locations within layers 3-2- and 3-4-BX-FS only reached magnitudes of $r_u \leq 0.65$. All these trends were repeated in results *CM2*, with the exception of the top of sub-layer 3-3-BX-FS. Figure 8.3 shows the critical locations in sub-layers 3-1- and 3-2-BX-FS where very close proximity between *CM1* and *CM2* results can be observed, with the expected delay in pore pressure evolution in *CM2*-results compared to *CM1*. The top of layer 3-1-BX-FS triggered liquefaction at $t \approx 4.80s$ and $t \approx 5.15s$ in *CM1* and *CM2*, respectively, describing a remarkably similar behaviour of PM4Sand given the two calibrated parameter sets, whereas *CM2* results at the bottom of layer 3-1-BX-FS triggered liquefaction before *CM1* (at $t \approx 6.15s$ compared to $t \approx 7.10s$), in addition to reaching r_u-magnitudes above 1.0, which was not expected. The rise of r_u-magnitudes above 1.0 could be explained, according to (Idriss and Boulanger, 2008) due to an increase in mean total stress, which indirectly increased the presence of pore pressures in the analysed location, a phenomenon which can occur under general loading conditions in numerical models[4]. This in turn could explain the earlier activation of the $r_u = 0.95$ marker in *CM2*, as the curve shape was still very similar to that of *CM1*, with no apparent phase. Furthermore, a slight delay in pore pressure evolution was experienced at the bottom of 3-1-BX-FS, relative to the top, which could be explained due to the indirect influence of the larger cyclic resistance of layer 3-2-BX-FS, which did not develop significant r_u-magnitudes (approximately 0.3 and 0.18 for *CM1* and *CM2* respectively). However, this situation would involve the partial dissipation of pore pressures to adjacent regions, which cannot be confirmed given the fully-undrained analysis type used for this part[5]. Lastly, the centre of layer 3-1-BX-FS activated marker $r_u = 0.95$ at approximately the same time as in the top and also exhibited r_u-magnitudes larger than 1.0 in the case of *CM2*, whereas r_u-values in *CM1* remained below or at $r_u = 1.0$.

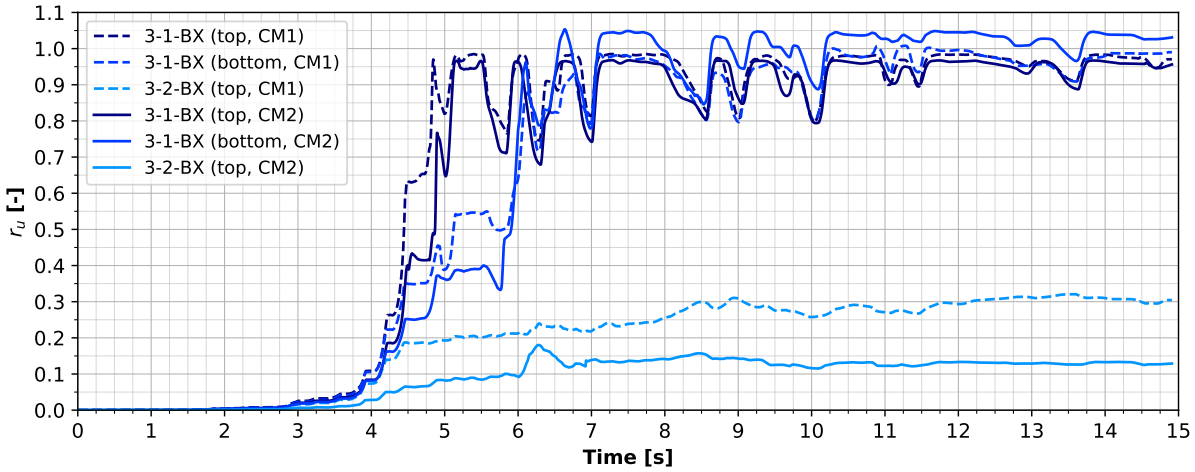

(a) r_u-evolution in sub-layers 3-1 and 3-2 of 3-BX-FS

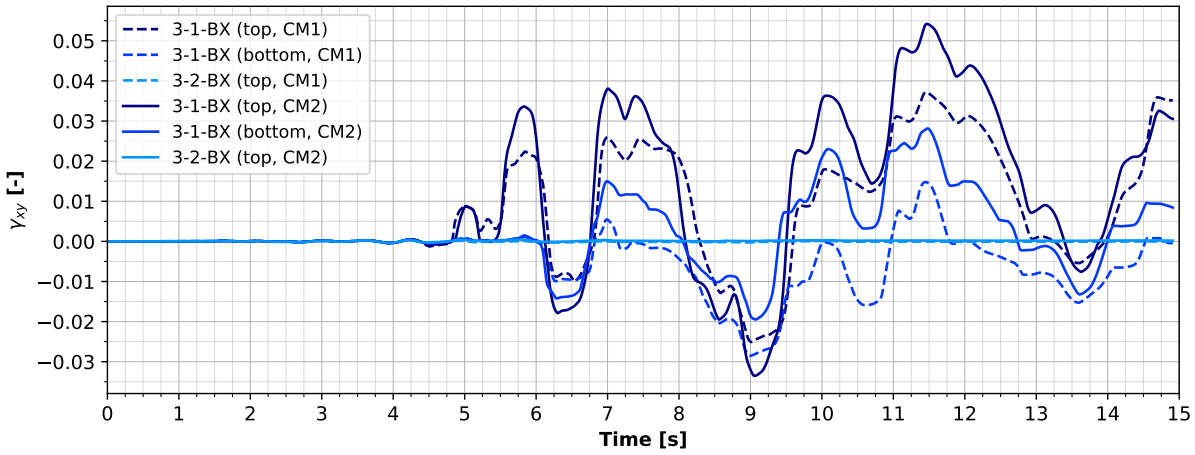

(b) γ-evolution in sub-layers 3-1 and 3-2 of 3-BX-FS

Figure 8.3: r_u- and γ-time histories responses to the Umbria Marche *BDBE* signal at select points within layer 3-BX-FS.

When contrasting the r_u-time histories with the γ-evolution of the same layers, *CM2*-results exhibited larger accumulation of shear strains compared to *CM1*, reaching differences of up to 2% in post-liquefaction. Both *CM1* and *CM2* passed the 2% γ-threshold after approximately 5.6 seconds ($t \approx 5.75s$ and $t \approx 5.55s$, respectively) at he top of layer 3-1-BX-FS, whereas at the bottom of 3-1-BX-FS, *CM1* triggered liquefaction slightly earlier than *CM2*, at $t \approx 8.50s$ and $t \approx 9.10s$[6], respectively. The r_u- and γ-triggering moments at the top of layer 3-1-BX-FS for both calibration methodologies were consistent, as there were only slight time differences present. As for at the bottom of layer 3-1-BX-FS, both *CM1* and *CM2* experienced a 2-second-delay between the activation of $r_u = 0.95$ and $\gamma = 2\%$, which was still considered acceptable given the slight differences in marker activation times specified at the end of chapter 3. This lead to the confirmation of liquefaction of the entirety of sub-layer 3-1-BX-FS, confirmed by both *CM1* and *CM2*. As for the rest of layer 3-BX-FS, Figure 8.4 presents the r_u- and γ-time histories of sub-layers 3-3- and 3-4-BX-FS. Here, r_u *CM1*-results indicated that all locations in layer 3-3-BX-FS triggered liquefaction approximately 6 seconds after the start of the signal ($t \approx 6.00s$, $t \approx 5.95$, and $t \approx 5.90$, respectively), whereas layer 3-4-BX-FS reached a maximum magnitude of $r_{u,max} \approx 0.55$. As for the *CM2* model, results showed distinct deviations from those of *CM1*, reaching only $r_{u,max} \approx 0.07$ in layer 3-4-BX-FS, discarding liquefaction at the top of layer 3-3-BX-FS and delaying the accumulation of pore pressures for both the centre and

bottom of layer 3-3-BX-FS. In the former case, the triggering of $r_u = 0.95$ occurred $13.75s$ into the response, whereas the latter activated the marker at $t \approx 7.30s$. In contrast with layer 3-1-BX-FS, *CM1* and *CM2* did vary significantly from each other, which was caused by the higher D_{R0}-values compared to layer 3-1-BX-FS.

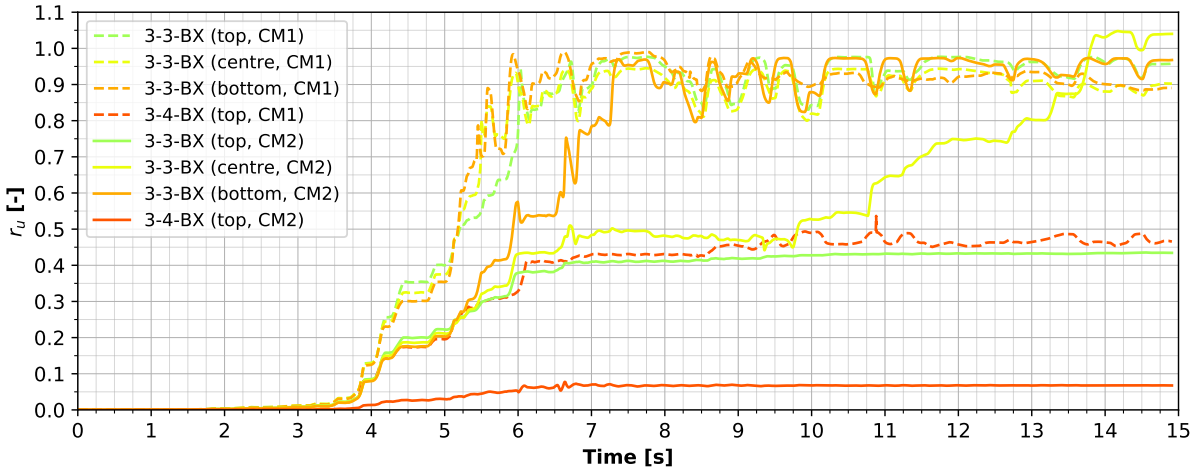

(a) r_u-evolution in sub-layers 3-3 and 3-4 of 3-BX-FS

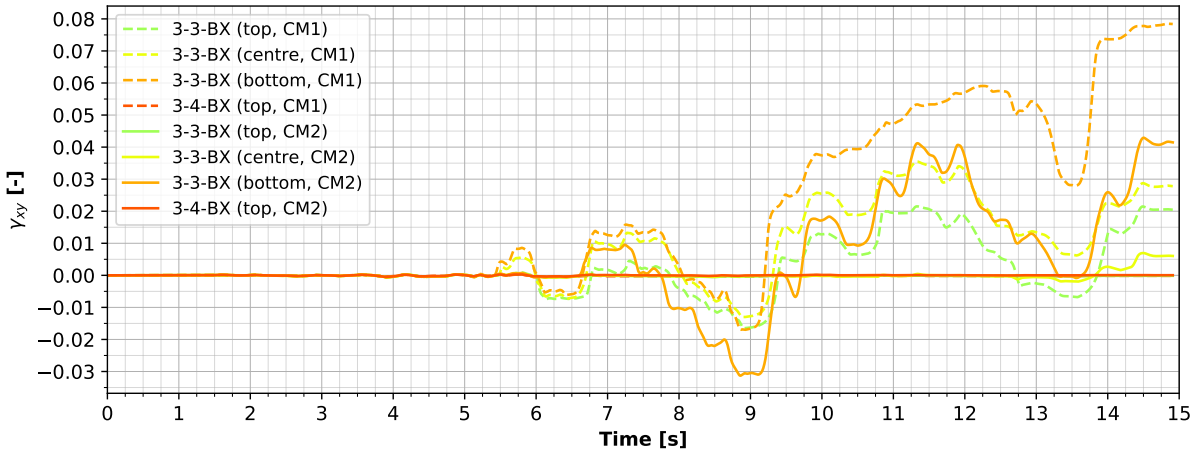

(b) γ-evolution in sub-layers 3-3 and 3-4 of 3-BX-FS

Figure 8.4: r_u- and γ-time histories responses to the Umbria Marche *BDBE* signal at select points within layer 3-BX-FS (continued).

Furthermore, when analysing the evolution of shear strains, *CM1* accumulated greater overall deformations, passing the 2% threshold after approximately $10.90s$, $9.75s$ and $9.30s$, at the top, centre and bottom of layer 3-3-BX-FS. As for *CM2*, the top of layer 3-3-BX-FS only accumulated very small shear strains, the bottom triggered liquefaction after approximately $8.30s$ and the centre only accumulated 0.5% shear strains before the end of shaking. When contrasting the triggering moments based on r_u and γ, *CM1* did not exhibit compatibility between their calibrated liquefaction-triggering criteria, as time differences oscillated between $3.40s$ and $4.90s$. In the case of the bottom of layer 3-3-BX-FS, *CM2* did exhibit compatibility in terms of r_u and γ, maintaining only a small difference in time between the activation of markers. In the case of layer 3-4-BX-FS, both *CM1* and *CM2* coincided with their r_u-counterparts and discarded liquefaction. Overall, it was concluded that sub-layers 3-2- and 3-4-BX-FS had no significant liquefaction risk, while layer 3-1- and 3-3-BX-FS exhibited complete and partial liquefaction, respectively. Here the *CM2* model managed to identify liquefaction maintaining coherence between r_u- and γ liquefaction markers in most cases. In some instances, apparent increases in mean total stress (p),

which also caused r_u-magnitudes > 1.0 in the r_u-curves, indirectly accelerated the increase in pore pressures, triggering the $r_u = 0.95$ marker earlier than expected (see entries with asterisked values in Table 8.1) and affecting the consistency between the activation of the r_u- and γ-markers.

Lastly, layers 5-BX-MS and 7-EE-MS Figures 8.5 and 8.6 show the r_u- and γ-time histories of both *CM1* and *CM2* at a modified scale, as the pore pressures and shear strains developed were very low. Model parameters for *CM1* and *CM2* in layer 5-BX-MS were still different, so a clear delay in pore pressure accumulation was visible, as well as lower magnitudes in *CM2*-results. However, given that layer 5-BX-MS had a very high cyclic resistance, differences in total experienced pore pressures and shear strains between *CM1* and *CM2* were minimal. Differences in layer 7-EE-MS were even smaller, but for different reasons. Given that *CM1* and *CM2* model parameters were the same in this layer (see Table 7.1), the responses should have been exactly the same. However, since the upper layers behaved differently due to variations in calibration methodology, layer 7-EE-MS was indirectly affected, causing minor deviations from each other.

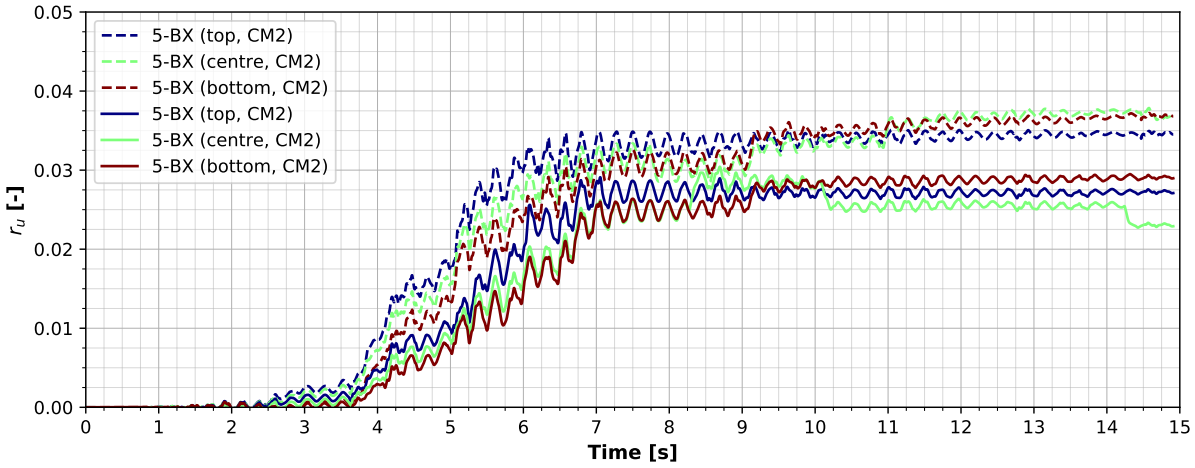

(a) r_u-evolution in all sub-layers of 5-BX-MS

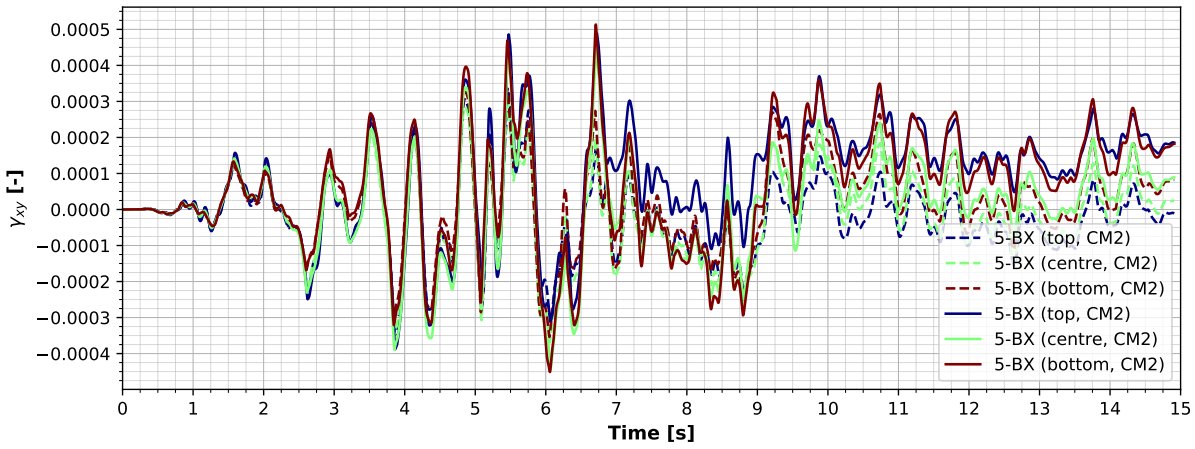

(b) γ-evolution in all sub-layers of 5-BX-MS

Figure 8.5: r_u- and γ-time histories responses to the Umbria Marche *BDBE* signal at select points within layer 5-BX-MS.

[4]In cases like these, Idriss and Boulanger suggest that analysis should shift focus to σ'_v rather than r_u. This however was not included in the evaluation due to time constraints.

[5]Further research could help determine the validity of this suggested explanation.

[6]As mentioned earlier, instances where the threshold was not reached by a very low difference were considered to have been practically-reached. Here, shear strains reached 1.95%, which was considered close enough.

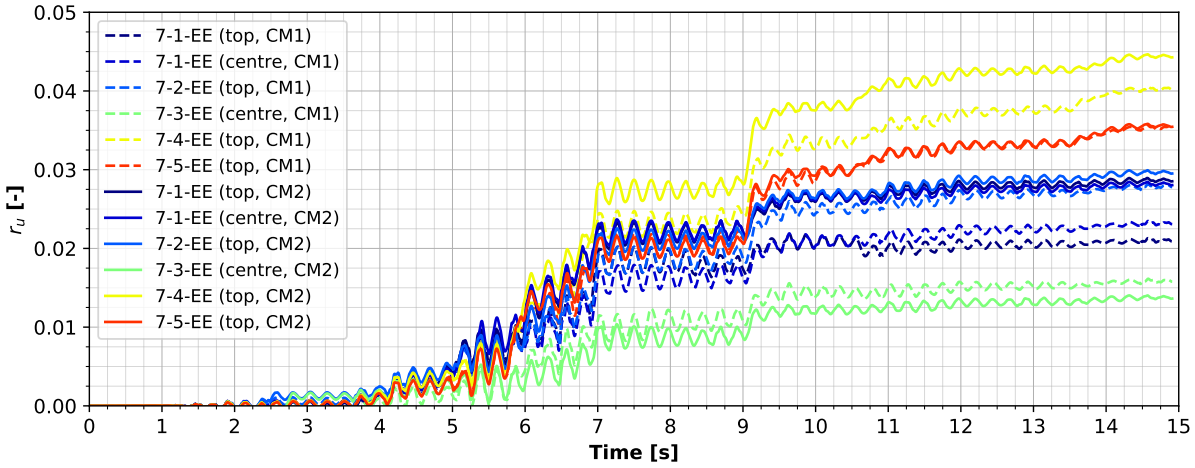

(a) r_u-evolution in all sub-layers of 7-EE-MS

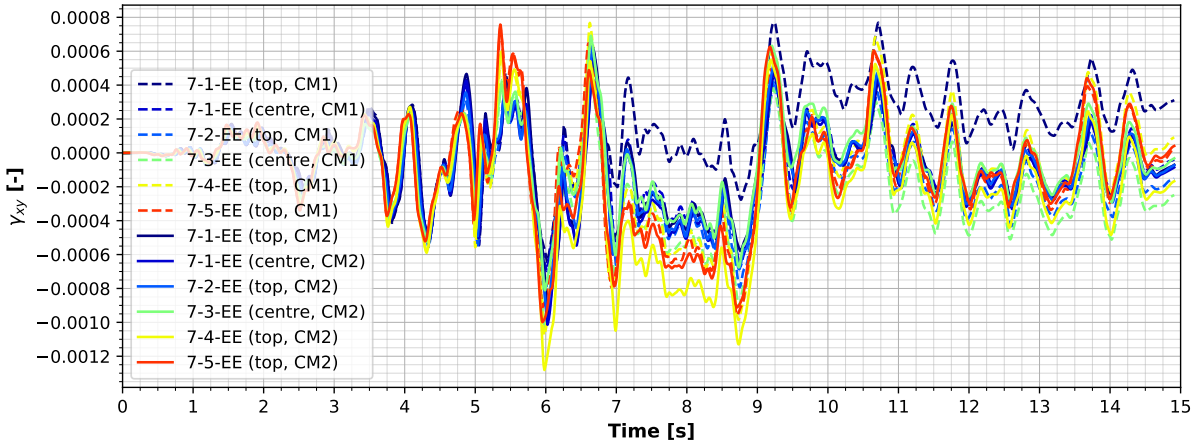

(b) γ-evolution in all sub-layers of 7-EE-MS

Figure 8.6: r_u- and γ-time histories responses to the Umbria Marche *BDBE* signal at select points within layer 7-EE-MS.

Analysis of overall $r_{u,max}$- and γ-profiles and *ATHs*

Having identified liquefaction in layers 3-1-BX-FS and 3-3-BX-FS through the local r_u- and γ-time histories, it was deemed necessary to complement the liquefaction hazard evaluation through $r_{u,max}$- and γ-profiles of the entire soil column, as well as with an alternative approach using *ATHs* at the local level, after recommendations from Kramer (1996) and Kramer et al. (2016). The use of profiles of specific data was very useful as it provides maximum experienced results in the model, which were relevant for the liquefaction potential analysis performed, as well as continuous data over depth which could show areas of potential liquefaction the local time-history analysis may have missed. For the case of Umbria Marche, Figure 8.7 presents the maximum experienced pore pressure ratios ($r_{u,max}$) and shear strains over depth for both *CM1* and *CM2* up to a depth of -52 m (relative to the model surface at 0.0 m). Basing the evaluation on the previously-established liquefaction-triggering criteria ($r_u = 0.95$ and $\gamma \geq 2\%$), the data profiles provided further confirmation of the lack of liquefied regions in layer 1-NASC-MS, as γ-magnitudes in both *CM1* and *CM2* remained below approximately 1.5%. Also, previously-found inconsistencies between the activation of r_u- and γ-markers were easily visible, such as in the *CM1*-results in layer 1-NASC-MS, where $r_{u,max}$-values reached magnitudes close to 1.0, whereas shear strain magnitudes were not large enough to establish a liquefied state. In turn, liquefaction was confirmed in layers 3-1- and 3-3-BX-FS, where maximum experienced r_u- and γ-magnitudes

did in fact surpass the established thresholds for liquefaction triggering, both in the *CM1* and *CM2* models.

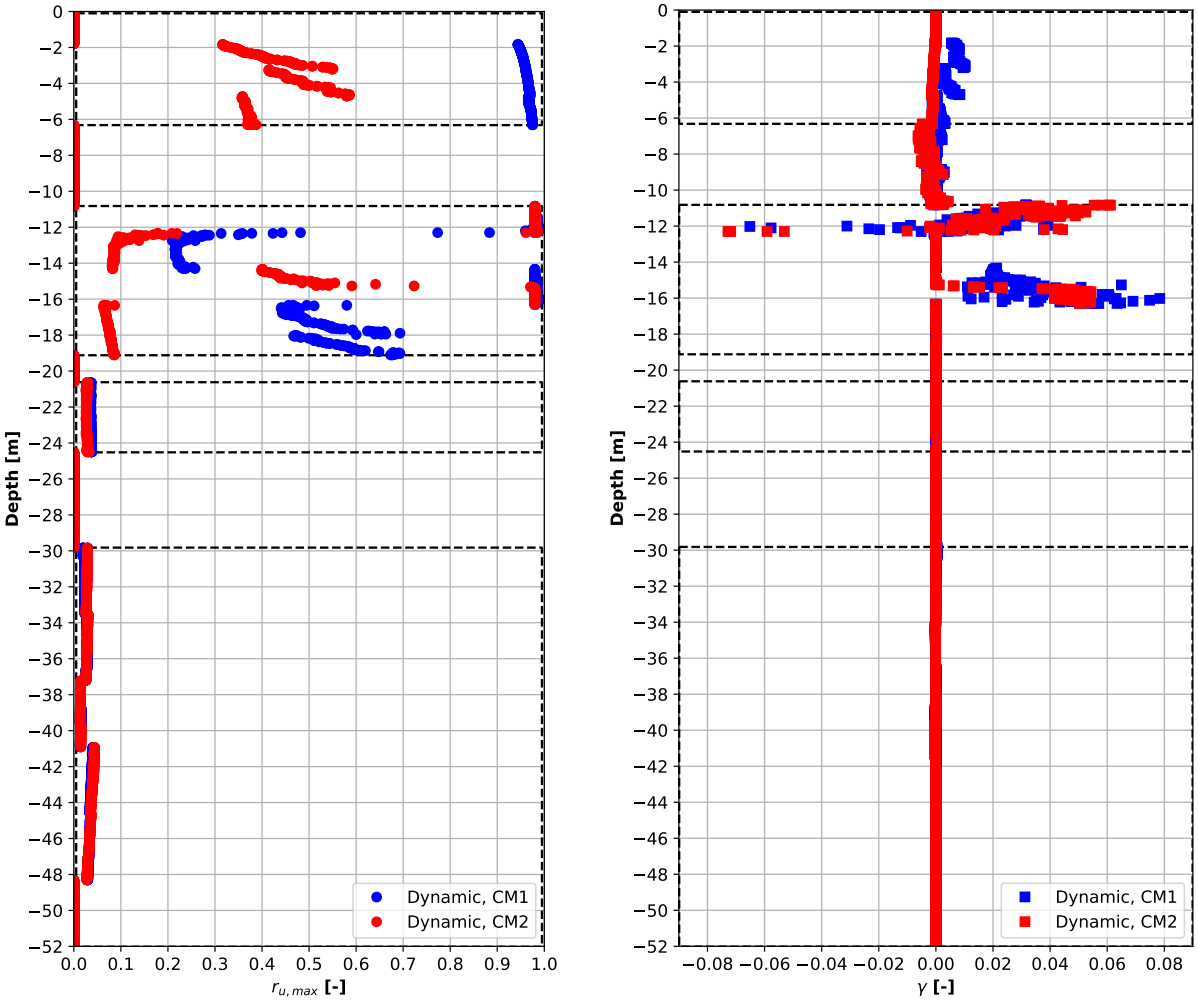

(a) $r_{u,max}$-profile

(b) γ-profile

Figure 8.7: Comparison of Umbria Marche *BDBE* $r_{u,max}$- and γ- profiles of *CM1* and *CM2* models

Lastly, as a final complementary method to identify liquefaction, was the method proposed in Kramer (1996) and Kramer et al. (2016), which uses *ATHs* and frequency content at the local level to identify potentially liquefied soil profiles. Given that *ATHs* are sensitive to filtering by soil deposits adjacent to the one that is being analysed, it was important to analyse the *ATHs* by starting from the deepest to the shallowest layer. That way, progressive deterioration of the frequency content of the signal can be distinguished from potential liquefaction effects. In the case of a numerical modelling setting, the best way to tackle this part of the analysis was to compare the *ATHs* of the *SRA* with those of the *LPA*, where the moment of liquefaction triggering could be identified. The presence of a liquefied layer could be identified by a distinct lack of high frequencies in the *LPA* signal, in contrast to the *SRA's* and by the appearance of phases between the *LPA* and *SRA ATHs*. However, one important aspect that needed consideration was that the *ATH* of a specific layer would always be influenced by the soil deposits beneath it. This meant that, if soft or liquefied soil deposits were present beneath the analysed layer, the *ATH* would indirectly inherit said properties, as the dynamic behaviour of a specific layer was indirectly dependent on the deformability of the inferior layers. Having said this, and for illustrative

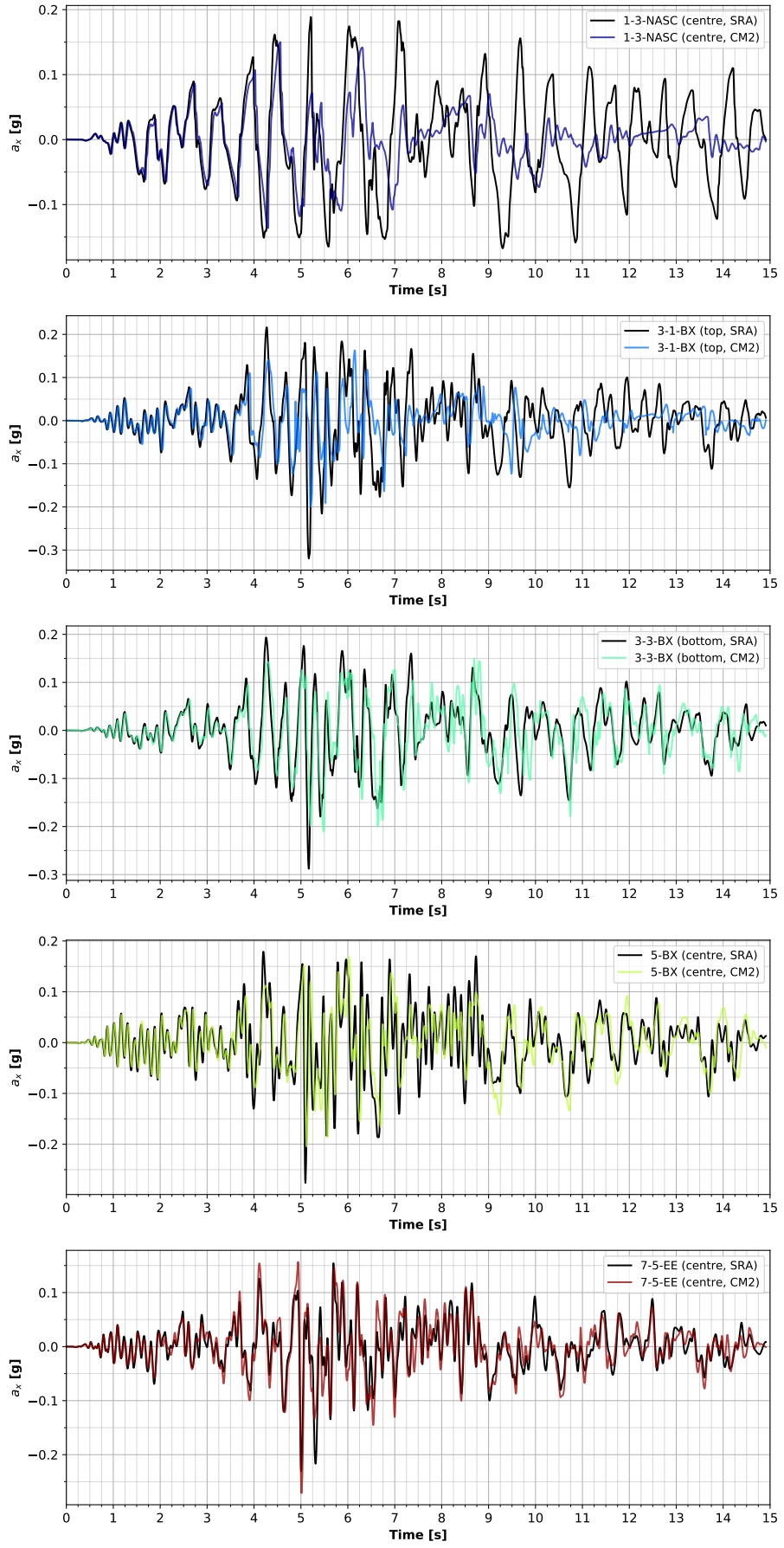

Figure 8.8: Comparison of Umbria Marche *BDBE SRA* and *LPA-CM2* acceleration time histories at select locations along depth

purposes in the case of Umbria Marche, Figure 8.8 shows the comparison of *LPA-CM2* and *SRA* acceleration time histories in layers 1-3-NASC-MS, 3-1-, 3-3-BX-FS, 5-BX-MS and 7-5-EE-MS (for a more detailed view of the Umbria Marche *BDBE ATHs* refer to Figures 10.22 through 10.27 in the Appendix). If one were to look at these signals from the bottom upwards, a distinct deterioration of the signals over depth could be observed. Layers 7-5-EE-MS and 5-BX-MS show some diminution and amplification of certain acceleration peaks, effect which was more evident in layer 5-BX-MS, as more soil layers below it were active compared to 7-5-EE-MS. Moving upward to layer 3-3-BX-MS, the *LPA-ATH* started to exhibit a distinct shift compared to the *SRA*'s *ATH*, which started approximately $14.5s$ into the response. This moment in time was consistent with the liquefaction-triggering findings based on r_u- and γ-time histories at the same location. Moving up along the soil profile, the upper parts of layer 3-3-BX-FS exhibited greater shifts in their *ATHs*, which were further increased within layer 3-1-BX-FS, which had liquefied in its entirety. Here, the phase between the two *ATHs* was evident from $t \approx 6.25s$ onwards, showing also some frequency filtering, as well as greater reductions in amplitude. Additionally, the approximate time of the start of deterioration of the *ATH* signal at $6.5s$ was very close to the r_u- and γ-based triggering of liquefaction found previously in the same layer (see Table 8.1). Lastly, moving up towards the surface layers, the *LPA-ATH* showed a very deteriorated shape in comparison to the *SRA-ATH*. However, given that no liquefaction was found in those layers, the deterioration of the *ATH* signal was attributed to the effect of the inferior soft and liquefied layers.

8.3 Comparison of numerical and semi-empirical liquefaction hazard assessment results

As mentioned in earlier sections, one of the important parts of this dissertation was to compare the numerically-obtained results to ones calculated through the semi-empirical method proposed by Idriss and Boulanger (2014). This part was particularly relevant for practical, not only academic, engineering design purposes, as it compared optimised numerical results with traditional methods of liquefaction hazard assessment. To be able to compare both results, it was assumed that the $r_{u,max}$-results could be equivalent to an overall safety factor of liquefaction. Considering the emphasis that this dissertation put on evaluating liquefaction based on both pore pressures and shear strains, assuming that $r_{u,max}$ could be used as a safety factor meant that it could adequately represent overall liquefaction, which in turn meant that it would need to be consistent with the experienced shear strains. This was not an issue for *CM2*, was it was evidenced that the calibration method could consistently identify liquefaction. However, *CM1* did not have this condition in certain layers. Therefore, given that this part of the dissertation was for comparative purposes only, an exception was made for the sake of comparison, but greater importance is given to results from *CM2*. Having said this, the transformation to safety factors from $r_{u,max}$ was performed considering the limits $r_u = 0$ and $r_u = 1$ equal to $SF = 2$ and $SF = 1$, respectively, where transformed safety factors of 1.0 or very close to 1 were considered to have liquefied. As for the calculation of the semi-empirical safety factors, the simplified method by Seed and Idriss (1971) was selected to estimate an equivalent *CSR* and the method from Idriss and Boulanger (2014), the same as used for the calibration, was employed to estimate the *CRR*-profile (see section 7.2.5. Figure 8.9 shows the comparison of numerically- and semi-empirically-obtained safety factors and it can be observed that the numerical model significantly reduced the liquefaction hazard of the site whereas Idriss and Boulanger's correlation indicated almost complete liquefaction throughout all cohesionless layers (within dashed rectangles). This was proof of the advantage that numerical tools bring to the table, as they allow the inclusion of many more parameters and design conditions than semi-empirical methods use. With the proper calibration of the PM4Sand model, greater insight can be provided on the liquefaction hazard in a given soil profile.

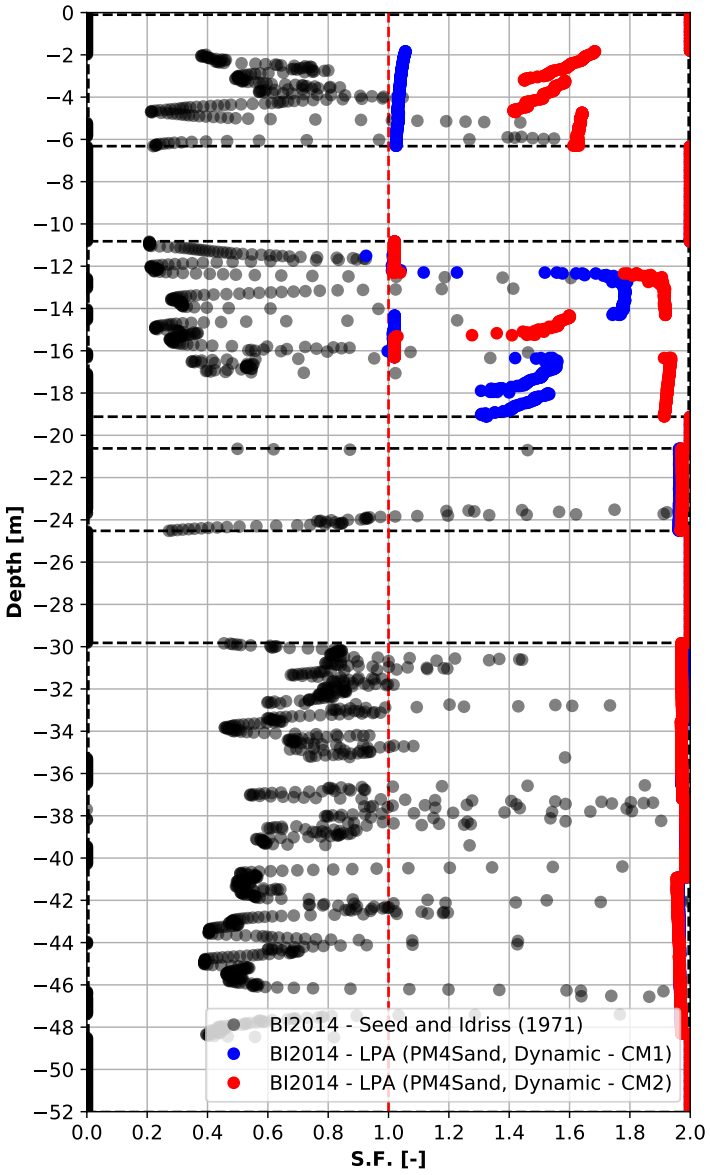

Figure 8.9: Comparison of semi-empirically-calculated and numerically-calculated safety factors against liquefaction using *CRR*-values calculated with method proposed by Idriss and Boulanger (2014).

8.4 Discussion and preliminary conclusions regarding the liquefaction potential analysis in a 1D setting

- Based on the comparison of *PGD*-responses of *SRA* and *LPA* results, the HSsmall model behaves in a stiffer manner compared to the PM4sand model in regions were liquefaction hazard is non-existent. This could be explained by the formulation of the PM4Sand model, which allows the soil's shear modulus to have hysteretic behaviour. Both models allow for shear modulus degradation, but this degradation was greater in the PM4sand response.

- The presence of liquefied layers can indirectly affect the maximum experienced acceleration values below and above the compromised region. Specifically, the presence of liquefied layers allows for the dissipation of energy through deformation and filters reflecting and refracting seismic waves, tending to indirectly reduce experienced accelerations in layers which are still structurally sound.

- Potentially liquefied regions can be preliminarily identified by highly dispersed data points when observing the *PGA*- and *PGD*-profiles of a soil column. These findings, however, need to be confirmed by r_u- and γ-data.

- In the case of Umbria Marche, experienced delays in pore pressure accumulation at the bottom of layer 3-1-BX-FS, compared to the top, could be explained due to pore pressure dissipation into the top of layer 3-2-BX-FS, which had accumulated lower pore pressures. This hypothesis, however, needs to be confirmed by future research.

- The time-history analyses of r_u and γ proved useful in showing the effectiveness of calibration methodology *CM2*in dense and shallow layers, where consistency between r_u- and γ-based liquefaction triggers was achieved compared to the literature-proposed *CM1*.

- The combined use of $r_{u,max}$- and γ-profiles was crucial to conclusively identify liquefied regions. Time-histories at specific points were of great use as well, but were considered more of an academic tool to evaluate how the pore pressures and shear strains evolve during the seismic response, as they provided a lot of extra information which was not needed if one only wished to determine if the soil had liquefied. Of course, this conclusion was only valid as long as the calibration parameters are sound and the model behaves in a consistent manner. Otherwise, profiles could be insufficient to properly identify liquefied regions and time-histories may be needed after all.

- The use of *ATHs* at specific depths in liquefaction hazard assessment and liquefaction-triggering analysis was a valid tool, as the signals identified potential liquefaction regions through a deteriorated *ATH* in contrast to that obtained in the *SRA*. However, conclusions regarding potentially liquefied layers could only be considered as preliminary, since the filtering, amplification or diminution of the original *SRA-ATH* could also be explained by the presence of very soft deposits, such as those found beneath layer 1-NASC-MS.

- Purely semi-empirical liquefaction hazard assessment methods predicted that most the cohesionless layers, be them shallow or deep, would liquefy if subjected to either *BDBE* signal. However, a preliminary comparison using a stress-profile from performed *SRAs* drastically reduced that liquefaction risk, although it was still considered quite conservative.

- PM4Sand is able to adequately identify locations were layers have incurred in liquefaction.

- Preliminary liquefied areas could be identified from the *PGA*- and *PGD*-profile of the soil columns.

- The numerical liquefaction hazard assessment performed using PM4Sand drastically reduced the liquefaction risk of the overall profile compared to semi-empirical methods, pinpointing locations where pore pressures did induce liquefaction. Although this method still could have things that need to be improved, its results greatly underlines the perks related to using numerical tools to analyse liquefaction potential in a 1D setting.

- When subjected to the Umbria Marche *BDBE* signal under fully-undrained conditions, the 1D model calibrated with *CM1* exhibited liquefaction in all 1-NASC layers, as well as layers 3-1- and 3-3-BX-FS, whereas with calibration methodology *CM2*, only layers 3-1- and 3-3-BX-FS reached liquefaction. This was expected, as the recalibration of D_{R0} and h_{p0} caused pore pressure evolution to be delayed in comparison to *CM1*. Given this, it could be argued that, based on the used liquefaction-triggering criteria for calibration, the results obtained with *CM2* had more validity, as both r_u- and γ-based evaluation procedures described did not identify liquefaction in any other layer besides those two.

- The time differences between the activation of liquefaction-triggering criteria within a liquefied layer decreased in model *CM2*, relative to *CM1*, and had a more consistent onset of liquefaction in terms of affinity to experimental observations.
- Given the layers which experienced liquefaction during the Umbria Marche signal, it was decided that the structure's foundation, for the 2D liquefaction hazard analysis, would be located at the top of layer 5-BX-MS, since itself and no layer beneath it experienced significant pore pressure or shear strain build-up, discarding a cliff-edge scenario.
- *CM2* had some side effects in layers with low to intermediate overburden pressure which experienced liquefaction, which was that excessive shear strains developed.
- The effect of *CM1* and *CM2* on cyclic resistance of upper layers had an indirect influence on the behaviour of deeper layers, where parameter sets were equal for *CM1* and *CM2*. This small influence caused the responses from both calibration methodologies at all locations in layer 7-EE-MS to vary slightly, variations which increased with decreasing cyclic resistance the sub-layer was calibrated at.
- The presence of plateaus in terms of r_u-evolution in specific sub-layers was caused by a reduction of induced stresses due to a deeper layer which had started to liquefy around the same time of the start of the plateau. Specifically, the transmission of seismic waves through that deeper liquefied layer was compromised, causing the accumulation of pore pressures in the upper layers to halt. The same was observed in γ-evolution graphs.
- r_u-time histories which show magnitudes greater than 1.0 can be explained by increases in mean total pressure, which indirectly increases pore pressures in the given location (Idriss and Boulanger, 2008).
- Additionally, this phenomenon is also observed when comparing the *SRA* and *LPA* responses in a specific sub-layer between in terms of *ATHs*.

Chapter 9

2D liquefaction hazard

A very important aspect of any liquefaction hazard assessment is the link between the in-situ liquefaction hazard of the soil profile, related to a structure-free domain, and the liquefaction hazard that is experienced by the soil profile with the presence of a structure. Semi-empirical liquefaction correlations cannot account for such interactions, as they only consider basic and intrinsic soil properties and information related to the input signal to make an assessment. When numerical models are implemented at the design stage, usually only a *SRA* or a 1D-*LPA*, like the ones in chapter 8 are implemented to evaluate the liquefaction hazard of the site and little has been found regarding the effect of the presence of a structure on the immediate liquefaction hazard in the soil relative to the hazard of the half-space conditions of the domain itself. Mostly, 2D soil-structure interaction models which analysed liquefaction were aimed at solely evaluating the effect of liquefaction on the structure in a post-earthquake setting and contrasting the model's results to measured values in an effort to validate the implemented constitutive model in an academic setting. However, it has yet to be established how changes in liquefaction hazard due to soil-structure interactions should be implemented as modifications at the design stage. Therefore, this chapter's main objective was to analyse how the presence of a structure influences the free-field liquefaction hazard of a soil profile and how that change can be helpful in improving the seismic design of the entire soil-structure system in a qualitative way. Along the way to answering this main question, additional sub-questions appeared related to the effects of mesh and domain size increases when transitioning from a 1D to a 2D setting and if structural load variations generated any distinct changes in liquefaction hazard. These questions were answered in the following paragraphs.

Given that the design philosophy implemented in this dissertation was related to the design of a critical facility (see section 7.1), and that the scope of the dissertation was focused on the effects of soil-structure interaction on the liquefaction hazard of the soil profile, and not on the said effects on the integrity of the structure, a simple rectangular structure with a shallow foundation at the top of layer 5-BX-MS was assumed. The structure was modelled in Plaxis as a 2D elastic and non-porous soil polygon assuming a $40x40$ m base with a rooftop at 20 m above surface, giving a total height of 40.62 m from foundation to rooftop. A nominal load of 640 MN, considering was assumed, which considered dead and live loads of the structure. On the same note, for the evaluation of structural load variation effects on the liquefaction hazard, the design loads were increased to 705 and 750 MN, which was considered to include quasi permanent loads and static and live loads of mechanical equipment. As for the mechanical and physical properties of the soil polygon, it was assumed that it would have high-grade reinforced concrete characteristics with reduced unit weights to match the specified volume and loading conditions, leading to unit weights of 9.85, 10.85 and 11.55 kN/m^3 for the soil polygon. For the mechanical properties of the polygon, a reference unconfined characteristic compressive strength of concrete (f_{ck}) of 40 MPa was used, from which the unconfined elastic modulus was estimated using correlations from CEN

(2004). A Poisson's ratio (ν) of 0.2, characteristic for non-reinforced concrete was also assumed. Furthermore, since the scope of the dissertation was focused on the dynamic aspects of the design, only basic ultimate bearing capacity and uplift checks were performed. For the bearing capacity, direct CPT-based methods were used[1], including recommendations from Mayne et al. (2012) and Gavin (2018). Based on averaged q_c-values, a lower boundary safety factor of 4.0 was estimated for the bearing capacity at the foundation level. The uplift check was performed with a total stress-based approach, assuming a nominal ground water table (GWT) at -1.82 m below the surface and flood GWT at 2.0 m above surface. The initial nominal load was compliant with the nominal GWT, whereas the specified load of 705 MN complied with the flood GWT[2]. Having said this, the chapter was structured in the following manner.

- Domain- and mesh-size sensitivity analyses performed on a 1D soil column.
- Analysis of soil-structure interaction effects on liquefaction hazard.
- Preliminary conclusions and suggestions related to the effect of soil-structure interaction on liquefaction hazard.

9.1 Mesh- and domain-size sensitivity analyses

Prior to the evaluation of soil-structure interaction effect on the liquefaction hazard, mesh- and domain-size sensitivity analyses were performed on the 1D soil column. Besides the calibration of the material constitutive models, it was important to explore the behaviour of stress-wave propagation in the model when transitioning from a relative 1D-state towards proper 2D-sized domain as well as how discretisation affected the onset of liquefaction in susceptible layers. For this purpose, the domain size analysis included 1D liquefaction hazard simulations with 6 increasing domain widths (0.25, 0.50, 1.00, 1.50, 2.00 and 4.50 m) at a constant mesh size of 0.25 m, which provided insight to the differences in dynamic behaviour of the soil model when including, or not, 2D-effects. As for the mesh-size sensitivity analysis, a 4.50 m soil column was modelled with increasing average mesh size[3], starting at 0.25 m and up to 15 m, using 6-noded elements. The maximum domain size of 4.50 m was selected based on the maximum element size within the 2D model. For both cases, given that liquefaction hazard was the main interest of this dissertation, maximum experienced r_u-magnitudes, or $r_{u,max}$, were evaluated along the entirety of the soil column's domain, in both the vertical and horizontal directions. The distribution of $r_{u,max}$ data along the X- and Y-axes of the soil column domain proved particularly useful when evaluating the sensitivity of the model to mesh size, as it was able to show if certain meshing conditions increased the liquefaction hazard.

9.1.1 Mesh size sensitivity

The first step towards a 2D liquefaction hazard assessment was the mesh size sensitivity of the model. As mentioned earlier, a constant domain width of 4.50 m was used to evaluate different mesh sizes, ranging from 0.25 m to 15.00 m. It is worth remembering that the here-specified

[1] The static bearing capacity at the foundation layer was also evaluated using Terzaghi's general ultimate bearing capacity equation as presented in Das (2010), which resulted in much higher safety factors compared to the direct CPT-method used.

[2] $GWTs$ were only used to check against uplift conditions and were not modified during the liquefaction hazard analysis. The original GWT at -1.82 m was maintained in this section of the dissertation.

[3] The average mesh size was relative, as the enhanced meshing conditions provided by Plaxis did not allow a larger mesh size than was appropriate for the height of the layer to be included in the analysis. In this case, mesh sizes larger than 4.50 m (which was the domain width) were viewed simply as coarser versions of the same mesh. The reason why a 15 m mesh size, for example, was indicated was because that was the numeric reference value that was used in Plaxis to create the coarser mesh.

mesh sizes were only referential and that Plaxis generated its own meshing conditions based on the original specifications. Table 9.1 shows the mesh sizes specified and the average mesh size created by Plaxis, with their respective element, node and stress-point numbers. Models *M1* to *M3* generated the same mesh geometry, but had some slightly varying results, as can be seen in Figure 9.1a, which shows the vertical distribution of $r_{u,max}$-magnitudes in all liquefiable layers. Adding to the previously-mentioned cases, model *M4*, with a very similar number of elements, also obtained comparable results. As can be evidenced, there were only very slight variations present with no specific trends between the 4 specified mesh sizes. As for the horizontal distribution of $r_{u,max}$-magnitudes, shown in Figure 9.5, it can be observed that all three models showed similar and evenly-distributed $r_{u,max}$-magnitudes along the width of the domain, which was evidence of proper 1D stress-wave propagation. Lastly, Figure 9.3a summarises these aspects by grouping the overall occurrences of $r_{u,max}$-magnitudes into finite ranges, showing that all three model have a very similar behaviour in pore pressure evolution, with minute differences which can be considered negligible. These comparisons led to the conclusion that, for models using specified mesh sizes of up to 2.00 m (approximately 0.53 m average mesh size), the behaviour of liquefiable layers using PM4Sand had negligible variations and can be considered equivalent.

Desig.[4]	**Specified mesh size [m]**	**Average mesh size [m]**	**Element type**	**Number of**		
				Elements	**Nodes**	**Stress-points**
M1	0.25 m	0.514 m	6-node	3690	8644	11070
M2	0.50 m	0.514 m	6-node	3690	8644	11070
M3	1.00 m	0.514 m	6-node	3690	8644	11070
M4	2.00 m	0.526 m	6-node	3518	8246	10554
M5	3.00 m	0.749 m	6-node	1670	4154	5010
M6	4.00 m	0.936 m	6-node	1092	2838	3276
M7	4.50 m	1.119 m	6-node	746	2022	2238
M8	10.0 m	1.883 m	6-node	259	813	777
M9	15.0 m	2.069 m	6-node	186	616	558

Table 9.1: Average mesh size, element, node and stress-point numbers per specified referential mesh size.

When further comparing the distribution of $r_{u,max}$-magnitudes over the soil columns' domains, it was observed that models with a specified mesh size of 3.00 m and higher started exhibiting different trends and groupings of frequencies of occurrence of $r_{u,max}$. Figure 9.1b presents a comparison between the vertical distribution of $r_{u,max}$-values for *M1*, *M5* and *M6*, clearly showing the reduction in overall number of stress points (5010 and 32760 for models M5 and M6, compared to the 11070 stress points of model M1) with less values of $r_{u,max}$ between 0.50 and 1.00. The increase in mesh coarseness caused not only the reduction of the overall available elements, but also increased the model relative stiffness, which in turn attracted more stress, increasing the speed of accumulation of pore pressures at the available stress points. This effect can be clearly seen in Figure 9.3b where the curves of models *M5* and *M6* show reduced richness of $r_{u,max}$-magnitudes, within ranges of $0.50 < r_{u,max} \leq 0.85$ and $0.90 < r_{u,max} \leq 0.95$, compared to *M1*-curve, and a slight increase in $r_{u,max}$-magnitudes within ranges of $0.85 < r_{u,max} \leq 0.90$ and $0.95 < r_{u,max} \leq 1.0$. The before-mentioned conditions were even clearer when comparing results from model *M1* and *M7* to *M9* (shown in Figures 9.2 and 9.4), where $r_{u,max}$-magnitude richness

[4]Designation.

kept gradually reducing with increasing mesh coarseness, while specific $r_{u,max}$-ranges close to 1.0 increased in frequency of occurrence. The only notable difference experienced in models *M8* and *M9* was that layer 3-3-BX-FS was not able to reach liquefaction (see Figures 9.2a and 9.2b). It may have been that the increase in stiffness was not as significant in that region, compared to adjacent sections, as it did not attract that much stress to reach liquefaction.

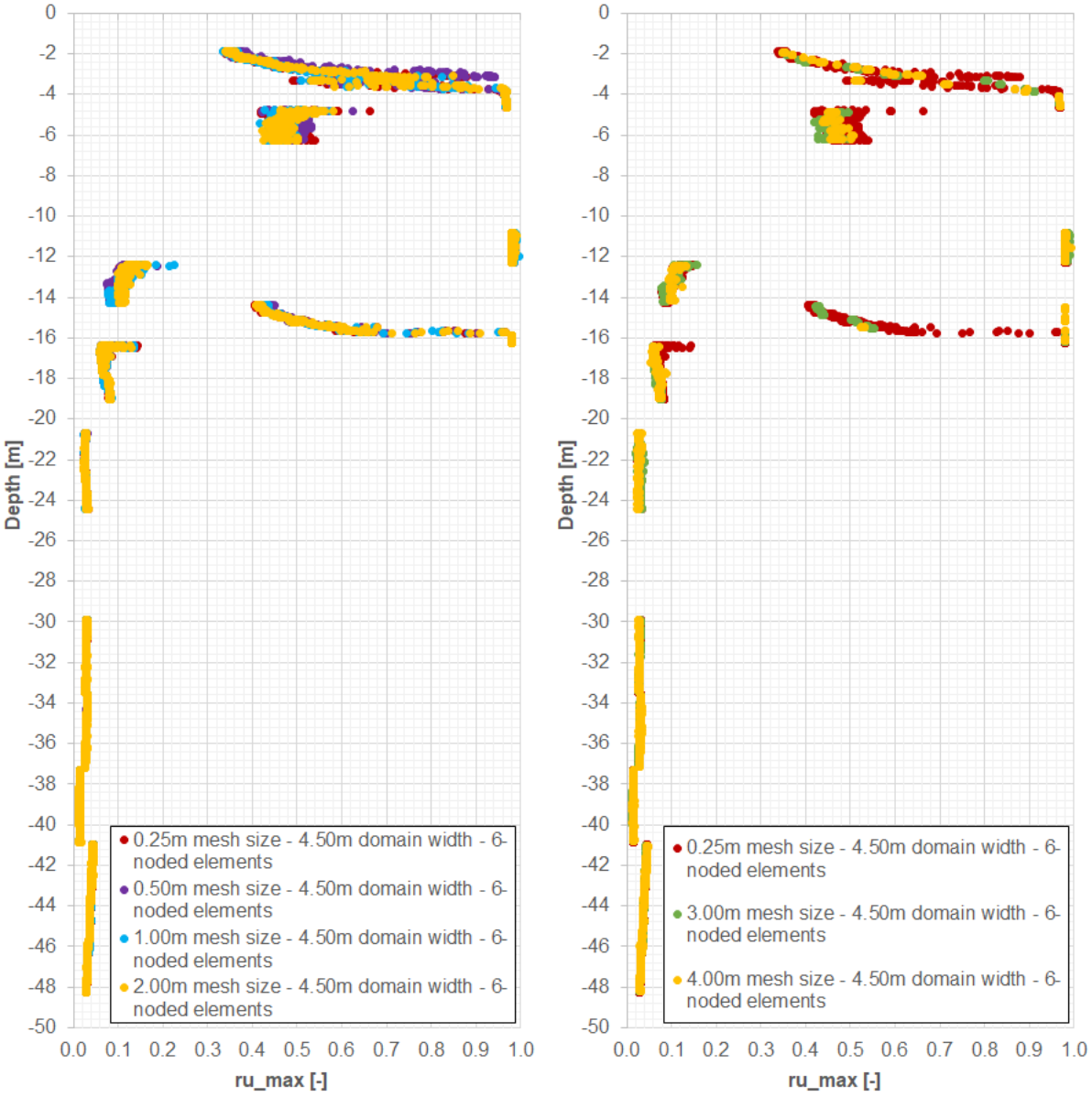

(a) Models M1 to M4

(b) Models M1, M5 and M6

Figure 9.1: Vertical distribution of $r_{u,max}$-magnitudes in models with specified mesh sizes of 0.25 m to 4.00 m.

Therefore, it was concluded that, for a domain width of 4.50 m, models with a specified mesh size of up to 2.00 m provided the same resistance to liquefaction, and that for coarser meshes, the models experienced an increase in relative stiffness which caused a faster a accumulation of pore pressures within the model elements and, therefore, provided a lower resistance to liquefaction compared to models with finer meshes. Nevertheless, it could be observed that even if coarser meshes did not have that many stress points to provide a rich distribution of $r_{u,max}$-magnitudes, the models still followed general trends both vertical and horizontal extensions of the model,

which was considered acceptable, even if coarser meshes did not exactly follow specific $r_{u,max}$-trends within each potentially liquefiable layer. This condition was crucial, as it allowed the 2D model to have a lower mesh refinement, significantly reducing computational time[5].

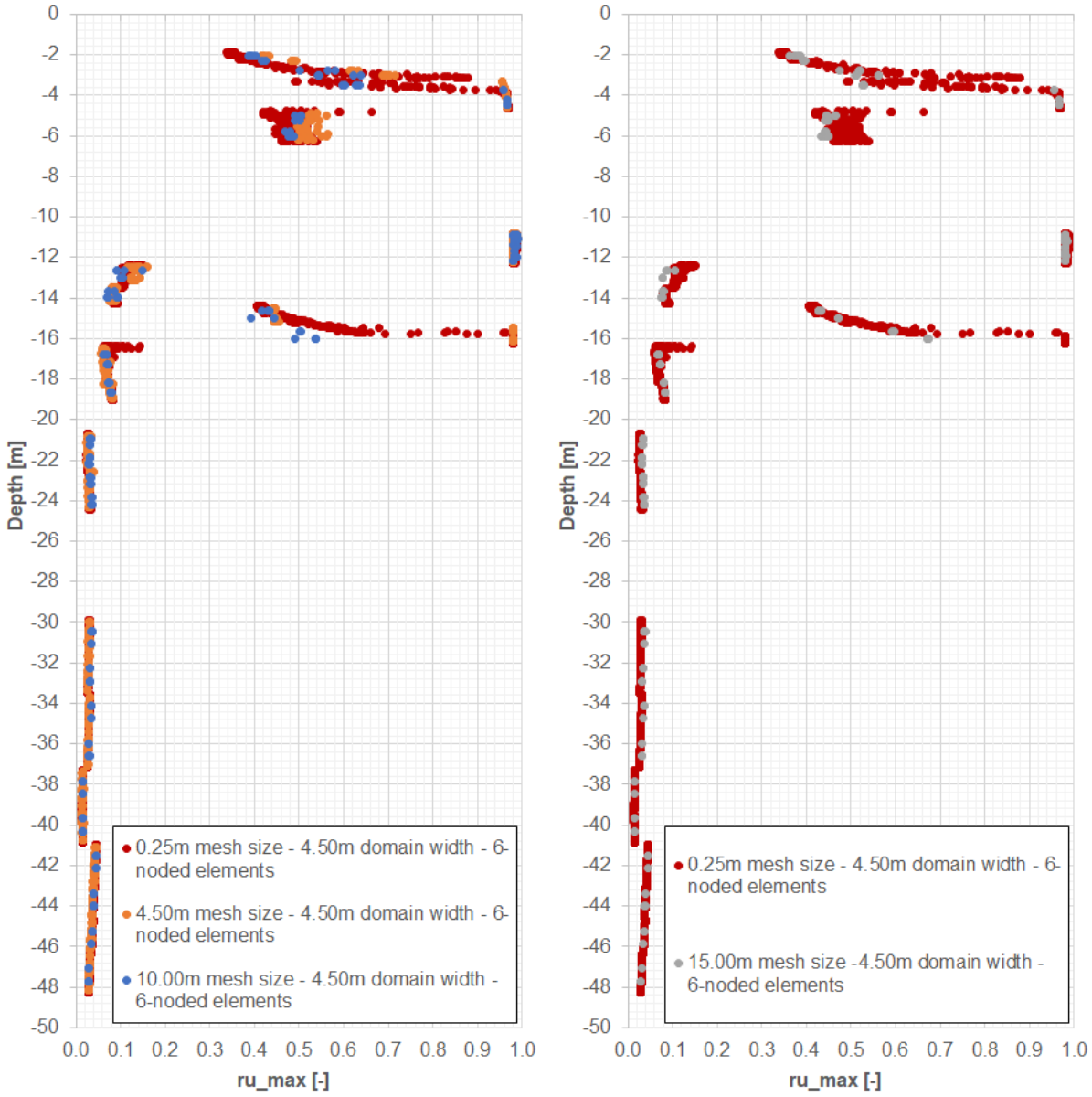

(a) Models M1, M7 and M8

(b) Models M1 and M9

Figure 9.2: Vertical distribution of $r_{u,max}$-magnitudes in models with specified mesh sizes of 0.25 m and 4.50 m to 15.00 m.

[5]The average simulation time for a single 2D model with a medium coarseness factor (specified in Plaxis) was approximately 2.75 hrs per second of dynamic signal (give or take depending on the available processing power), which created a significant problem, since even very short earthquake signals would take days to calculate; considerably more if the mesh size was refined even a little.

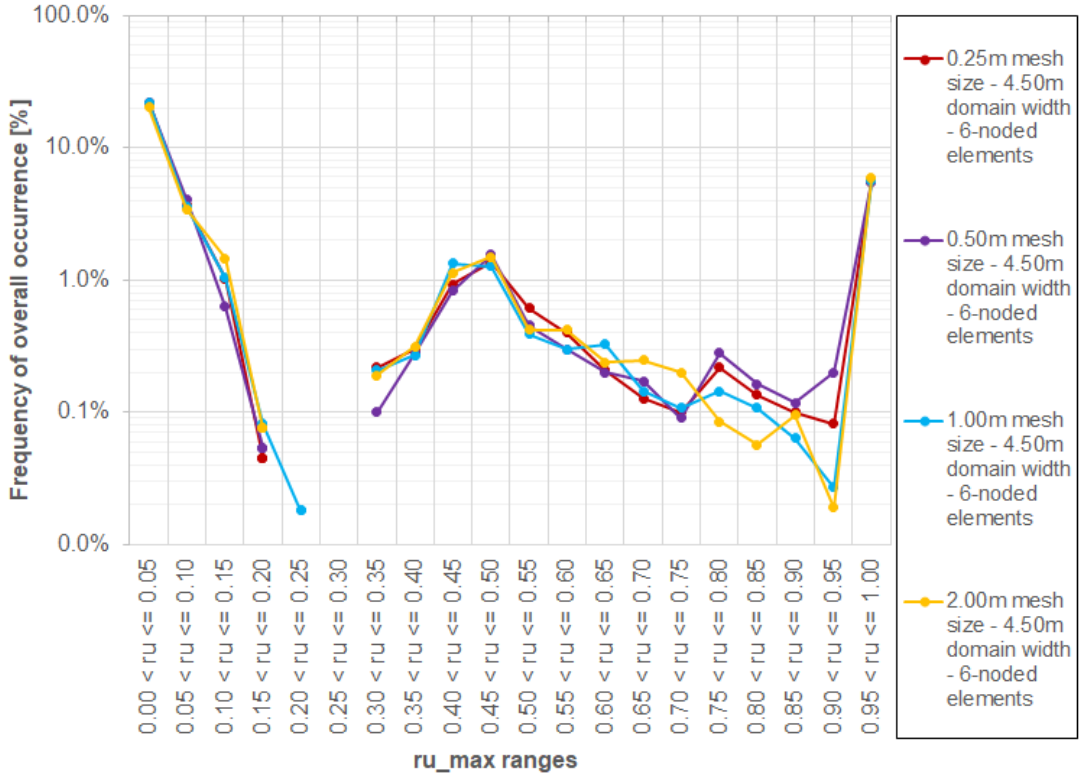

(a) Models M1 to M4

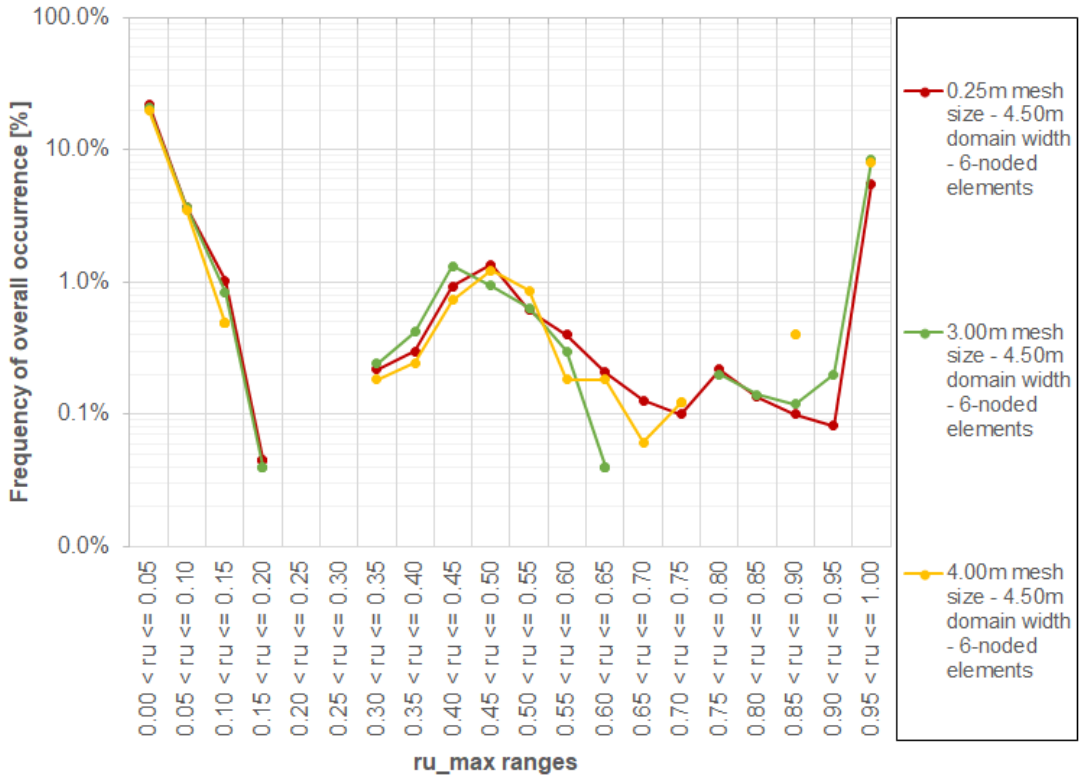

(b) Models M1, M5 and M6

Figure 9.3: Percentage of frequency of occurrence within specific $r_{u,max}$-ranges.

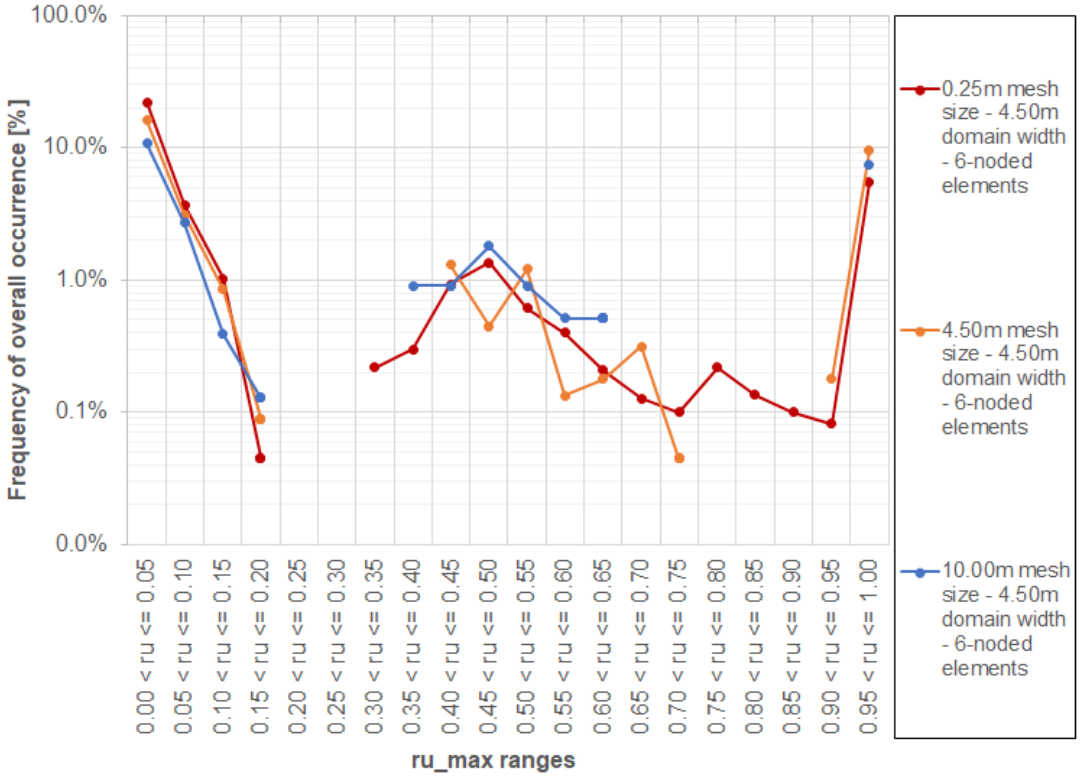

(a) Models M1, M7 and M8

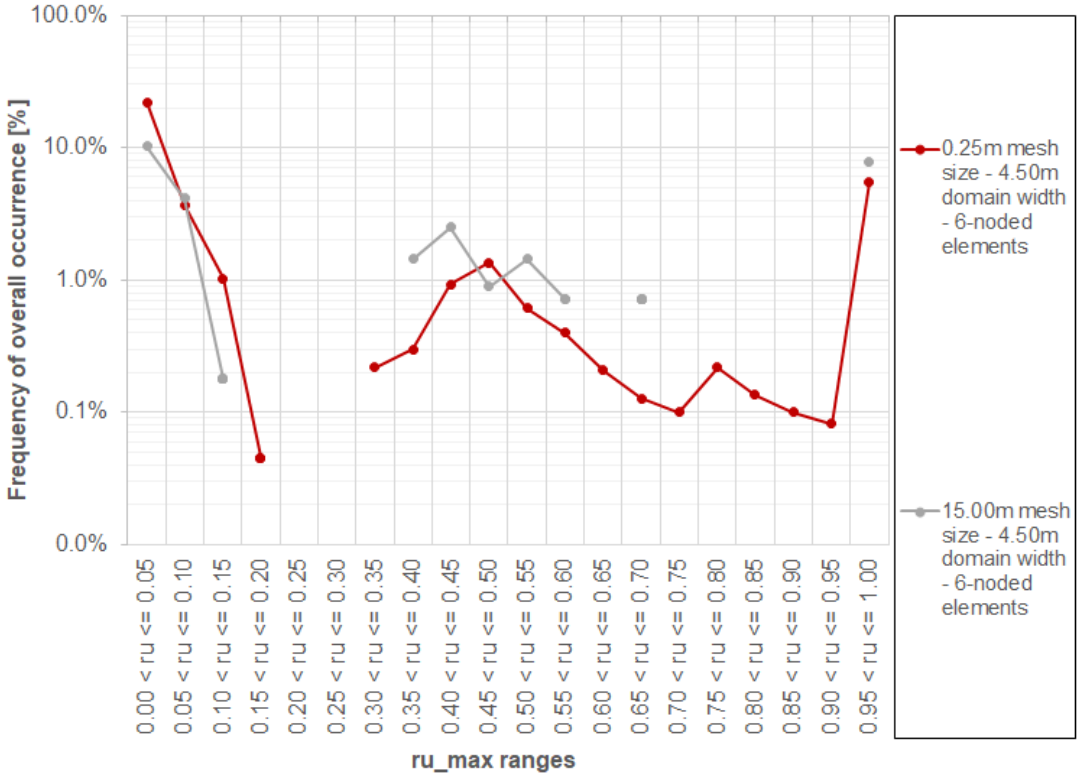

(b) Models M1 and M9

Figure 9.4: Percentage of frequency of occurrence within specific $r_{u,max}$-ranges.

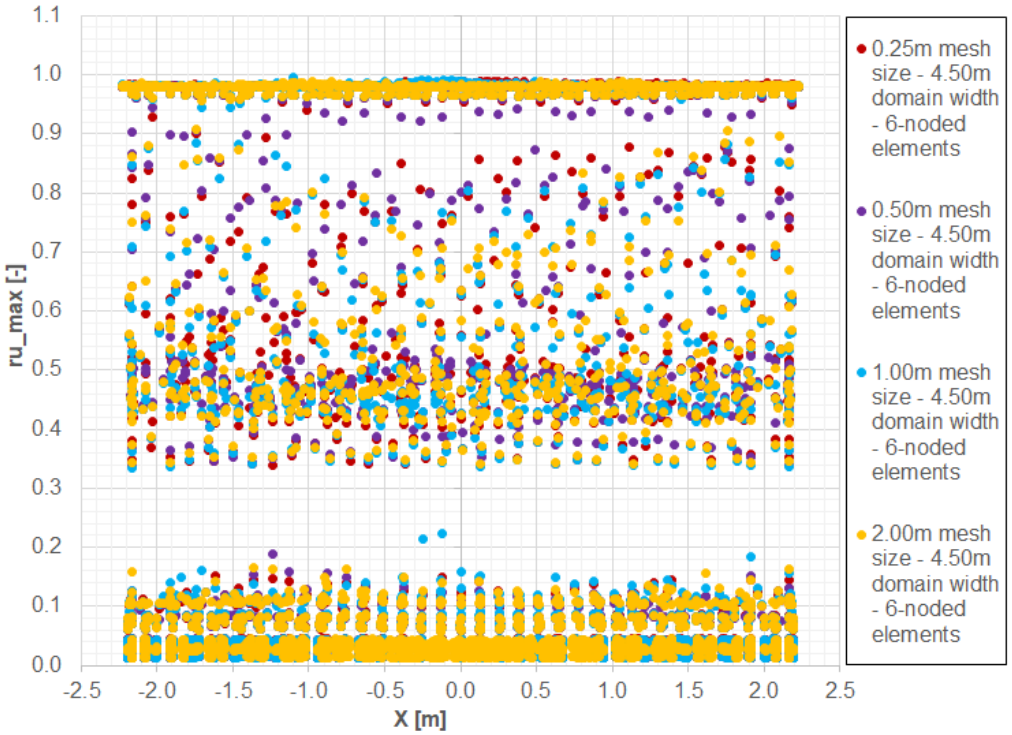

Figure 9.5: Horizontal distribution of $r_{u,max}$-magnitudes of models with specified mesh sizes of 0.25 m to 2.00 m.

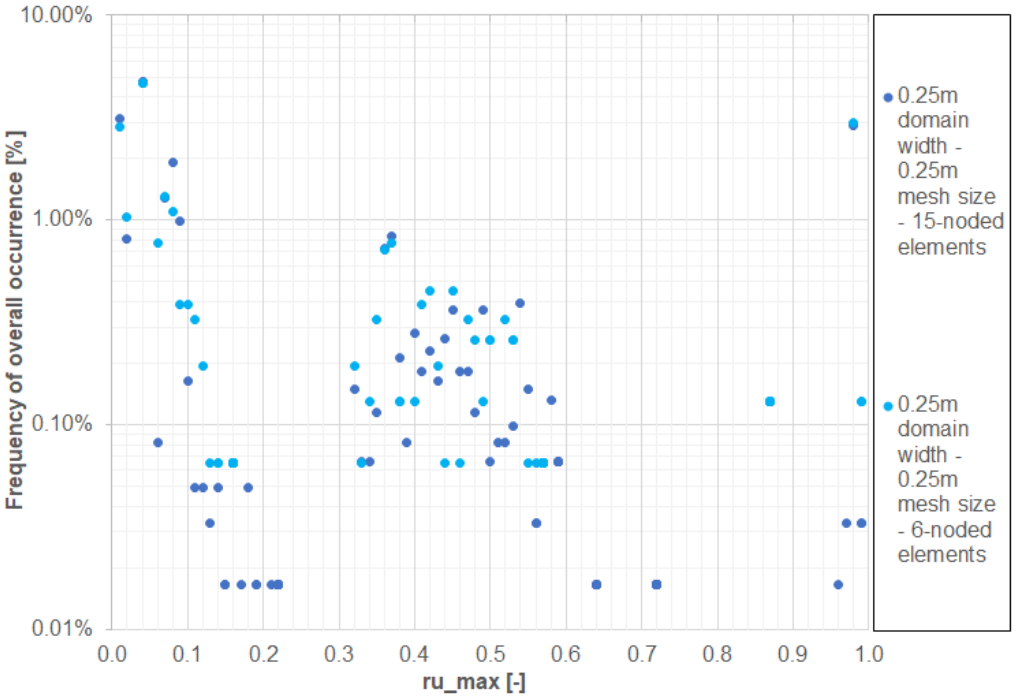

Figure 9.6: Comparison of $r_{u,max}$-magnitude distributions between models using 15-node and 6-node elements.

Lastly, to try and compensate for the coarser mesh that was used in the 2D model, 15-node elements, instead of 6-node, were used in the model. This allowed for an increase in calculations nodes and stress-points with the same number of elements. Figure 9.6 shows a comparison be-

tween $r_{u,max}$-magnitude distributions in two 0.25-m-wide models, with an average mesh size of 0.356 m, using 15-node and 6-node elements. Both models provided very similar distributions of $r_{u,max}$-values, which also was present in both the vertical and horizontal extensions throughout the domain. 6-noded elements provided accurate enough data, following overall trends in pore pressure accumulation, but the model with 15-node elements provided richer distributions. Therefore, it was decided that the 2D model would include 15-node elements (as did the 1D models in the previous chapter), to try and compensate for the reduced accuracy a coarser mesh provided, even if it meant fractionally increasing computational time.

9.1.2 Domain size sensitivity

Next on the way towards a 2D liquefaction hazard assessment was the analysis of potential divergence in results when expanding a very slender soil column to a larger horizontal domain. The domain width was expanded from 0.25 m to 4.50 m, using the same specified mesh size, as presented in Table 9.2. The first assumption was that, when increasing the width of the soil model, $r_{u,max}$-magnitudes would remain approximately the same across the horizontal extent. However, after the domain size sensitivity was performed, it was clear that domain size did influence the resistance to liquefaction of the soil columns. A possible explanation was that the increase in domain width, accompanied by the increase in calculation elements, created an increase in the overall stiffness of the model towards dynamic excitation. That way, there were not only more output points available, but those output points accumulated more pore pressures within the same amount of time, reducing the resistance to liquefaction with increasing domain size. This can be clearly observed in Figure 9.7, where vertical distribution trends of $r_{u,max}$-magnitudes shifted towards higher r_u-values as the domain width grew. Additionally, this effect can be further observed in Figure 9.8, where frequency of occurrence of $r_{u,max}$-magnitudes have shifted towards greater r_u-values with increasing domain size.

Desig.[4]	**Domain width [m]**	**Average mesh size [m]**	**Element type**	**Number of**		
				Elements	**Nodes**	**Stress-points**
D1	0.25 m	0.356 m	6-node	514	2566	1542
D2	0.50 m	0.537 m	6-node	420	2072	1260
D3	1.00 m	0.518 m	6-node	812	2860	2436
D4	2.00 m	0.526 m	6-node	1574	4392	4722
D5	4.50 m	0.514 m	6-node	3690	8644	11070

Table 9.2: Average mesh size, element, node and stress-point numbers per specified domain width.

In summary, having analysed the variation of the model's resistance to liquefaction when varying mesh and domain size, it was clear that transitioning towards a large domain, with a large mesh size, would attract more stress within the elements, increasing the speed of accumulation of pore pressures within the liquefiable layers. It can therefore be expected that, under supposed free-field conditions (without the presence of a structure), the model will generate more pore pressures in a 2D setting than in a 1D setting even if the same meshing conditions are maintained, leading to possible liquefied states in 2D, contrary to 1D. Given that time constraints were an issue, performing 2D calculations without a structure was not possible. Therefore, for the comparison between 1D- and 2D-conditions in a supposed free-field scenario, the closest meshing and domain size were used, which in this case was model M9.

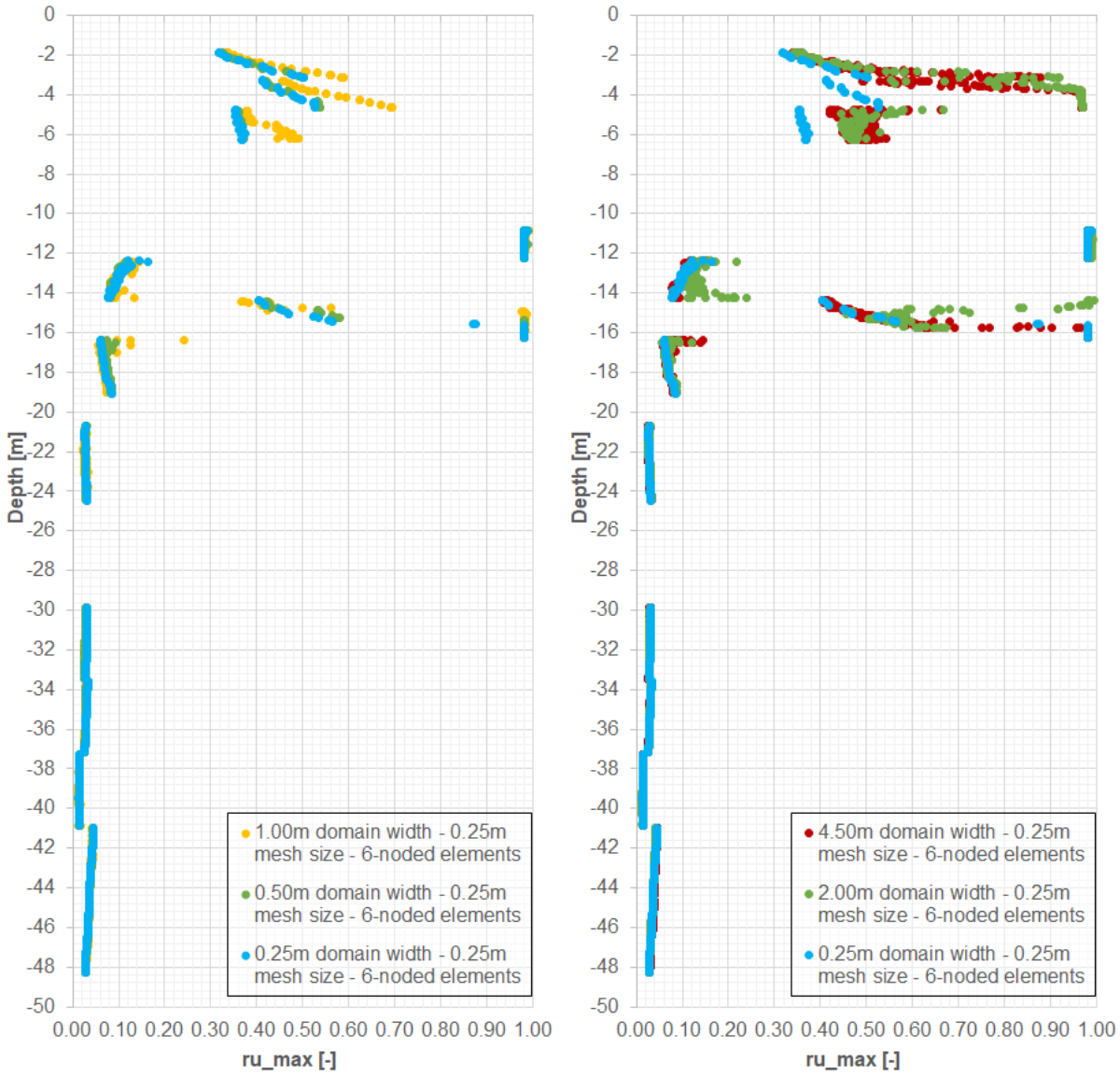

(a) Models D1 to D3

(b) Models D1, D4 and D5

Figure 9.7: Vertical distribution of $r_{u,max}$-magnitudes in models with domain sizes from 0.25 m to 4.50 m.

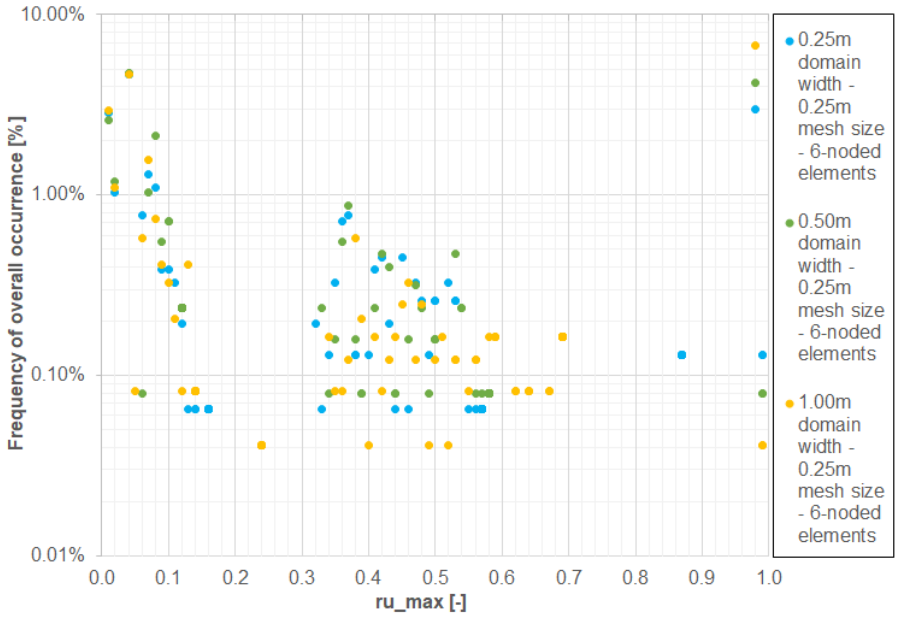

(a) Models D1 to D3

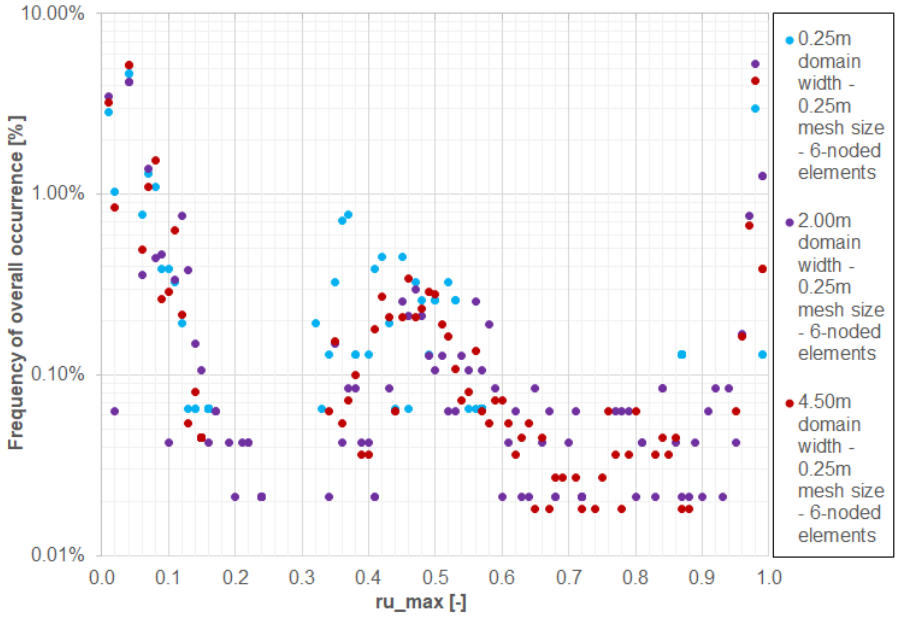

(b) Models D1, D4 and D5

Figure 9.8: Percentage of frequency of occurrence within specific $r_{u,max}$-ranges in domain-size sensitivity analysis

9.2 Soil-structure interaction effects on liquefaction hazard

As mentioned before, this last section of the dissertation analysed the possible effects of soil-structure interaction on liquefaction hazard in the evaluated soil profile, using only calibration methodology *CM2*, as it provide better overall consistency in the triggering of liquefaction compared to the *CM1* method. Furthermore, the 2D model was only subjected to the Umbria Marche *BDBE* signal, as including longer signals would have increased computational time exponentially[6]. Given that equivalent free-field conditions were of interest as well, a quick static

load sensitivity analysis of the soil domain was performed for all three previously-defined structural loads to determine the range of influence of the structure. This sensitivity analysis checked different soil domain widths and used the resultant elastic and plastic deformations experienced along the soil bulbs below and adjacent to the critical facility. In the end, a soil domain of 270 m was defined as sufficient to obtain an in-situ-like (free-field) stress-state near the boundaries of the 2D model. Figure 9.9 shows the area of influence of the larges structural load considered for the analysis (750 MN) in terms of induced deformations at the static stage (before the start of the earthquake signal).

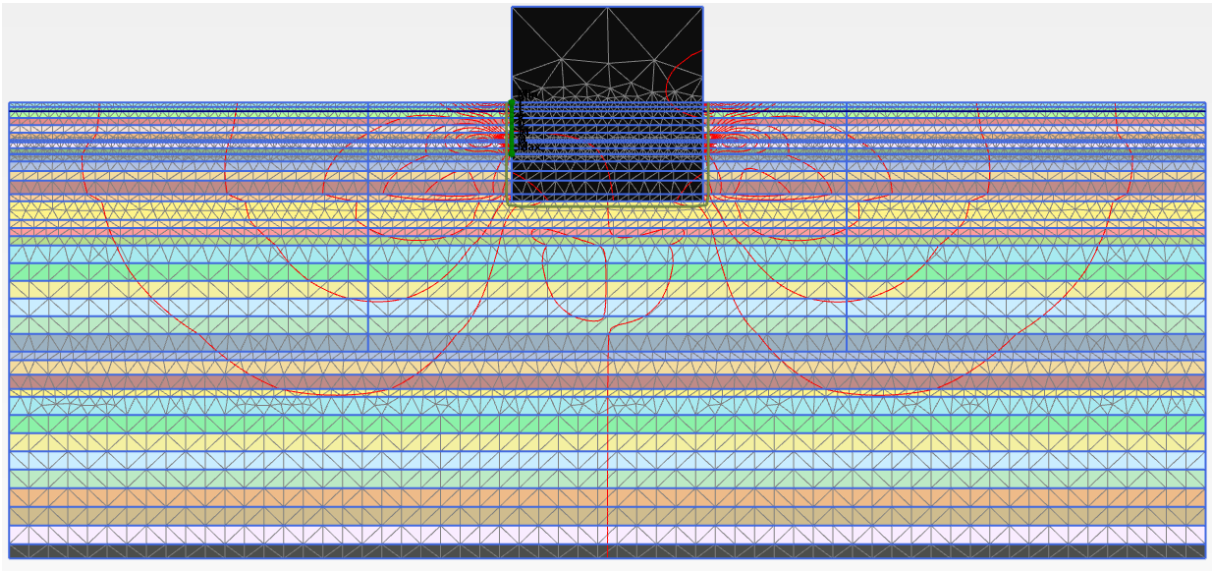

Figure 9.9: Area of influence of static structural load before the start of the earthquake signal

Given the replicability of the obtained data, the three structural load responses of the soil-structure system were presented simultaneously. Results were presented in terms of *PGD*-, *PGA*- and $r_{u,max}$-profiles at select distances from the centre of the model domain, which also coincided with the centre of the structure. γ-profiles were not presented because the near-structure shear strains were too erratic to perform any conclusive analysis, which is why, under the assumption that *CM2* was able to maintain consistency in terms of both r_u- and γ-based liquefaction triggering (as demonstrated in chapter 8), liquefaction was only evaluated based on $r_{u,max}$-magnitude profiles. To adequately view the results, the reader is advised to analyse the figures in the Appendix through a digital medium, as this will help the visibility of the results. Nevertheless, select cases and comparative scenarios were included in the main text for illustrative purposes.

9.2.1 Comparison of 1D and 2D liquefaction hazard under supposed free-field conditions

To start, it was necessary to compare $r_{u,max}$-profiles obtained from the 1D and 2D models at free-field[7] conditions to get a sense of the effect the domain- and mesh-size increases had on the liquefaction hazard of the soil profile. Figure 9.10 presents the $r_{u,max}$-profiles of two 1D-soil columns in combination with the results obtained in the 2D model (the largest structural

[6]Calculation times of the model subjected to the Umbria Marche *BDBE* signal fluctuated between 40 to 48 hrs with the available computational capabilities during the making of this research. Applying longer signals, such as, for example, Imperial Valley signal would have increased the computation al time from 2 days to approximately a week.

load response is presented here for illustrative purposes), outside the area of influence described before. As was observed before in section 9.1, increases in domain size increased the liquefaction hazard in the model, especially in layer 1-NASC-MS, behaviour which was also replicated in the 2D model results. Given these variations, the performance of this comparison was very advantageous, as liquefaction hazard results would definitely be amplified, not necessarily by the presence of the structure, but by the increase in domain and mesh size. Therefore, for comparative purposes between 1D and 2D results under free-field conditions, modellers must be careful when interpreting results, as modelling conditions are very sensitive. Despite this divergence in liquefaction hazard results, comparison of liquefaction hazard at different locations within the model was appropriate, since the same meshing conditions have been applied throughout the model domain.

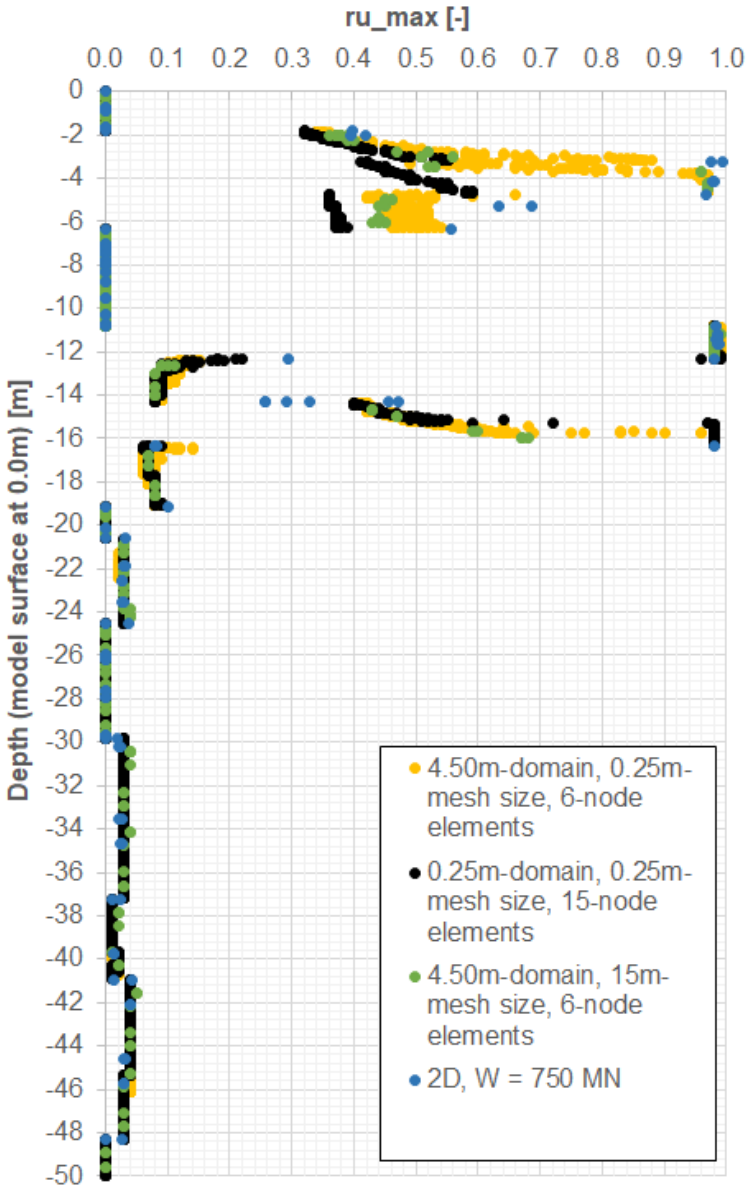

Figure 9.10: Comparison of $r_{u,max}$-profiles at supposed free-field conditions in 1D and 2D settings

[7]Free-field conditions refer to the in-situ stress state of the soil without the presence of any type of structure which might alter the propagation of stress waves through the soil layers from the source.

9.2.2 Evaluation of soil-structure interaction effects on liquefaction hazard over distance

Having established a comparative baseline for the liquefaction hazard at free-field conditions in section 9.2.1, potential soil-structure interaction effects were evaluated in this section. The first part of the analysis of all three structural load scenarios was based on *PGD*- and *PGA*-profiles at select distances between the left boundary of the model, at X = -132.5 m, and the centre of the model, at X = 0.0 m, which also coincided with the centre of the structure. Figures 10.29 and 10.31 (see the Appendix) present the *PGA*- and *PGD*-profiles, respectively, at approximately every 20 m from the boundary to the edge of the structure, with the addition of 2 more profiles below the structure. Figures 10.30 and 10.32 also show *PGA*- and *PGD*-profiles but at greater detail in the immediate vicinity of the structure. Looking first at Figures 10.29 and 10.30, it can be observed that *PGA*-magnitudes up to X = -30 m in all three scenarios remained very similar to those observed at the boundary (free-field condition). However, the liquefaction hazard increased significantly as the profile came very close to the structure, which was shown through the increased dispersion of acceleration points[8]. When looking closer at the vicinity of the structure in Figure 10.30, it could be observed that liquefaction hazard started to increase significantly from X = -24 m onwards, distance which tended to increase with structural load increase, as more dispersed acceleration points were present in the upper layers at farther distances in the latter two structural load scenarios. On the other hand, *PGA*-profiles below the foundation level remained essentially the same throughout all analysed distances, with the exception of those located immediately below the structure. Both findings were to be expected, as the liquefaction hazard in layers 5-BX-MS and below was essentially null, and the acceleration of soil deposits below the structure were compacted due to the presence of the structure, which created a stiffer response and, therefore, exhibited greater accelerations. Shifting towards the *PGD*-profiles in Figures 10.31 and 10.32, it can be observed that layers from X = -30 m inwards exhibited large differential deformations compared to profiles from distances farther away from the centre. Essentially, layer 3-1-BX-FS seemed to have liquefied at X = -30 m, in addition to all sub-layers in layer 1-NASC-MS. This trend increased when moving closer to the structure, which was confirmed by the detailed overview. Figure 10.32 showed that all cohesionless layers in the region between X = -30 m and X = -20 m from layer 3-1-BX-FS upwards had liquefied and had experienced very larger deformations. This new information complemented the preliminary assumptions which were based on the *PGA*-profiles, and stated more conclusively that the upper layers from X = -30 m inwards experienced a drastic decrease in cyclic resistance due to the soil-structure interaction in the vicinity of the structure. As for the layers below the foundation layer, it was expected that deformations would not vary that much from those obtained close to the boundary of the model. In all three scenarios, displacements even reduced compared to locations which were not vertically confined by the structure (locations X = -20.0 m to X = 0.0 m). Lastly, the $r_{u,max}$-profiles shown in Figures 10.33 to 10.36 were evaluated and used to complement the previous findings. The general overview of accumulated pore pressures over distance to the centre of the domain showed that no significant changes in $r_{u,max}$-magnitudes were present in profiles at locations from X = -30 m outwards, whereas significant increases occurred the closer the profiles got to the structure. Layer 3-BX-FS showed a very clear increasing trend in $r_{u,max}$-values with proximity to the structure, whereas this trend was not so clear in layer 1-NASC-MS. The increasing trend was there, but a lot of dispersion in data points accompanied it, reaching r_u-magnitudes as low as 0.02. A plausible explanation to this variations was that, since layer 1-NASC-MS was only confined at low overburden pressures, the soil layers experienced some dilation which allowed pore pressures not to build up in discontinuous regions. This was particularly evident in profiles which were very close to the structure (within a 5 m distance).

[8]Scenario *W2* did not include data points above the foundation level due to a data-extraction error. However, given the increasing trend in *PGA*-magnitudes with increasing structural load, it was safe to assume that *PGA*-

In summary, it was clear that soil-structure interaction did have significant effects on the liquefaction resistance, significantly lowering the cyclic resistance of cohesionless soils layers 1-NASC-MS and 3-BX-FS, especially within a 10 m distance outward from the face of the structure. Figure 10.28 shows an overview of the liquefied layers in the entire domain (in red). Additionally,

9.2.3 Evaluation of effects of structural load variation on liquefaction hazard over distance

Lastly, the effects of structural load variation on liquefaction hazard were analysed using select profiles from the three structural loading scenarios. When observing Figures 10.37 and 10.38, *PGA*-profiles did not show major differences between varying structural loads along the entire profile. However, some differences did arise at the location close to the boundary, which was not repeated in most of the soil domain until the vicinity of the structure was reached. This divergence in responses could have been the consequence of modelling issues, or by the reduced effect of a lower structural load, which may have caused increased acceleration magnitudes around the boundary. However, these explanations remained inconclusive as the trends did not continue inwards towards the centre of the domain. When looking at profiles within the 10-m vicinity of the structure, layers 1-NASC-MS and 3-BX-FS reached liquefaction, but no clear trend was visible in terms of acceleration magnitudes. Next, when analysing the *PGD*-profiles in Figures 10.39 and 10.40, some divergences and trends started to come to light. Profiles from all three scenarios at the boundary did not exhibit any differences between each other. This, however, started to change as the profile locations moved inwards, as greater differential deformations were experienced with increasing structural loads. This was to be expected, as greater inertial forces could have forced around larger volumes of soil. In liquefied layers, this trend was not as clear, as the complete liquefaction of layer 3-1-BX-FS made deformation trends in the upper layers unclear relative to effects of the magnitude of the applied structural load. Lastly, the $r_{u,max}$-profiles in Figures 10.33 to 10.36 also did not find any clear trends in terms of the effect of structural load variability on generation of pore pressures.

Therefore, in summary, it was concluded that no evident effects of structural load variability was visible in any of the data-profiles evaluated, which suggested that weight variations was not an important issue in liquefaction hazard. However, if said increase in weight was accompanied by an increase in size of the structure, then it would be expected that soil-structure interaction effects would be present.

9.3 Discussion and preliminary conclusions regarding the soil-structure interaction effect on liquefaction hazard in 2D

Overall, it was demonstrated that soil-structure interaction effects do alter the liquefaction hazard of a given soil profile, as cohesionless soils in the vicinity of the structure exhibited greater liquefied regions compared to free-field conditions. In addition, it was also found that structural load variability did not induce specific types of behaviour on the liquefaction hazard of the soil profile at any location along the domain width. More specific discussion points and preliminary conclusions regarding the 2D evaluation of soil-structure interaction on liquefaction hazard were presented below.

- Models using a specified mesh size of up to 2.0 m (average mesh size of 0.53 m in this case) obtained very similar behaviour in liquefiable layers. The differences were negligible and cyclic resistance was considered converged for specified mesh sizes ≤ 2.0 m.

magnitudes would be within ranges of 0.4 and 1.2 g.

- Meshes with specified mesh sizes of $\geq 3.0\ m$ induced increases in the relative stiffness of the soil column, effectively attracting more stress and, therefore, more pore pressures in liquefaction-vulnerable layers.
- In Plaxis, increases in mesh coarseness, depending on the subdivision of the modelled layers, may maintain smaller-sized elements in thinner layers, increasing the mesh coarseness where possible. This indirectly affected some layers which did not reach liquefaction in coarser meshes, as increases in stiffness in adjacent regions may have attracted more stress, which caused a reduction in stress accumulation in the liquefiable layer (case of layer 3-3-BX-FS).
- Increases in mesh coarseness should be performed with care, as reduction of available stress points can also become a problem when trying to distinguish liquefied regions from others.
- Increases in the width of the soil domain apparently created a stiffer soil column due to its larger overall width, which in turn attracted more stress towards the stress points. The general trend found was that the liquefaction resistance of the overall soil column decreased with increasing domain size.
- Free-field liquefaction hazard in the 2D model followed trends related to domain- and mesh-size increase in numerical modelling of liquefiable layers, triggering liquefaction in parts of layers 1-NASC-MS and 3-BX-FS.
- In addition the layers 3-1- and 3-3-BX-FS, layer 1-3-NASC-MS also liquefied at the free-field condition location. This attraction of pore pressures to the shallower layer was consistent with what was explained in the mesh sensitivity, which stated that, given the coarser mesh size, the region would attract more stress, increasing the likelihood of reaching liquefaction earlier.
- *PGD*-profile-based evaluation of liquefaction was very useful, as the experienced deformations in the vicinity of the structure showed very clear trends that meant the layers had liquefied. *PGA*-profiles were useful in providing some preliminary conclusions as to which regions exhibited liquefaction. Therefore, the combined use of *PGA*-, *PGD*- and $r_{u,max}$-profiles was essential to fully confirm the effects of soil-structure interaction over distance.
- Essentially, soil-structure interaction effects caused significant increases in liquefaction hazard from X = -30 m onwards, whereas its effect on cyclic resistance beyond that limit towards the boundary of the model was negligible.
- Upper layers close to the structure experienced dilation in discrete regions, not allowing the accumulation of pore pressures in local points even in close vicinity of the structure.
- *PGA*-magnitude divergences were present between the three structural loading scenarios at the boundary location. However, given that the observed trends did not continue inwards, the effect was associated to possible modelling issues related to boundary interactions.
- No distinguishable trends were present when evaluating the sensitivity of the liquefaction hazard of the soil domain to variations in structural load magnitude. However, further research should be oriented towards the analysis of soil-structure interaction effects with increases in both weight and volume.
- The overall behaviour of the 2D model at supposed free-field conditions was adequate and accurate enough compared to its respective 1D counterpart in terms of identifying liquefied layers.

Part IV

Conclusions and recommendations

Chapter 10

Conclusions and recommendations

As Charles F. Richter once mentioned in the preface to his book *Elementary Seismology*, "*Great harm is done by poorly trained people*[1] *who hasten about in the field, observe a small part of the evidence, and publish premature conclusions which are actual obstacles to serious investigation.*", this research offers, more than strong affirmations and conclusions related to the presented results, which were obtained on the basis of limited data, a different perspective on liquefaction potential analysis with the use of FE modelling, and how changing small but important assumptions regarding the triggering of liquefaction can, at times and under specific conditions, drastically affect results.

10.1 Conclusions

10.1.1 Regarding the characterisation of Ottawa F-65 sand

- Cyclic resistance of loose Ottawa sand increased with increasing overburden pressure, which contradicted the established $K-\sigma$-effect, whereas dense sands exhibited reductions in cyclic resistance with increasing overburden pressure. This contradicting trend in cyclic resistance in loose sands was also present in Fraser river sand Naesgaard (2011).
- Reduction in overall pore pressures once cyclic mobility was reached was caused due to imperfect boundary conditions which allowed volumetric dilation.
- the number of tests for a given set of shearing conditions were at times not sufficient to discard variation in results due to the intrinsic heterogeneity of the soil.

10.1.2 Regarding the identification of quantitative measurements to define liquefaction

Based on the detailed analysis performed in section 3.1 on the nature of liquefaction triggering using the *CUDSS* database from Parra (2016), this dissertation was able to quantitatively characterise the triggering of liquefaction for sands sheared a different conditions, answering the firs research sub-question presented in the introduction. The following conclusions could be established regarding the behaviour of liquefaction-triggering and how that knowledge can be applied in the calibration of the PM4Sand model.

- The triggering of liquefaction under any type of shearing, confinement and initial state conditions has to be evaluated through r_u- and γ-based approaches so that physical consistency during liquefaction triggering is maintained.

[1]The word "people" was paraphrased from the original word "men".

- Given that on-site developed shear strains could be lower compared to those from laboratory testing, a proposition for the evaluation of liquefaction in a practical setting, say a numerical liquefaction potential analysis of a soil column, could use a conservatively-reduced γ-threshold of $\geq 2\%$.
- For the calibration of the PM4Sand constitutive model at the single element level (or even with real geometry testing conditions in a numerical modelling setting), $r_u = 0.95$ and $\gamma = 3\%$ were defined, as they identified liquefaction in a physically-consistent manner.

10.1.3 Regarding the modelling effectiveness of PM4Sand

- The PM4Sand model was not able to simulate different shearing and initial state conditions using only one parameter set.
- The PM4Sand model was able to adequately simulated the behaviour of loose sands sheared at low to intermediate *CSRs* and confined at most overburden pressures.
- The PM4Sand model was not able to adequately model post-liquefaction strains or pre-liquefaction pore pressures in dense sands without shifting towards the calibration methodology *CM2*.
- Adequate pore pressure evolution during the first cycles could not be adequately modelled, especially in dense sands sheared at high *CSRs*. These variations could be solved by modifying internal secondary or tertiary model parameters which are restricted in Plaxis or just be a consequence of the model stiffness given its homogeneous nature.
- PM4Sand could not adequately simulate the cyclic fluctuation of pore pressures and shear strains in dense sands when sheared at intermediate or higher *CSRs*. The large dilation components that are present during shearing in dense sands were not able to be represented by the PM4Sand model, which was better suited to model looser and stiffer behaviour.
- Peak r_u-magnitudes were underestimated in a lot of cases due to the position of the locus of the stress path that PM4Sand sets. This could be the consequence of the default value of an inaccessible secondary or tertiary model parameter within Plaxis.

10.1.4 Regarding the proposed calibration methodology

- The original calibration methodology *CM1* could not adequately identify the triggering of liquefaction consistently based on on r_u and γ combined in dense sands or sands which exhibited net dilative tendencies.
- *CM2* allowed the triggering of the r_u- and γ-based markers to be more consistent with experimental findings.
- The implementation of *CM2* was not needed in scenarios where the model exhibited a tendency towards contractive behaviour.

10.1.5 Regarding the 1D liquefaction hazard analysis

- The PM4Sand model was able to identify liquefaction in vulnerable layers.
- Proper 1D stress wave propagation was confirmed.
- The presence of a liquefied layer affected the acceleration and displacement magnitudes of non-liquefied layers immediately below and above.

- *CM1* was not able to trigger liquefaction in a consistent manner for most of cases as the model anticipated the accumulation of pore pressures too much. *CM2*, however, was able to exhibit physically-consistent liquefaction, creating an improvement compared to *CM1*-results, which showed inconsistencies.
- The numerical model results showed a significant reduction in the liquefaction hazard compared to the ones obtained through semi-empirical methods.
- The combined use of $r_{u,max}$- and γ-profiles was crucial to conclusively identify liquefied regions. Time-histories at specific points were of great use as well, but were considered more of an academic tool to evaluate how the pore pressures and shear strains evolve during the seismic response, as they provided a lot of extra information which was not needed if one only wished to determine if the soil had liquefied.

10.1.6 Regarding soil-structure interaction effects on liquefaction hazard

- Increases in mesh and domain size increased liquefaction hazard of the soil profile, as it increased the stiffness of the model.
- Soil-structure interaction effects caused significant increases in liquefaction hazard from X = -30 m inwards, whereas its effect on cyclic resistance beyond that limit towards the boundary of the model was negligible.
- No evident effects of structural load variability was visible in any of the data-profiles evaluated

10.2 Recommendations

10.2.1 Regarding future research

There were many instances in this research where the author proposed certain conditions or methods to be improved or validated through further research. The list below summarises the main directions future research could head along and improve current knowledge regarding the physical process of liquefaction and calibration of liquefaction constitutive models in numerical modelling.

- Given that only fully-undrained dynamic analyses were run, future research related to this topic could involve the proper study of the use of partially-drained (or *Dynamic with consolidation*, as known in Plaxis) dynamic analyses and the sensitivity of the model to changing hydraulic conductivities. Tziolas (2019) and Toloza (2018) partially included simulations performed with this setting, but a more detailed analysis could be performed.
- Given the dependence of e_{max} and e_{min} on overburden pressure and particle size distribution, Ottawa F-65 sand index testing should involve a more detailed analysis of the ranges in void ratio under different initial state conditions.
- As far as laboratory test data available for the study of liquefaction, the level of detail of the analysed *CRR*-magnitudes, relative densities, overburden pressures and shearing time was considered at times sub-optimal. A suggestion for future research could involve a detailed *CUDSS* and *MUDSS* test programme which could provide enough points for the adequate characterisation of the critical state line and allow a much more detailed analysis of the onset of liquefaction under a wider range of conditions. *CSR* equivalency between different values of D_{R0} is crucial in trying to understand liquefaction better.

- The author of this dissertation strongly recommends further research to try and validate the unified calibration methodology *CM2* and its assumptions with the help of different experimental sources, such as the geo-centrifuge tests from LEAPs and other laboratory test databases which thoroughly study the phenomenon of liquefaction, in combination with real-geometry FE (or FD) simulations of said experiments.

- It is strongly recommended that Plaxis implements an add-on feature to the PM4Sand model which would allow the modification of its internal secondary and tertiary parameters. This implementation does not need to be visible, but at least available so that the model can be more flexible for academic purposes.

- Future research could include the adaptation of the PM4Sand model formulation so that it can model dense sand behaviour more accurately as well as allow for the stress path loci to shift more towards the centre. In both cases, it would mean to change the formulation to allow: the stiffness to degrade faster, greater magnitudes of peak r_us.

- Limitations of databases that were used to build penetration-based *CRR*-correlations, were mainly regarding the availability of data at locations deeper than 15 m. If one wishes to analyse the liquefaction hazard of deep cohesionless layers, these databases must be updated to include deeper points where liquefaction has been observed, not only at the surface or near surface through visual identification, but through other auscultation methods like boreholes or geophysical surveys. This, of course, is no simple endeavour. In fact, it is one of the most difficult parts of investigating the behaviour of liquefaction, not to mention that expanding said databases conveys considerable cost.

- Section 8.2.1 evaluated situations where delays in pore pressure evolution within the same layer with increasing overburden pressure could be explained through dissipation of pore pressures to regions with lower accumulations of stress. However, future research needs to confirm whether fully-undrained simulations are actually capable of doing this.

- Further research could be oriented towards analysing the effect of a combined increase in volume and weight of the structure has on liquefaction hazard.

10.2.2 Regarding engineering applications

Cyclic undrained behaviour and selecting liquefaction-triggering criteria

Before the use of any constitutive model, especially one as sensitive as the PM4Sand model, it is mandatory to determine the assumptions that the modeller will base its calibration on. As the saying goes: "*Garbage in, garbage out*". For the proper modelling of liquefaction, one must properly identify the liquefaction-triggering criteria which are needed to represent it adequately in a physically-consistent way. Therefore, if one wished to use PM4Sand in another benchmark calibration study using a different standardised sand, the author would recommend that a thorough *CUDSS* and *MUDSS* test batch be performed so that the model can be properly calibrated using adequate assumptions.

Calibration of the PM4Sand model using a holistic approach

If one were to evaluate whether to use *CM1* or *CM2* within a liquefaction hazard assessment of a project, the author would recommend the use of *CM2* with caution. Given that this is the first time that a holistic calibration methodology has been proposed, its validity still needs to be confirmed by other studies. However, from the results that have been presented in this thesis, it was clear that *CM2* provided more physically-consistent results than *CM1*.

Identification of triggering of liquefaction in a 1D setting

As mentioned throughout the dissertation, since the identification and calibration of liquefaction in practice and through the PM4Sand model, respectively, have been performed using a pore pressure and shear strain basis, the proper evaluation of liquefaction needs to be performed in terms of both parameters as well. If only one parameter indicates liquefaction while the other does not, care must be taken before conclusions can be drawn. However, in the case of contradicting results, it is usually safest to assume that liquefaction hazard is a possibility, but not a certainty.

Considerations to take into account when modelling liquefiable layers in a 2D setting

One of the most important things to take into account when transitioning from 1D to 2D is the meshing conditions. 1D and 2D wave propagation will not be the same and therefore, if one wished to compared them, an equivalent mesh-size must be selected for the 2D model. However, this may lead to excessively large computational costs, which is why a solution would be to proceed with a coarser mesh and evaluate how the liquefaction hazard diverges and take precautions based on that. Additionally, now that it is known that liquefaction hazard does indeed increase with the presence of a structure, around its vicinity, liquefaction mitigation plans must adapt for this condition.

Bibliography

Alarcón-Guzmán, A., J. L. Chameau, G. A. Leonards, and J. D. Frost (1989). "Shear modulus and cyclic strength behaviour of sands". In: *Soils and Foundations* 29.4, pp. 105–119.

Andrus, R. D., H. Hayati, and N. P. Mohanan (2009). "Correcting liquefaction resistance for aged sands using measured to estimated velocity ratio". In: *Journal of Geotechnical and Environmental Engineering* 135.6, pp. 735–744. DOI: https://doi.org/10.1061/(ASCE)GT.1943-5606.0000025.

Andrus, R. D., P. Piratheepan, J. Zhang, B. S. Ellis, and C. H. Juang (2004). "Comparing liquefaction evaluation methods using penetration-Vs relationships". In: *Soil Dynamics and Earthquake Engineering* 24, pp. 713–721. DOI: https://doi.org/10.1016/j.soildyn.2004.06.001.

Andrus, R. D. and K. H. Stokoe (2000). "Liquefaction resistance of soils from shear-wave velocity". In: *Journal of Geotechnical and Environmental Engineering* 126.11, pp. 1015–1025. DOI: https://doi.org/10.1061/(ASCE)1090-0241(2000)126:11(1015).

ANVS (2017). *Seismic design and qualification for nuclear power plants*. (revised version of IAEA standard NS-GS-1.6, 2010). English. Authority for Nuclear Safety and Radiation Protection.

Armstrong, R. J. (2018). "Numerical analysis of LEAP centrifuge tests using a practice-based approach". In: *Soil Dynamics and Earthquake Engineering* 133, pp. 793–803. DOI: http://dx.doi.org/10.1016/j.soildyn.2017.06.025.

ASTM International (2014a). *Designation: D422-63 (Reapproved 2007). Standard test method for particle-size analysis for soils*. English.

ASTM International (2014b). *Designation: D854-14. Standard test methods for specific gravity of soil solids by water pycnometer*. English.

ASTM International (2016). *Designation: D44254-16. Standard Test Methods for Minimum Index Density and Unit Weight of Soils and Calculation of Relative Density*. English.

Baldi, G., R. Bellotti, V. Ghionna, M. Jamiolkowski, and D. C. F. Lo Presti (1989). "Modulus of sands from CPTs and DMTs". In: *12th International Conference of Soil Mechanics and Foundation Engineering*. Rotterdam, NL, pp. 165–170.

Baldi, G., R. Bellotti, V. Ghionna, M. Jamiolkowski, and E. Pasqualini (1986). "Interpretation of CPTs and CPTUs; 2nd part: drained penetration of sands". In: *4th International Geotechnical Seminar*. Singapore, pp. 143–156.

Bolton, M. D. (1986). "The strength and dilatancy of sands". In: *Géotechnique* 36.1, pp. 65–78.

Bommer, J. J., B. Dost, B. Edwards, P. P. Kruiver, P. Meijers, M. Ntinalexis, A. Rodríguez-Marek, E. Ruigrok, J. Spetzler, and P. J. Stafford (2017a). "V4 ground-motion model (GMM) for response spectral accelerations, peak ground velocity, and significant durations in the Groningen field. Version 2.1". In:

Bommer, J. J., B. Dost, B. Edwards, P. P. Kruiver, P. Meijers, M. Ntinalexis, A. Rodríguez-Marek, E. Ruigrok, J. Spetzler, and P. J. Stafford (2017b). "V4 ground-motion model (GMM) for response spectral accelerations, peak ground velocity, and significant durations in the Groningen field. Version 2". In:

Bommer, J. J., B. Edwards, P. Kruiver, A. Rodríguez-Marek, P. J. Stafford, B. Dost, M. Ntinalexis, E. Ruigrok, and J. Spetzler (2018). "V5 ground-motion model for the Groningen field. Revision 1". In:

Boulanger, R. W. (2003). "Relating Kα to relative state parameter index". In: *Journal of Geotechnical and Geoenvironmental Engineering* 129.8, pp. 770–773. DOI: https://doi.org/10.1061/(ASCE)1090-0241(2003)129:8(770).

Boulanger, R. W., R. B. Seed, C. K. Chan, H. B. Seed, and J. Sousa (1991). *Liquefaction behavior of saturated sands under uni-directional and bi-directional monotonic and cyclic simple shear loading*. UCB/GT/91-08. University of California, Berkeley.

Boulanger, R. W. and K. Ziotopoulou (2017). *PM4Sand, a sand plasticity model for earthquake engineering applications (Version 3.1)*. University of California, Davis.

Brinkgreve, R. B. J., M. H. Kappert, and P. G. Bonnier (2007). "Hysteretic damping in a small-strain stiffness model". In: *Numerical models in geomechanics - NUMGE 2007*. London, UK, pp. 737–742. ISBN: 978-0-415-44027-1.

Carey, T. J., T. Hashimoto, D. Cimini, and B. L. Kutter (2018). "LEAP-GWU-2015 centrifuge test at UC Davis". In: *Soil Dynamics and Earthquake Engineering* 113, pp. 663–670. DOI: https://doi.org/10.1016/j.soildyn.2017.01.030.

CEN (2004). *Eurocode 2: Design of concrete structures. Part 1-1: General rules and rules for buildings*. English.

Cimini, D. (2015). *Hydraulic conductivity data Ottawa F-65 sand*. Cooper Lab.

Cooper Lab (2013). *Dry densities Ottawa F-65 sand*. Cooper Lab.

Dafalias, Y. F. and M. T. Manzari (2004). "Simple plasticity sand model accounting for fabric change effects". In: *Journal of Engineering Mechanics* 130.6, pp. 622–634. DOI: https://doi.org/10.1061/(ASCE)0733-9399(2004)130:6(622).

Darendeli, M. B. (2001). "Development of a new family of normalized modulus reduction and material damping curves". PhD thesis. The University of Texas at Austin.

Das, B. M. (2010). *Principles of geotechnical engineering*. 7th. Cengage Learning.

El Ghoraiby, M. A. and M. T. Manzari (2018). *Liquefaction Experiments and Analysis Projects (LEAP): Stress-strain response of Ottawa F-65 sand in cyclic direct simple shear tests*. George Washington University.

El Ghoraiby, M. A., H. Park, and M. T. Manzari (2017). *LEAP 2017: Soil characterization and element tests for Ottawa F65 sand*. George Washington University.

Fear, C. E. and P. K. Robertson (1995). "Estimating the undrained strength of sand: a theoretical framework". In: *Canadian Geotechnical Journal* 32, pp. 859–870.

FEMA (2007). *Design Guide for improving critical facility safety from flooding and high winds. Risk management series*.

Gavin, K. (2018). "Use of CPT for the design of shallow and deep foundations on sand". In: *Cone Penetration Testing 2018*. Delft, Netherlands, pp. 45–61. ISBN: 978-1-138-58449-5.

Hegazy, Y. A. and P. W. Mayne (1995). "Statistical correlations between V_s and cone penetration data for different soil types". In: *International Symposium on Cone Penetration Testing, CPT '95*. Linkoping, Sweden, pp. 173–178.

Huang, B., T. Xia, H. Qiu, X. Zhou, and W. Chen (2017). "Shear wave velocity in sand considering the effects of frequency based on the particle contact theory". In: *Wave Motion* 72, pp. 173–186. DOI: http://dx.doi.org/10.1016/j.wavemoti.2017.02.006.

Hudson, M., I. M. Idriss, and M. Beikae (1994). *User's manual for QUAD4M. A computer program to evaluate the seismic response of soil structures using finite element procedures and incorporating a compliant base*. Version 3.12. University of California, Davis.

IAEA (2004). *Geotechnical aspects of site evaluation and foundations for nuclear power plants. NS-G-3.6*. English.

IAEA (2010). *Seismic design and qualification for nuclear power plants. NS-G-1.6*. English.

Idriss, I. M. (1999). "An update to the Seed-Idriss simplified procedure for evaluating liquefaction potential". In: *Proceedings of TRB workshop on New Approaches to Liquefaction*. Federal Highway Administration. Washington DC, USA.

Idriss, I. M. and R. W. Boulanger (2008). *Soil liquefaction during earthquakes*. EERI Publications. ISBN: 9781932884364.

Idriss, I. M. and R. W. Boulanger (2010). *SPT-based liquefaction triggering procedures*. UCD/CGM-10/02. University of California, Davis.

Idriss, I. M. and R. W. Boulanger (2014). *CPT and SPT based liquefaction triggering procedures*. UCD/CGM-14/01. University of California, Davis.

Jamiolkowski, M., C. C. Ladd, J. T. Germaine, and R. Lancellotta (1985). "New developments in field and laboratory testing of soils". In: *11th International Conference on Soil Mechanics and Foundation Engineering, Vol. 1*. San Francisco, USA, pp. 57–153.

Klar, A., M. Roed, I. Rocchi, and I. Paegle (2019). "Evaluation of horizontal stresses in soil during direct simple shear by high-resolution distributed fiber optic sensing". In: *Sensors* 19, pp. 3684–3698. DOI: https://doi.org/10.3390/s19173684.

Kokkali, P., T. Abdoun, and M. Zeghal (2018). "Physical modeling of soil liquefaction: Overview of LEAP production test 1 at Rensselaer Polytechnic Institute". In: *Soil Dynamics and Earthquake Engineering* 113, pp. 629–649. DOI: http://dx.doi.org/10.1016/j.soildyn.2017.01.036.

Konstantinou, M., C. Zwanenburg, and P. Meijers (2017). *Dynamic behaviour of Groningen peat - Analysis and parameter assessment*. Deltares.

Kramer, S. L. (1996). *Geotechnical Earthquake Engineering*. 1st. Prenctice Hall. ISBN: 0-13-374943-6.

Kramer, S. L., S. S. Sideras, and M. W. Greenfield (2016). "The timing of liquefaction and its utility in liquefaction hazard evaluation". In: *Soil Dynamics and Earthquake Engineering* 91, pp. 133–146. DOI: https://doi.org/10.1016/j.soildyn.2016.07.025.

Kulhawy, F. H. and P. W. Mayne (1990). *Manual on estimating soil properties for foundation design*. Cornell University.

Kutter, B. L., B. L. Carey, B. L. Zheng, A. Gavras, and N. Stone (2018). "Twenty-four centrifuge tests to quantify sensitivity of lateral spreading to Dr and PGA". In: *Geotechnical Earthquake Engineering and Soil Dynamics V*. Austin, USA, pp. 383–393. DOI: https://doi.org/10.1061/9780784481486.040.

Kutter, B. L., T. J. Carey, T. Hashimoto, M. Zeghal, T. Abdoun, P. Kokkali, G. Madabushi, S. Haigh, F. Burali d'Arezzo, S. Madabushi, W.-Y. Hung, C.-J. Lee, H.-C. Cheng, S. Iai, T. Tobita, T. Ashino, J. Ren, Y.-G. Zhou, Y.M. Chen, Z.-B. Sun, and M. T. Manzari (2015). *LEAP-GWU-2015 experiment specifications, results and comparisons*. University of California, Davis.

Laera, A. and R. B. J. Brinkgreve (2015a). *Ground response analysis in Plaxis 2D*. Plaxis B.V.

Laera, A. and R. B. J. Brinkgreve (2015b). *Site response analysis and liquefaction evaluation*. Plaxis B.V.

Manzari, M. T., M. El Ghoraiby, B. L. Kutter, M. Zeghal, T. Abdoun, P. Arduino, R. J. Armstrong, M. Beaty, T. Carey, Y.M. Chen, A. Ghofrani, D. Gutierrez, N. Goswami, S. K. Haigh, W.-Y. Hung, S. Iai, P. Kokkali, C.-J. Lee, S. P. G. Madabhushi, L. Mejía, M. Sharp, T. Tobita, K. Ueda, Y. G. Zhou, and K. Ziotopoulou (2018). "Liquefaction experiment and analysis projects (LEAP): Summary of observations from the planning phase". In: *Soil Dynamics and Earthquake Engineering* 113, pp. 714–743. DOI: http://dx.doi.org/10.1016/j.soildyn.2017.05.015.

Mayne, P. W., M. Uzielli, and F. Illingworth (2012). *Shallow footing response on sands using a direct method based on cone penetration tests*.

Menq, F-. Y. (2003). "Dynamic properties of sand and gravelly soils". PhD thesis. The University of Texas at Austin.

Morales, B. and K. Ziotopoulou (2018). *Direct simple shear testing of Ottawa F-65 sand. Soil interactions laboratory data report*.

Naesgaard, E. (2011). "A hybrid effective stress - total stress procedure for analyzing soil embankments subjected to potential liquefaction and flow". PhD thesis. The University of British Columbia.

NEN (2016). *Nederlandse norm NEN 9997-1. Geotechnisch ontwerp van constructies - Deel 1: Algemene regels*. Dutch.

NRC (1985). *Liquefaction of soils during earthquakes*. CETS-EE-001. National Research Council.

Obermeier, S. F., E. C. Pond, and S. M. Olson (2001). *Paleoliquefaction studies in continental settings: Geology and geotechnical factors in interperations and back-analysis*. 01-29. USGS.

Parra, A. M. (2016). "Ottawa F-65 Sand charaterization". PhD thesis. University of California Davis.

PEER (2014). *Guidelines for performing hazard-consistent one-dimensional ground response analysis for ground motion prediction*. PEER 2014/16. Pacific Earthquake Engineering Research Center (PEER).

PLAXIS (2019a). *PLAXIS 2D reference manual 2019*. Plaxis B.V.

PLAXIS (2019b). *PLAXIS material models manual 2019*. Plaxis B.V.

Powrie, W. (2004). *Soil mechanics: Concepts and applications*. 2nd. Taylor Francis London.

Richter, C. F. (1958). *Elementary Seismology*. 1st. San Francisco and London: W. H. Freeman and Company.

Rix, G. J. and K. H. Stokoe (1991). "Correlation of initial tangent modulus and cone penetration resistance". In: *1st International Symposium on Calibration Chamber Testing (ISOCCT1)*. Potsdam, USA, pp. 351–362.

Robertson, P. K. (1990). "Soil classification using the cone penetration test". In: *Canadian Geotechnical Journal* 27, pp. 151–158. DOI: https://doi:10.1139/t90-014.

Robertson, P. K. (2010). *Soil behaviour type from the CPT: an update*. Gregg Drilling & Testing Inc.

Robertson, P. K. and K. L. Cabal (2015). *Guide to cone penetration testing for geotechnical engineering*. Gregg Drilling & Testing Inc.

Robertson, P. K., D. J. Woeller, and W. D. L. Finn (1992). "Seismic CPT for evaluating liquefaction potential". In: *Canadian Geotechnical Journal* 29, pp. 686–695.

Robertson, P. K. and C. E. Wride (1998). "Evaluating cyclic liquefaction potential using the cone penetration test". In: *Canadian Geotechnical Journal* 35, pp. 442–459.

Ruffatto, M. (2013). "Recommendation for a new standard sand for use at the UC Davis Geotechnical Modeling Center". MSc thesis. University of California, Davis.

Salgado, R., J. K. Mitchell, and M. Jamiolkowski (1997). "Cavity expansion and penetration resistance in sand". In: *Journal of Geotechnical and Geoenvironmental Engineering* 123.4, pp. 344–354. DOI: https://doi-org.tudelft.idm.oclc.org/10.1061/(ASCE)1090-0241(1997)123:4(344).

Seed, H. B. and I. M. Idriss (1971). "Simplified procedure for evaluating soil liquefaction potential". In: *Journal of Soil Mechanics and Foundations Division* 97.9, pp. 1249–1273.

Soos, P. von (1990). *Properties of soil and rock. Part 4*. German. 4 vols. Berlin: Ernst & Sohn.

Sriskandakumar, S. (2004). "Cyclic loading response of Fraser River sand for validation of numerical models simulating centrifuge tests". MSc thesis. University of British Columbia.

Tobita, T., T. Ashino, J. Ren, and S. Iai (2018). "Kyoto University LEAP-GWU-2015 tests and the importance of curving the ground surface in centrifuge modelling". In: *Soil Dynamics and Earthquake Engineering* 113, pp. 650–662. DOI: http://dx.doi.org/10.1016/j.soildyn.2017.10.012.

Toloza, P. (2018). "Liquefaction modelling using the PM4Sand constitutive model in Plaxis 2D". MSc thesis. Technische Universiteit Delft.

Tziolas, A. (2019). "Evaluation of the PM4Sand constitutive model for the prediction of earthquake-induced and static liquefaction in hydraulic fills". MSc thesis. Technische Universiteit Delft.

Vasko, A., M. El Ghoraiby, and M. T. Manzari (2014). *An investigation into the behavior of Ottawa F-65 sand under monotonic and cyclic shear tests*. George Washington University.

Vilhar, G., A. Laera, F. Foria, A. Gupta, and R. B. J. Brinkgreve (2018). *Implementation, validation and application of PM4Sand model in PLAXIS*. Geotechnical Special Publication, 2018-June (GSP 292). Technische Universiteit Delft.

Wijewickreme, D., A. Dabeet, and P. Byrne (2013). "Some observations on the state of stress in the direct simple shear test using 3D discrete element analysis". In: *Geotechnical Testing Journal* 36.2, pp. 1–8.

Wu, J., A. M. Kammerer, M. F. Riemer, R. B. Seed, and J. M. Pestana (2004). "Laboratory study of liquefaction triggering criteria". In: *13th World Conference on Earthquake Engineering*. Vancouver, Canada.

Youd, T. L. and I. M. Idriss (1997). *Proceedings of the NCEER workshop on evaluation of liquefaction resistance of soils*. NCEER-97-0022. National Center for Earthquake Engineering Research.

Zhou, Y.-G., Z.-B. Sun, and Y.-M. Chen (2018). "Zhejiang University benchmark centrifuge test for LEAP-GWU-2015 and liquefaction responses of a sloping ground". In: *Soil Dynamics and Earthquake Engineering* 113, pp. 698–713. DOI: http://dx.doi.org/10.1016/j.soildyn.2017.03.010.

Ziotopoulou, K., R. W. Boulanger, and S. L. Kramer (2012). *Site response analysis of liquefying sites*. University of California, Davis.

Ziotopoulou, K., J. M. Montgomery, A. M. Parra, and B. Morales (2018). "Cyclic strength of Ottawa F-65 sand: Laboratory testing and constitutive model calibration". In: *Geotechnical Earthquake Engineering and Soil Dynamics V*. Austin, USA, pp. 180–189. DOI: https://doi.org/10.1061/9780784481486.019.

Ziotopoulou, K., J. M. Montgomery, D. Tsiaousi, P. Tasiopoulou, J. Ugalde, and T. Travasarou (2019). "Effect of numerical modeling protocols on the seismic response of a liquefiable slope". In: *Earthquake Geotechnical Engineering for Protection and Development of Environment and Constructions*. Rome, Italy, pp. 5913–5921. ISBN: 978-0-367-14328-2.

Appendix - Additional relevant figures

The appendix of this dissertation contains additional relevant figures which are to be used by the reader as a reference while reading the document. Given that a lot of information was analysed, most of the figures were not included in the main text, but here. The appendix's figures are presented in the following order:

1. Figures related to the calibration of the case study PM4Sand layers, section 7.3.
2. Figures related to the 1D liquefaction hazard assessment of the Umbria Marche *BDBE* signal, section 8.2.1.
   (a) r_u-time histories
   (b) γ-time histories
   (c) ATHs
   (d) Frequency contents
3. Figures related to the 2D liquefaction hazard assessment and soil-structure interaction of hypothetical critical facility, section 9.2.

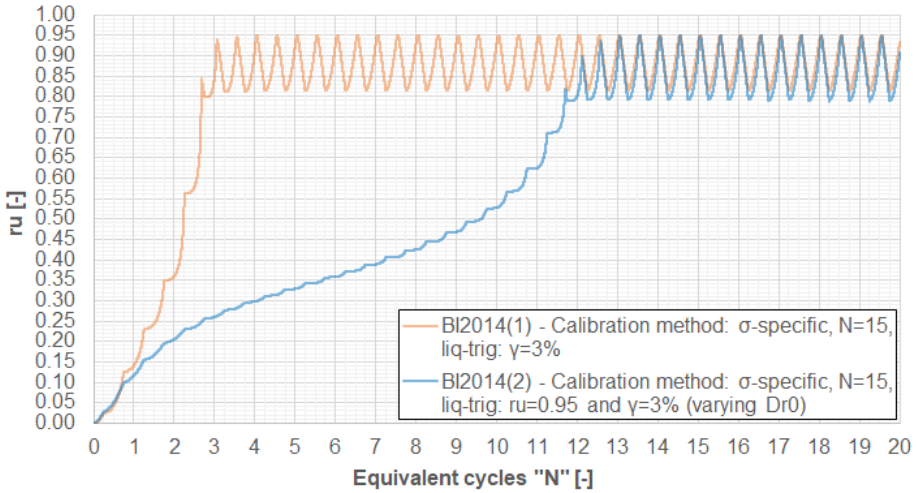

(a) r_u-evolution

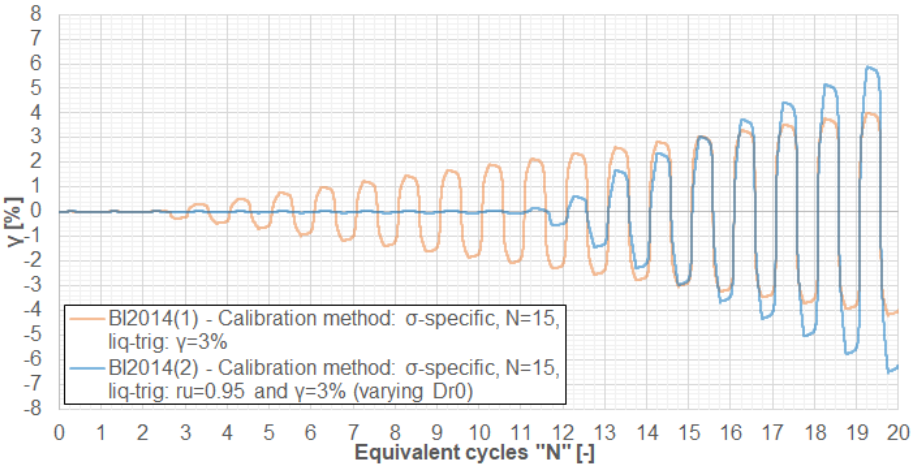

(b) γ-evolution

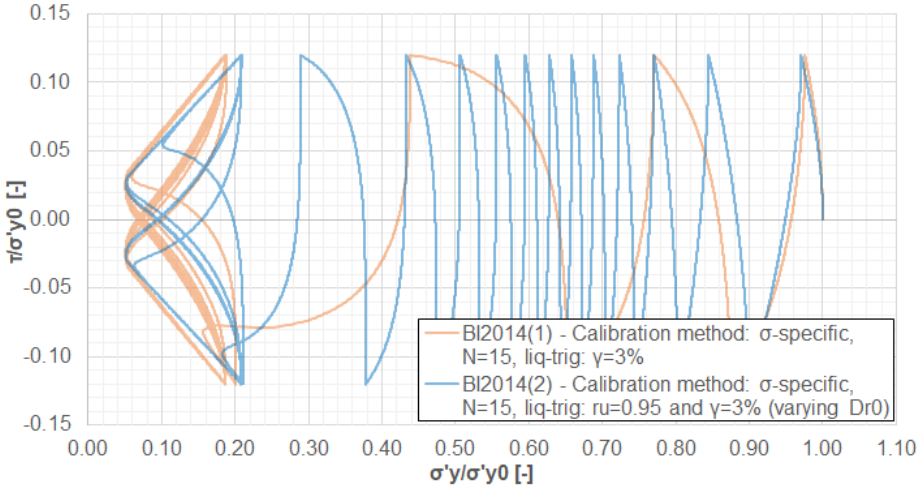

(c) $\frac{\sigma'_y}{\sigma'_{v0}}$-$\frac{\tau}{\sigma'_{v0}}$ space

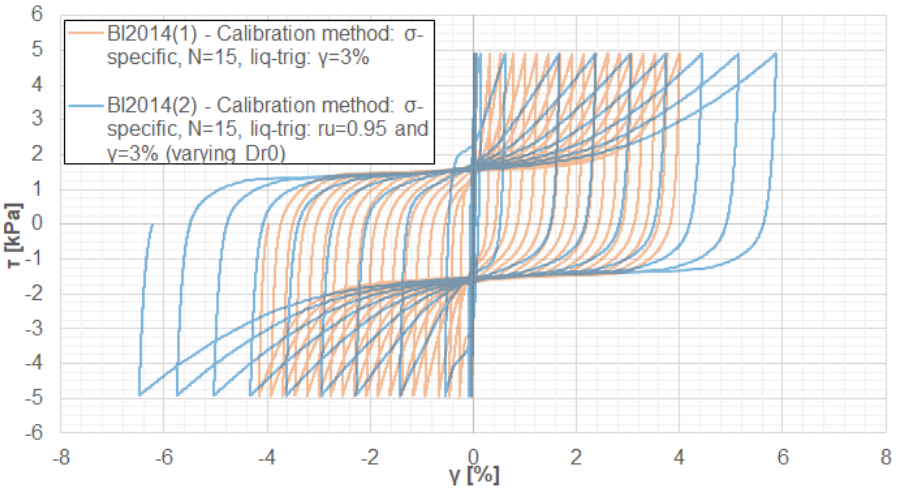

(d) γ-τ space

Figure 10.1: Comparison of calibrated *CM1* and *CM2* models in layer 1-3-NASC-MS

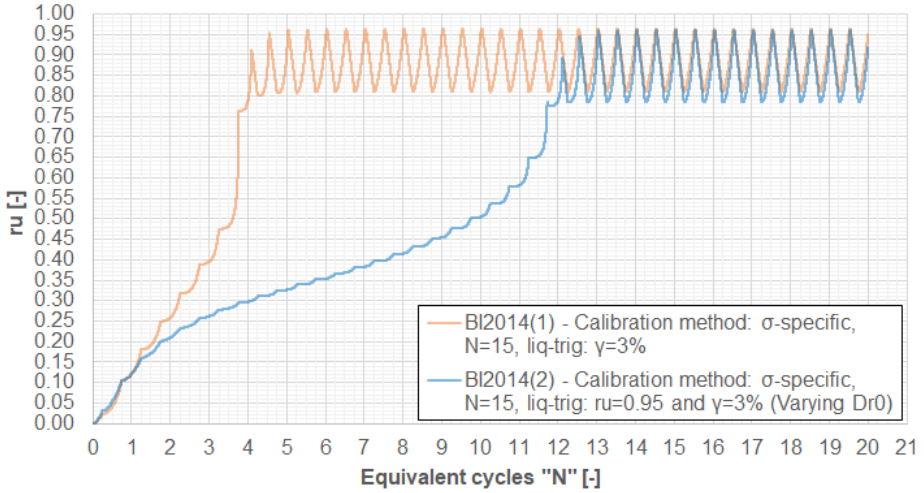

(a) r_u-evolution

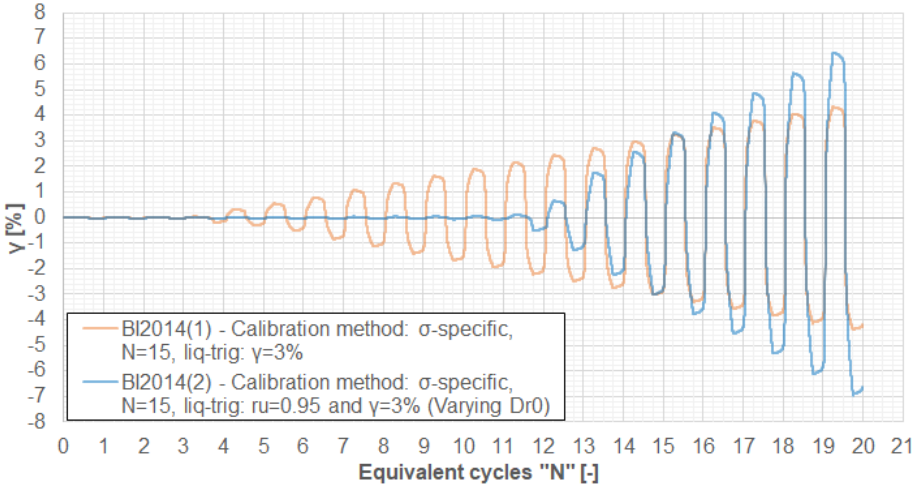

(b) γ-evolution

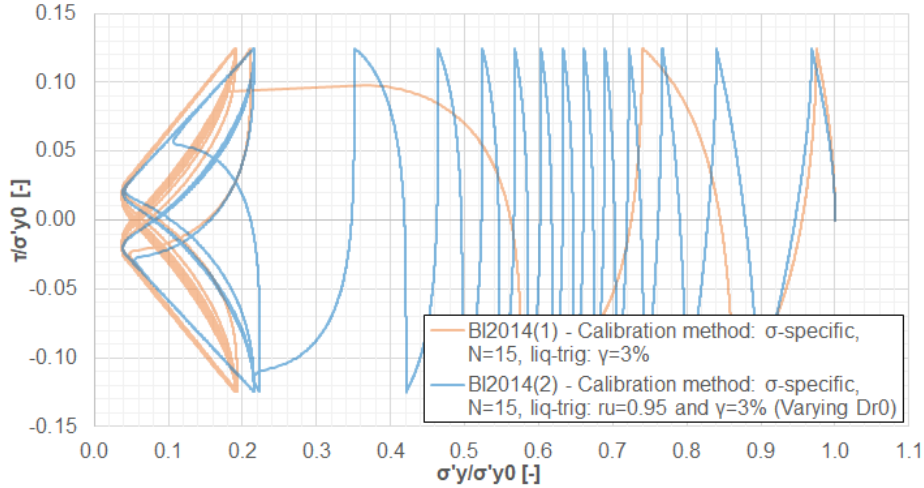

(c) $\frac{\sigma'_v}{\sigma'_{v0}}$-$\frac{\tau}{\sigma'_{v0}}$ space

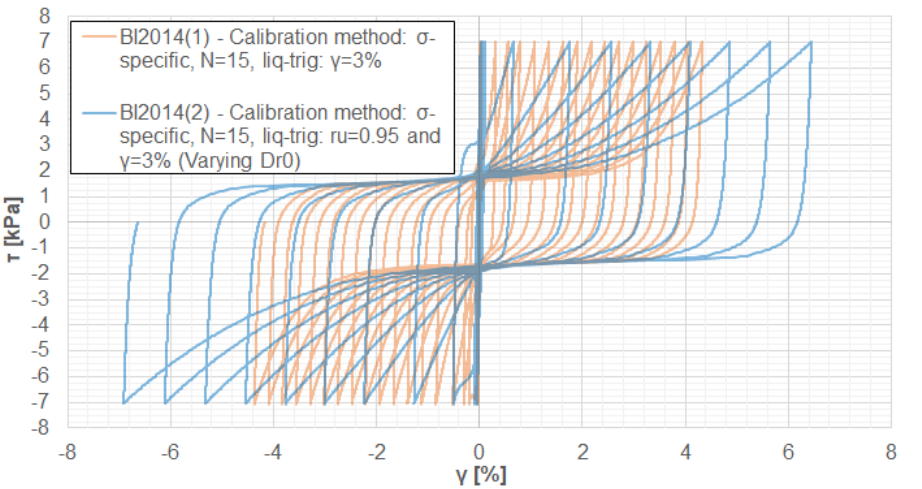

(d) γ-τ space

Figure 10.2: Comparison of calibrated *CM1* and *CM2* models in layer 1-4-NASC-MS

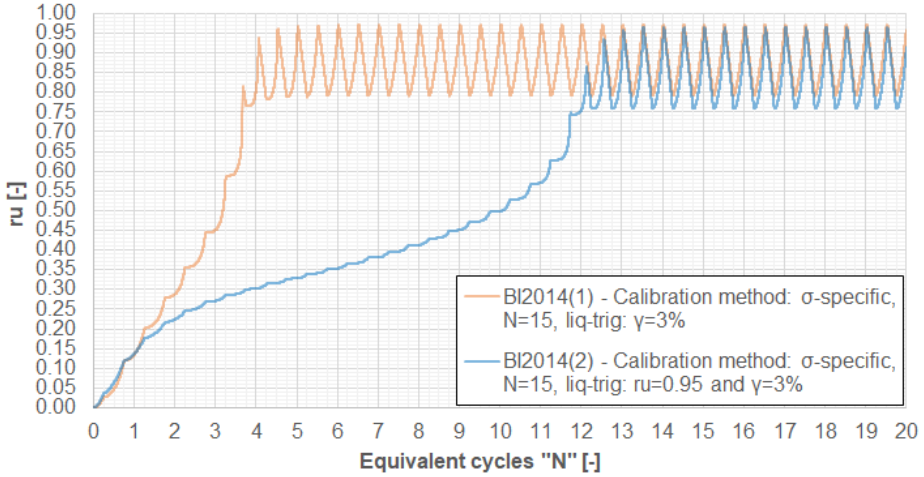

(a) r_u-evolution

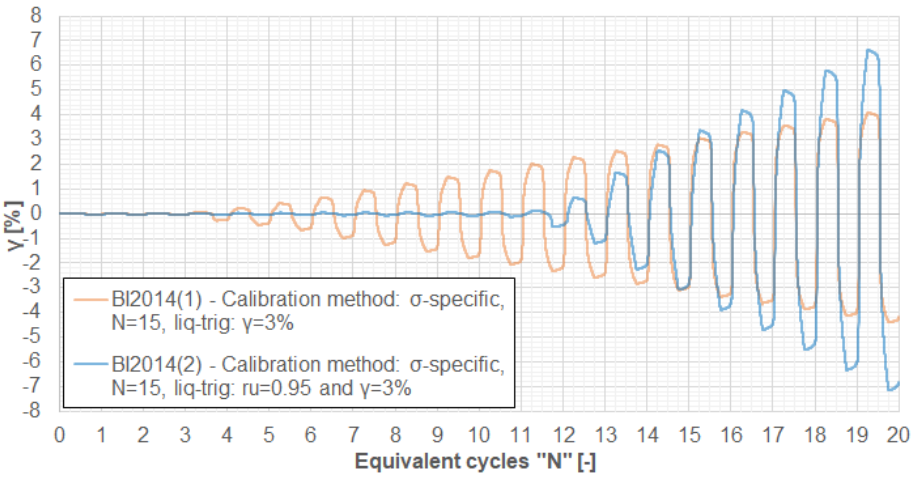

(b) γ-evolution

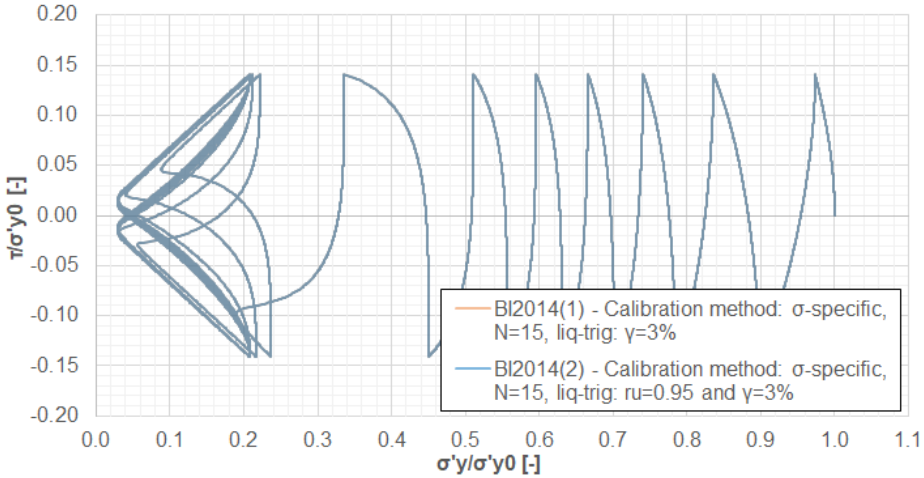

(c) $\frac{\sigma'_v}{\sigma'_{v0}}$-$\frac{\tau}{\sigma'_{v0}}$ space (erratum)

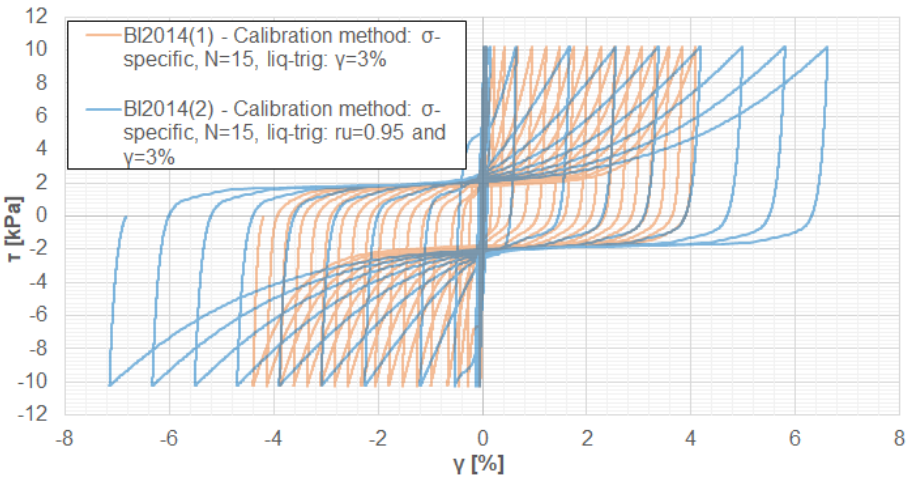

(d) γ-τ space

Figure 10.3: Comparison of calibrated *CM1* and *CM2* models in layer 1-5-NASC-MS

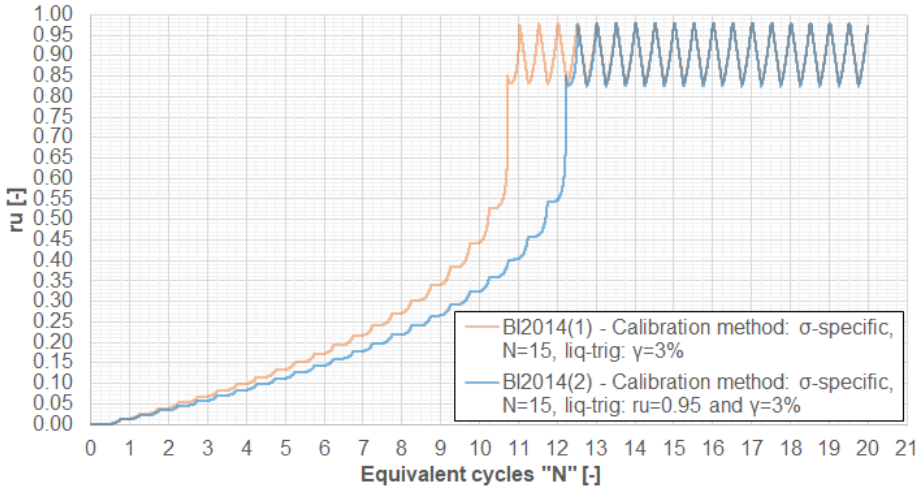

(a) r_u-evolution

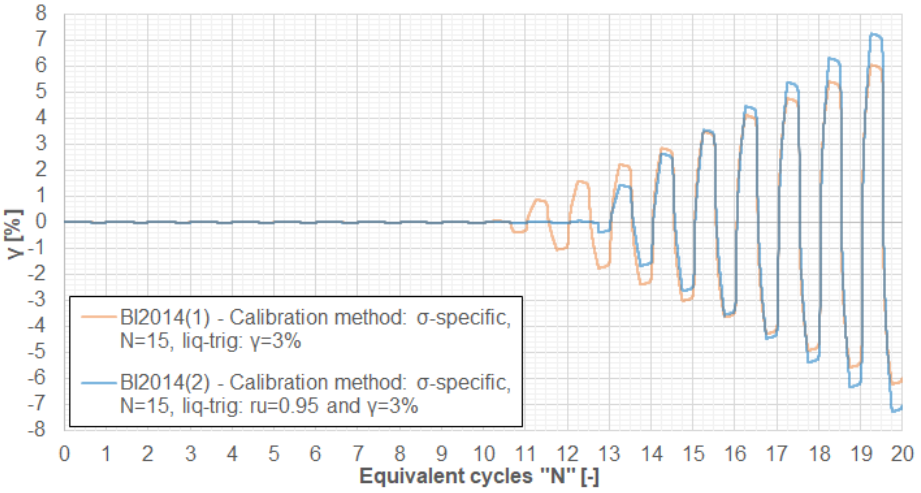

(b) γ-evolution

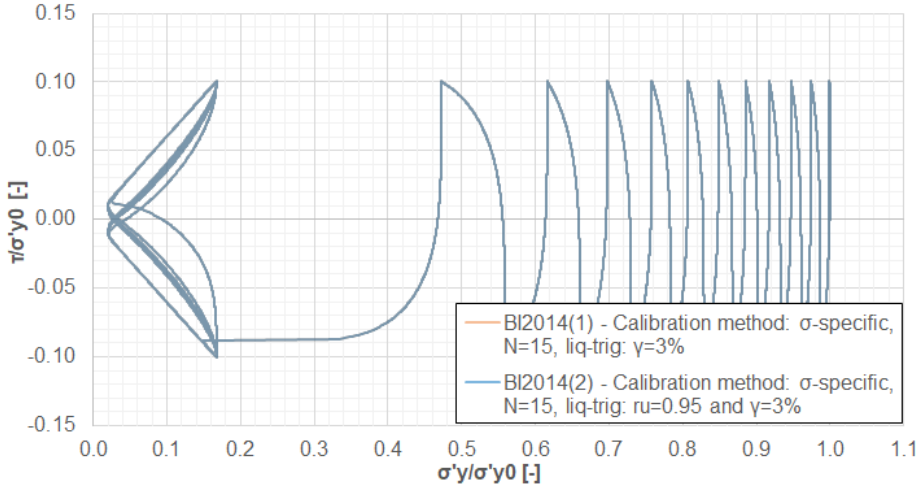

(c) $\frac{\sigma'_v}{\sigma'_{v0}}$-$\frac{\tau}{\sigma'_{v0}}$ space (erratum)

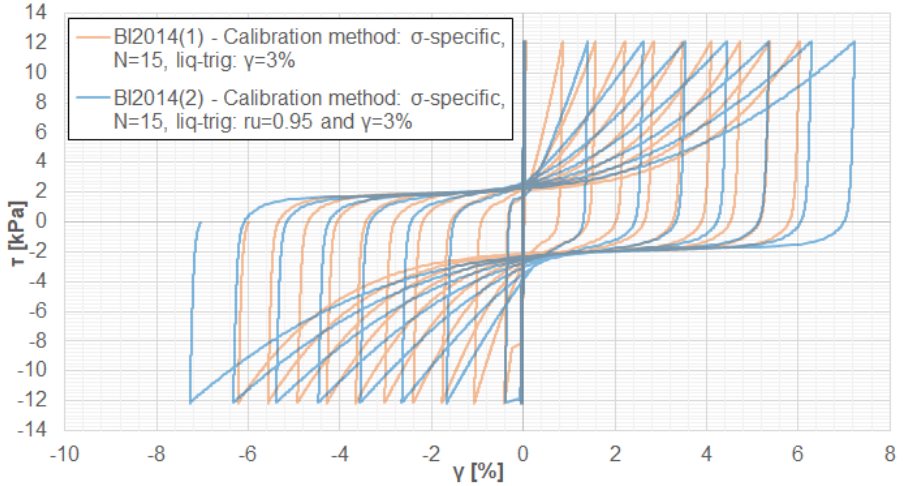

(d) γ-τ space

Figure 10.4: Comparison of calibrated *CM1* and *CM2* models in layer 3-1-BX-FS

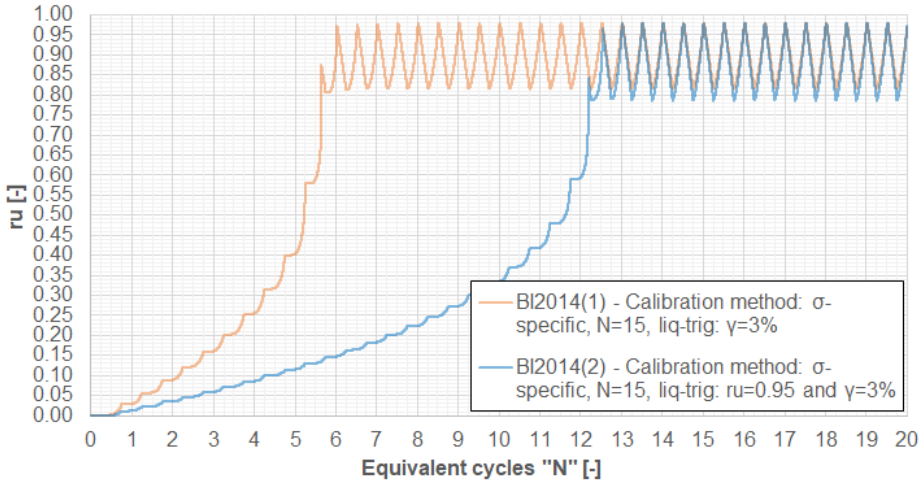

(a) r_u-evolution

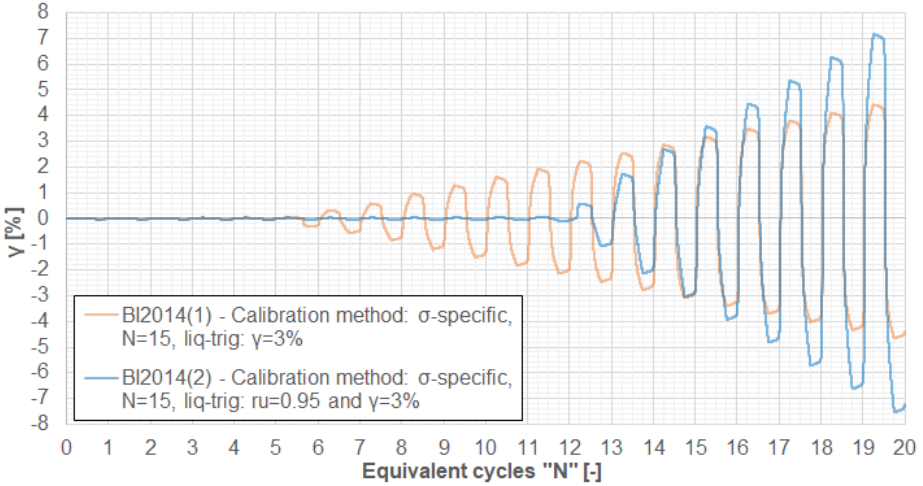

(b) γ-evolution

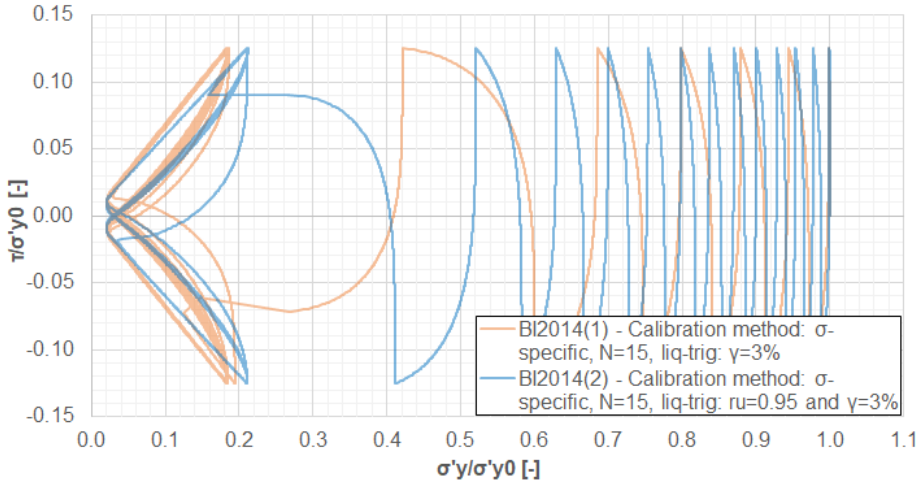

(c) $\frac{\sigma'_v}{\sigma'_{v0}}$-$\frac{\tau}{\sigma'_{v0}}$ space

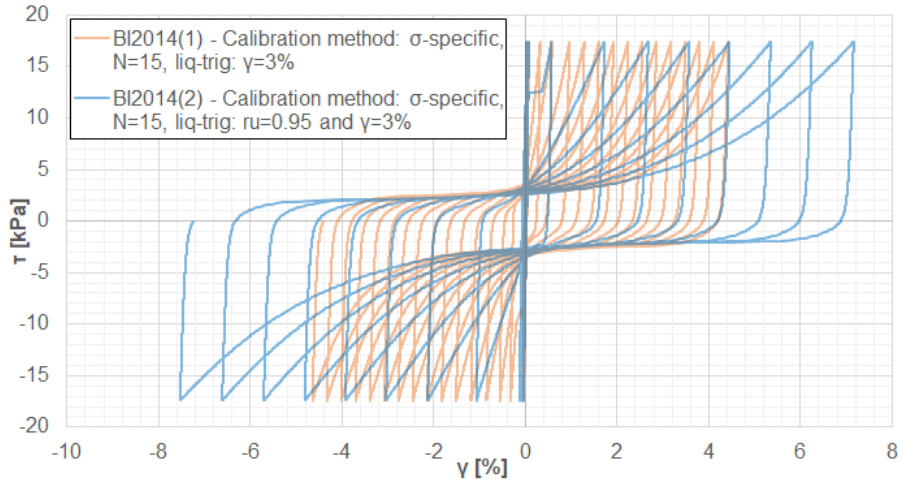

(d) γ-τ space

Figure 10.5: Comparison of calibrated *CM1* and *CM2* models in layer 3-2-BX-FS

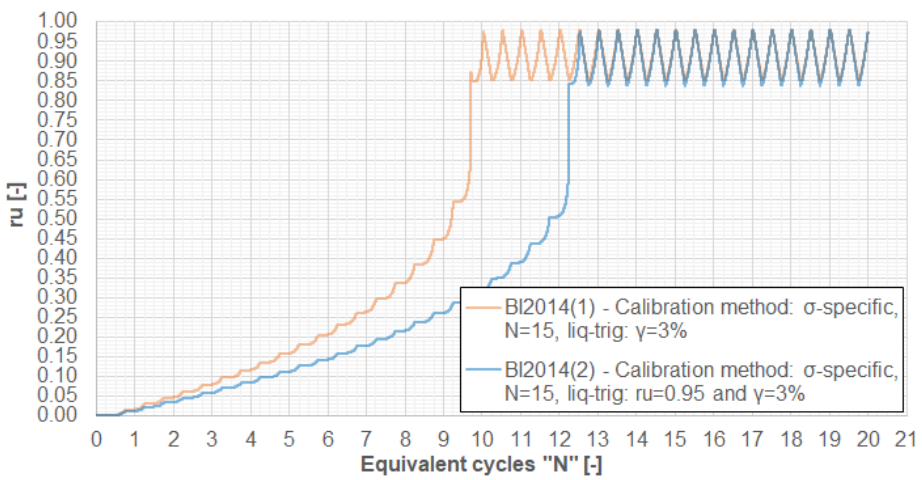

(a) r_u-evolution

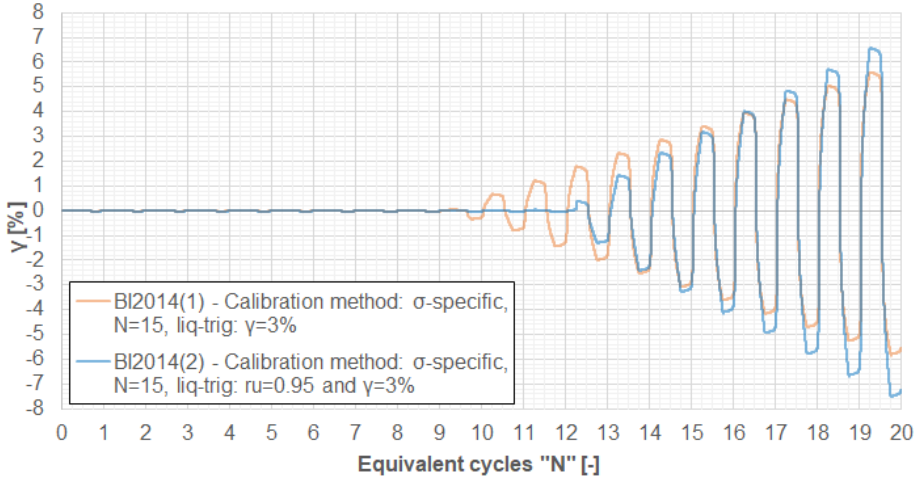

(b) γ-evolution

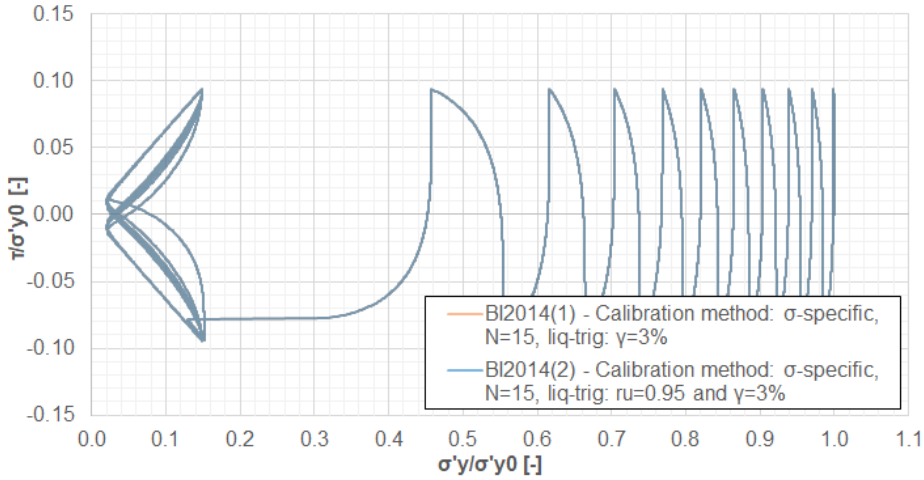

(c) $\frac{\sigma'_v}{\sigma'_{v0}}$-$\frac{\tau}{\sigma'_{v0}}$ space (erratum)

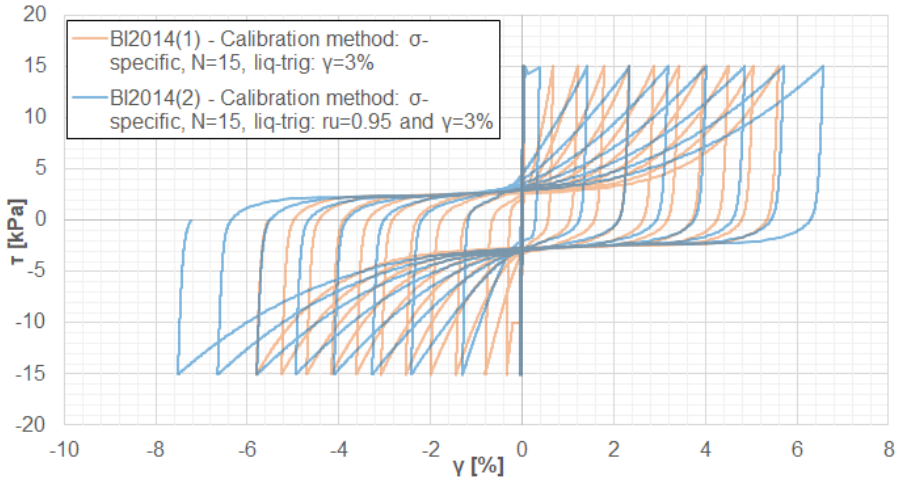

(d) γ-τ space

Figure 10.6: Comparison of calibrated *CM1* and *CM2* models in layer 3-3-BX-FS

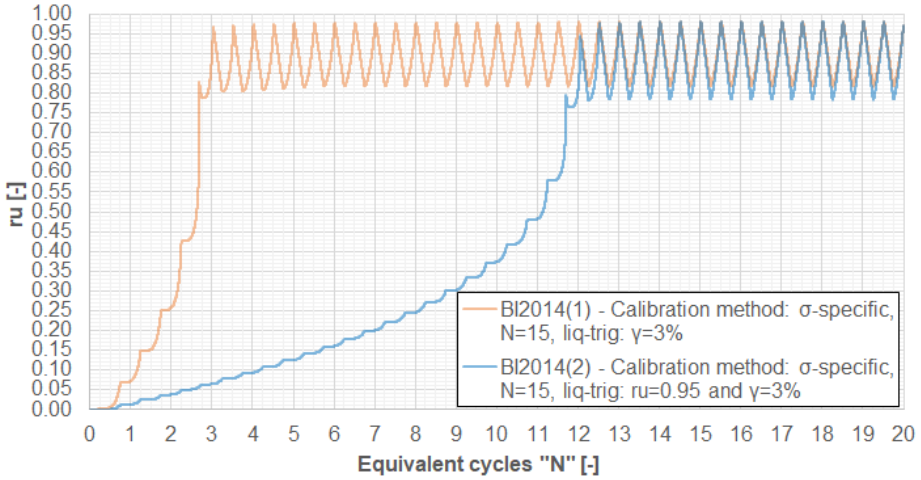

(a) r_u-evolution

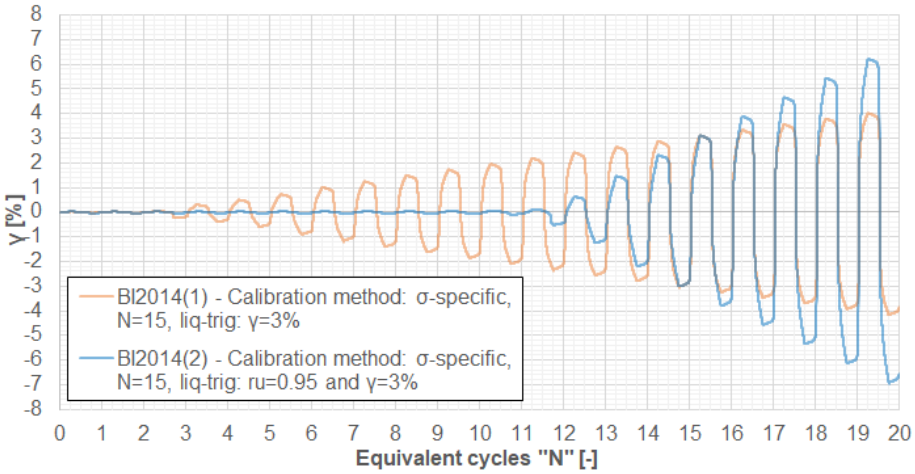

(b) γ-evolution

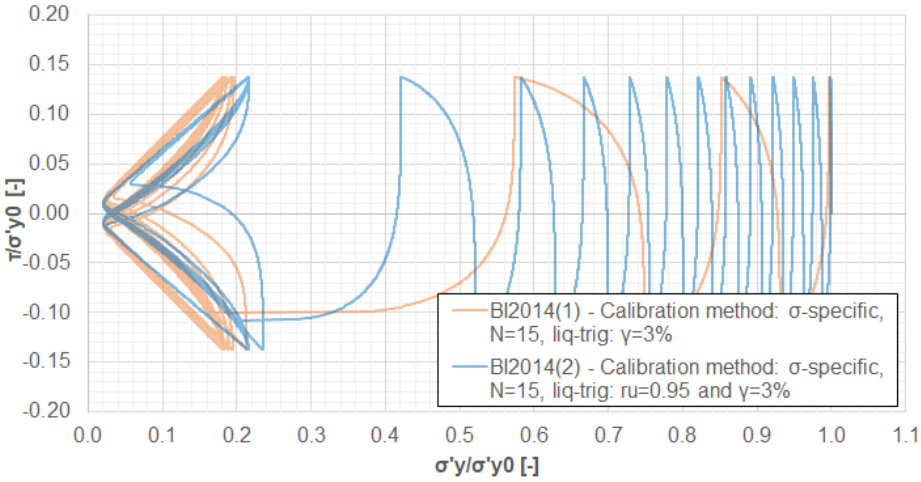

(c) $\frac{\sigma'_v}{\sigma'_{v0}}$-$\frac{\tau}{\sigma'_{v0}}$ space

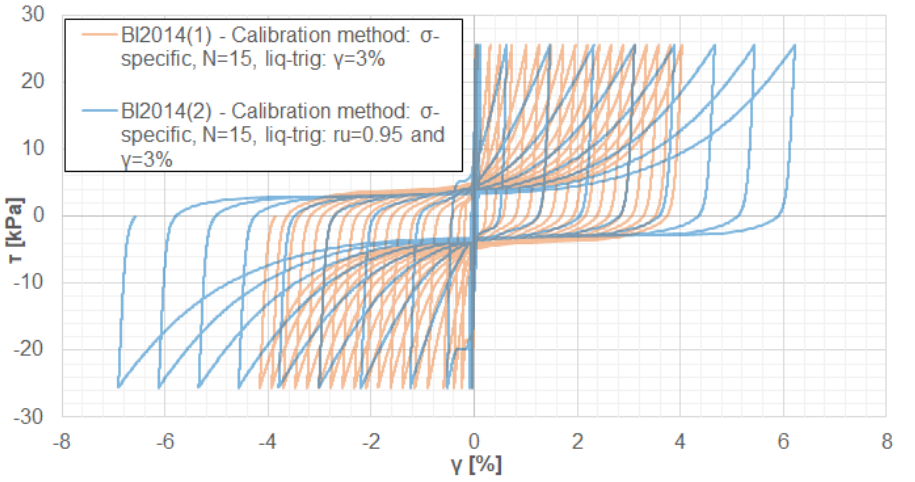

(d) γ-τ space

Figure 10.7: Comparison of calibrated *CM1* and *CM2* models in layer 3-4-BX-FS

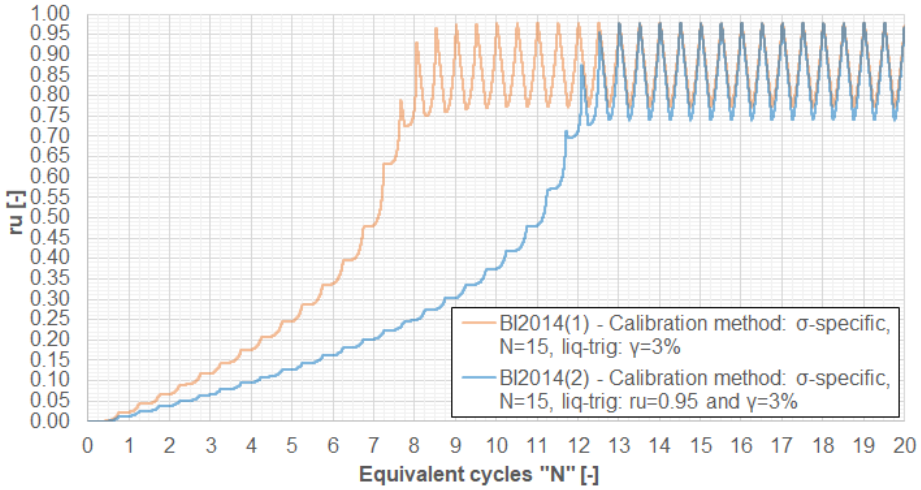

(a) r_u-evolution

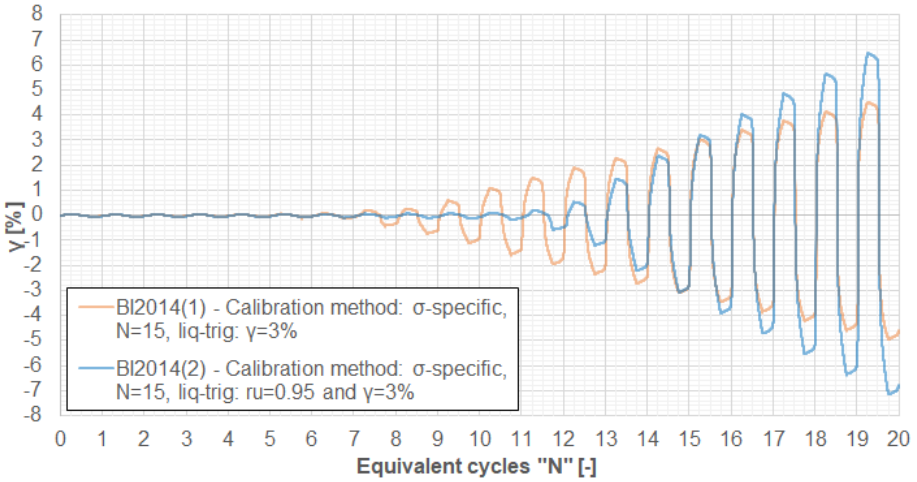

(b) γ-evolution

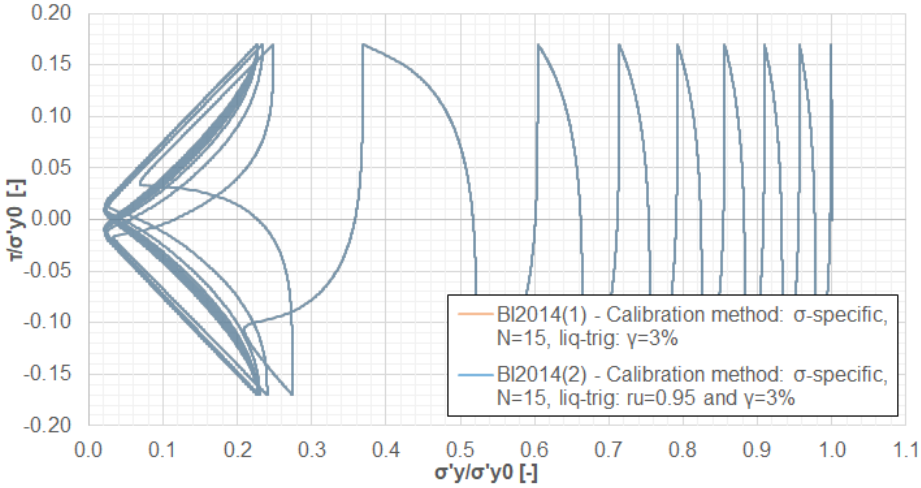

(c) $\frac{\sigma'_v}{\sigma'_{v0}}$-$\frac{\tau}{\sigma'_{v0}}$ space (erratum)

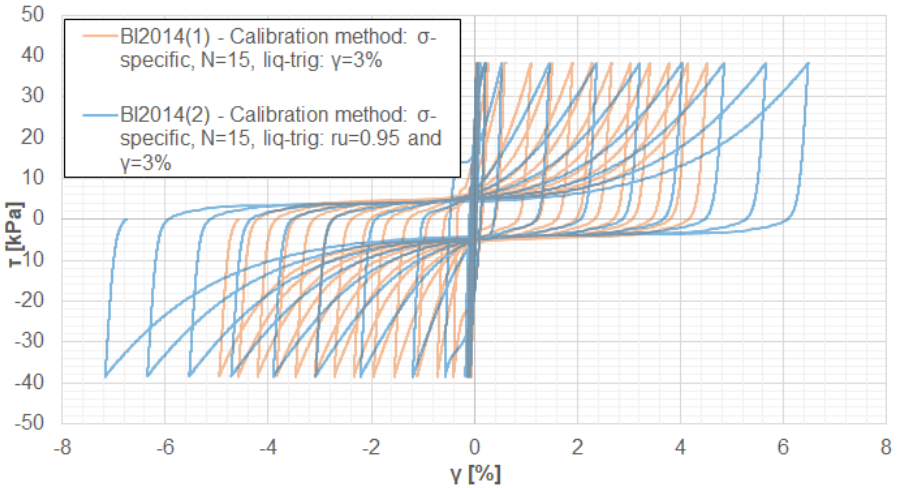

(d) γ-τ space

Figure 10.8: Comparison of calibrated *CM1* and *CM2* models in layer 5-BX-MS

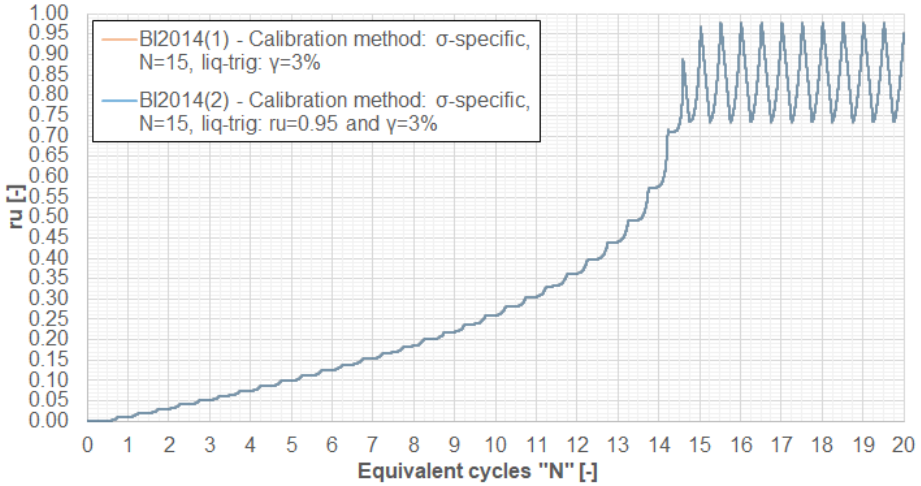

(a) r_u-evolution

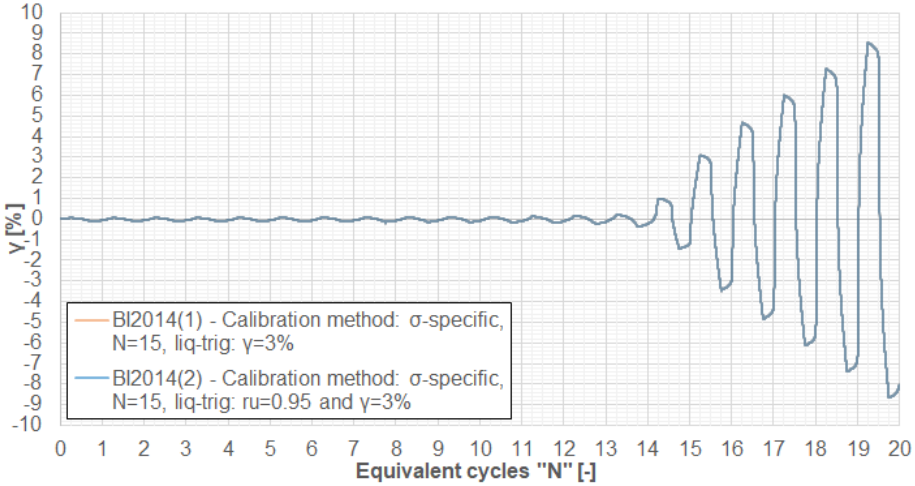

(b) γ-evolution

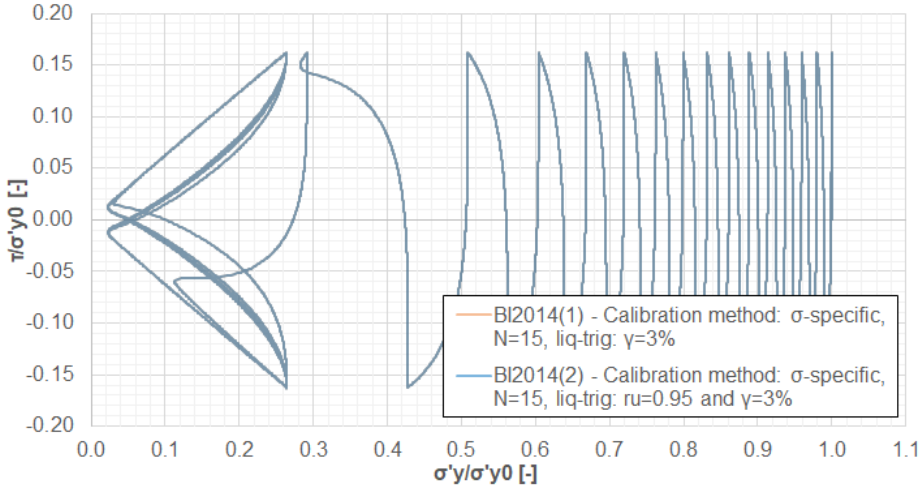

(c) $\frac{\sigma'_v}{\sigma'_{v0}}$-$\frac{\tau}{\sigma'_{v0}}$ space

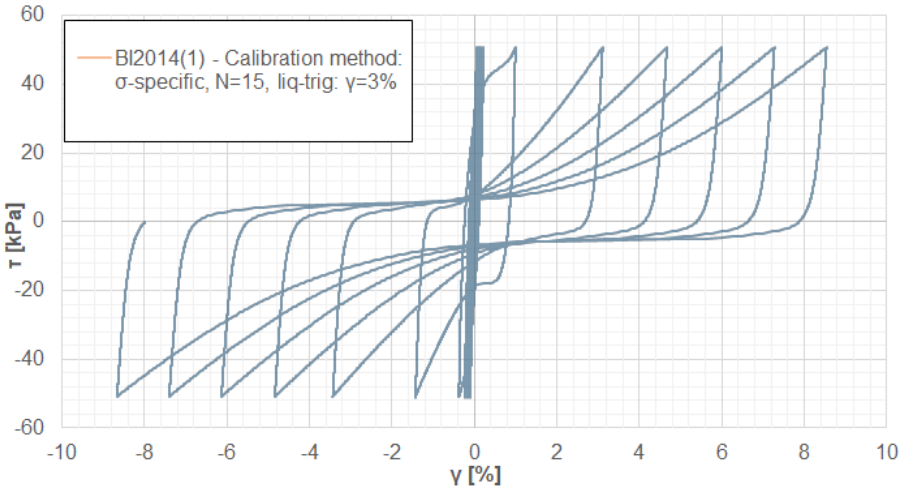

(d) γ-τ space

Figure 10.9: Comparison of calibrated *CM1* and *CM2* models in layer 7-1-EE-MS

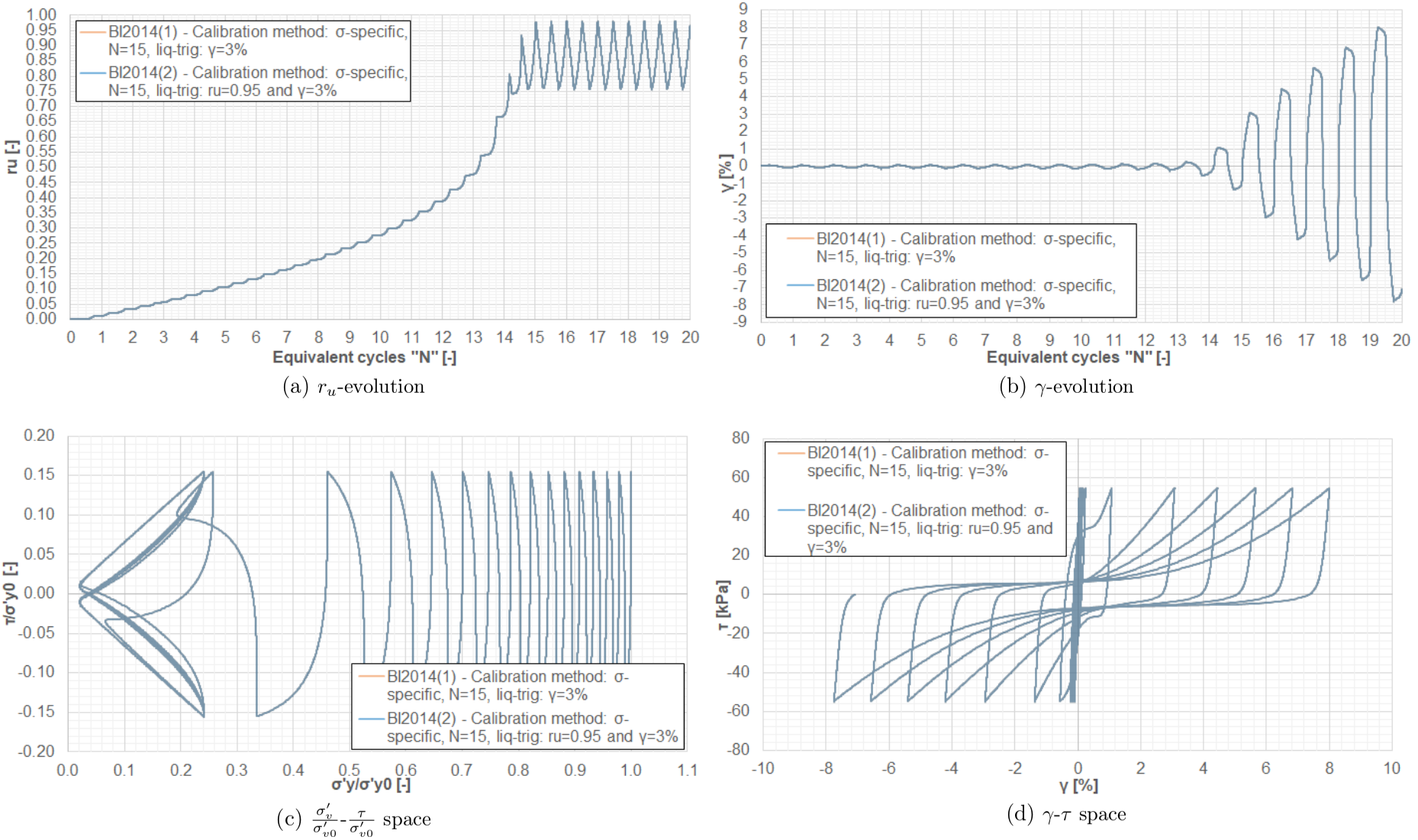

(a) r_u-evolution

(b) γ-evolution

(c) $\frac{\sigma'_v}{\sigma'_{v0}}$-$\frac{\tau}{\sigma'_{v0}}$ space

(d) γ-τ space

Figure 10.10: Comparison of calibrated *CM1* and *CM2* models in layer 7-2-EE-MS

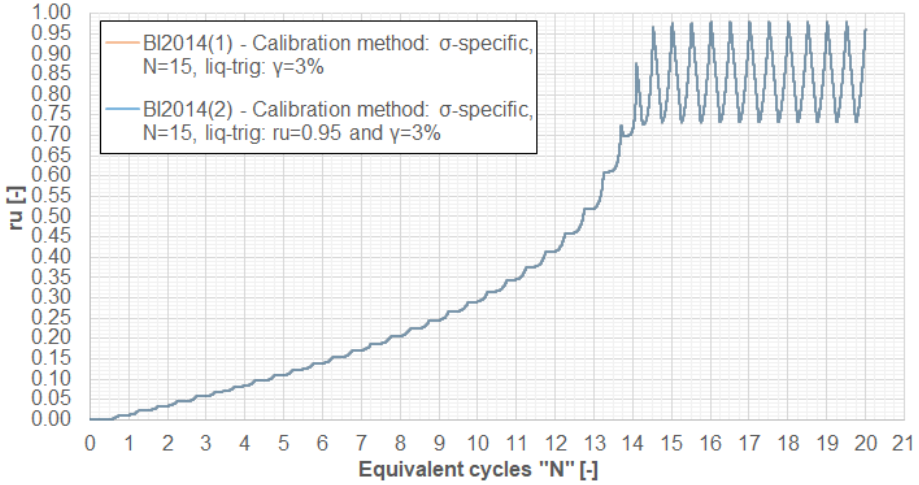

(a) r_u-evolution

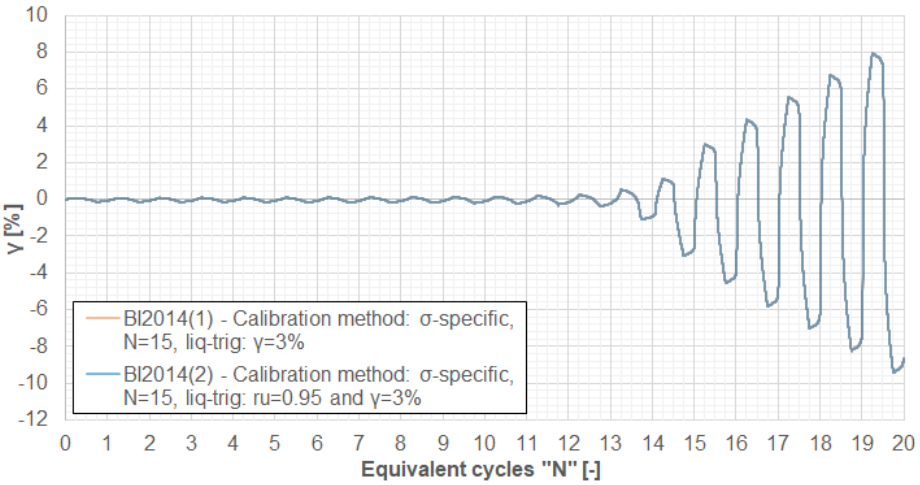

(b) γ-evolution

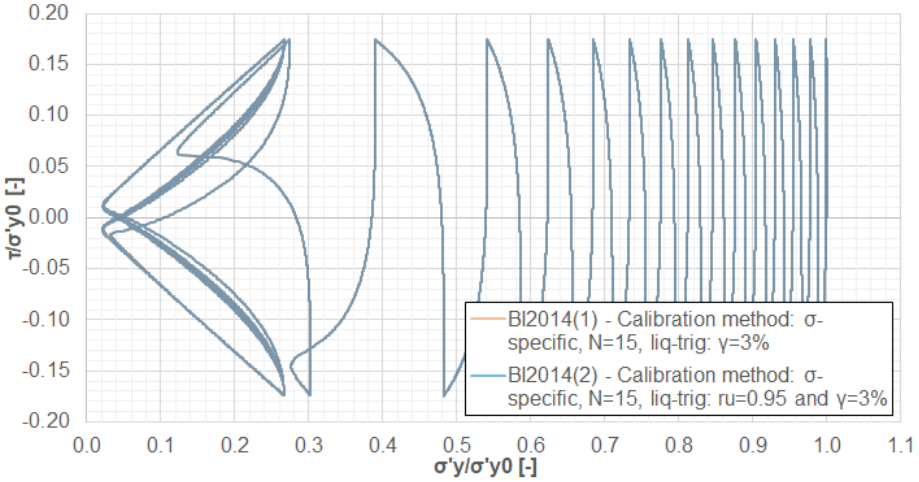

(c) $\frac{\sigma'_v}{\sigma'_{v0}}$-$\frac{\tau}{\sigma'_{v0}}$ space

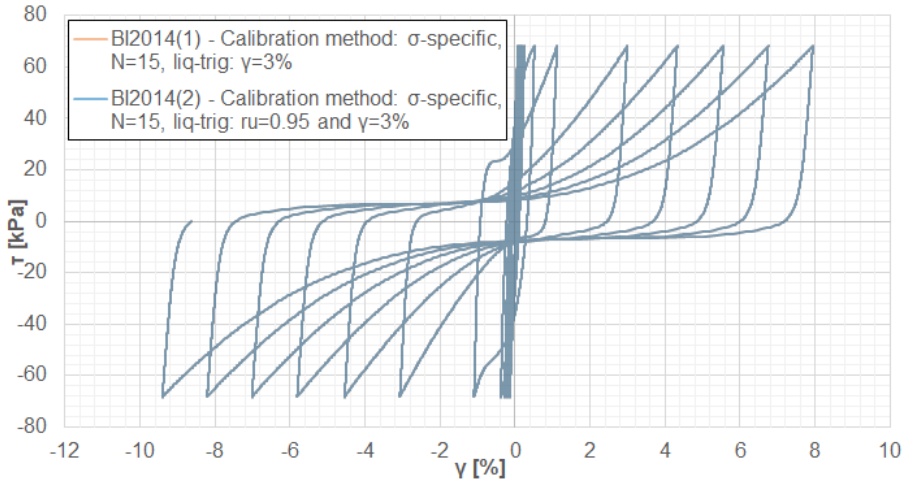

(d) γ-τ space

Figure 10.11: Comparison of calibrated *CM1* and *CM2* models in layer 7-3-EE-MS

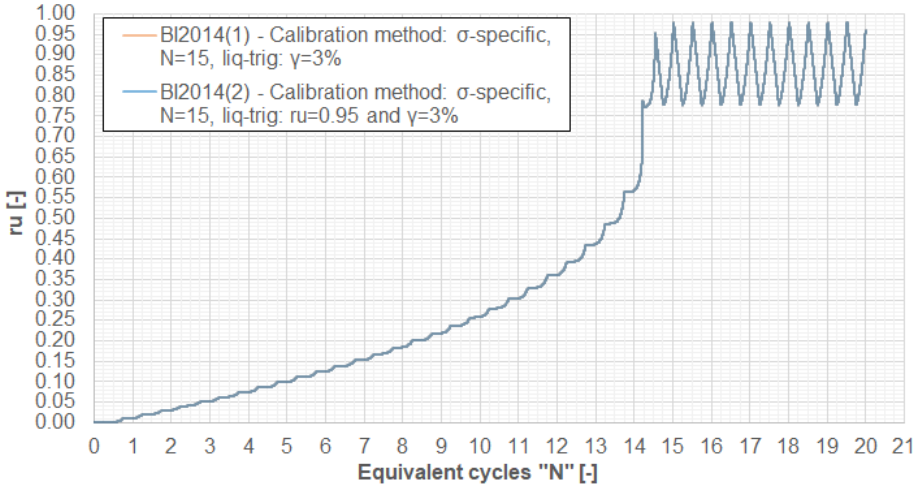

(a) r_u-evolution

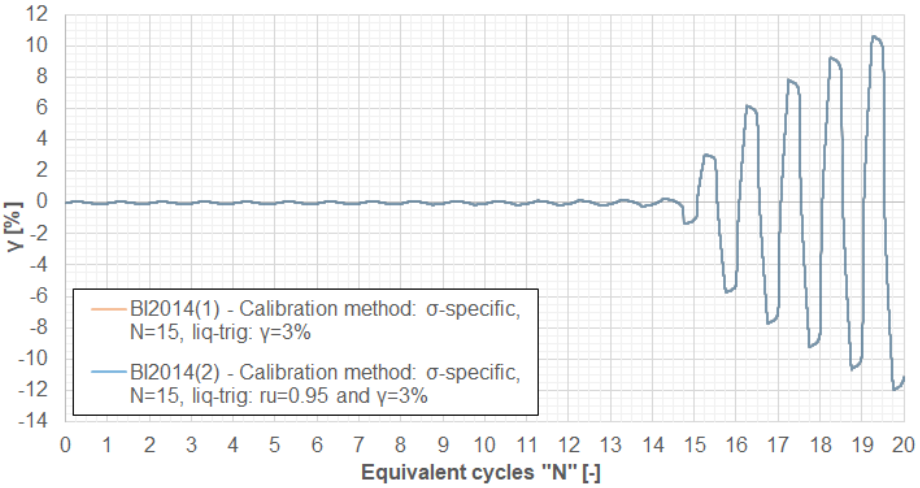

(b) γ-evolution

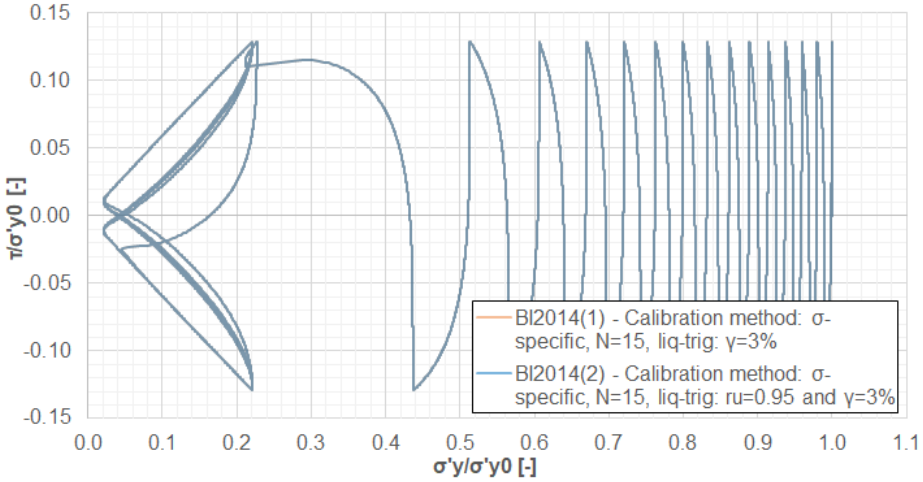

(c) $\frac{\sigma'_v}{\sigma'_{v0}}$-$\frac{\tau}{\sigma'_{v0}}$ space

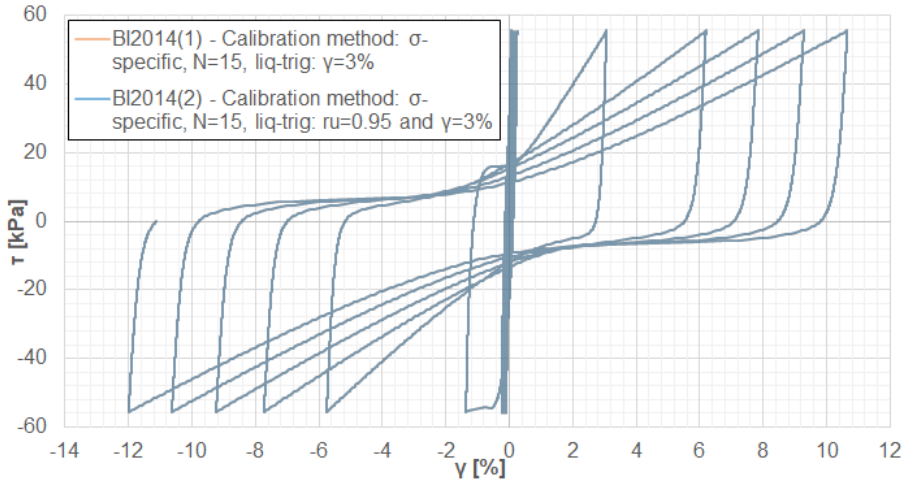

(d) γ-τ space

Figure 10.12: Comparison of calibrated *CM1* and *CM2* models in layer 7-4-EE-MS

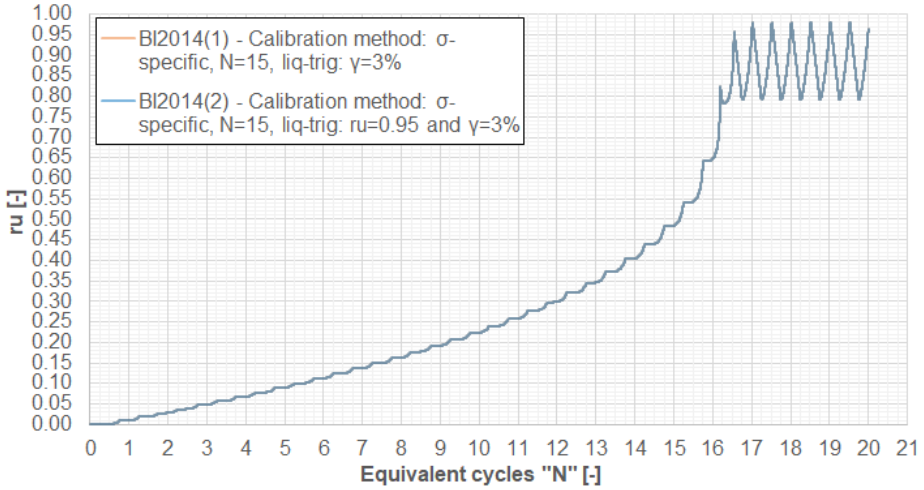

(a) r_u-evolution

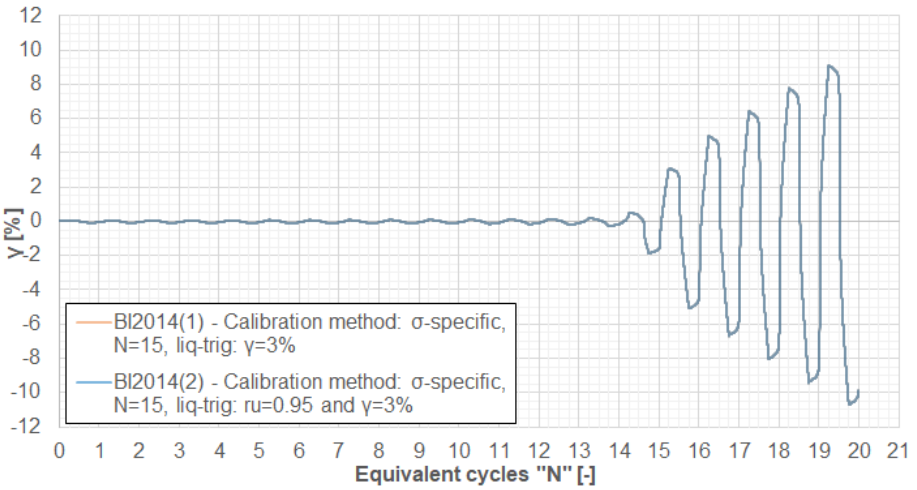

(b) γ-evolution

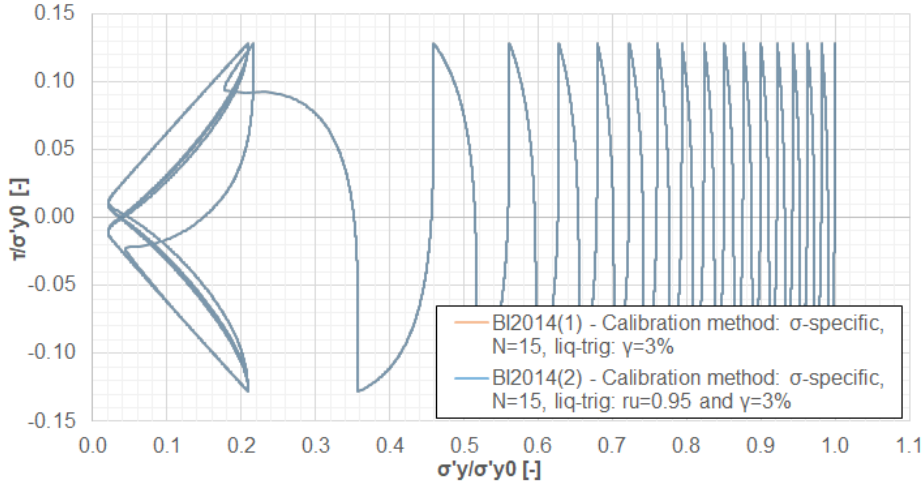

(c) $\frac{\sigma'_v}{\sigma'_{v0}}$-$\frac{\tau}{\sigma'_{v0}}$ space (erratum)

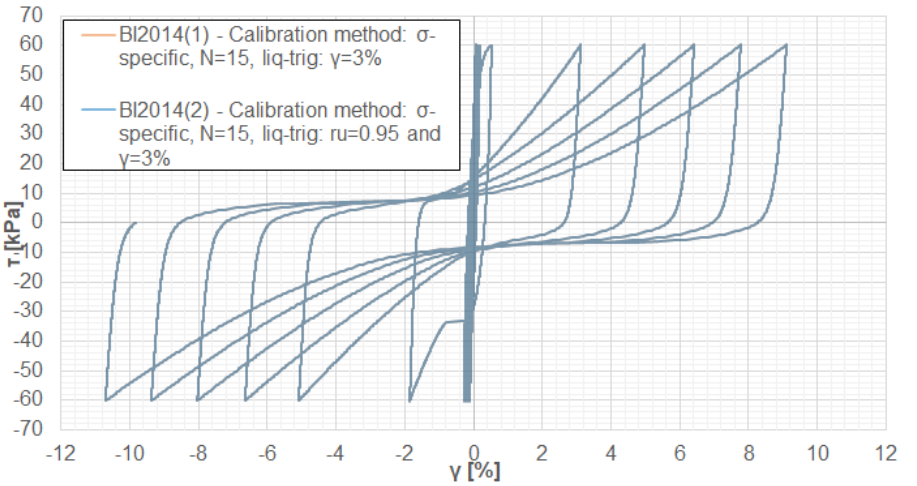

(d) γ-τ space

Figure 10.13: Comparison of calibrated *CM1* and *CM2* models in layer 7-5-EE-MS

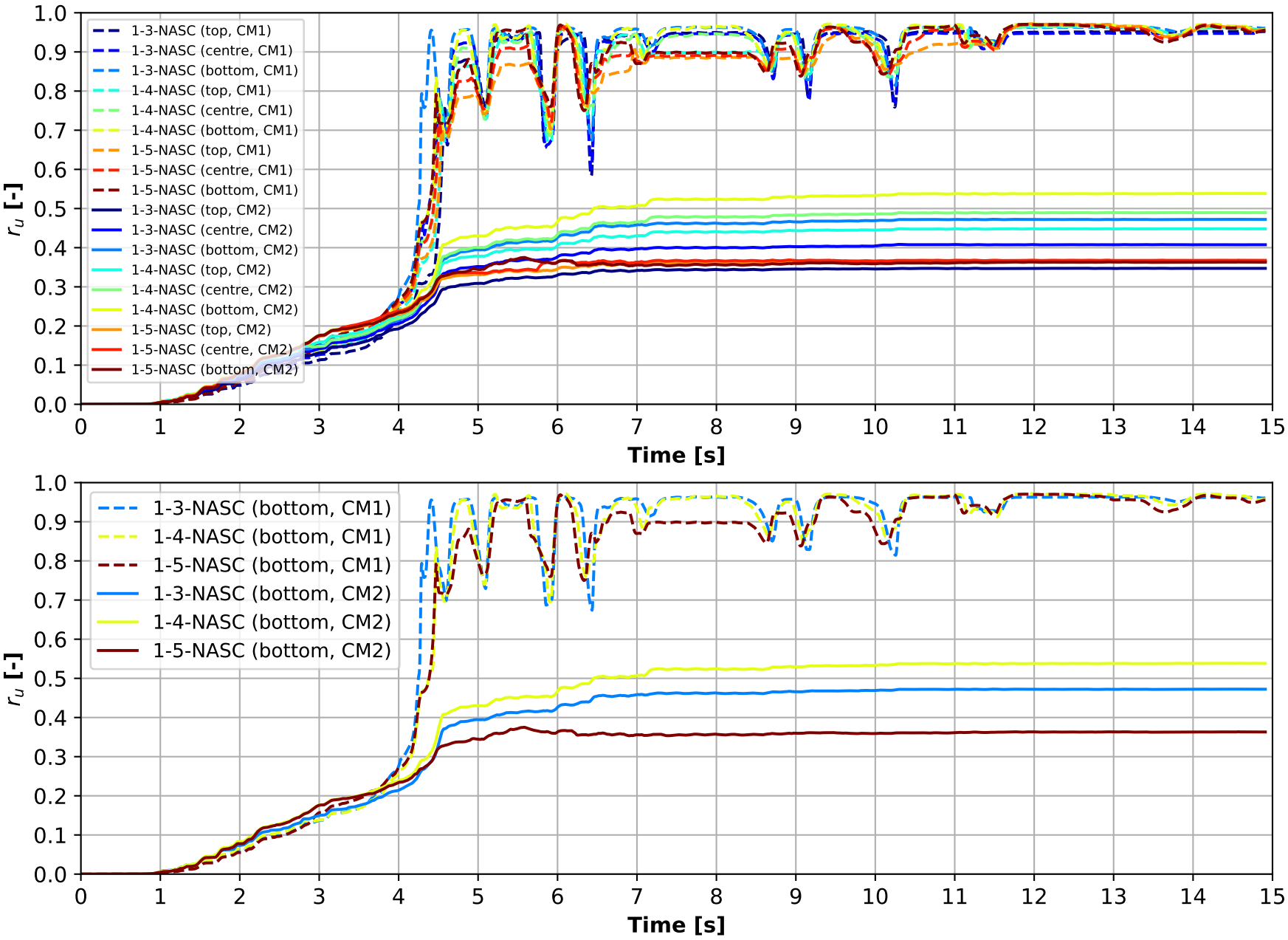

Figure 10.14: 1D r_u-time history response of layer 1-NASC-MS at all and select locations to Umbria Marche *BDBE* signal

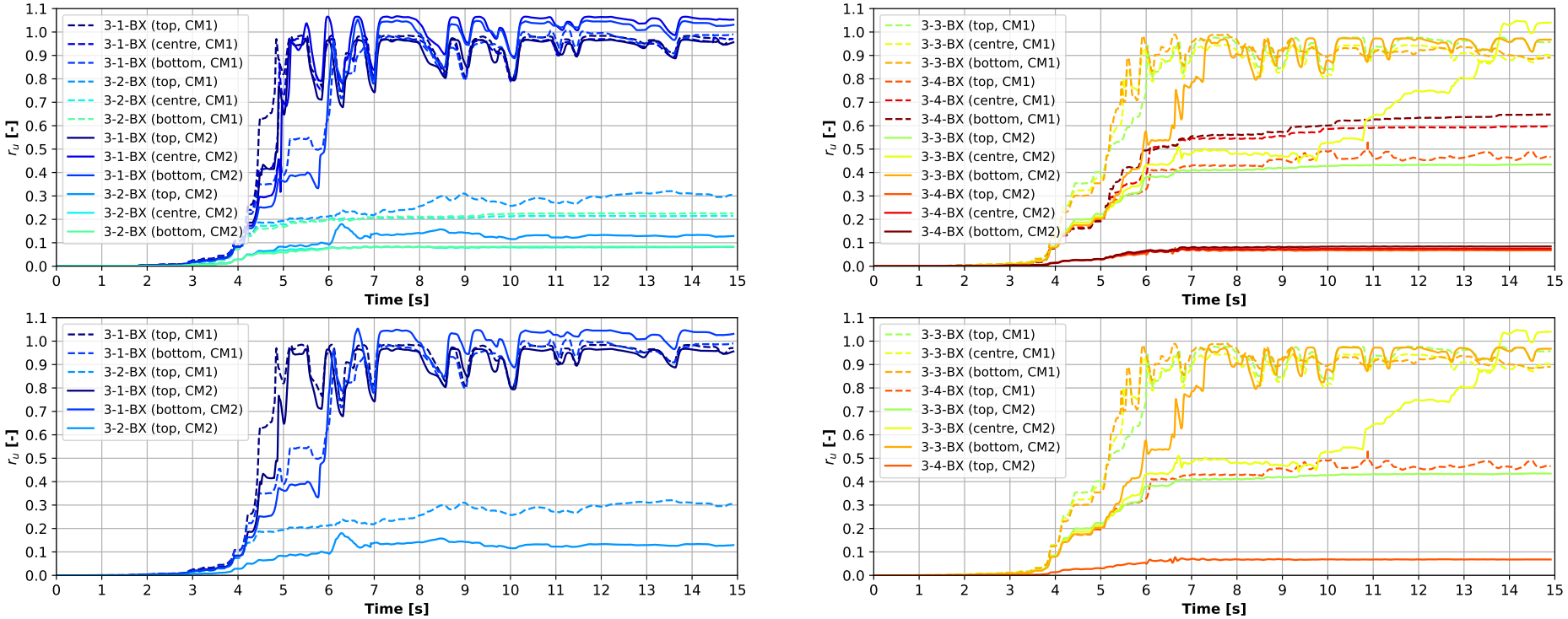

Figure 10.15: 1D r_u-time history response of layer 3-BX-FS at all and select locations to Umbria Marche *BDBE* signal

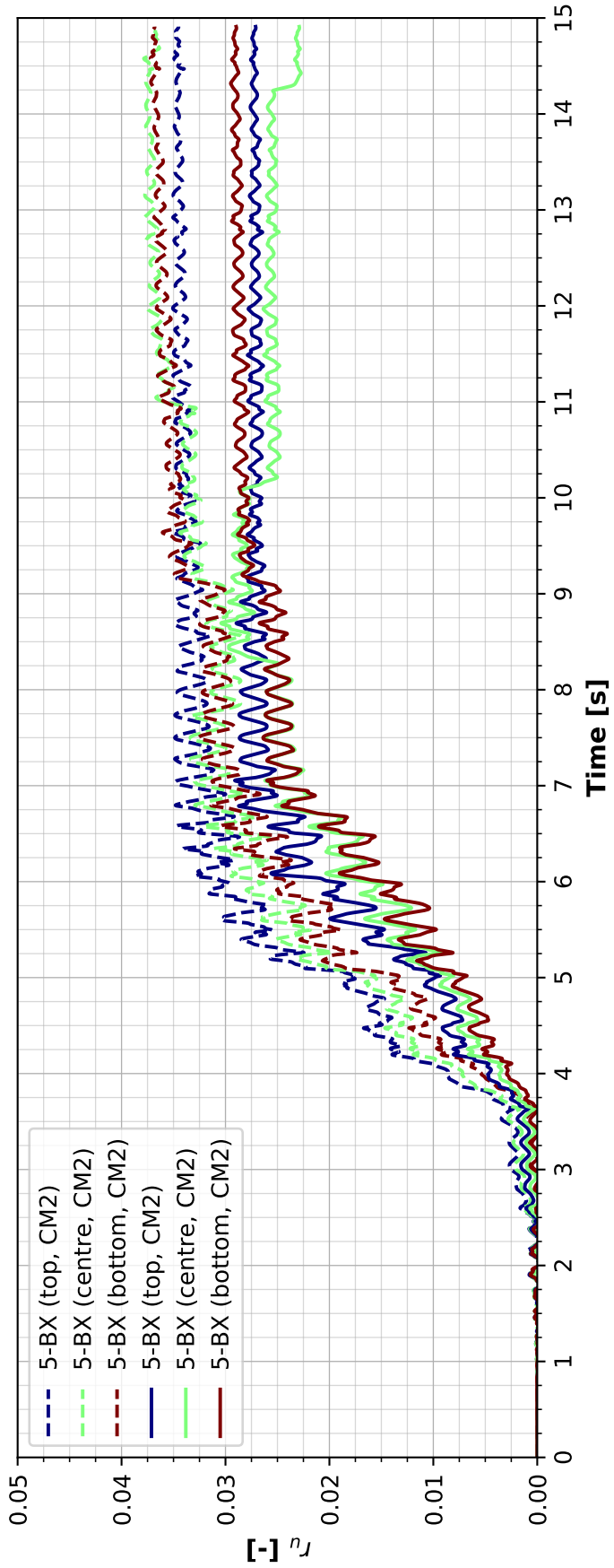

Figure 10.16: 1D r_u-time history response of layer 5-BX-MS at all and select locations to Umbria Marche *BDBE* signal

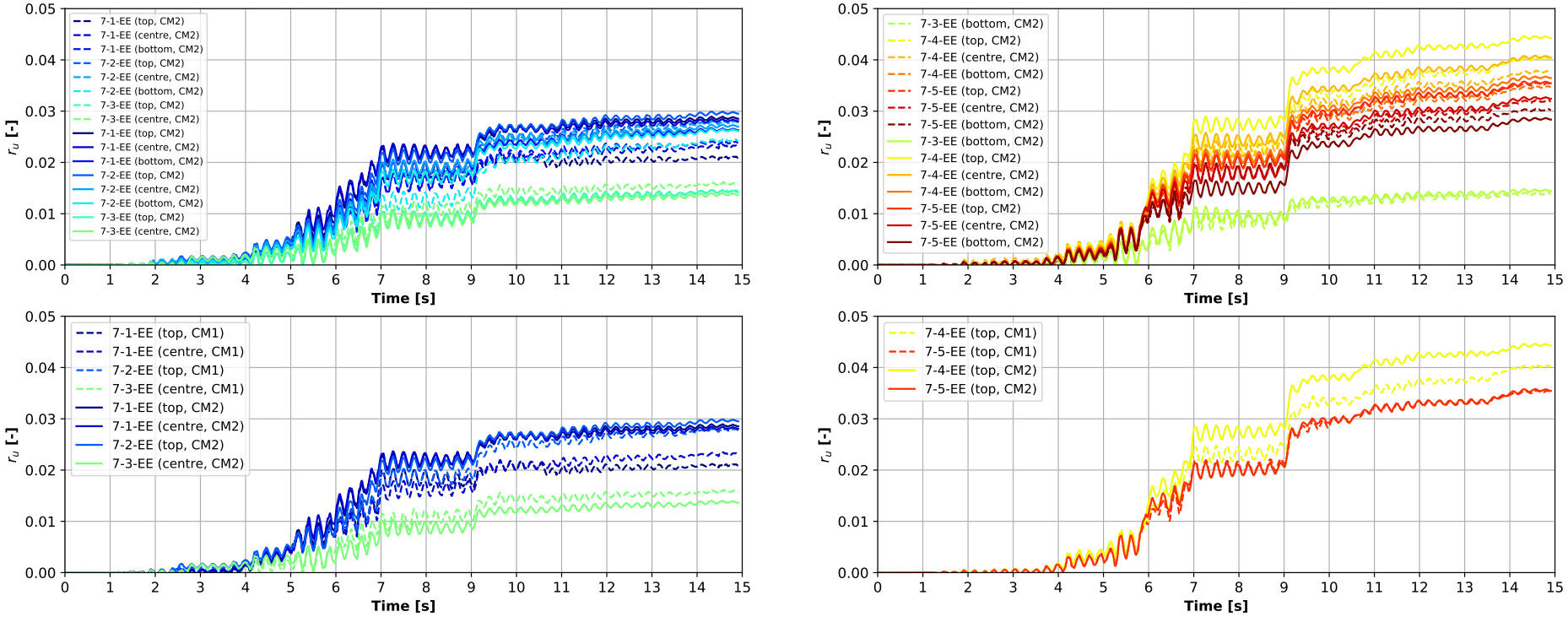

Figure 10.17: 1D r_u-time history response of layer 7-EE-MS at all and select locations to Umbria Marche *BDBE* signal

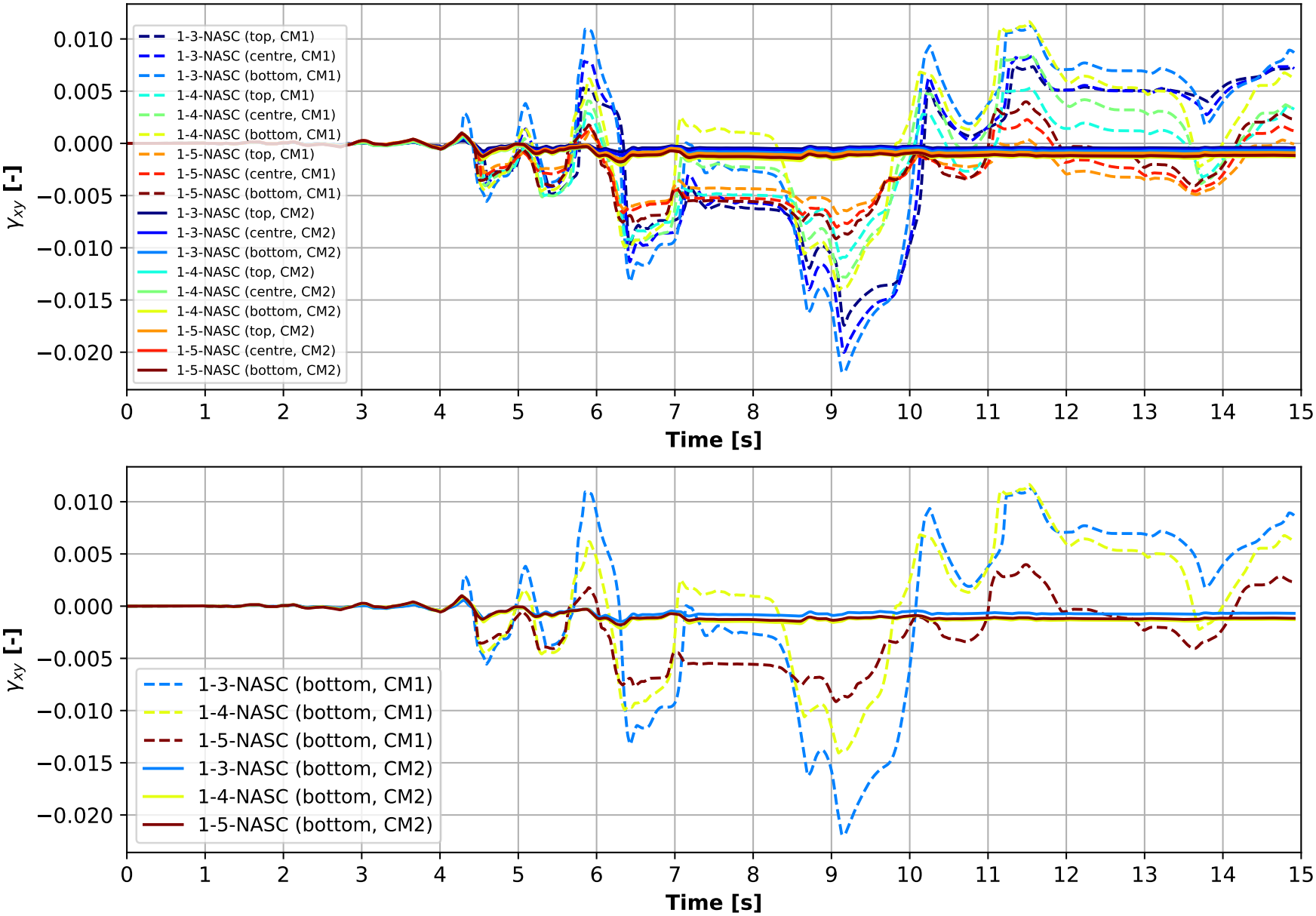

Figure 10.18: 1D γ-time history response of layer 1-NASC-MS at all and select locations to Umbria Marche *BDBE* signal

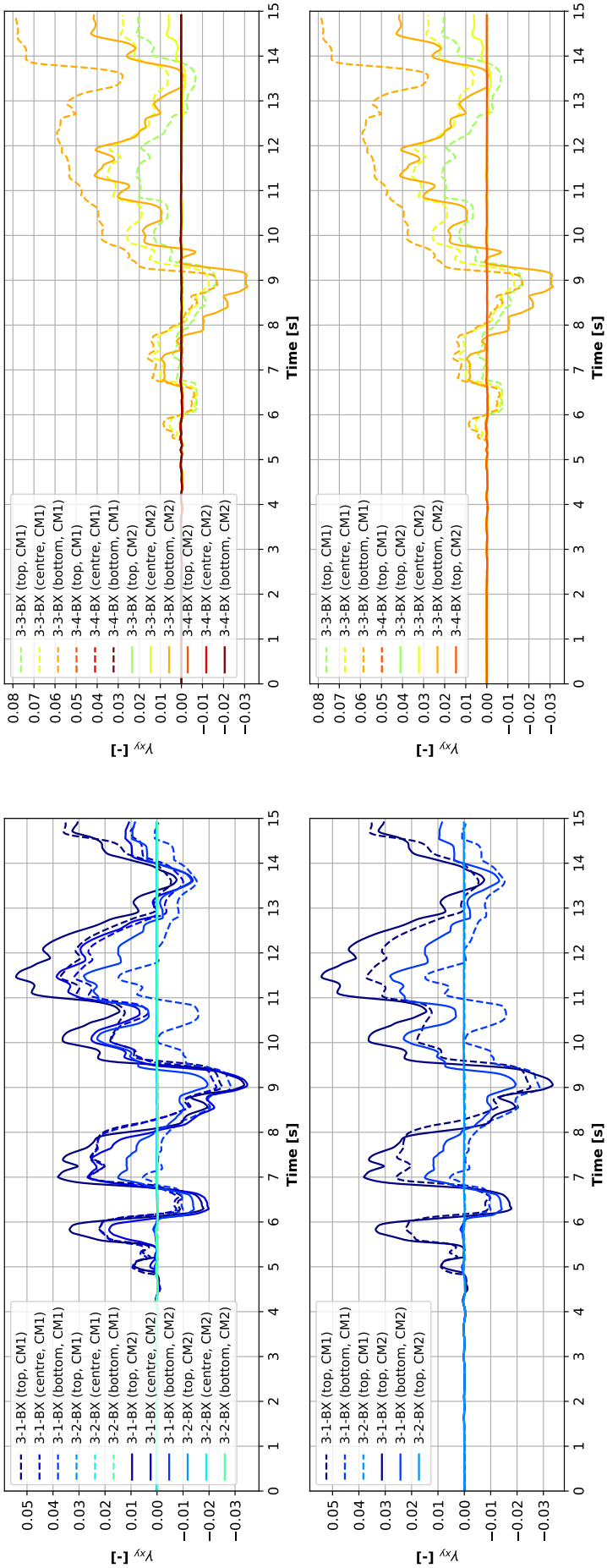

Figure 10.19: 1D γ-time history response of layer 3-BX-FS at all and select locations to Umbria Marche *BDBE* signal

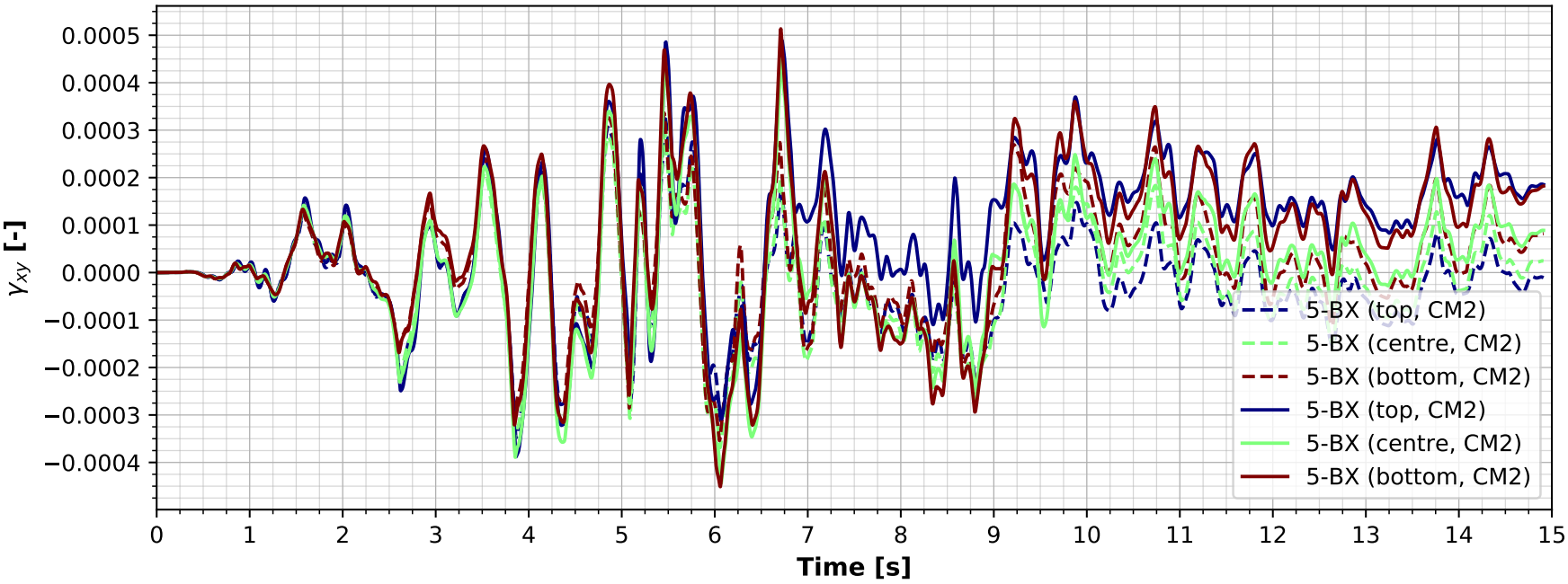

Figure 10.20: 1D γ-time history response of layer 5-BX-MS at all and select locations to Umbria Marche *BDBE* signal

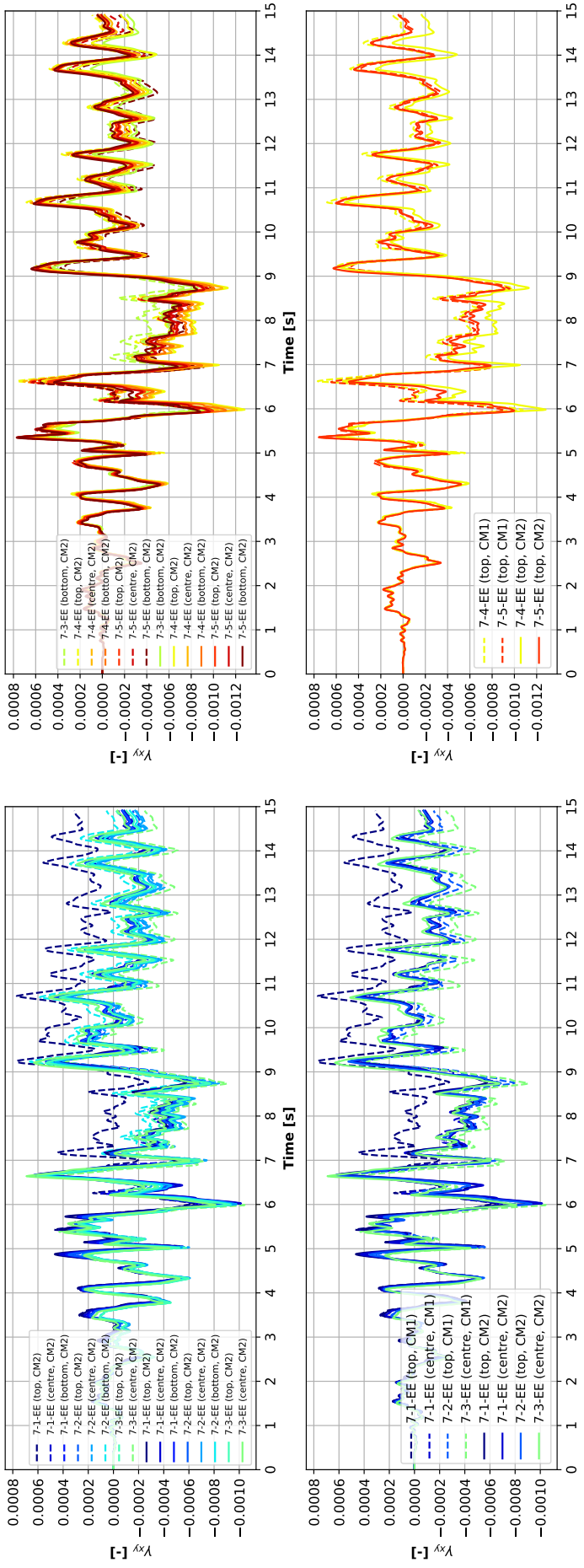

Figure 10.21: 1D γ-time history response of layer 7-EE-MS at all and select locations to Umbria Marche *BDBE* signal

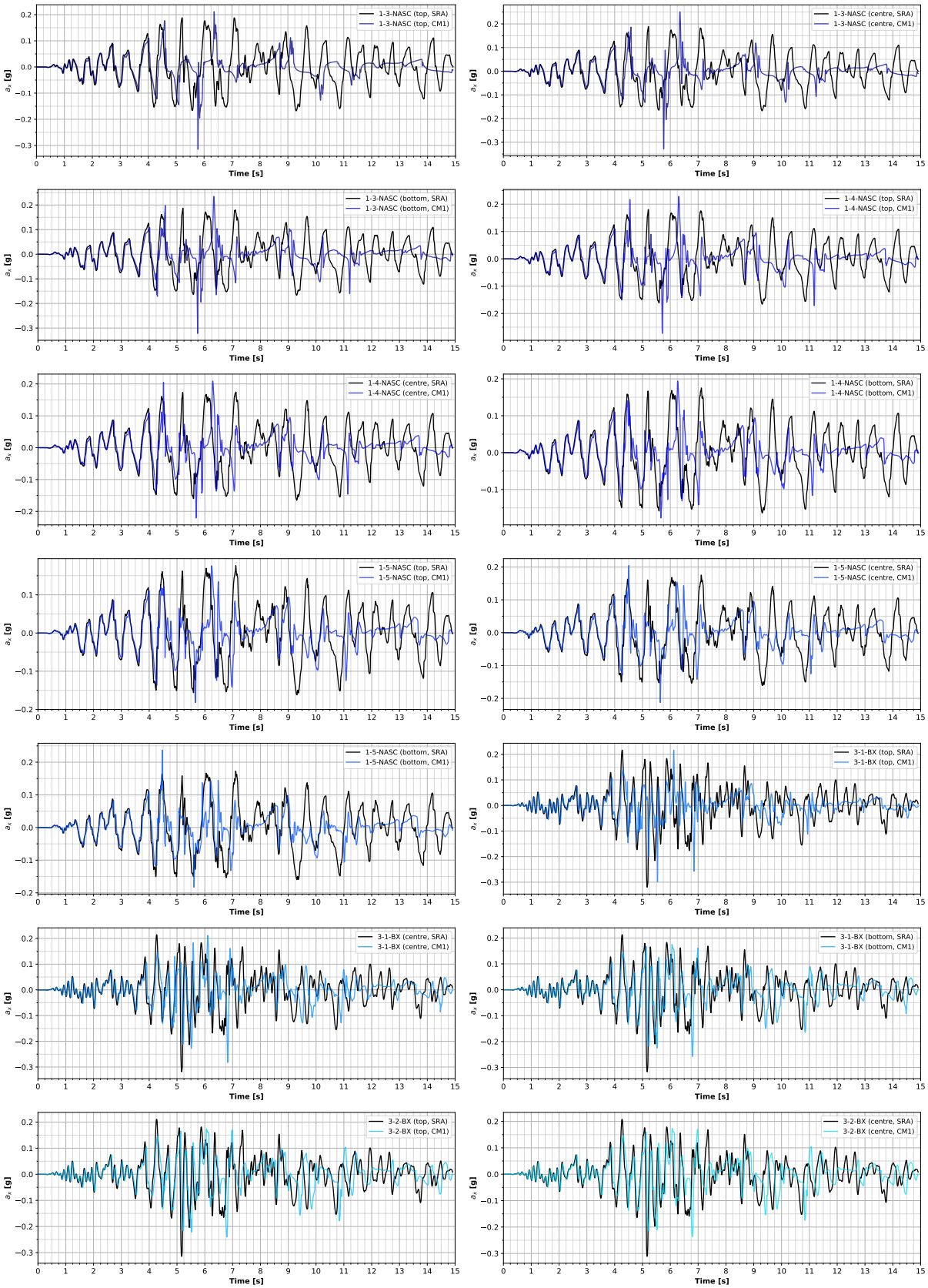

Figure 10.22: Umbria Marche *BDBE* comparison of *SRA* and *LPA-CM1 ATHs*

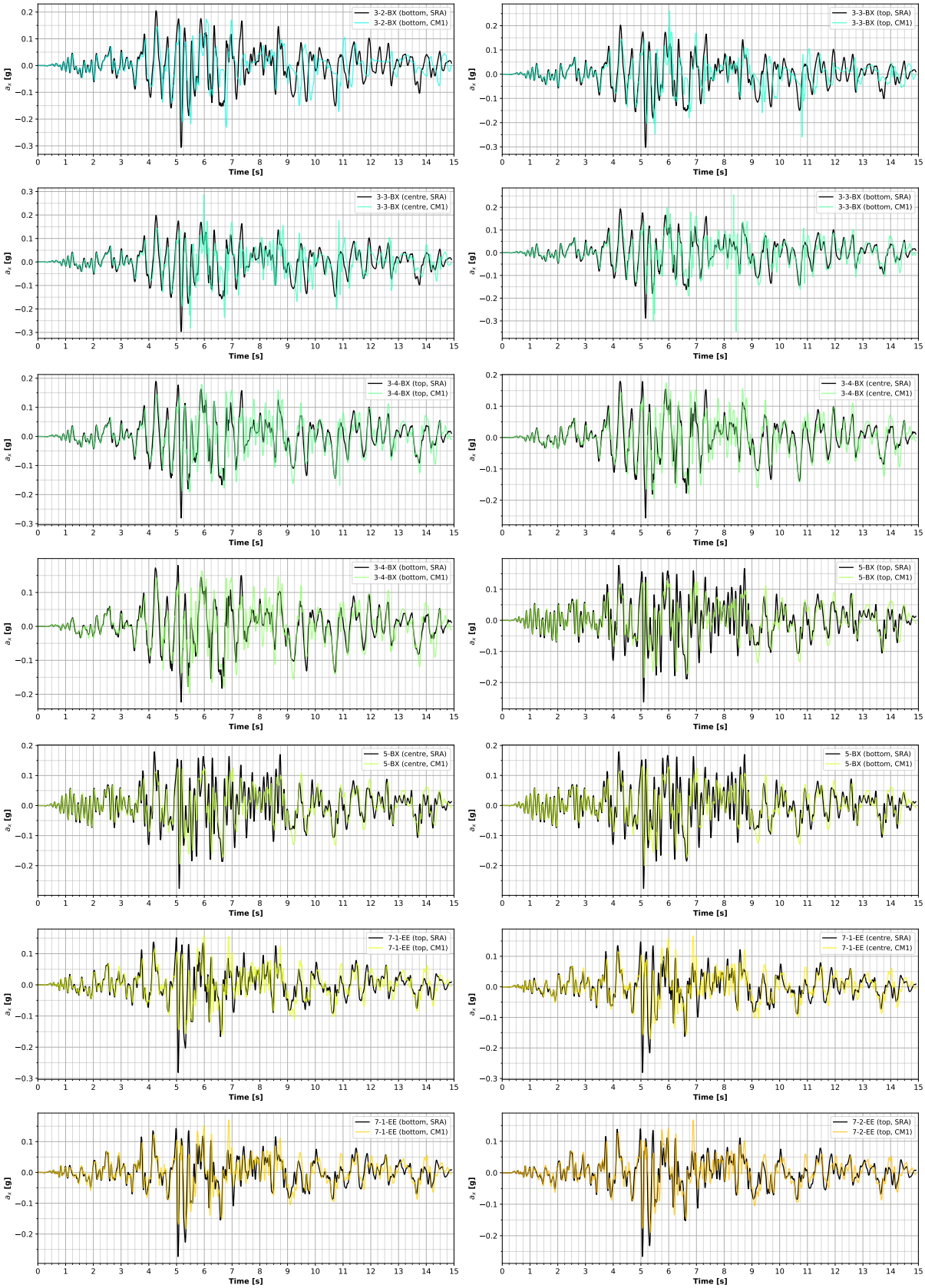

Figure 10.23: Umbria Marche *BDBE* comparison of *SRA* and *LPA-CM1 ATHs* (continued)

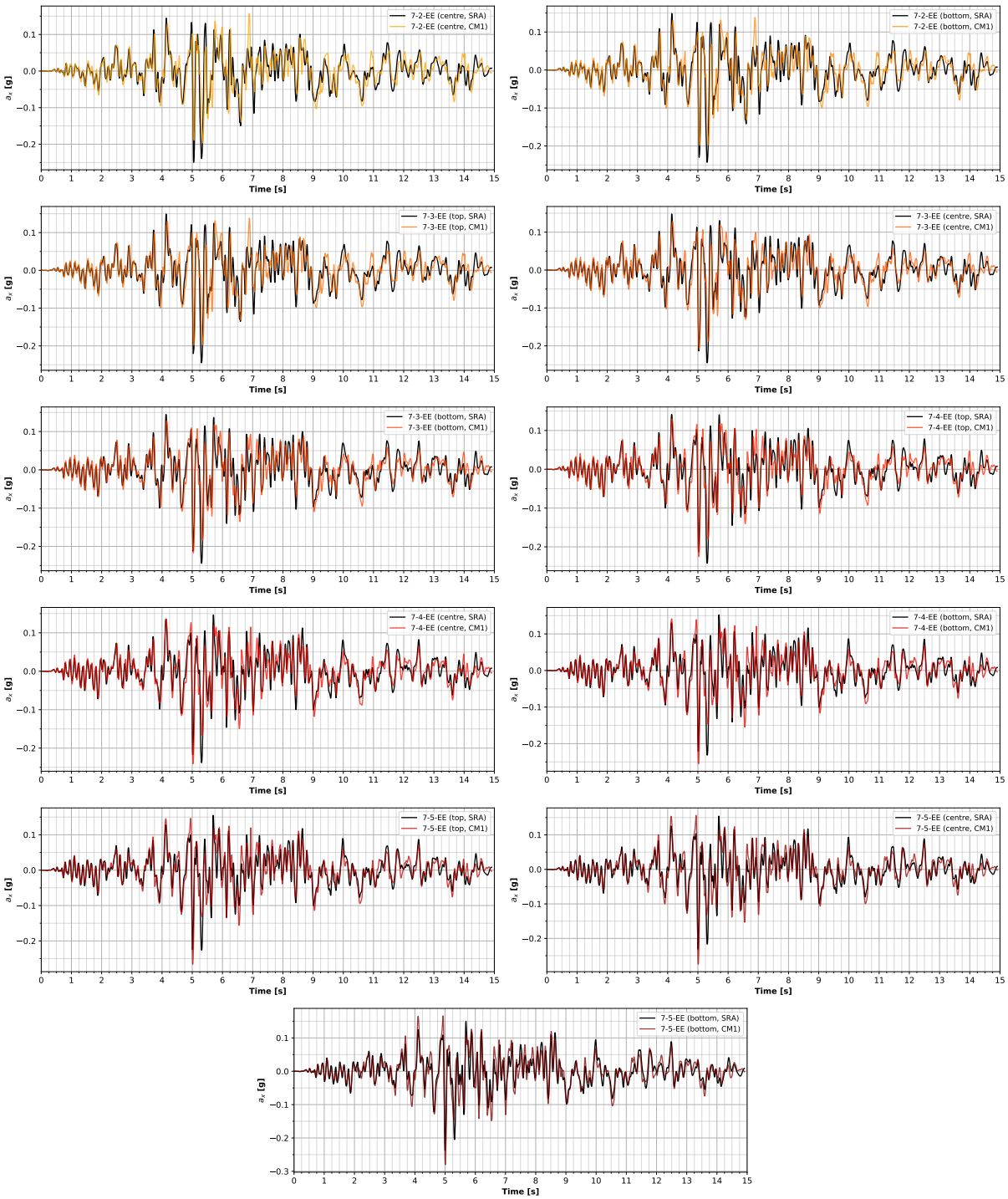

Figure 10.24: Umbria Marche *BDBE* comparison of *SRA* and *LPA-CM1 ATHs* (continued)

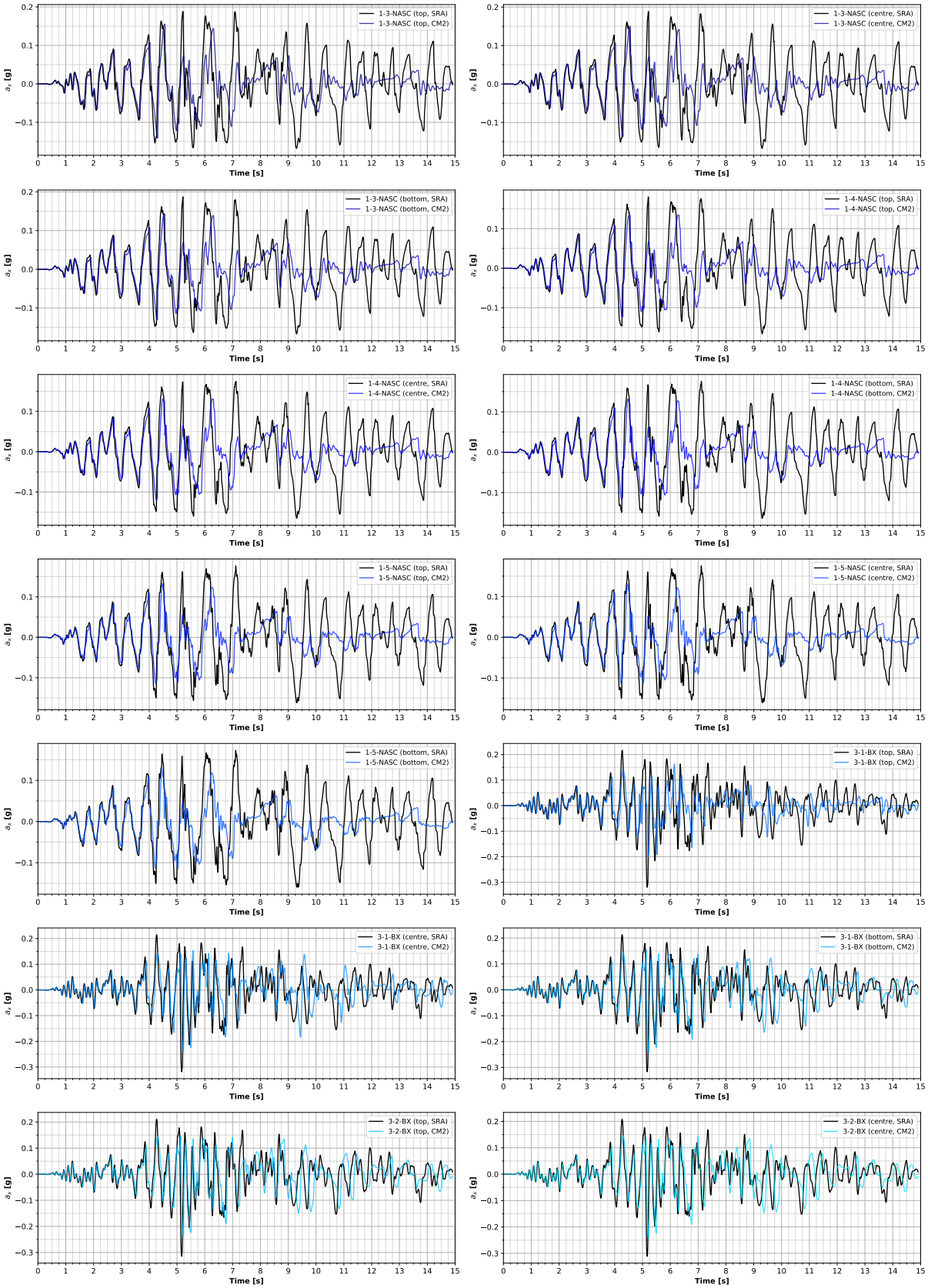

Figure 10.25: Umbria Marche *BDBE* comparison of *SRA* and *LPA-CM2 ATHs*

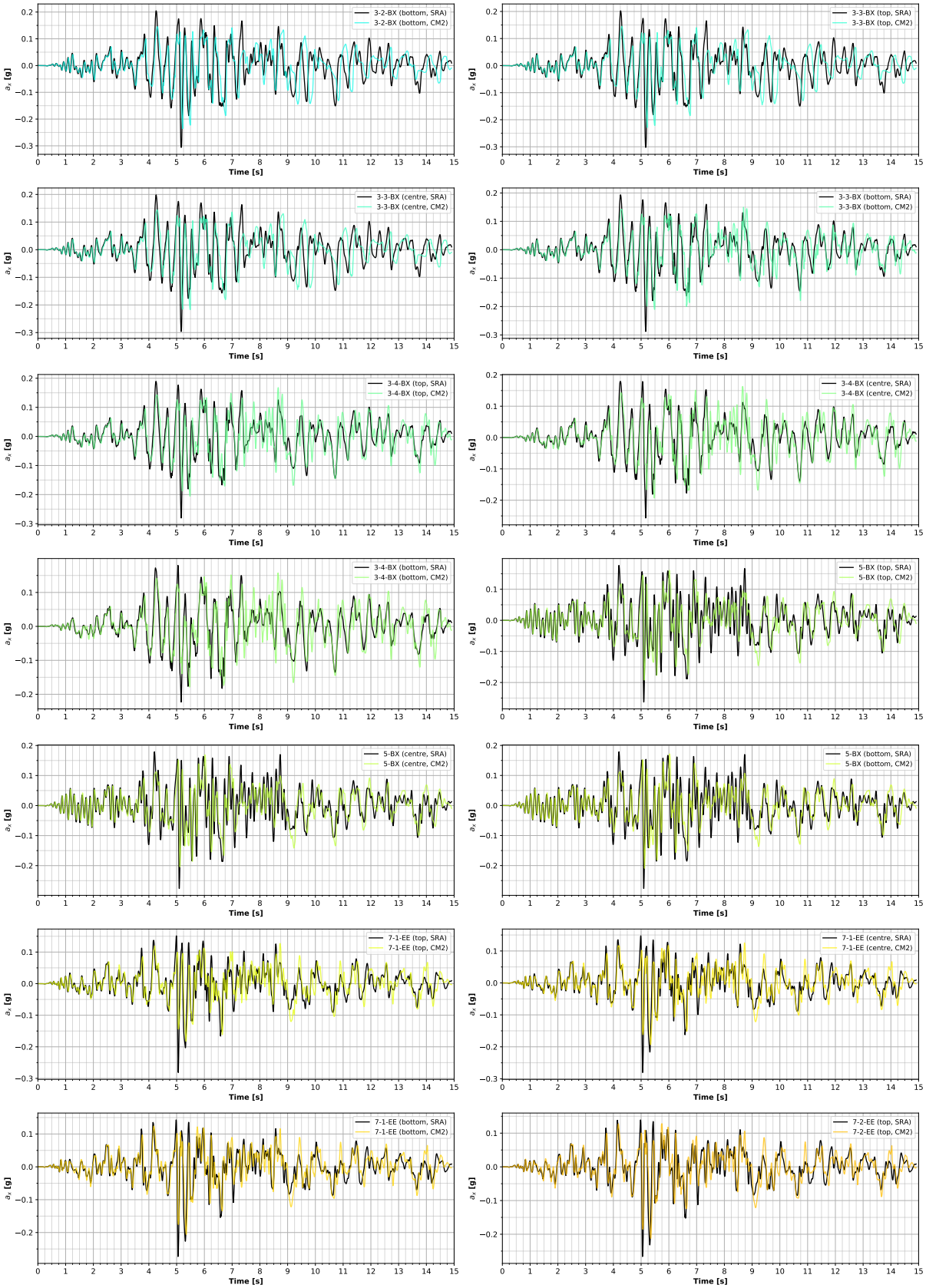

Figure 10.26: Umbria Marche *BDBE* comparison of *SRA* and *LPA-CM2 ATHs* (continued)

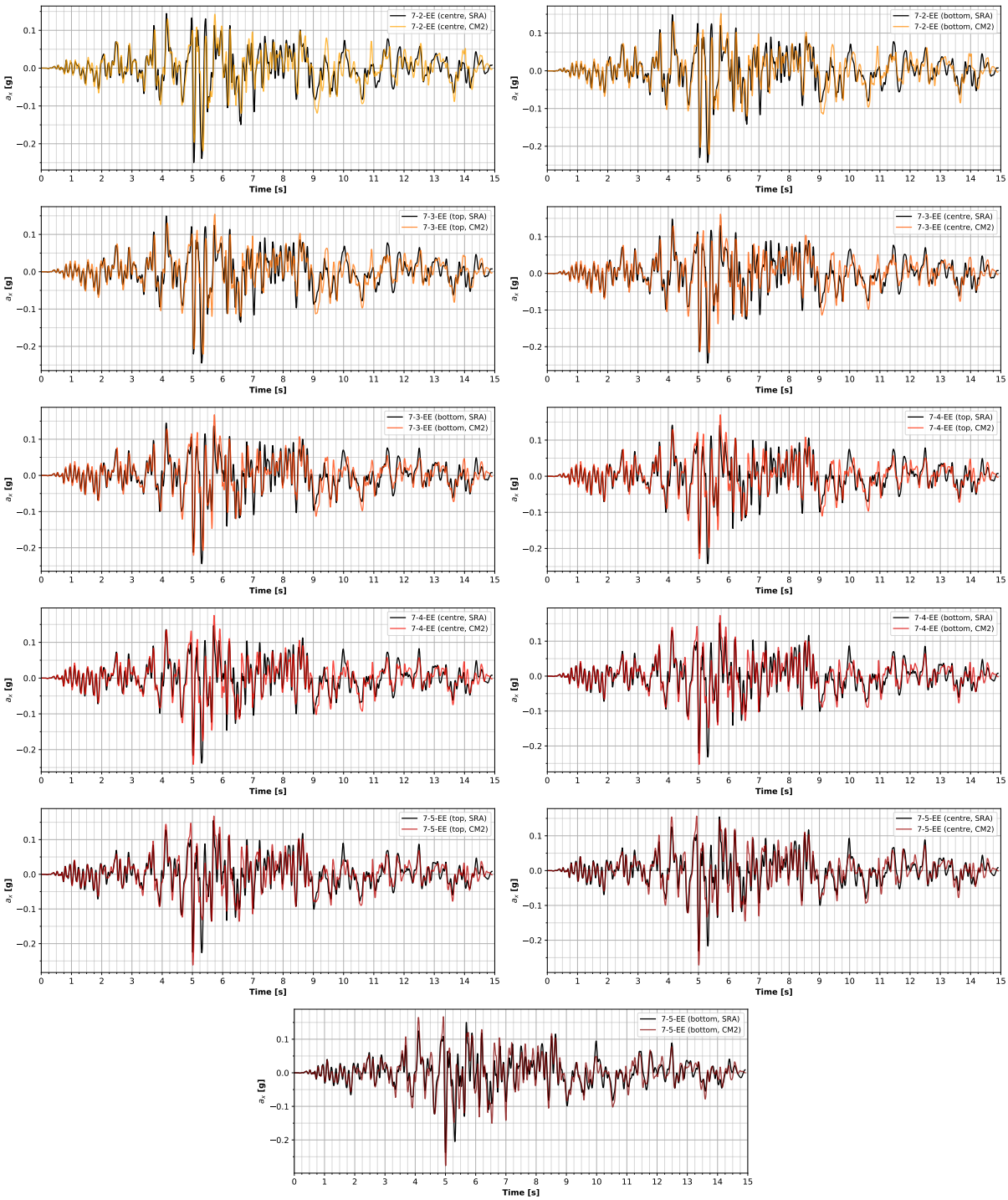

Figure 10.27: Umbria Marche *BDBE* comparison of *SRA* and *LPA-CM2 ATHs* (continued)

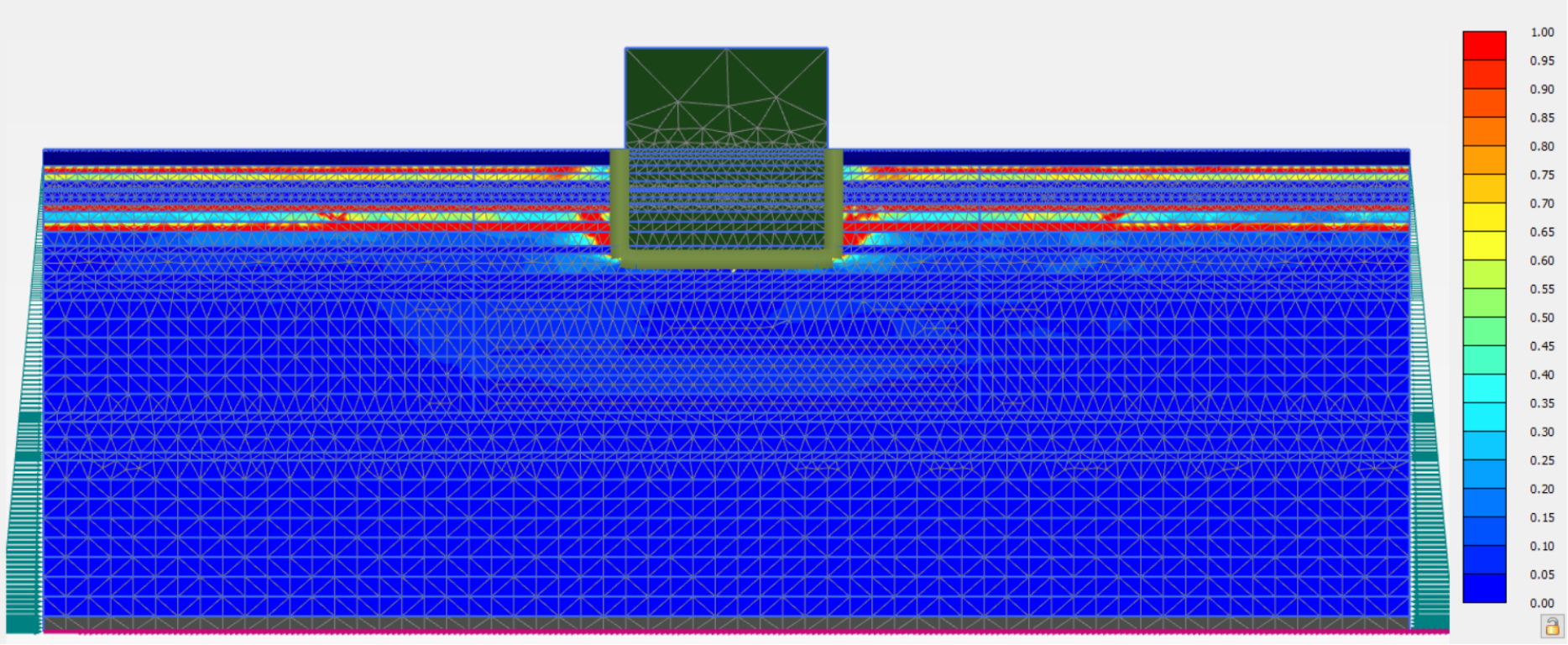

Figure 10.28: $r_{u,max}$-contour map of the 2D model at the end of the Umbria Marche *BDBE* signal

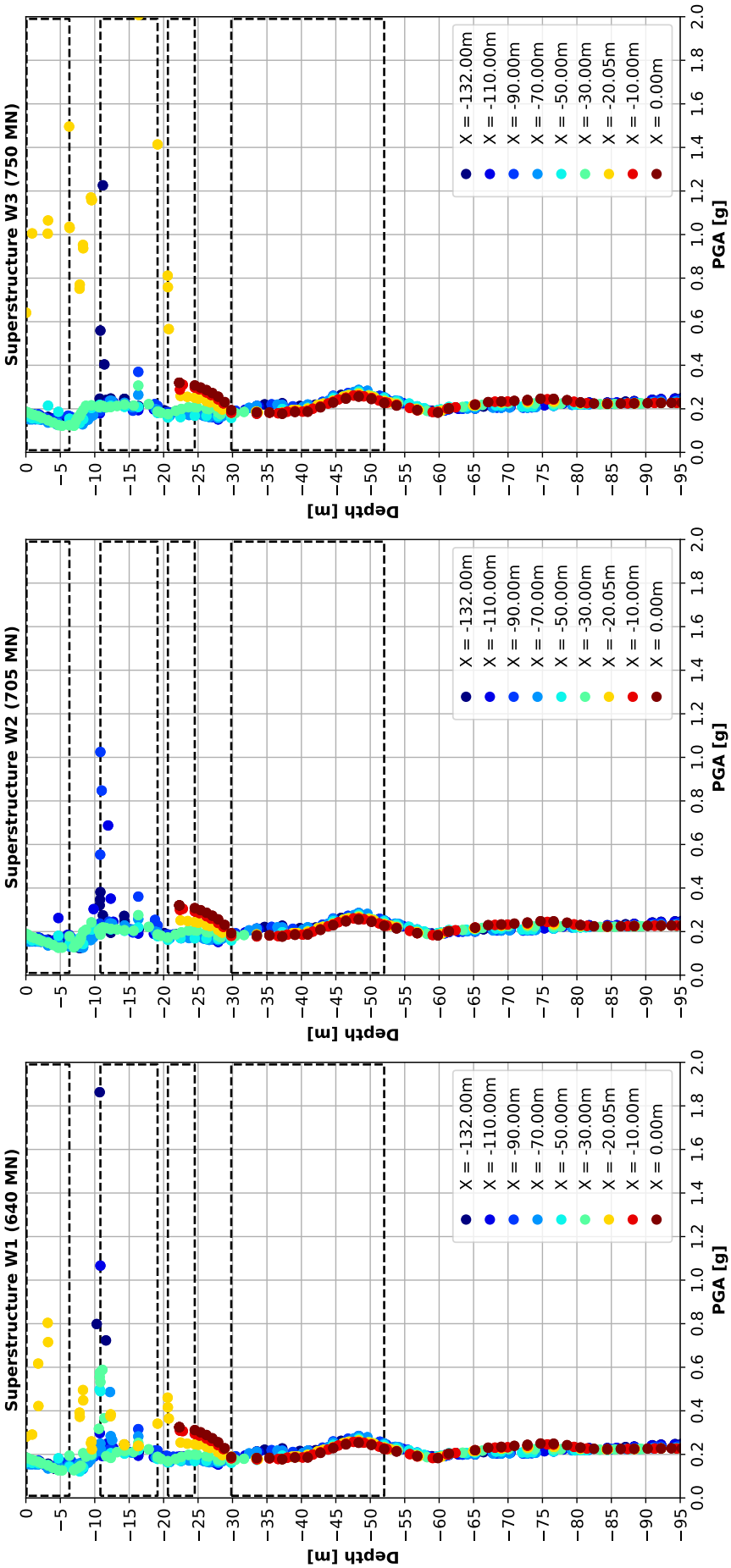

Figure 10.29: Comparative overview of PGA-profiles at select distances from the centre of the structure for all three structural loads

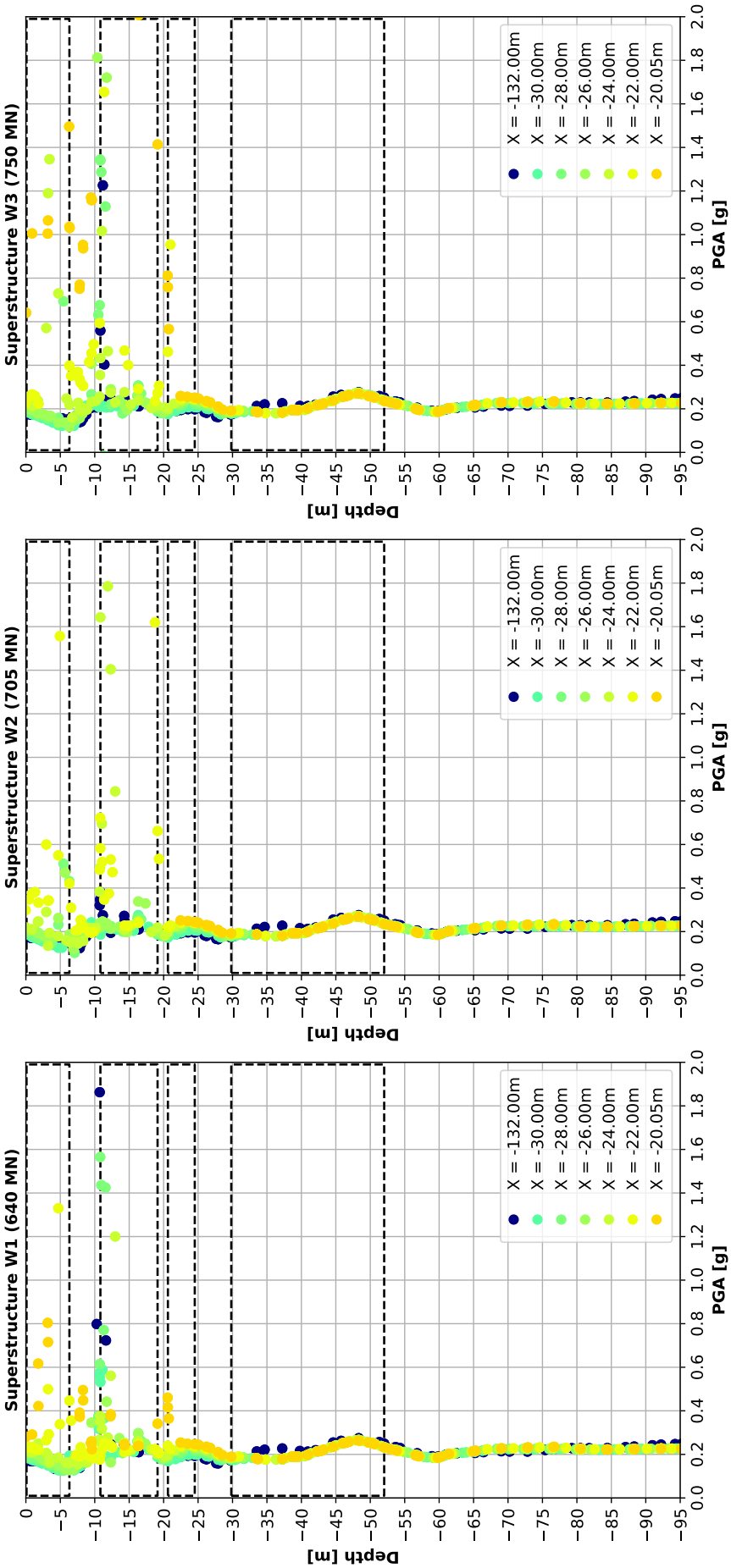

Figure 10.30: Comparative overview of PGA-profiles at select distances in the vicinity of the structure for all three structural loads

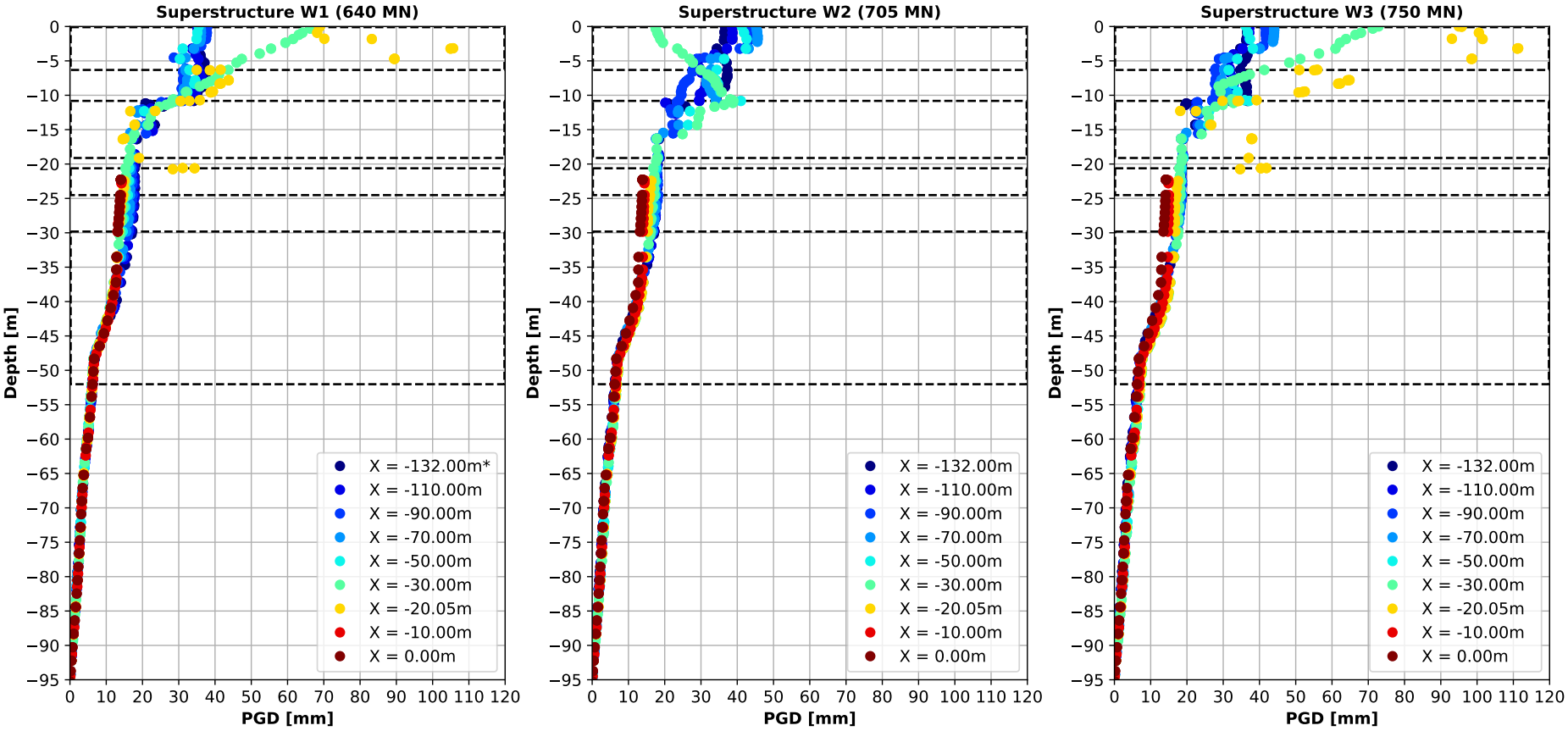

Figure 10.31: Comparative overview of *PGD*-profiles at select distances from the centre of the structure for all three structural loads

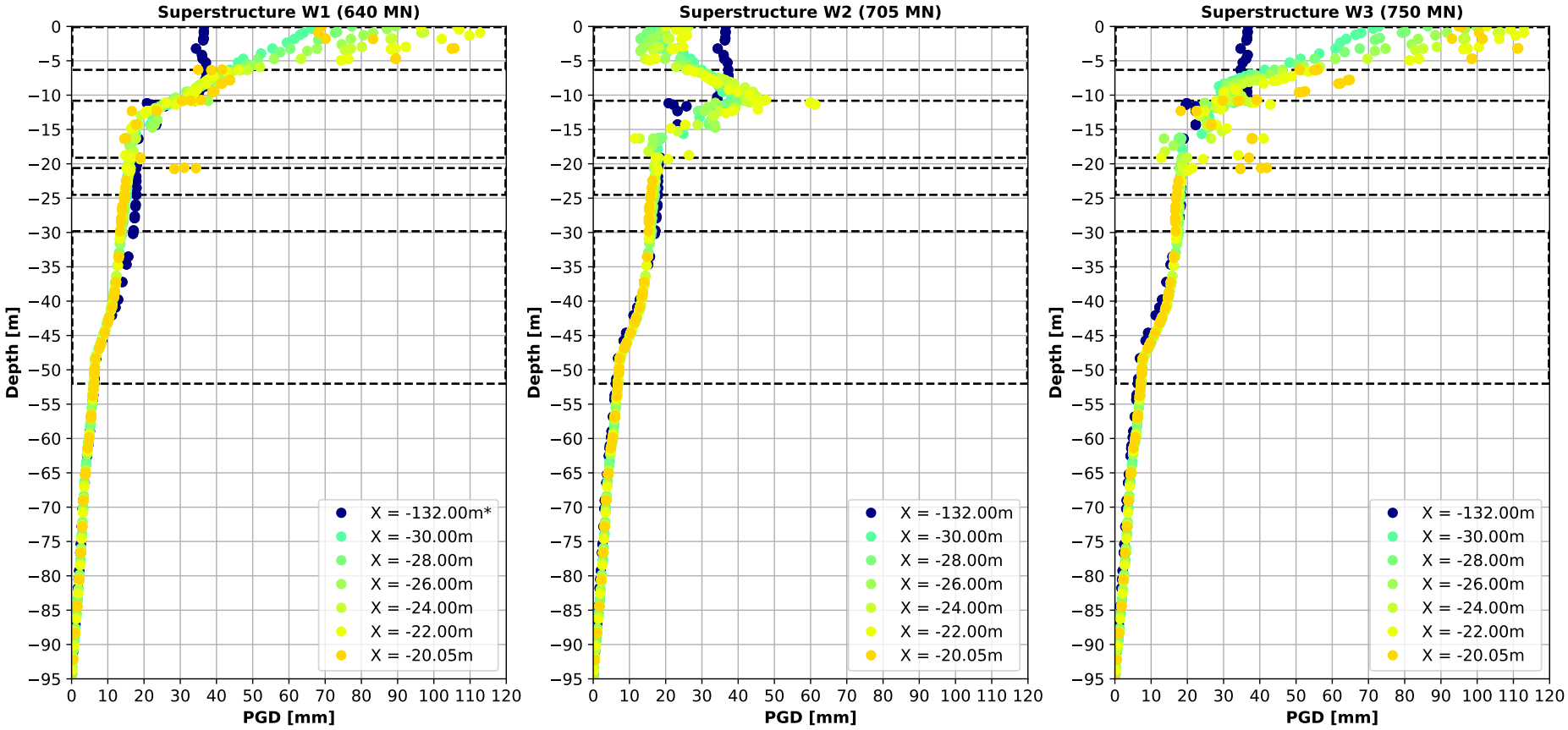

Figure 10.32: Comparative overview of *PGD*-profiles at select distances in the vicinity of the structure for all three structural loads

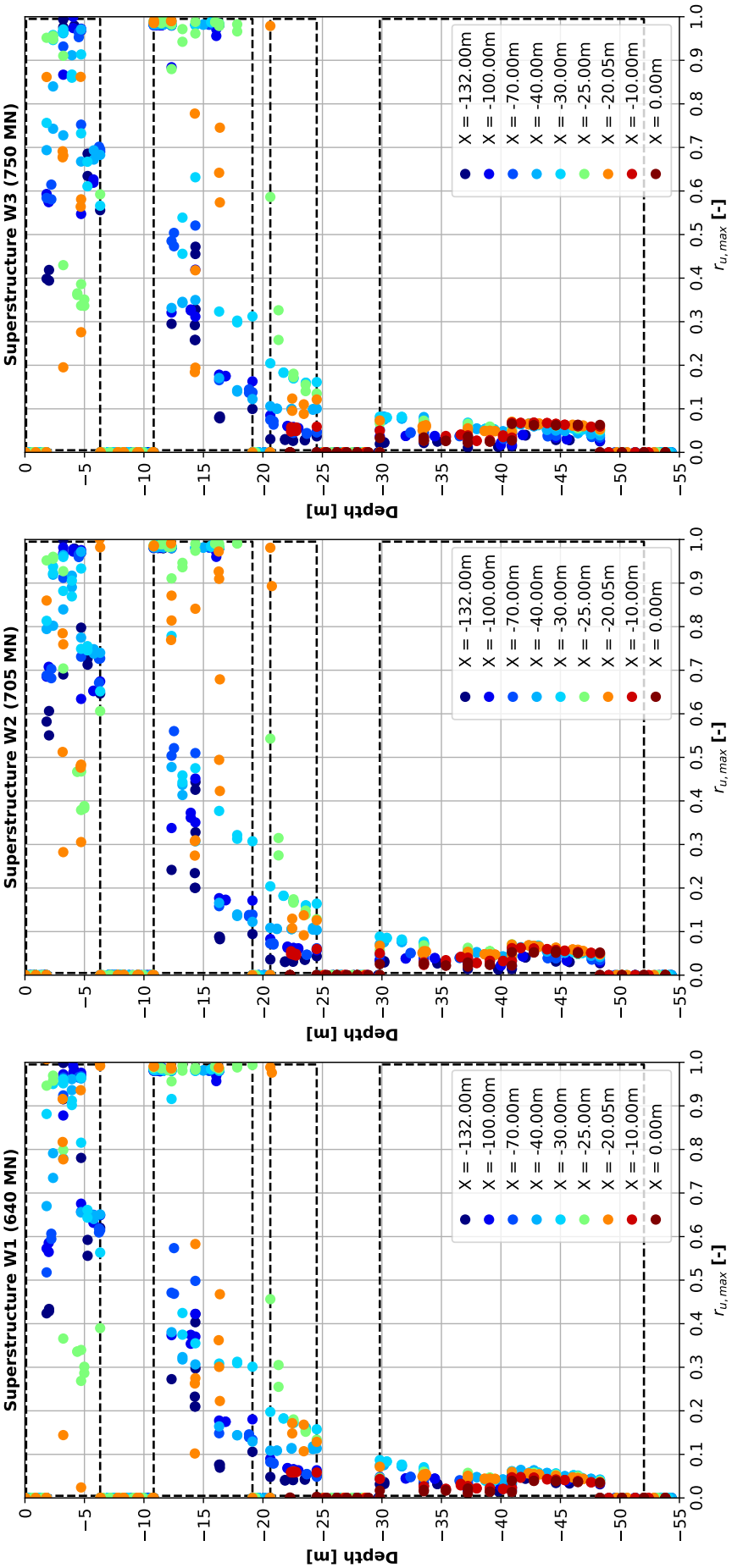

Figure 10.33: Comparative overview of $r_{u,max}$-profiles at select distances from the centre of the structure for all three structural loads

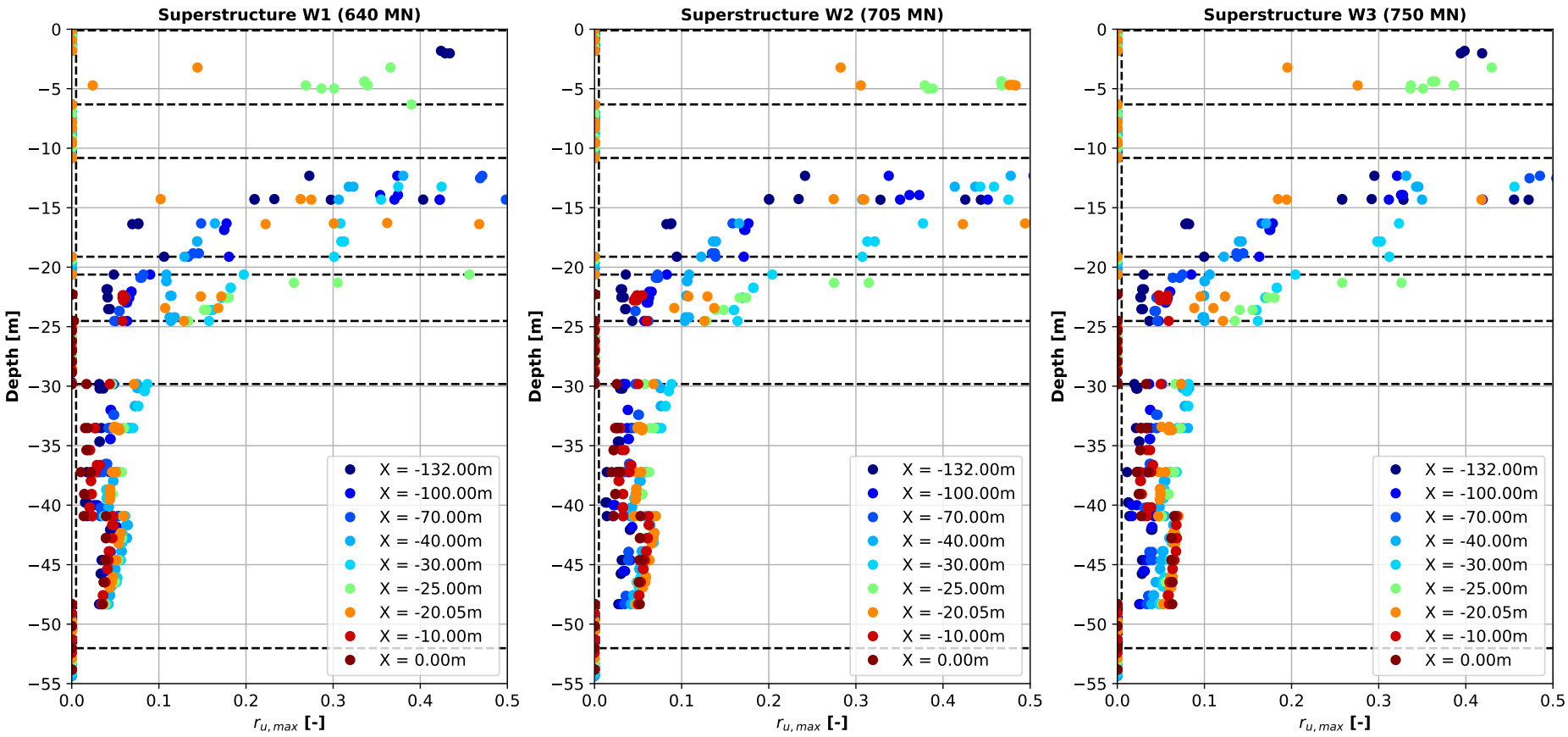

Figure 10.34: Comparative overview of $r_{u,max}$-profiles at select distances from the centre of the structure for all three structural loads (reduced r_u-scale)

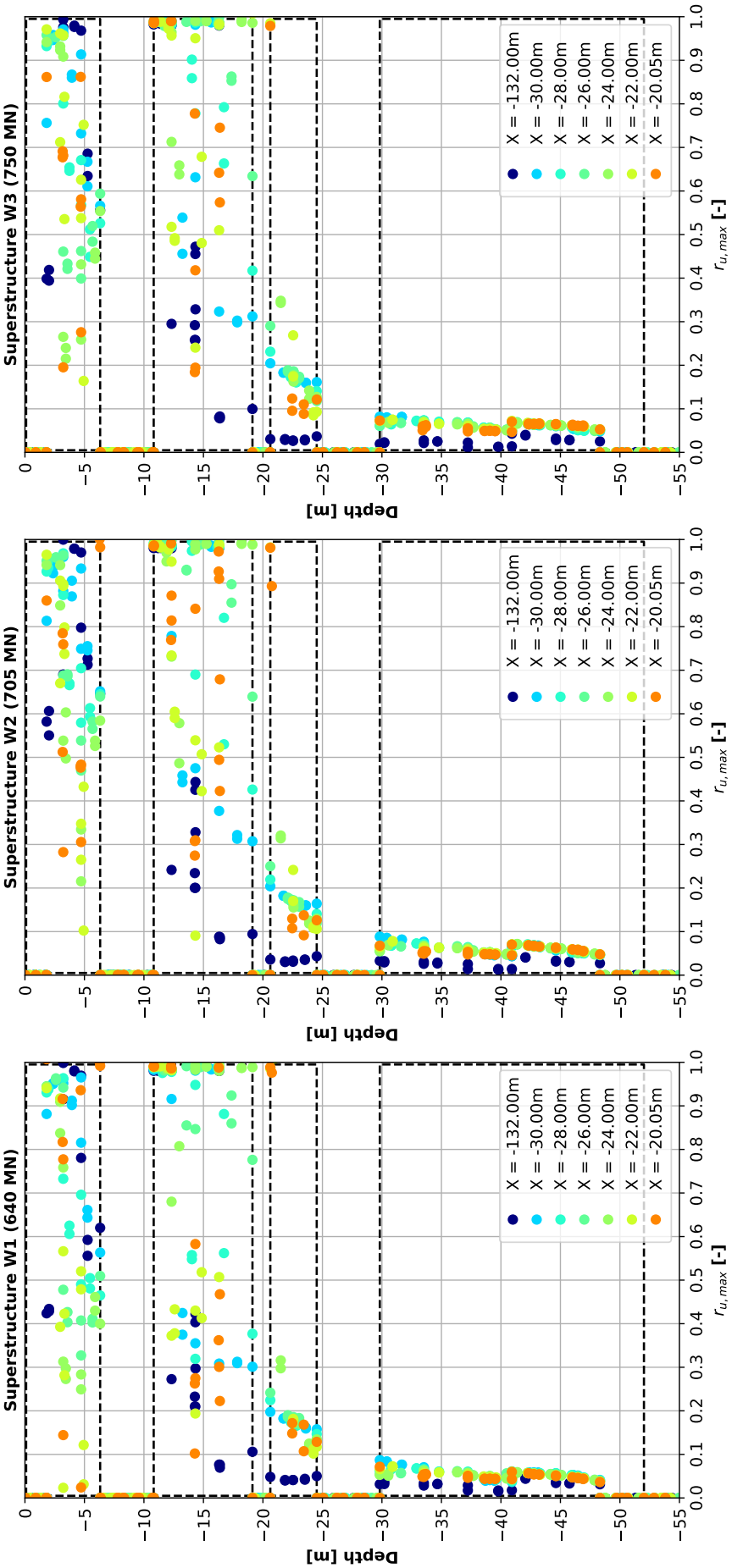

Figure 10.35: Comparative overview of $r_{u,max}$-profiles at select distances in the vicinity of the structure for all three structural loads

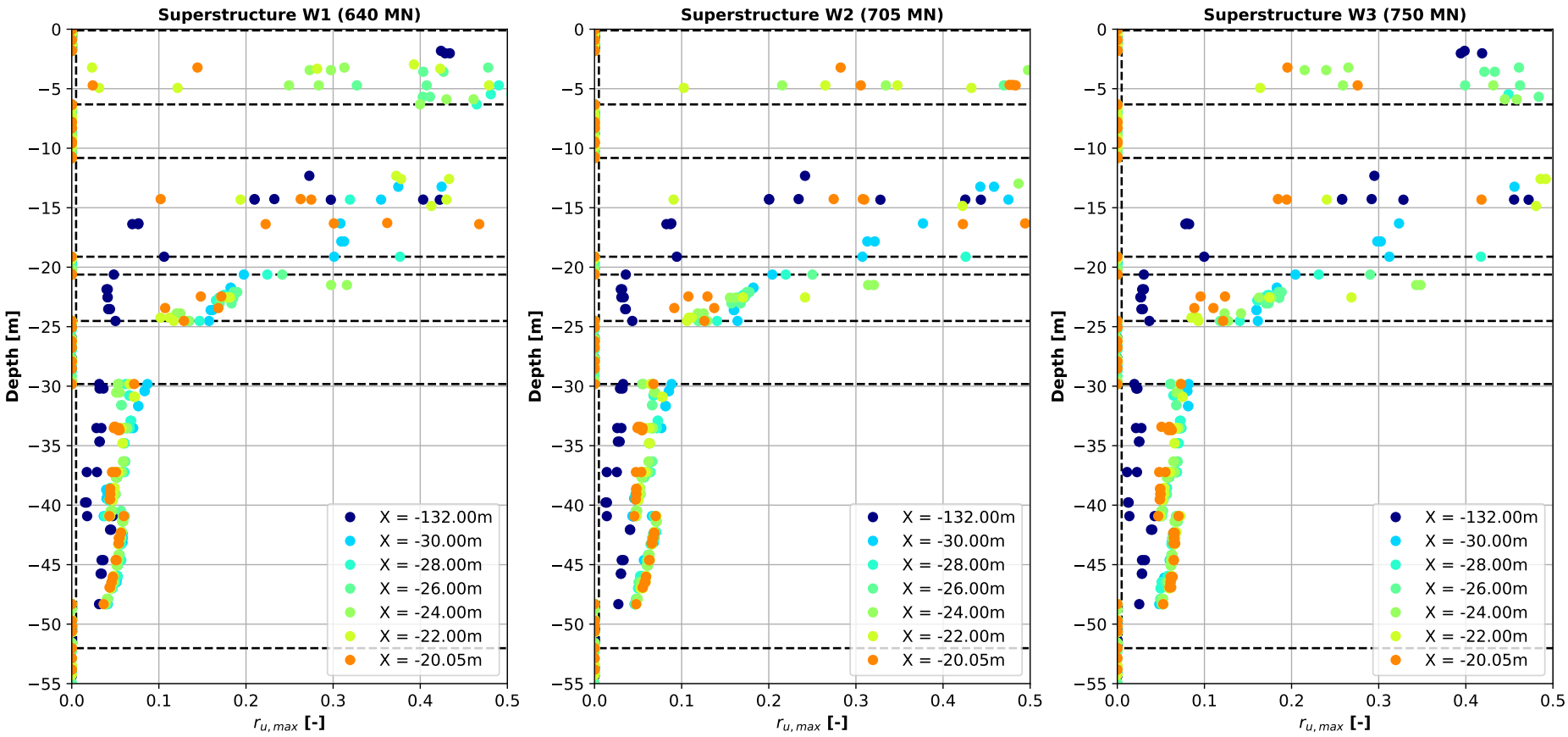

Figure 10.36: Comparative overview of $r_{u,max}$-profiles at select distances in the vicinity of the structure for all three structural loads (reduced r_u-scale)

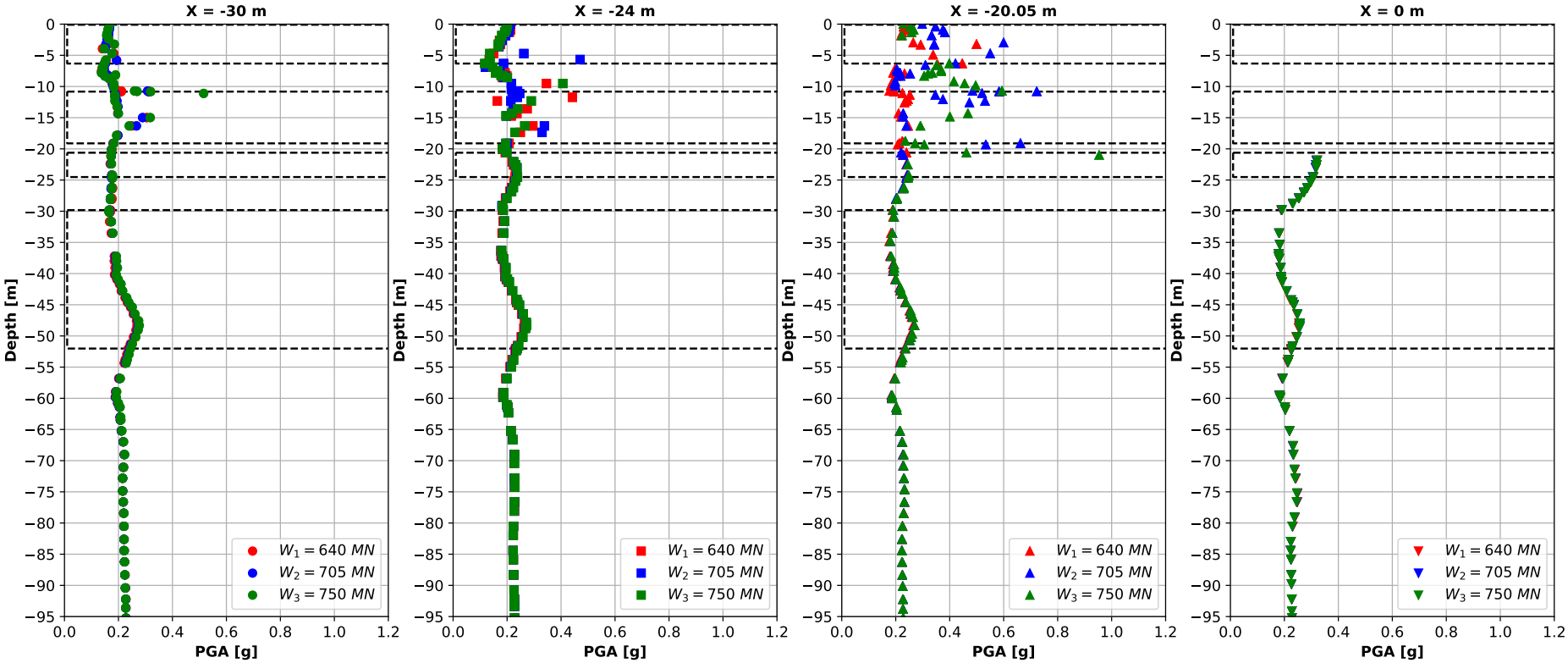

Figure 10.37: Comparative analysis of effect of structural load on *PGA*-profiles at select distances from the centre of the structure (reduced *PGA*-scale)

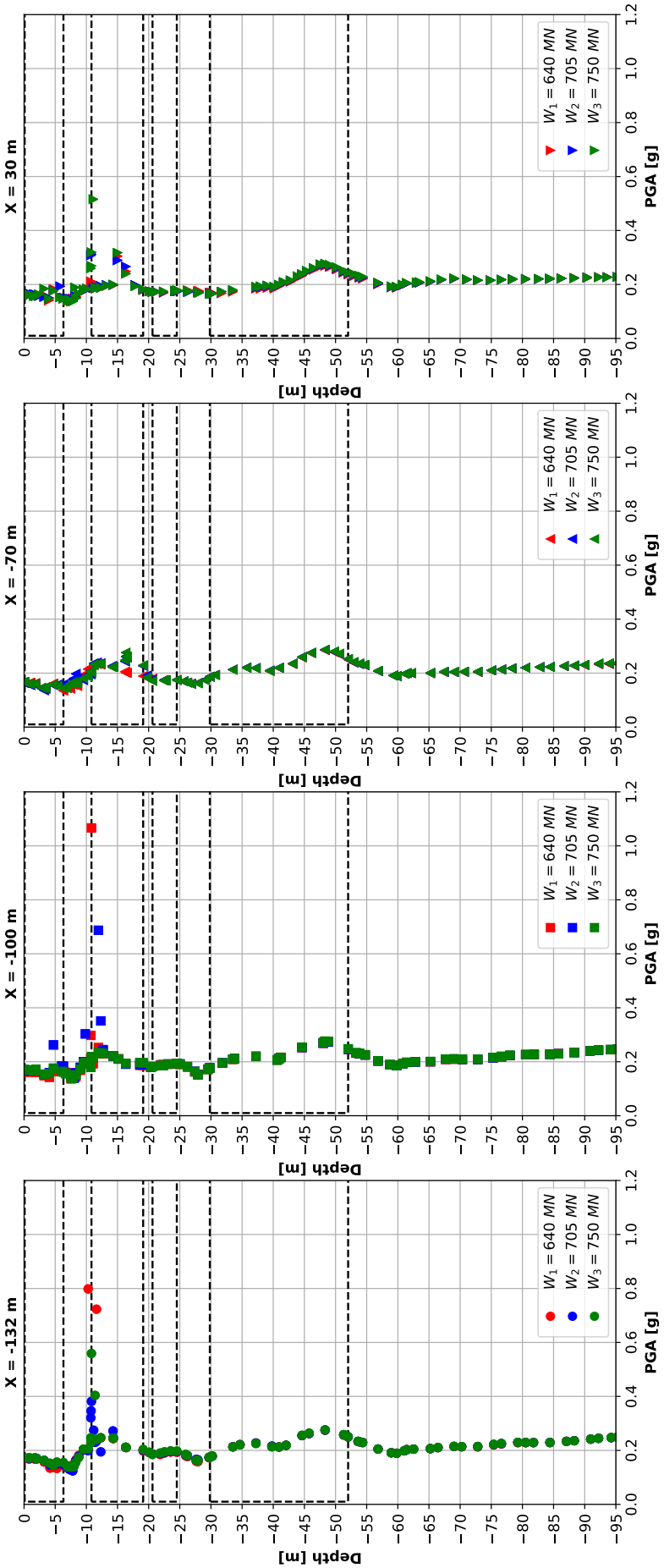

Figure 10.38: Comparative analysis of effect of structural load on PGA-profiles at select distances from the centre of the structure

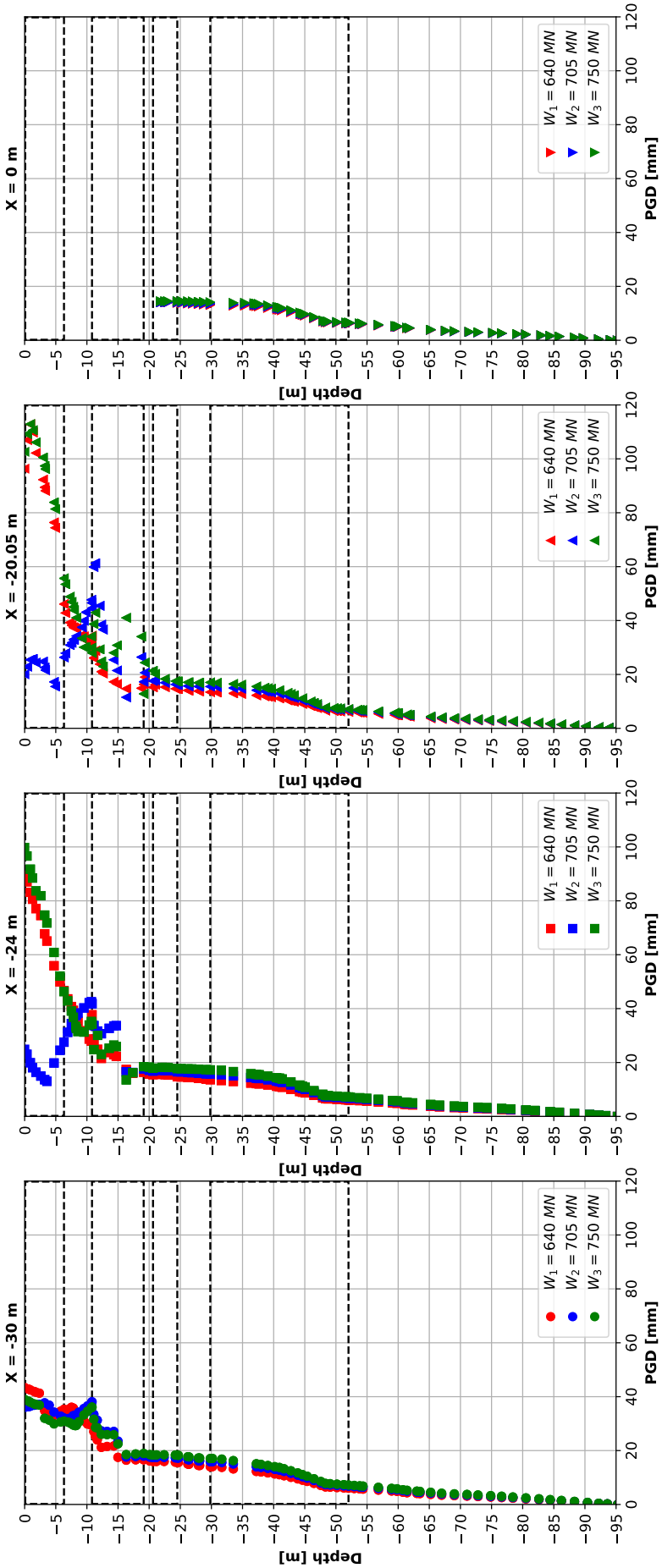

Figure 10.39: Comparative analysis of effect of structural load on PGD-profiles at select distances from the centre of the structure (reduced PGD-scale)

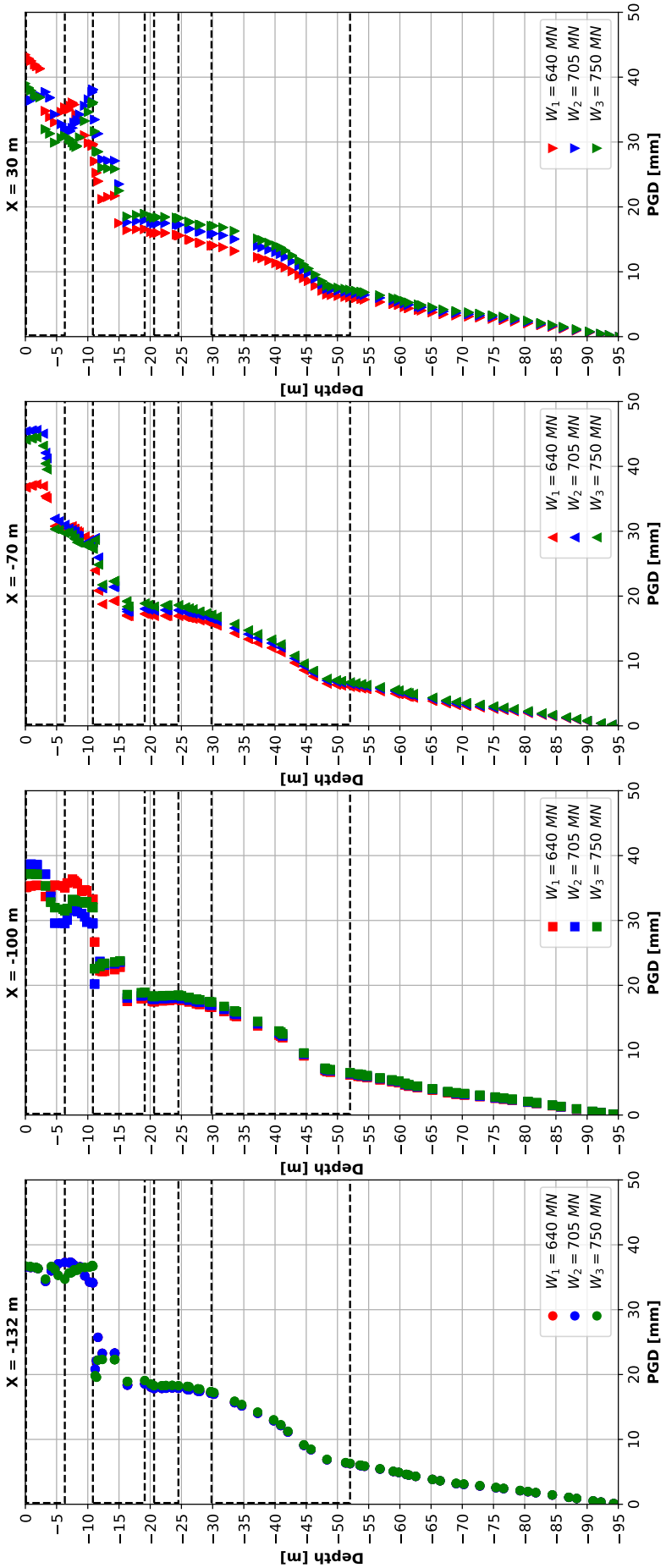

Figure 10.40: Comparative analysis of effect of structural load on PGD-profiles at select distances from the centre of the structure

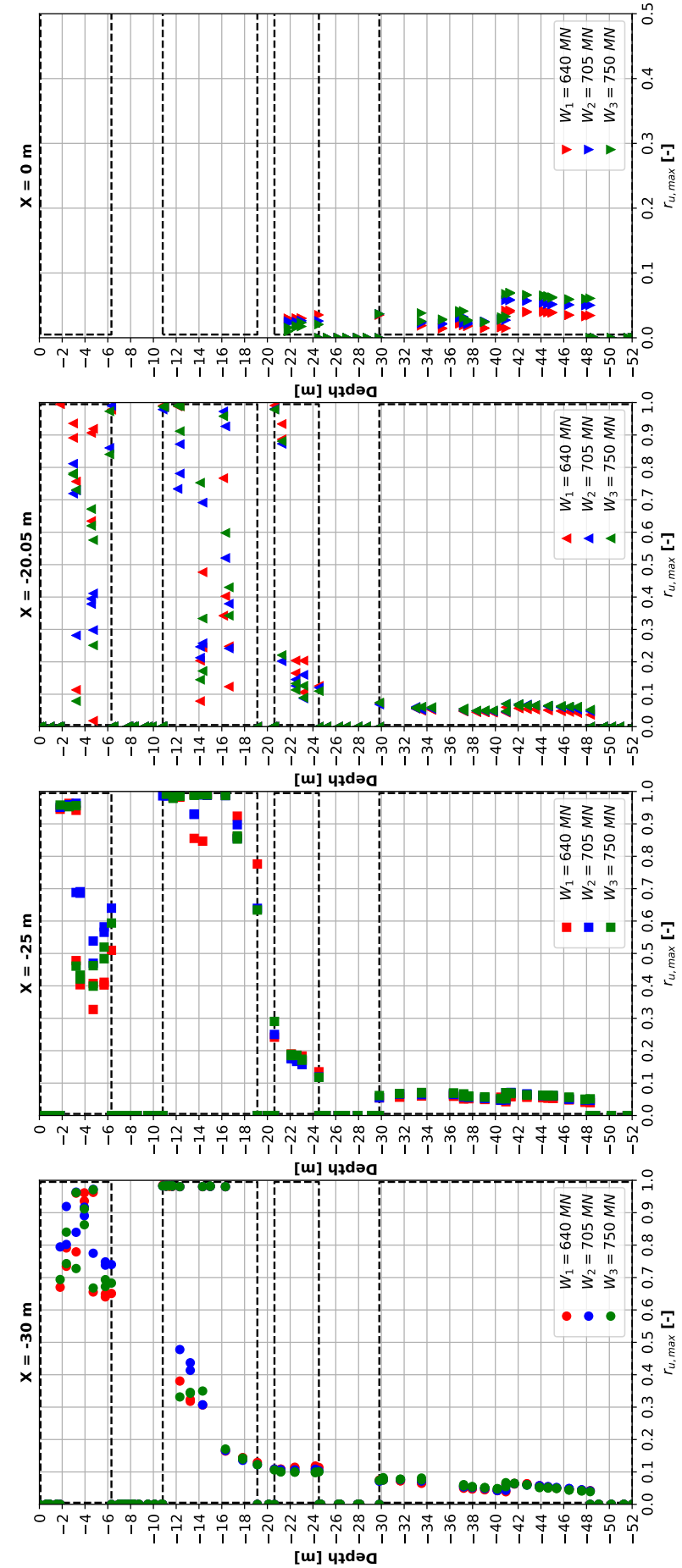

Figure 10.41: Comparative analysis of effect of structural load on $r_{u,max}$-profiles at select distances from the centre of the structure (reduced PGD-scale)

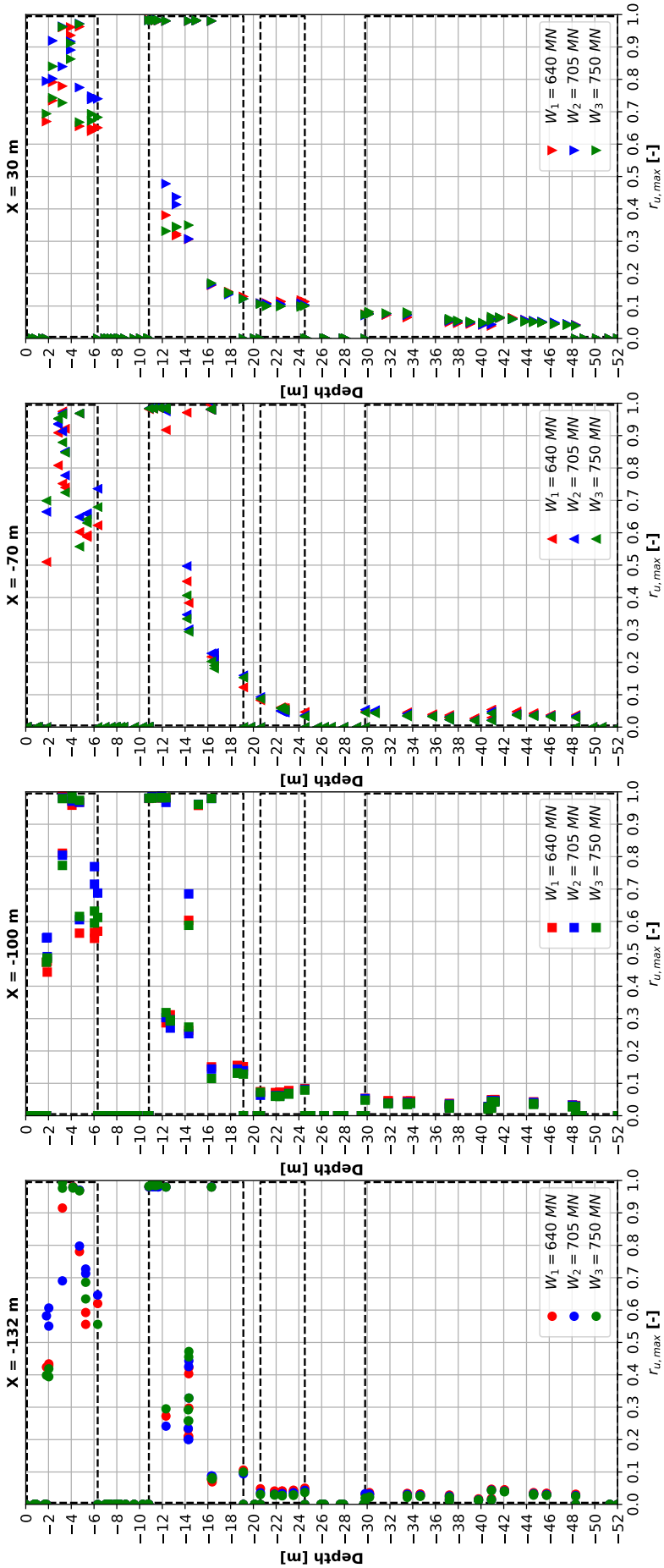

Figure 10.42: Comparative analysis of effect of structural load on $r_{u,max}$-profiles at select distances from the centre of the structure